

“When we long for life without difficulties, remind us that oaks grow strong in contrary winds and diamonds are made under pressure” – Peter Marshall

INDEX

LIST OF ABBREVIATIONS	vi
LIST OF FIGURES	xi
LIST OF TABLES	xvi
NEDERLANDSE SAMENVATTING	1
SUMMARY	9
<u>CHAPTER 1: GENERAL INTRODUCTION AND AIMS</u>	16
1.1 BIOSENSOR DEVELOPMENT IN THE FRAMEWORK OF BIO-ELECTRONICS	17
1.1.1 Description of a biosensor	17
1.1.2 History of biosensor development	18
1.1.3 Biosensor construction	21
1.1.3.1 <i>Biological receptor molecules</i>	21
1.1.3.2 <i>Attachment of biological receptor molecules</i>	21
1.1.3.3 <i>Types of transducers</i>	23
1.2 THE ROLE OF DIAMOND IN BIOSENSORS	26
1.2.1 Classification of diamond	26
1.2.1.1 <i>Natural diamond</i>	26
1.2.1.2 <i>Synthetic diamond</i>	28
1.2.2 Properties of diamond	32
1.2.2.1 <i>Electronic properties</i>	32
1.2.2.2 <i>Physical properties</i>	37
1.2.2.3 <i>Biochemical properties</i>	39
1.3 CLASSIFICATION OF A BIOSENSOR	46
1.3.1 Electrochemical transduction	47
1.3.1.1 <i>Amperometric</i>	47
1.3.1.2 <i>Coulometric</i>	53
1.3.1.3 <i>Potentiometric</i>	53

1.3.1.4	Conductimetric	55
1.3.1.5	Impedimetric.....	57
1.3.1.6	Field-effect	65
1.3.2	Optical transduction principle	69
1.3.2.1	Indirect	69
1.3.2.2	Direct.....	74
1.3.3	Piezo-electric transduction principle	77
1.4	AIM OF THE STUDY	83
 <u>CHAPTER 2: MATERIALS AND METHODS.....</u>		87
2.1	BUFFERS AND SOLUTIONS	88
2.1.1	Homemade.....	88
2.1.1.1	Coating buffer.....	88
2.1.1.2	Conjugation buffer.....	88
2.1.1.3	CRP buffer	88
2.1.1.4	Hybridisation buffer	88
2.1.1.5	10× Phosphate buffered saline (PBS), pH 7.2	89
2.1.1.6	Sodium chloride/sodium citrate (SSC), pH 7.5.....	89
2.1.1.7	10× Tris-buffered saline (TBS), pH 7.6.....	89
2.1.2	Purchased	89
2.2	EXPERIMENTAL PROCEDURES	90
2.2.1	Synthesis, cleaning and hydrogenation of NCD	90
2.2.1.1	Homemade.....	90
2.2.1.2	Purchased	91
2.2.2	Synthesis of NH ₂ -modified and fluorescently labelled dsDNA.....	91
2.2.3	Impedance spectroscopy	92
 <u>CHAPTER 3: EDC-MEDIATED DNA ATTACHMENT TO NANOCRYSTALLINE CVD DIAMOND FILMS</u>		93
	ABSTRACT	94
3.1	INTRODUCTION	95
3.2	MATERIALS AND METHODS	97

3.2.1 Materials	97
3.2.2 NCD functionalisation	97
3.2.3 Denaturation-rehybridisation	99
3.2.4 Fluorescence measurements	100
3.2.5 PCR and gel electrophoresis	101
3.3 RESULTS	102
3.3.1 FITC sensitivity determination of Lightcycler fluorescence module	102
3.3.2 Denaturation and rehybridisation monitored by fluorescence measurements	102
3.3.3 Denaturation and rehybridisation monitored by PCR and gel electrophoresis	103
3.4. DISCUSSION	105
3.5. CONCLUSIONS	108
ACKNOWLEDGEMENTS	109

**CHAPTER 4: TOPOGRAPHICAL AND FUNCTIONAL CHARACTERI-
SATION OF THE SSDNA PROBE LAYER GENERATED THROUGH
EDC-MEDIATED COVALENT ATTACHMENT TO NANOCRYSTAL-
LINE DIAMOND USING FLUORESCENCE MICROSCOPY.**..... 110

ABSTRACT	111
4.1. INTRODUCTION	112
4.2. MATERIALS AND METHODS	114
4.2.1 Materials	114
4.2.2 NCD functionalisation	114
4.2.3 DNA hybridisation	116
4.2.4 Confocal fluorescence microscopy and software	116
4.3. RESULTS AND DISCUSSION	118
4.3.1 Optimisation of EDC-mediated covalent DNA attachment	118
4.3.1.1 <i>Effect of washing buffers</i>	118
4.3.1.2 <i>Effect of probe ssDNA length</i>	121
4.3.1.3 <i>Effect of probe ssDNA concentration</i>	123
4.3.1.4 <i>Effect of 10-undecenoic acid (10-UDA)</i>	124

4.3.1.5 Patterning	127
4.3.2 Optimisation of DNA hybridisation	128
4.3.3 Effect of COOH/OH mixed surface functionalities	130
4.4. CONCLUSIONS	135
ACKNOWLEDGEMENTS	136

CHAPTER 5: TOWARDS A REAL-TIME, LABEL-FREE DIAMOND-

BASED DNA SENSOR	137
ABSTRACT	138
5.1. INTRODUCTION	139
5.2. MATERIALS AND METHODS	141
5.2.1 Materials	141
5.2.2 NCD functionalisation	141
5.2.3 Sensor setup	142
5.2.4 Impedance spectroscopy	143
5.3. RESULTS	145
5.3.1 Impedance changes during hybridisation	145
5.3.1.1 Sequential measurements in a single-cell setup	145
5.3.1.2 Simultaneous measurements in a double-cell setup	146
5.3.1.3 Effect of buffer composition and temperature	148
5.3.2 Impedance changes during denaturation	148
5.3.2.1 Sequential measurements in a single-cell setup	148
5.3.2.2 Simultaneous measurements in a double-cell setup	151
5.3.2.3 Effects of temperature	152
5.4. DISCUSSION	154
5.4.1 Hybridisation	154
5.4.2 Denaturation	159
5.5. CONCLUSIONS	162
ACKNOWLEDGEMENTS	163

CHAPTER 6: TOWARDS A REAL-TIME, LABEL-FREE DIAMOND-

BASED IMMUNOSENSOR	164
---------------------------------	------------

ABSTRACT	165
6.1. INTRODUCTION	166
6.2. MATERIALS AND METHODS	169
6.2.1 Materials.....	169
6.2.2 NCD functionalisation.....	169
6.2.3 Reference ELISA procedure to verify formation of antibody/antigen-complex on NCD	169
6.2.4 Sensor setup	170
6.2.5 Impedance spectroscopy	172
6.3. RESULTS	173
6.3.1 Reference ELISA procedure to verify formation of antibody/antigen-complex on NCD	173
6.3.2 Specificity of the immunosensor.....	174
6.3.2.1 Low frequency.....	174
6.3.2.2 High frequency.....	176
6.3.3 Sensitivity of the immunosensor.....	177
6.3.3.1 Low frequency.....	177
6.3.3.2 High frequency.....	179
6.4. DISCUSSION.....	180
6.4.1 Specificity	180
6.4.2 Sensitivity	183
6.5. CONCLUSIONS	186
ACKNOWLEDGEMENTS	187
<u>CHAPTER 7: DISCUSSION AND CONCLUDING REMARKS.....</u>	188
7.1 DISCUSSION.....	189
7.2 CONCLUDING REMARKS AND FUTURE PROSPECTS	205
REFERENCE LIST	210
CURRICULUM VITAE	221
DANKWOORD	224

LIST OF ABBREVIATIONS

1-UD	= 1-undecene
9-DO	= 9-decen-1-ol
10-UDA	= 10-undecenoic acid
A	= adenine
	= ampere
AC	= alternating current
Ag	= silver
AgCl	= silver chloride
AP	= alkaline phosphatase
Au	= gold
B	= boron
BSA	= bovine serum albumin
C	= capacitance
	= carbon
	= cytosine
CBM	= conduction band minimum
CH ₃	= methyl
CH ₄	= methane
CO ₂	= carbon dioxide
COOH	= carboxylic acid
CRP	= C-reactive protein
cTnI	= cardiac troponin I
Cu	= copper
CV	= Cyclic Voltammetry
CVD	= Chemical Vapour Deposition
	= cardiovascular disease
Cy3	= cyanine 3
Cy5	= cyanine 5
DGGE	= Denaturing Gradient Gel Electrophoresis
DNA	= deoxyribonucleic acid
ssDNA	= single-stranded DNA

dsDNA	= double-stranded DNA
cDNA	= complementary DNA
dNTP	= deoxiribonucleoside triphosphate
EDC	= 1-ethyl-3-(3-dimethylaminopropyl)-carbodiimide
E_F	= Fermi level
EIS	= Electrochemical Impedance Spectroscopy
ELISA	= Enzyme-Linked Immunosorbent Assay
eV	= electron volts
FET	= field-effect transistor
FITC	= fluorescein isothiocyanate
G	= guanine
Ge	= germanium
H	= hydrogen
H_2	= hydrogen gas
H_2O	= water
H_2O_2	= hydrogen peroxide
H_2SO_4	= sulphuric acid
HBV	= Hepatitis B Virus
HCl	= hydrogen chloride
HFCVD	= hot filament chemical vapour deposition
HIV	= Human Immuno-deficiency Virus
HPHT	= High Pressure – High Temperature
HRP	= horse radish peroxidise
Hz	= Herz
kHz	= kilohertz
MHz	= megahertz
I	= current
IDE	= interdigitated electrode
Ig	= immunoglobulin
IR	= infrared
ISE	= ion-sensitive electrode
ITO	= indium-tin oxide
K	= Kelvin
KNO_3	= potassium nitrate

L	= inductance
M	= molar
mM	= millimolar (10^{-3} M)
μ M	= micromolar (10^{-6} M)
nM	= nanomolar (10^{-9} M)
pM	= picomolar (10^{-12} M)
fM	= femtomolar (10^{-15} M)
MCD	= microcrystalline diamond
MES	= 2-(N-morpholino)-ethanesulphonic acid
MPECVD	= microwave plasma enhanced chemical vapour deposition
μ	= chemical potential of the electrolyte
N	= nitrogen
NAD ⁺	= nicotinamide adenine dinucleotide
NADH	= reduced form of NAD ⁺
NADPH	= reduced form of NADP ⁺ (nicotinamide adenine dinucleotide phosphate)
NaOH	= sodium hydroxide
NCD	= nanocrystalline diamond
NH ₂	= amino
NH ₃	= ammonia
NH ₄ ⁺	= ammonium ion
NHS	= N-hydroxy-succinimide
O ₂	= oxygen
OH	= hydroxyl
ω	= frequency
P	= phosphor
Pa	= pascal
hPa	= hectopascal
PAA	= poly-acrylic acid
PAH	= Phenylalanine Hydroxylase
PANI	= poly-aniline
PBS	= phosphate buffered saline
PCD	= polycrystalline diamond
PCR	= Polymerase Chain Reaction

ϕ	= phase shift
Pt	= platinum
Q	= constant phase element
QCM	= Quartz Crystal Microbalance
R	= resistance
RNA	= ribonucleic acid
mRNA	= messenger RNA
SAM	= self-assembled monolayer
SCD	= single-crystalline diamond
sccm	= standard cubic centimetre per minute at STP (standard temperature and pressure)
SCE	= saturated calomel electrode
SDS	= sodium dodecyl sulphate
SELEX	= Systematic Evolution of Ligands by Exponential Enrichment
SEM	= Scanning Electron Microscope
SH	= thiol
Si	= silicon
SiO ₂	= silicon dioxide
σ	= sigma
SNP	= single nucleotide polymorphism
SOCl ₂	= thionyl chloride
SPR	= Surface Plasmon Resonance
SSC	= sodium chloride/sodium citrate
SSMCC	= sulphosuccinimidyl-4-(N-maleimido-methyl)cyclohexane-1-carboxylate
STR	= small tandem repeat
SULT1A1*2	= polymorphism of the gene for cytosolic sulfotransferase
T	= thymidine
TFAAD	= trifluoro-acetamide acid
θ	= resonance angle
Ti	= titanium
TIR	= Total Internal Reflection
TIRF	= Total Internal Reflection Fluorescence
UNCD	= ultrananocrystalline diamond

UV = ultraviolet
V = voltage, volts
VBM = valence band maximum
Vif = virion infectivity factor
W = Watt
Z = impedance
Re(Z) = real part of Z
Im(Z) = imaginary part of Z

LIST OF FIGURES

Figure 1.1: Graphical representation of a biosensor, including a biological receptor component being exposed to a target-containing sample, and a physical transducer component.....	18
Figure 1.2: Historical timeline displaying the evolutionary milestones in biosensor development.	19
Figure 1.3: Schematic diagram of the lattice structure of diamond, showing the tetrahedral orientation of each C atom.	27
Figure 1.4: SEM image of a 600 μm thick freestanding homo-epitaxial SCD film grown at a 10% CH_4/H_2 ratio removed from the substrate by laser cutting	30
Figure 1.5: SEM images of a MCD film on Si.....	31
Figure 1.6: SEM images of a NCD film on Si.....	31
Figure 1.7: SEM images of a UNCD film on Si.	32
Figure 1.8: Cyclic voltammograms comparing various electrode materials.....	33
Figure 1.9: Energies of the valence and conduction band edges of several conventional semiconductors, including H-terminated and as-grown diamond relative to the vacuum level, E_{VAC}	34
Figure 1.10: Schematic diagram of the diamond/electrolyte interface.....	35
Figure 1.11: E_{F} and μ alignment at the diamond/electrolyte interface at pH 0 and pH 14.....	35
Figure 1.12: Schematic diagram of an n-type and p-type semiconductor material at the atomic level.....	37
Figure 1.13: Reaction process used by Ushizawa for the covalent attachment of PCR-amplified dsDNA to thymidine-modified diamond powder.....	40

Figure 1.14:	
Reaction process used by Wang for the covalent attachment of thiolated ssDNA to aminophenyl-modified P-type SCD.....	42
Figure 1.15:	
Reaction process used by Yang for the covalent attachment of thiolated ssDNA to photochemically activated NCD.	43
Figure 1.16:	
Schematic diagram of a third generation amperometric measurement principle.	49
Figure 1.17:	
Schematic diagram of the potentiometric measurement principle.....	53
Figure 1.18:	
Bode plot of the complex impedance, Z , and of the phase shift, ϕ , versus frequency, ω , for a parallel RC circuit.....	58
Figure 1.19:	
Nyquist plot, displaying $-\text{Im}(Z)$ versus $\text{Re}(Z)$, for a parallel RC circuit.....	59
Figure 1.20:	
Generation of thermodynamic equilibrium in p-type and n-type semiconductors through downward and upward band bending, respectively.....	61
Figure 1.21:	
Schematic diagram of a FET structure.	66
Figure 1.22:	
Schematic diagram of the varying source-drain current density as a function of semiconductor type and gate voltage.....	67
Figure 1.23:	
Schematic diagram of an oligonucleotide microarray and a cDNA microarray...	73
Figure 1.24:	
Schematic diagram of SPR.....	76
Figure 3.1:	
Photoattachment of 10-UDA acid to the NCD surface through irradiation with 254 nm UV light.....	97
Figure 3.2:	
Covalent attachment of FITC-labelled NH_2 -modified dsDNA to 10-UDA on an NCD substrate using an EDC-mediated reaction.	98
Figure 3.3:	
Denaturation-rehybridisation-washing (d-r-w) cycle on COOH-modified NCD..	100

Figure 3.4: Fluorescence detection of FITC-labelled DNA.....	102
Figure 3.5: Results obtained for paramagnetic beads after the first and the second denaturation-rehybridisation reaction via 2 % agarose gel electrophoresis.	103
Figure 3.6: Analysis of the denaturation-rehybridisation cycles on NCD samples via 2 % agarose gel electrophoresis.	104
Figure 4.1: Comparison of fluorescence intensity of IMO NCD samples after treatment with 30 pmol of NH ₂ -modified and Alexa 488-labelled ssDNA (8 b) using different washing steps.....	120
Figure 4.2: Comparison of fluorescence intensity of rho-BeSt NCD samples after covalent attachment of DNA molecules of different lengths.....	122
Figure 4.3: Comparison of fluorescence intensity between rho-BeSt NCD samples treated with varying amounts of NH ₂ -modified Alexa 488-labelled probe ssDNA.....	123
Figure 4.4: Comparison of fluorescence intensity between IMO NCD samples treated with varying amounts of NH ₂ -modified Alexa 488-labelled probe ssDNA.	124
Figure 4.5: Comparison between differently functionalised diamond samples for their suitability for functional ssDNA attachment.	125
Figure 4.6: Fluorescence image of a diamond sample with covalently attached NH ₂ - modified and Alexa 488-labelled ssDNA (8 b) after patterning with a Cu TEM grid (~3 mm in diameter, 45 μm ² open squares, 20 μm wide bars) during photochemical modification.	128
Figure 4.7: Relative fluorescence intensity values of ssDNA (36 b)-modified IMO NCD samples after hybridisation with complementary and 1-mismatch target ssDNA (29 b) at different hybridisation and stringency washing temperatures.	129
Figure 4.8: Relative fluorescence intensity values of NCD samples with different ratios of mixed COOH- and OH-functionalities after covalent attachment of 300 pmol of NH ₂ -modified and Alexa 488-labelled ssDNA (8 b) and their corresponding negative controls.	131

Figure 4.9:	Relative fluorescence intensity values of NCD samples with different ratios of mixed COOH- and OH-functionalities after covalent attachment of 300 pmol of NH ₂ -modified ssDNA (36 b) and hybridisation with 600 pmol of Alexa 488-labelled complementary and non-complementary target ssDNA (29 b).	132
Figure 4.10:	Comparison of hybridisation efficiencies on NCD samples modified with different amounts of NH ₂ -modified unlabelled probe ssDNA.....	133
Figure 5.1:	SEM images of a IMO and a rho-BeSt NCD sample.....	141
Figure 5.2:	Schematic representation of the double-cell setup for the simultaneous measurements.....	143
Figure 5.3:	Sequential impedance measurement of a hybridisation reaction with complementary and 1-mismatch target DNA.....	146
Figure 5.4:	Simultaneous impedance measurement of a hybridisation reaction with complementary and 1-mismatch target DNA.....	147
Figure 5.5:	Sequential impedance measurement of a denaturation reaction of complementary and non-complementary DNA.....	149
Figure 5.6:	Real-time denaturation curves at 100 Hz and 1 MHz for complementary, 1-mismatch or non-complementary target DNA.....	150
Figure 5.7:	Simultaneous impedance measurement of a denaturation reaction of complementary and 1-mismatch DNA.	152
Figure 5.8:	The electrical circuit model used for fitting the impedance data.	155
Figure 5.9:	Nyquist plot of the complex impedance before and after hybridisation with complementary target DNA in 10× PCR buffer..	156
Figure 5.10:	Nyquist plot of the complex impedance before and after heating the setup from 30°C to 50°C in 10× PCR buffer.	157
Figure 5.11:	Schematic representation of the energy diagram at the diamond-solution interface.	159

Figure 5.12:	
Formation of a new equilibrium during denaturation.....	160
Figure 6.1:	
Graphical diagrams of the immunosensor setups used in the experiments....	171
Figure 6.2:	
Colorimetric measurements of differently functionalised NCD samples, displaying the efficiency of the antibody/antigen-complex formation and the amount of aspecific adsorption of CRP and AP-labelled anti-CRP.....	173
Figure 6.3:	
Nyquist plots showing the effect of antigen addition on the impedance.	175
Figure 6.4:	
Effect of 0.1× PBS after CRP and non-specific FITC addition on the impedance at 1 MHz.	176
Figure 6.5:	
Real-time impedance spectra at 100 Hz illustrating the concentration sensitivity of the sensor for CRP.	178
Figure 6.6:	
Real-time impedance spectra at 1 MHz illustrating the concentration sensitivity of the sensor for CRP.	179
Figure 6.7:	
The electrical circuit model used for fitting the impedance data.	180
Figure 6.8:	
Decrease in capacitance of the molecular layer due to its increased thickness by the CRP antigens that have been recognised by anti-CRP.	181
Figure 6.9:	
The shapes of the Nyquist plots for the samples in the four-well setup.	184

LIST OF TABLES

Table 1.1: Overview comparing the physical properties of three semiconductors: diamond, Si, and Ge.....	25
Table 1.2: Biosensor classification based on the type of biological receptor molecule.	46
Table 1.3: Biosensor classification based on the transduction principle.	46
Table 1.4: Literary overview of the types of biosensors, classified according to transduction principle and biological receptor molecule, including key measurement parameters.	81
Table 5.1: Exponential decay time during the first minutes of denaturation, summarised according to hybridisation and denaturation parameters.	153
Table 5.2: Results of fitting the impedance spectra before and after hybridisation with complementary DNA at 30°C in 10× PCR buffer	156
Table 5.3: Results of fitting the impedance spectra before and after heating the setup from 30°C to 50°C in 10× PCR buffer	158
Table 6.1: Results of fitting the impedance spectra before and after addition of CRP and FITC.....	181
Table 7.1: Summary of effects observed with a prototype DNA-sensor during hybridisation and denaturation.	194
Table 7.2: Overview comparing typical features between three different methods of mutation analysis.....	198
Table 7.3: Summary of effects observed with the immunosensor during selectivity and sensitivity testing.....	200

NEDERLANDSE SAMENVATTING

Bio-elektronica heeft de evolutie van 'micro'-wetenschap naar 'nano'-wetenschap sterk gestimuleerd. Dit is een onderdeel van de wetenschap dat de prestaties in de moleculaire biologie koppelt aan de successen in de elektronica om een hogere gevoeligheid, specificiteit en snelheid te bekomen. Biosensoren hebben een cruciale rol gespeeld in dit onderzoeksgebied. Dit zijn analytische toestellen die bestaan uit biomoleculen die dienst doen als herkenningselementen, gebonden aan een vaste drager, een transducer. De transducer 'vertaalt' de biologische herkenning tussen het receptormolecule en zijn target naar een uitleesbaar signaal. Het biosensoronderzoek kende zijn start bij de uitvinding van de zuurstof (O_2)-elektrode door Clark *et al.* in 1956 [Cla56]. Sindsdien is enorme vooruitgang geboekt wat biosensorontwikkeling betreft, en vele biosensoren zijn reeds gevestigde waarden in de klinische en wetenschappelijke wereld. Biosensoren kunnen ingedeeld worden volgens het biologische receptor-type vastgehecht aan de transducer, of volgens het principe van signaaltransductie, zoals beschreven in **Hoofdstuk 1**. Echter, slechts weinige daarvan kennen hun toepassing in point-of-care-gebruik. Het succes en de toepasbaarheid van biosensoren als diagnostische en analytische point-of-care-apparaten is afhankelijk van vier vereisten. Zij dienen gevoelig, specifiek, snel en goedkoop te zijn. Vele populaire transductiematerialen, zoals silicium (Si), zijn ontvankelijk voor hydrolyse, hetgeen leidt tot het verlies van bioreceptormoleculen van het Si-oppervlak en daarmee tot de instabiliteit van het sensorplatform. De onstabiele biofunctionalisatie verslechtert uiteraard de gevoeligheid en de specificiteit van de sensor. Om deze reden verschuift de aandacht stilaan naar diamant, hetgeen Si en germanium (Ge) op vele gebieden overtreft. De belangrijkste eigenschappen van synthetisch diamant worden aangehaald in het tweede deel van **Hoofdstuk 1**. Bovendien wordt in vele gevallen een eindpunt-detectie toegepast, gebaseerd op de vergelijking tussen vóór en na toevoeging van het target. Dit vertraagt niet alleen de analysetijd, maar verliest ook waardevolle informatie uit het oog die kon worden bekomen tijdens de reactie (vooral wat betreft de DNA-sensor). Dit is het geval voor een aantal elektrochemische meettechnieken, en ook voor

optische biosensoren die target-labelling vereisen. Optische detectie stelt nog een bijkomende uitdaging, omdat zowel de reagentia vereist voor de labelling als het gespecialiseerde materiaal voor de label-afhankelijke target-detectie duur zijn, wat implementatie in point-of-care-toepassingen bijna onmogelijk maakt. Een bijkomend aspect dat de kostprijs nog zal verhogen, is het feit dat de meeste biosensoren niet herbruikbaar zijn.

In deze PhD-thesis wilden wij een generisch platform ontwikkelen dat in staat is om de vier hierboven genoemde vereisten te vervullen, terwijl de veel voorkomende uitdagingen betrokken bij biosensoronderzoek worden aangepakt. In deze studie ontwikkelden wij een real-time, en dus snel, label-vrij impedimetrisch biosensorplatform dat gebaseerd is op chemisch inert nanokristallijn diamant (NCD). Synthetisch NCD blijkt een flexibel transducer-materiaal voor het bekomen van stabiele interfaces met DNA en eiwitten (antilichamen). Voor het prototype van de DNA-sensor, bereikten wij single nucleotide polymorphism (SNP)-gevoeligheid, hetgeen klinisch relevant is wegens het groot aantal genetische aandoeningen die te wijten zijn aan puntmutaties. Bovendien toonden we aan dat ons real-time DNA-sensor prototype zowel gebruikt kan worden gedurende de hybridisatiereactie als gedurende de denaturatiereactie. Dit geeft belangrijke bijkomende informatie wat betreft de sequentie, waarvan gebruik kan worden gemaakt in toekomstige methoden voor mutatie-identificatie. Het is eveneens de eerste keer dat real-time denaturatie wordt toegepast in een biosensor. Voor het prototype van een C-reactive protein (CRP)-gerichte immunosensor werd een concentratie-afhankelijke gevoeligheid bekomen in het fysiologisch relevante concentratiegebied (1 μ M – 10 nM). De aangetoonde stabiliteit van de biofunctionalisatie van NCD met DNA of eiwit, in combinatie met de herbruikbaarheid van het NCD, en, in geval van de DNA-sensor, de regenereerbaarheid van het NCD tot op het probe-niveau via denaturatie, maakt van onze sensor een veelbelovend generisch platform voor gebruik in biosensoren in lab-on-chip of point-of-care-toepassingen. Dit laatste is mogelijk omdat er geen label, en een relatief goedkope impedantie-analyser is vereist. De volgende paragrafen geven een samenvatting hoe dit generisch biosensor-platform werd ontwikkeld.

In **Hoofdstuk 3** werd aangevangen met de ontwikkeling van een eenvoudige maar efficiënte tweestapsreactie om DNA covalent aan NCD te hechten. De methode is gebaseerd op de fotochemische aanhechting van een ω -onverzadigd vetzuur, 10-undecenzuur (10-UDA), aan H-getermineerd NCD, gevolgd door de aanhechting van amino (NH_2)-gemodificeerd DNA aan de fotochemisch geïntroduceerde carboxyl (COOH)-groepen op het NCD met 1-ethyl-3-(3-dimethylaminopropyl)-carbodiimide (EDC). Onze procedure biedt een vereenvoudiging van deze ontwikkeld door Yang *et al.* [Yan02]. Bovendien is EDC een zero-length crosslinker, waarmee wordt bedoeld dat het molecuule slechts de reactie medieert, maar geen deel zal uitmaken van de uiteindelijke peptidebinding tussen het DNA en het 10-UDA op het NCD. Hierdoor zullen de DNA-moleculen zich dichterbij het oppervlak bevinden, hetgeen elektronische hybridisatie-detectie zal bevorderen. Echter, de lengte van de DNA-moleculen gebruikt in ons eerste prototype, 250 bp Polymerase Chain Reaction (PCR) amplicons, zorgden voor wat praktische problemen. Lange DNA-moleculen zullen zich niet enkel aan het oppervlak aanhechten via hun eindtermini, maar zullen een conformatie aannemen die lijkt op flexibele krullen die op meerdere plaatsen van hun lengte aan het oppervlak vasthechten. Dit veroorzaakte een lage bindingscapaciteit en de aanwezigheid van niet-covalent geadsorbeerd DNA. Ondanks het feit dat het onmogelijk bleek de gebonden DNA-moleculen rechtstreeks te detecteren via fluorescentie-microscopie, werd via PCR en gelelektroforese, uitgevoerd op reactievloeistoffen van herhaalde denaturaties en hybridisaties, aangetoond dat een EDC-gemedieerde covalente en functionele aanhechting van DNA aan NCD werd bewerkstelligd.

In **Hoofdstuk 4** werd onze immobilisatietechniek verbeterd om de lage bindingscapaciteit en de niet-covalente adsorptie van DNA aan NCD te elimineren. Het verfijnen van deze procedure leidde tot de aanhechting van een monolaag van DNA aan 10-UDA in plaats van tot een opstapeling van 10-UDA waarvan enkel de bovenste, niet-gebonden en dus oncontroleerbare laag beschikbaar was voor DNA-aanhechting. Bovendien werd aangetoond dat kort ssDNA, hetgeen een conformatie zal aannemen van stijve, rechtopstaande staven, efficiënter was voor de aanhechting aan NCD dan langer DNA. Geometrisch gezien zullen immers meer moleculen in deze rechtopstaande conformatie op het oppervlak passen. Een DNA-hoeveelheid van 10^{14} moleculen

(300 pmol) in het reactiemengsel gaf de hoogste, nog steeds functionele, DNA-dichtheid op het NCD. Het feit dat dit kon worden gereproduceerd op NCD-oppervlakken van een andere bron van herkomst toonde de robuustheid aan van de bindingsprocedure. Deze hoeveelheid DNA in het reactiemengsel is uiteraard een overschatting van de uiteindelijke hoeveelheid aangehecht DNA. De feitelijke dichtheid zal de meest geciteerde waarde in de literatuur benaderen: 10^{12} moleculen.cm⁻². COOH-terminatie bleek eveneens cruciaal voor DNA-aanhechting. Immers, geen of niet-functioneel DNA werd gebonden aan H-getermineerd en O-getermineerd NCD, respectievelijk. Het feit dat H-getermineerd NCD een efficiënte barrière vormt tegen niet-covalente adsorptie is veelbelovend in het gebied van de micro-elektronica, waar de lokatie van de proben op voorhand dient te worden bepaald. Deze unieke eigenschap laat een reproduceerbare, makkelijke en efficiënte manier toe voor het 'arrayen' van het sensoroppervlak. Zelfs al zou de H-terminatie gedeeltelijk teniet worden gedaan door O₂, zal dit niet leiden tot functionele aanhechting van DNA in deze gebieden. De H-getermineerde regio's zullen nog steeds de signaal-genererende gebieden zijn. Wij onderzochten ook het effect van gemengde functionele groepen op het NCD-oppervlak, in navolging van Huang *et al.*, die een hogere bindingsefficiëntie van antilichamen en een lagere niet-specifieke adsorptie van analyten waarnamen op Si-substraten [Hua05]. Echter, wanneer NCD-substraten gefunctionaliseerd met COOH-groepen werden vergeleken met NCD-substraten gefunctionaliseerd met carboxyl (COOH)- en hydroxyl (OH)-groepen in verschillende verhoudingen, bleken enkel de COOH-getermineerde NCD-substraten te resulteren in functioneel aangehecht DNA. De OH-groepen vormden waarschijnlijk fosfaatesters met de ruggengraat in het DNA, wat leidt tot een DNA-conformatie die ongeschikt is voor hybridisatie. Deze studie resulteerde in een zeer reproduceerbare oppervlaktefunctionalisatie van het NCD met covalent gebonden ssDNA, dat een optimale functionele activiteit en unieke 'arraying'-eigenschappen vertoont wanneer H-getermineerd, DNA-afstotend NCD wordt gebruikt, gescheiden van regio's met gebonden DNA.

In **Hoofdstuk 5** ontwikkelden wij een prototype van een impedimetrische DNA-sensor gebruik makend van onze verbeterde biofunctionalisatieprocedure voor de aanhechting van DNA aan NCD. Op deze manier bereikten we SNP-gevoeligheid in een real-time-analyse vanuit twee afzonderlijke maar

aanvullende uitgangspunten: tijdens de hybridisatie en tijdens de denaturatie. Tijdens de hybridisatie in 10× PCR buffer werd een real-time daling waargenomen in de complexe impedantie voor complementair target DNA in het frequentiegebied tussen 1000 en 1500 Hz. Deze daling werd weerspiegeld in een verkleining van de semi-cirkel van de Nyquistplot. Via het fitten aan een equivalent circuit, bestaande uit een vloeistofweerstand R_s , een capaciteit C en een bijhorende weerstand R_C in parallel, en een constante-fase-element Q met een bijhorende weerstand R_Q in parallel, kon deze verkleining van de semi-cirkel verklaard worden door een daling in R_Q , verbonden aan het ruimte-ladingsgebied. Door de toenadering van negatief geladen DNA naar het NCD-oppervlak tijdens de hybridisatie worden positieve ladingsdragers in het lichtjes p-type NCD aangetrokken tot het oppervlak, hetgeen de depletiezone vernauwt en de weerstand verlaagt. Tijdens hybridisatie met 1-mismatch DNA werd geen significant effect waargenomen. Dit onderscheid was zichtbaar binnen 10 minuten. Het gebruik van 10× PCR buffer laat bovendien de integratie in een lab-on-chip toe samen met een amplificatie-onderdeel, gebruik makend van hetzelfde buffersysteem. Zeer interessant was het bekomen van een betrouwbaar onderscheid tussen complementair, 1-mismatch en niet-complementair DNA in real-time gedurende de eerste minuten van de denaturatiereactie met 0.1 M natriumhydroxide (NaOH). In het frequentiegebied tussen 100 en 15000 Hz, hetgeen overeenkomt met de moleculaire laag en de dubbellaag (100 – 500 Hz), en met het ruimte-ladingsgebied (500 – 15000 Hz), werd een impedantiestijging waargenomen. Denaturatie verwijdert de DNA-strengen en hun geassocieerde tegenionen van het NCD-oppervlak. Dit verklaart de geobserveerde impedantiestijging in de moleculaire laag. Omdat meer duplexen werden gevormd tijdens de complementaire hybridisatie dan tijdens de hybridisatie met 1-mismatch DNA, is de impedantiestijging groter tijdens de complementaire denaturatie. Niet-complementair DNA zal waarschijnlijk enkel hebben geadsorbeerd aan het NCD-oppervlak. Aangezien nabijheid tot het oppervlak van de elektrode recht evenredig is met de efficiëntie van signaaldetectie, hetgeen ook een significant veldeffect veroorzaakte gedurende de 'hybridisatie' met niet-complementair DNA, zal de verwijdering van deze moleculen de grootste real-time impedantiestijging teweeg brengen. Denaturatie beïnvloedt ook het ruimte-ladingsgebied in het NCD. De verwijdering van

negatief geladen DNA tijdens de denaturatie zal de effecten in het ruimteladingsgebied tijdens de hybridisatie volledig teniet doen. De depletiezone zal breder worden, hetgeen zal resulteren in een stijging in weerstand. Dit effect is het meest uitgesproken tijdens de denaturatie van complementair DNA. Op de hoogste frequentie (1 MHz), wat de vloeistofweerstand R_S weerspiegelt, werd tijdens de denaturatie een impedantiedaling waargenomen in real-time. Dit is geassocieerd met de toename in negatief geladen ssDNA en tegenionen in de buffer. Onderscheid tussen de drie soorten DNA was mogelijk na het fitten van de impedantiedaling op deze frequentie aan een exponentieel verval. Relatief gezien is de langste vervaltijd geassocieerd met complementaire denaturatie, terwijl de kortste tijd gelinkt is met denaturatie van 1-mismatch DNA. Wanneer 0.1 M NaOH wordt toegevoegd aan een staal dat voordien werd behandeld met niet-complementair DNA, ligt de vervaltijd er tussenin. Zoals reeds aangehaald zal de verschillende manier van aanhechting van niet-complementair DNA aan het NCD verantwoordelijk zijn voor de kinetische verschillen tijdens de vrijstelling in de oplossing. Onderscheid tussen de drie soorten DNA was mogelijk binnen 5 minuten. Alles tesamen ontwikkelden wij een reproduceerbare en efficiënte label-vrije impedimetrische biosensor met SNP-gevoeligheid. Bovendien wordt in dit geval de kinetica van het hybridisatie- en denaturatieproces, hetgeen typische sequentie-afhankelijke parameters zijn, met real-time-impedantiemetingen bestudeerd. Tenslotte is ons prototype van een DNA-sensor goedkoper en sneller dan de huidige state-of-the-art-technieken die gebruikt worden voor mutatie-analyse zoals microarrays en Denaturerende Gradiënt Gelelektroforese (DGGE), en is tegelijk veelbelovend wat betreft het ontdekken van nieuwe mutaties gebaseerd op kinetische afwijkingen gedurende hybridisatie en/of denaturatie.

In **Hoofdstuk 6** evalueerden we of NCD ook kon dienst doen als een immunosensor-platform. We bepaalden eerst de geschiktheid van H-getermineerd NCD als een platform voor de adsorptie van antilichamen met behulp van een Enzyme-linked Immunosorbent Assay (ELISA)-referentiemethode met een colorimetrische uitlezing. Vervolgens breidden we deze colorimetrische methode uit naar een impedimetrische NCD-gebaseerde immunosensor specifiek voor CRP-detectie, een acute-fase-eiwit dat gebruikt wordt als een belangrijke risicofactor voor het ontwikkelen van cardiovasculaire

aandoeningen (CVD). De selectiviteit van de anti-CRP immunosensor werd geëvalueerd met fluoresceïne isothiocynaat (FITC) als niet-specifiek target. Op lage frequentie (100 Hz) vertoonde de impedantie een real-time stijging tijdens CRP-behandeling, terwijl de behandeling met FITC geen effect teweeg bracht op deze frequentie. Dit effect werd in de Nyquistplot weerspiegeld in een stijging in het 'staart'-gebied. Na het fitten aan een equivalent circuit bestaande uit een serieschakeling van een vloeistofweerstand R_s , een constante-fase-element Q_1 en een bijhorende weerstand R_{Q_1} in parallel, en een constante-fase-element Q_2 en een bijhorende weerstand R_{Q_2} in parallel, werd deze daling in het 'staart'-gebied in verband gebracht met een daling in Q_1 , geassocieerd met de moleculaire laag. Door de toename in dikte van de moleculaire laag door de CRP-herkenning, zal de capaciteit van deze laag afnemen, hetgeen de daling in Q_1 verklaart. Aangezien FITC verbonden was met ssDNA, veroorzaakte de behandeling met dit analyt een DNA-gemedieerd impedantie-effect analoog aan Hoofdstuk 5. De impedantie daalde in het frequentiegebied tussen 1000 en 50000 Hz, en was gecorreleerd aan een daling in R_{Q_2} , overeenkomend met het ruimte-ladingsgebied. Op de hoogste frequentie (1 MHz), wat de vloeistofweerstand R_s weerspiegelt, werd een verschillend effect waargenomen vóór en na antigeenbehandeling, in $0.1 \times$ PBS. Het impedantieniveau van de vloeistof in de post-antigeen-spoelfase lag consequent hoger dan het niveau van de pre-antigeen-stabilisatiefase voor het CRP-behandelde staal. Het impedantieniveau van de vloeistof in de post-antigeen-spoelfase van het FITC-behandelde staal verschilde niet noemenswaardig van dat van de pre-antigeen-stabilisatiefase. Dit kan te wijten zijn aan het feit dat significante ionische herverdeling heeft plaatsgevonden aan het oppervlak door CRP-herkenning, hetgeen bufferionen zal onttrekken van de vloeistof. Uiteraard was dit niet het geval voor het FITC-behandelde staal. De gevoeligheid van de CRP-gerichte immunosensor werd ook onderzocht. NCD-stalen gecoat met anti-CRP werden geïncubeerd met verschillende CRP-concentraties (uiteindelijke concentraties bedroegen 1 μ M, 100 nM, and 10 nM), inclusief een staal dat werd geïncubeerd met zuivere CRP-buffer. Verschillende graden van impedantiedaling werden waargenomen in real-time voor elke conditie op lage (100 Hz) frequentie, wat een duidelijk onderscheid mogelijk maakte tussen de verschillende CRP-verdunningen en tussen de verdunningen en de zuivere CRP-buffer. Het

gestabiliseerde impedantieniveau steeg met afnemende CRP-concentratie. Binnen 10 minuten kon een duidelijk onderscheid worden gemaakt, en vertoonde de laagste concentratie van 10 nM nog steeds een duidelijk verschil met dat van buffer. De impedantiestijging tijdens CRP-behandeling die werd waargenomen bij de selectiviteitsexperimenten werd niet gereproduceerd. Dit was waarschijnlijk te wijten aan het feit dat de Nyquistplots in dit geval nagenoeg volledig werden ingenomen door semi-cirkel, en geen 'staart'-gebied. Het gebied dat het gevoeligste is voor de gebeurtenissen in de moleculaire laag en de dubbellaag was niet vertegenwoordigd. Hoe dan ook, we slaagden in de ontwikkeling van een snelle, real-time impedimetrische CRP-gerichte immunosensor met een gevoeligheid die het fysiologische concentratie-gebied benadert (<10 nM).

In **Hoofdstuk 7** werden onze bekomen resultaten kritisch geëvalueerd en werden enkele toekomstperspectieven opgesomd. Verbeteringen in het ontwerp van de immunosensor en/of DNA-sensor zouden de stabiliteit, de reactietijd en de gevoeligheid kunnen verhogen, zoals miniaturisatie en het gebruik van interdigiterende elektroden (IDE's). Wij zullen ook overstappen naar covalent gebonden antilichamen. Dit zal de variabiliteit geassocieerd met mogelijk verlies van antilichamen van het oppervlak vermijden, en een meer solide en betrouwbaar systeem creëren. Met deze verbeterde opstelling zullen we het onderscheidend vermogen bestuderen tussen CRP en een niet-specifiek antigeen vergelijkbaar in gewicht en lading. De moeilijkheden betrokken bij de regeneratie van immunosensoren indachtig, zullen eveneens alternatieve platformen worden onderzocht om aan de nood aan herbruikbare antigeen-specifieke sensoren te beantwoorden. In deze context zullen cel-gebaseerde en aptameer-gebaseerde sensoropstellingen worden onderzocht. Het biosensor-platform dat in deze thesis werd ontwikkeld biedt voldoende flexibiliteit om deze alternatieve benaderingen te implementeren.

SUMMARY

The evolution from 'micro'-science into 'nano'-science has blossomed with the dawn of bio-electronics: a scientific field coupling the achievements in molecular biology with the advances in electronics to obtain higher sensitivity, specificity and speed. Biosensors have played a pivotal role in this research field. They are analytical devices consisting of biomolecules serving as recognition elements, coupled to a solid physical transducer. This transducer 'translates' the biological recognition event between the receptor molecule and its target into a readable signal. In fact, biosensor research has been evolving since the invention of the oxygen (O₂)-electrode by Clark *et al.* in 1956 [Cla56]. Huge advances have been made since then, and many biosensors have become established in the clinical and scientific world. They can be classified according to the type of biological receptor molecule attached to the transducer, or according to the principle of signal transduction, as described in **Chapter 1**. However, still few of them made it to point-of-care applications. The success and applicability of biosensors as point-of-care diagnostic or analytical tools is based on four requirements. They need to be sensitive, specific, fast and cheap. Many popular transduction materials, such as silicon (Si), are susceptible to hydrolysis, leading to loss of bioreceptor molecules from the Si surface and hence to instability of the sensor platform. The instability of the biofunctionalisation of course negatively influences the sensitivity and specificity of the sensor. For this reason, increased attention has been shifted towards diamond, which surpasses Si and germanium (Ge) on many levels. The most important properties of synthetically grown diamond are summarised in the second part of **Chapter 1**. Furthermore, in most cases an endpoint detection, based on the comparison of before and after target addition, is used. This not only increases analysis time dramatically, but also causes the loss of valuable information that could be gained during the reaction (especially for the DNA-sensor). This is true for various electrochemical measurement techniques, and also for optical biosensors that require additional target labelling. Optical detection poses an additional hurdle, since both the reagents necessary for labelling and the specialised equipment required for label-dependent target detection are expensive, making

it almost impossible to implement in point-of-care applications. Another point that will increase the cost even more, is the fact that most biosensors are not reusable.

With this PhD-thesis, we set out to develop a generic sensing platform that is able to guarantee all of the four requirements mentioned above, while tackling the issues so often encountered in biosensor research. In this work, we have developed a real-time, and hence fast, label-free impedimetric biosensor platform based on chemically inert nanocrystalline diamond (NCD). Synthetic NCD turns out to be a versatile transducing material yielding stable interfaces with both DNA and proteins (antibodies). For the prototype DNA-sensor, we obtained single nucleotide polymorphism (SNP) sensitivity, which is clinically relevant since numerous genetic illnesses are caused by single point mutations. Moreover, we demonstrated that our real-time prototype DNA-sensor can be used during both hybridisation and denaturation events, giving important additional sequence information that can be exploited in future mutation identification biosensor devices. This is also the first time that real-time denaturation is proven to be useful in a biosensor device. For the prototype C-reactive protein (CRP)-directed immunosensor, we obtained a concentration-dependent sensitivity in the relevant physiological range (1 μM – 10 nM). The proven stability of the biofunctionalisation of NCD with DNA or protein combined with the fact that NCD can be cleaned and reused, and for the DNA-sensor even regenerated to the probe-level by denaturation, makes our developed sensor indeed a promising generic platform for its use in biosensing devices needed in lab-on-chip or point-of-care applications. The latter, because no label is needed and only a relatively cheap impedance analyser is required. A summary of how this generic biosensor platform was developed in this thesis is given in the following paragraphs.

In **Chapter 3**, we embarked on this task by developing a simple but efficient two-step reaction to covalently attach DNA to NCD. It is based on the photochemical attachment of a ω -unsaturated fatty acid molecule, 10-undecenoic acid (10-UDA), to H-terminated NCD, followed by the attachment of amino (NH_2)-modified DNA to the photochemically introduced carboxylic acid (COOH)-groups on the NCD by 1-ethyl-3-(3-dimethylaminopropyl)-carbodiimide (EDC). Our procedure involves a significant simplification as compared to that

developed by Yang *et al.* [Yan02]. Moreover, EDC is a zero-length crosslinker, meaning that it acts as a mediator and will not be present in the resulting peptide bond between the DNA and the 10-UDA on the NCD. For this reason, the DNA molecules will be closer to the surface, which is beneficial for electronic detection of hybridisation. However, the length of the DNA molecules used in our first prototype, 250 bp Polymerase Chain Reaction (PCR) amplicons, caused some practical difficulties. Long DNA molecules will attach to a surface not only through an end-functionalisation, but will adopt a conformation resembling flexible coils that also latch to the surface on multiple locations along their length. This caused a low binding capacity, and the presence of non-covalently adsorbed DNA. Although it was impossible to detect the surface-attached DNA molecules directly using fluorescence microscopy, PCR and gel electrophoresis performed on the reaction fluids obtained from repeated denaturations and rehybridisations proved both the EDC-mediated covalent attachment of DNA to NCD and the functionality of this DNA.

In **Chapter 4**, our immobilisation technique was improved in order to tackle the low binding capacity and non-covalent adsorption of DNA to NCD. Fine tuning the procedure resulted in an attached monolayer of 10-UDA-attached DNA instead of piles of 10-UDA of which only at the top, an unattached and therefore uncontrollable layer was available to bind DNA. Furthermore, it was shown that short ssDNA, adopting the conformation of stiff and upright rods, was more efficiently attached to NCD than longer DNA, since, geometrically, more molecules of this conformation will fit on top of the surface. A DNA amount in the reaction mixture of 10^{14} molecules (300 pmol) yielded the highest DNA density on the NCD while still being functionally active. The fact that this could be reproduced on NCD samples from a different source proved the robustness of the attachment procedure. Of course, this amount of DNA is an overestimation of the final amount actually being attached to the NCD. The actual density will be close to the value most cited in literature: 10^{12} molecules.cm⁻². COOH-termination was also proven to be crucial for DNA attachment, since either no DNA or non-functional DNA was attached to H-terminated and O-terminated NCD, respectively. The fact that H-terminated NCD is an effective barrier against non-covalent adsorption, holds great promise in the field of micro-electronics, where one needs to predetermine the location of the probe DNA molecules. This

unique feature allows for a reproducible, easy and efficient array formation on the sensor surface. Even if the H-termination were to be compromised by O₂, this will not lead to functional DNA attachment in these locations. The H-terminated regions will still determine the signal-generating regions on the DNA-sensor. We also investigated the effect of mixed functionalities on the NCD surface, in accordance with Huang *et al.*, who observed higher binding efficiency of antibodies and lower non-specific adsorption of analytes on Si substrates [Hua05]. However, comparing NCD substrates only carrying COOH-functionalities with NCD samples modified with carboxyl (COOH)- and hydroxyl (OH)-groups in different ratios showed that the purely COOH-functionalised samples resulted in functional DNA attachment. The OH-functionalities likely formed phosphate esters with the backbone in the DNA, causing the DNA to become unfavourably attached for hybridisation. This study resulted in a highly reproducible NCD surface biofunctionalisation with covalently bound ssDNA, showing optimal functional activity and unique arraying properties using H-terminated, DNA-repelling, NCD separated from DNA-functionalised NCD areas.

In **Chapter 5**, we developed a prototype of an impedimetric DNA-based biosensor making use of our improved biofunctionalisation procedure for the attachment of DNA to NCD. This way we obtained SNP sensitivity in real-time analysis in two separate, but complementary view points: during hybridisation and during denaturation. During hybridisation in 10× PCR buffer, a real-time decrease in the complex impedance was observed for complementary target DNA in a frequency region between 1000 and 1500 Hz. This decrease was reflected as a reduction in the semi-circle of the Nyquist plot. Through fitting with an equivalent circuit composed of a series connection of a solution resistance R_s , a capacitor C and an associated resistance R_c in parallel, and a constant phase element Q and its associated resistance R_Q in parallel, this reduction of the semi-circle was caused by a decrease in R_Q , which was attributed to the space-charge region. Upon the approach of negatively charged DNA to the NCD surface during hybridisation, positive charge carriers from the slightly p-type NCD bulk are attracted to the surface, narrowing the depletion zone and decreasing its resistance. No significant effect was observed during hybridisation with 1-mismatch DNA. This discrimination was possible within 10 minutes. Moreover, the use of 10× PCR buffer can allow for the 'lab-on-chip'

integration together with a DNA amplification unit, using the same buffer system. Most interestingly, we also obtained a reliable discrimination between complementary, 1-mismatch and non-complementary DNA in real-time during the first minutes of denaturation with 0.1 M sodium hydroxide (NaOH). In a frequency range between 100 and 15000 Hz, corresponding to the molecular and double-layer (100 – 500 Hz) and to the space-charge region (500 – 15000 Hz), an impedance increase is observed. Denaturation removes the DNA strands and their associated counter-ions from the NCD surface. This explains the observed impedance increase in the molecular layer. Since more duplexes were formed during complementary hybridisation than with 1-mismatch DNA, the rise in impedance is larger during the former. Non-complementary DNA will probably only have adsorbed onto the NCD surface. Since proximity to the electrode surface is positively correlated with efficiency of signal detection, yielding also a significant field-effect during non-complementary 'hybridisation', removal of some of these adsorbed molecules shows the largest real-time impedance increase. The denaturation events also have an influence on the space-charge region of the NCD. Removing negatively charged DNA during denaturation will completely reverse the effects seen in the space-charge region during hybridisation. The depletion zone will become wider, resulting in an increase in resistance. This effect is more pronounced for the complementary case. At the highest frequency (1 MHz), reflecting the solution resistance R_s , an impedance decrease is observed in real-time during the denaturation process. This is associated with the release of negatively charged ssDNA and associated counter-ions into the buffer. Discrimination between the three types of DNA was possible after fitting the gradual impedance decrease observed at this frequency to an exponential decay. Relative to each other, the longest decay time is associated with complementary denaturation, while the shortest time correlates with 1-mismatch DNA. When adding 0.1 M NaOH to a sample previously treated with non-complementary DNA, the decay time lies in between. As mentioned, the different way of capturing non-complementary DNA will lead to differences in removal kinetics into the solution. Discrimination of the three types of DNA was possible within 5 minutes. Taken together, we constructed a reproducible and efficient label-free impedimetric biosensor with SNP sensitivity. Moreover, the kinetics of the hybridisation and denaturation processes, that are typical

sequence-dependent parameters, are addressed in real-time impedance measurements. Finally, our prototype of a DNA-based biosensor is cheaper and faster than current state-of-the-art mutation analysis techniques such as microarrays and Denaturing Gradient Gel Electrophoresis (DGGE), while holding promise of discovering new mutations based on kinetic discrepancies during hybridisation and/or denaturation.

In **Chapter 6**, we evaluated if our NCD could also be turned into an immunosensing platform. We first determined the suitability of H-terminated NCD as a platform for antibody adsorption using an Enzyme-Linked Immunosorbent Assay (ELISA) reference method with a colorimetric read-out. We then transferred this colorimetric setup into an impedimetric NCD-based immunosensor specific for CRP detection, which is an acute phase protein generally serving as an important risk assessment factor for the development of cardiovascular disease (CVD). The selectivity of the anti-CRP immunosensor was evaluated by challenging with fluorescein isothiocyanate (FITC) as a non-specific target. At low frequency (100 Hz), the impedance showed a real-time increase during CRP treatment, while treatment with FITC showed no effect at that frequency. This effect was reflected in the Nyquist plot by an increase in the 'tail' region. After fitting with an equivalent circuit composed of a series connection of a solution resistance R_s , a constant phase element Q_1 and an associated resistance R_{Q_1} in parallel, and a constant phase element Q_2 and its associated resistance R_{Q_2} in parallel, this increase in the 'tail' region was associated with a decrease in Q_1 , attributed to the molecular layer. By the increasing thickness in the molecular layer by CRP recognition, the capacitance of this layer will decrease, explaining the decrease in Q_1 . Since the FITC was linked to ssDNA, treatment with this analyte caused a DNA-mediated impedance effect analogous to Chapter 5. The impedance decreased in the 1000 – 50000 Hz frequency region, and was associated with a decrease in the space-charge region-linked R_{Q_2} . At the highest frequency (1 MHz), reflecting R_s , a differential effect could be observed before and after antigen treatment, in 0.1× phosphate buffered saline (PBS). The solution impedance level of the post-antigen rinsing phase was consistently higher than the level during the pre-antigen stabilisation phase for the CRP-treated sample. For the FITC-treated sample, the solution impedance level of the post-antigen rinsing phase did not differ much from the pre-antigen

stabilisation phase. This could be due to a significant ionic redistribution having occurred at the surface by CRP recognition, withdrawing buffer ions from solution. This of course did not occur with the FITC-treated sample. The sensitivity of the CRP-directed immunosensor was also investigated. The anti-CRP-coated NCD samples were incubated with different concentrations of CRP (final concentrations were 1 μ M, 100 nM, and 10 nM), including one sample that was incubated with pure CRP buffer. Different degrees of impedance decrease were observed in real-time for each condition at low (100 Hz) frequency, leaving the CRP dilutions clearly distinguishable from each other and from pure CRP buffer. The stabilised impedance level increased with decreasing CRP concentration. Within 10 minutes, a clear discrimination could be made, and the lowest concentration of 10 nM was still clearly distinguishable from buffer. The impedance increase during CRP treatment that was observed during the selectivity experiments was not reproduced, probably due to the fact that the Nyquist plots in this case were almost entirely occupied by semi-circle, and no tail region. The region most sensitive to the events in the molecular and double-layer was not represented. However, we succeeded in developing a fast, real-time impedimetric CRP-directed immunosensor with a sensitivity closely approaching the physiological range (<10 nM).

In **Chapter 7**, our obtained results are critically evaluated, and some prospects for the future are summarised. Improvements in the setup design of the immunosensor and/or DNA-sensor, such as miniaturisation and use of interdigitated electrodes (IDEs) could increase stability, reaction time and sensitivity. Also, we will transfer to an approach based on covalently bound antibodies. This will avoid the additional variable associated with the possible loss of antibodies from the surface, and create a more rigid and reliable system. With this improved setup, we will explore the ability to distinguish CRP from a non-specific antigen of comparable molecular weight and charge. Keeping in mind the often encountered difficulties associated with regeneration of immunosensors, alternative sensor platforms will be explored to satisfy the need for reusable antigen-specific sensors. In this context, we will investigate cell-based and aptamer-based sensor setups. The biosensing platform that was developed in this thesis offers sufficient flexibility to implement these alternative approaches.

Chapter 1:

General introduction and aims

1.1 BIOSENSOR DEVELOPMENT IN THE FRAMEWORK OF BIO-ELECTRONICS

The transition from 'macro' to 'micro' and recently to 'nano' has been noticeable in many scientific fields. In biology, the evolution towards research into the micro- and nanobiotic world has led to the identification of many disease-related pathogens. In the technological field, the progression from electronics into micro- and nano-electronics has enabled the miniaturisation of computers. Combining the enormous advances in biology with those attained in micro- and nano-electronics has laid the groundwork to study biology on a single molecule level and to embark into the 'nano'-world. In this context, nanometer-scale biomolecules have become an integrated component of electronic devices designed for early, reliable and affordable detection of target molecules. Hence, the development of these biosensors has been a pivotal point in the evolution of this new 'bio-electronics' field.

1.1.1 Description of a biosensor

A biosensor is an analytical device that consists of two main elements: a biological molecule that serves as a receptor, attached to a physical component that transduces the biological recognition event between the receptor molecule and its target into a readable signal, in combination with read-out and processing electronics. The latter is therefore called a 'transducer'. A schematic representation of a biosensor is shown in figure 1.1.

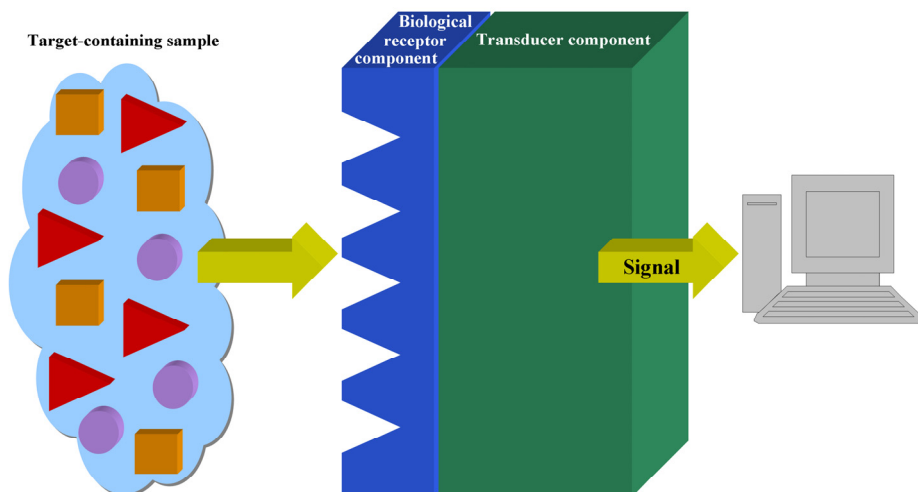


Figure 1.1: Graphical representation of a biosensor, including a biological receptor component being exposed to a target-containing sample, and a physical transducer component.

The sensitivity, stability and reliability of a biosensor is determined by several aspects. First of all, a key issue in biosensor development is to assure a high functional activity of the biological molecules immobilised onto the transducer over long periods of time. This is especially relevant for high-throughput sensing devices, in which the transducer surfaces are miniaturised to micro- or nanometer scale. Secondly, not only the functional integrity, but also the accessibility of each immobilised molecule onto the transducer is essential for efficient interaction with the target molecules, and hence, sensitivity. The biosensor should also be compact with high specificity and with resistance to non-specific adsorption or 'fouling'. In the following section, we give a brief historic overview of biosensor development as far as relevant for this thesis.

1.1.2 History of biosensor development

The evolutionary history of biosensor development is summarised in the timeline in figure 1.2. For details, the reader is referred to the text [Mal03].

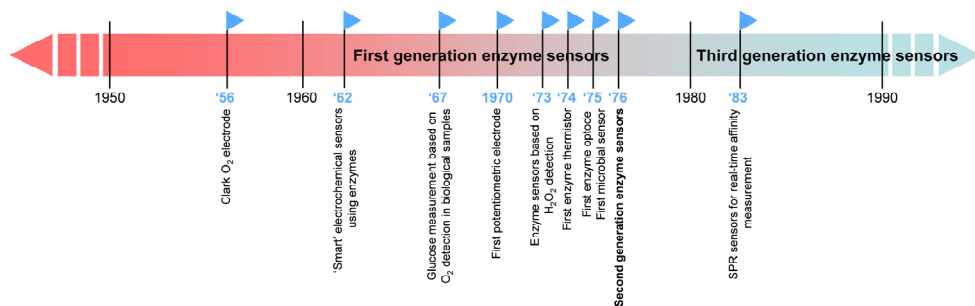


Figure 1.2: Historical timeline displaying the evolutionary milestones in biosensor development.

1956: Professor Leland Charles Clark Jr. has been widely considered to be the father of the biosensor concept. In this year, he published a paper describing an oxygen (O₂) electrode, an O₂-reducing platinum (Pt) working electrode, in order to continuously measure O₂ tension in the blood [Cla56].

1962: Wishing to expand the range of measurable targets in the body, he described at a New York Academy of Sciences symposium in 1962 how to make electrochemical sensors more intelligent by entrapping enzymes, exemplified by glucose oxidase, at the previously mentioned, and by now patented, Clark O₂ electrode using a dialysis membrane [Cla62]. The decrease in O₂ concentration in the electrolyte by the metabolism of glucose was proportional to the glucose concentration.

1967: Updike and Hicks implemented and expanded on Clark's work and described the first functional enzyme electrode based on glucose oxidase immobilised onto an O₂ sensor [Upd67]. Glucose concentration was specifically measured in biological solutions and in tissues *in vitro*. Research efforts into biotechnological and environmental applications of enzyme sensors soared.

1970: In this year, Guilbault and Montalvo described the first potentiometric enzyme-electrode. It was a urea-sensor based on the enzyme urease immobilised at an ammonium (NH₄⁺)-selective liquid membrane electrode [Gui70].

1973: Although Clark's design of O₂-based glucose detection was so effective that many variations were developed targeting other analytes, detection of hydrogen peroxide (H₂O₂) became more preferred. In 1973,

Guilbault and Lubrano first described a glucose and a lactate enzyme sensor based on such a H_2O_2 -detection at a Pt electrode [Gui73].

Mid 1970s: Three new groups of sensors were born in this period. A first type, developed by Klaus Mosbach, was a heat-sensitive enzyme sensor and was hence called an enzyme 'thermistor' [Mos74]. Lübbers and Opitz immobilised enzymes on a fibre-optic sensor for the detection of carbon dioxide (CO_2) or O_2 . These optical enzyme sensors were termed 'optodes' [Lüb75]. Last in the line of evolutionary sensors were the 'microbial electrodes' of Divis in 1975. He suggested that bacteria could be harnessed as the biological element for the measurement of alcohol [Div75].

The detection principle of enzyme sensors up to that time was largely based on the re-oxidation of H_2O_2 , and these sensors were termed '**first generation enzyme sensors**'. However, the high oxidising potential required to oxidise H_2O_2 resulted in significant interference from other compounds in the electrolyte, since they were also easily oxidised at the electrode.

1976: Roche (Switzerland) introduced the Lactate Analyser LA 640 in which a soluble redox mediator, hexacyanoferrate [$\text{Fe}(\text{CN})_6^{3-/4-}$], was used to mediate electron transport from the enzyme lactate dehydrogenase to an electrode for the detection of lactate [Gey85]. This was a pivotal point in enzyme sensor development. By using soluble electron mediators in the electrolyte, interference of non-specific analytes was substantially decreased. These redox species needed much lower oxidising potentials than those required for H_2O_2 -oxidation. The sensors were called '**second generation enzyme sensors**'.

1980s: Gradually, the transition was made into the development of '**third generation enzyme sensors**'. They resemble second generation enzyme sensors in that they are also often based on the use of electron mediators. However, they have progressed into the implementation of co-immobilised enzymes and mediators onto the same electrode instead of freely diffusing mediators in the electrolyte. There have even been reports of direct communication between the enzymes' redox centre and the electrode. Third generation biosensors offer all the advantages of second generation enzyme sensors, but additionally, they are said to be self-contained. There is no need to add either mediator or enzyme. Thus, third generation enzyme sensors allow repeated measurements, which minimises the sensor design costs [Cas84].

1983: In this year, Liedberg used surface plasmon resonance (SPR) to monitor affinity reactions in real-time [Lie83]. They were the first to pave the way for the commercial success of BIAcore (Pharmacia, Sweden), that was launched in 1990.

1.1.3 Biosensor construction

1.1.3.1 Biological receptor molecules

The type of biological receptor molecule determines the bio-selectivity, and hence the type of biosensor. Enzymes recognise their substrates and will convert it to a reaction product. The associated biosensors are termed 'catalytic or enzyme biosensors'. Other molecules identify their targets by forming an affinity-complex governed by hydrogen (H) bonds, hydrophobic interactions, electrostatic forces, and 'van der Waals' forces. These are all bonds of a weak, non-covalent nature, yet together most of these associations can be quite strong. Biosensors with a selectivity based on the formation of an affinity-complex are called 'affinity-based biosensors'. One of the most common biomolecules that recognises its target through such an affinity-complex, is the antibody. The affinity-based biosensor subgroup containing immobilised antibodies is termed 'immunosensor'. The receptor can also be a single-stranded DNA (ssDNA) molecule, yielding a 'DNA-based biosensor'. Furthermore, membrane receptors and even whole cells can serve as the biological part of a biosensor [Gor05].

1.1.3.2 Attachment of biological receptor molecules

Detection of target molecules and signal transduction usually must occur at a liquid-solid interface. For this reason, the efficient immobilisation of the biological receptor molecule onto the transducer is a crucial point for the biosensor performance. The benefit of the immobilisation technique must be two-fold: it should result in a stable layer of biomolecules and these

biomolecules should have retained their biological activity. The available immobilisation techniques can be grouped into two categories: non-covalent binding, by physical adsorption, and covalent binding [Gor05].

Non-covalent, physical adsorption

Generally, physical adsorption results in significant losses of biomolecules from the surface because of the rather weak bonds involved to immobilise them. Moreover, physical adsorption leads to random orientations of the molecules, more often than not rendering the part that engages in target recognition inaccessible, thereby lowering device sensitivity. However, some non-covalent binding approaches do yield a firmly immobilised and well-oriented biomolecule layer.

Streptavidin-modified surfaces bound with biotinylated biomolecules result in the strongest non-covalent bond known. The streptavidin-biotin complexes are also extremely stable over a wide range of temperatures and pH [Gor05].

Covalent binding

Covalent attachment of biomolecules to solid surfaces is the immobilisation technique of choice for biosensor fabrication. It results in a stable and long-term modification of the substrate with oriented biomolecules. The surface of the transducer can be modified to present desired functionalities (-NH₂, -COOH, -SH, ...). Concerning the fabrication of DNA-based biosensors, ssDNA can subsequently be coupled to these functional groups through its own range of possible end modifications, ensuring a covalently bound DNA molecule that is available for hybridisation. DNA molecules containing carboxylic acid (COOH)-functionalities can be bound with amino (NH₂)-groups and form peptide bonds (R-CO-NH-R). When they are modified with a thiol (SH)-group, linking with a COOH-functionality will yield a thiol ester (R-CO-S-R-), while binding with another SH-group will result in a disulfide bridge (C-S-S-C). SH-modified DNA can also react with the double bond of a maleimide compound [(CH)₂-(CO)₂-NH]) to form a stable carbon-sulfur bond (C-S).

Antibodies and enzymes, being proteins, contain NH_2 -groups, COOH -groups and SH -groups. Thus, they can also easily be covalently bound to NH_2 -, COOH - and SH -modified surfaces. Proteins are also often coupled to surfaces using the maleimide chemistry described above. Moreover, a widely used approach for efficient and well-oriented antibody attachment makes use of protein A or G. The latter proteins are immobilised onto the solid substrate, and form a linker layer for the covalent attachment of antibodies with their antigen-recognising Fab fragments protruding outwards.

Also, the capability of many organic molecules, such as alkylsilanes, to spontaneously self-assemble into monolayers on several solid substrates provides a very useful tool to engineer a desired environment on the transducer surface. These self-assembled monolayers (SAMs) have a well-defined and ordered molecular architecture. Widely used are the alkoxysilanes. In alkoxysilanes, two classes of moieties are attached to the silicon (Si) atom. There is an organic moiety that can be a carbon chain (alkyl), an aromatic group (aryl), an organofunctional group ($-\text{NH}_2$, $-\text{COOH}$, $-\text{SH}$, ...) or a combination of these. Alkyl and aryl silanes can form hydrophobic coatings and act as water repellants, while organofunctional silanes can react with other molecules to be attached in the ways described above. The alkoxy moiety usually consists of three methoxy or ethoxy groups. First, the two lateral alkoxy groups hydrolyse and cause condensation with other alkoxysilanes in a lateral assembly. The third alkoxy group first forms hydrogen bonds with and then covalently binds to sites on the surface while liberating water. [Gor05].

1.1.3.3 Types of transducers

Many kinds of substrate materials can be used for the immobilisation of biomolecules in biosensor construction. Common ones are polystyrene [Ras91], gold (Au) [Has94], silicon (Si) [Str00] and silicon oxide, beads [Kre87], and recently, **diamond**. When devising a biosensor, care must be taken in choosing the substrate material. This decision depends strongly on the signal generating mechanism one has in mind. Not all substrate materials are suitable for every type of transduction. So, next to the type of biological receptor molecule, the type of transducer material also partly determines the type of biosensor.

When envisaging an optical target detection, such as fluorescence or chemiluminescence, it is beneficial to use substrates with a low background luminescence. The conductivity of the substrate is of negligible importance. Glass, plastics or Si are often used.

For electrochemical biosensors, the role of the electrical properties of the transducer increases drastically. Materials such as Au, Si, germanium (Ge), Pt, etc. are optional. However, the linkages between metal electrodes such as Au and Pt and biomolecules are sensitive to oxidation, causing substantial loss of target receptors from the surface. Moreover, their metallic conductivity makes them perpetually conducting, hampering and even inhibiting the control of their electronic properties. For this reason, increased attention is being addressed towards semiconductor materials, such as Si and Ge. Nevertheless, biofunctionalised Si surfaces are very susceptible to hydrolysis, also leading to significant loss of bound biomolecules, decreasing their sensitivity over time [Yan02];[Neb07]. Recently, diamond has attracted much attention as a possible alternative semiconductor material. It surpasses the more generally used semiconductor electrode materials such as Si and Ge on many levels. An overview of the physical properties of diamond in comparison to Si and Ge is given in table 1.1 [Dav94];[www.ioffe.ru/SVA/NSM/Semicond/index.html]. The large bandgap of diamond will ensure that electrons will not easily enter the conduction band, compromising its intrinsic insulating properties. At the same time, UV-radiation, with an energy of a few to about 100 eV, can make valence electrons jump this gap, allowing applications as UV-photosensors. This bandgap feature also explains the high resistivity and high breakdown voltage of diamond. Its high thermal conductivity, combined with its low thermal expansion, makes diamond an ideal material to be used as a heat sink in high-powered devices without the risk of being thermally deformed. Also, diamond can function as a dielectric in capacitors. Its low dielectric constant allows diamond to withstand high electric fields, reflected in its high breakdown voltage.

Table 1.1: Overview comparing the physical properties of three semiconductors: diamond, Si, and Ge.

Property	Diamond	Si	Ge
Thermal expansion ($\times 10^{-6} \cdot K^{-1}$)	1.1	2.6	5.57
Band gap (eV)	5.47	1.12	0.66
Carrier mobility ($cm^2 \cdot V^{-1} \cdot s^{-1}$)			
→ electron	2200	1500	3900
→ hole	1600	475	1900
Breakdown voltage ($\times 10^5 \cdot V \cdot cm^{-1}$)	100	3	1
Dielectric constant	5.5	11.9	16.2
Resistivity ($\Omega \cdot cm$)	10^{13}	10^3	46-60
Thermal conductivity ($W \cdot cm^{-1} \cdot K^{-1}$)	9-23	1.68	0.599
Hardness ($kg \cdot mm^{-2}$)	8000	1150	780

The next section elaborates on these appealing properties and the applications of diamond in the bio-electronics field.

1.2 THE ROLE OF DIAMOND IN BIOSENSORS

The advances in biosensor development ultimately depend on the perpetual search for optimal transducer materials, allowing rapid, sensitive and selective biological signal detection and translation. Candidate materials must possess a number of important characteristics for them to be considered as transducers.

First of all, they need to be able to undergo biofunctionalisation. This factor has been investigated and obtained for several substrates, such as latex beads [Kre87], polystyrene [Ras91], carbon electrodes [Mil92], Au [Has94] and glass, as previously mentioned.

Secondly, the substrates need to be reasonably flat and homogeneous, and the resulting bio-interfaces should be able to be manufactured with a high reproducibility. These last features eliminate the possible use of beads, polystyrene and glass.

Finally, the bio-interfaces will be integrated into micro-electronics, requiring the materials to be compatible with micro-electronic processes, as is the case with carbon electrodes, Au and Si. Unfortunately, these are not chemically stable and the bio-interfaces degrade upon contact with aqueous electrolytes [Neb07].

Diamond has become an attractive alternative candidate for its use as a transducer material in bio-electronics. It is the only material that is compatible with processes applied in micro-electronics that does not show any degradation in electrolytes, even at fairly high potentials. The following sections will elaborate more on these appealing features as well as on the classification of diamond into different subtypes, not all of them being appropriate for biosensor development.

1.2.1 Classification of diamond

1.2.1.1 Natural diamond

In diamond, each carbon (C) atom forms 4 single sigma (σ) bonds, each consisting of a sp_3 -hybridised orbital, with 4 neighbouring C atoms in a

tetrahedron-structure. Each bond is at an angle of $109^{\circ}28'$ to the adjacent bond. Each tetrahedron is associated with 4 other tetrahedrons, forming a very stable and tightly bound covalent lattice or crystal structure. This explains the extreme hardness of diamond, one of its unique properties that will be described in section 1.2.2 [Pie93]. The diamond lattice is shown in figure 1.3.

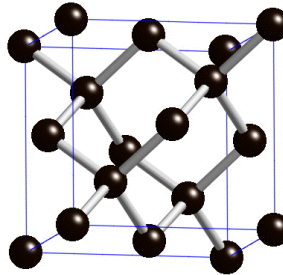


Figure 1.3: Schematic diagram of the lattice structure of diamond, showing the tetrahedral orientation of each C atom.

The classification system of natural diamond is based on the presence of nitrogen (N) impurities in the lattice structure, which can easily be assessed using Infrared (IR) absorption spectroscopy. The presence of these N impurities disturbs the perfect crystal structure of diamond. This causes certain vibrational modes to occur upon illumination with IR light that usually do not take place because of the lattice symmetry. About 98% of natural diamond contains enough N to be detectable by IR absorption spectroscopy.

Type I diamond

Type I diamond contains a lot of N, roughly $>10^{17} - 10^{18} \cdot \text{cm}^{-3}$. They are further divided into subdivisions [Zai01];[Wil91].

Type Ia is the most common type of natural diamond. 78% of all natural diamond is classified as type Ia. They usually contain clusters of N. Because these diamonds absorb blue light, they can have a pale yellow or brown colour.

If the N atoms are atomically dispersed throughout the carbon lattice, then the diamond is said to be a type Ib diamond. These diamonds absorb green light as well as blue light, and have a darker colour than type Ia diamonds.

Depending on the precise concentration and spread of the N atoms, these diamonds can appear deep yellow, orange, brown or green. The donor energy level of the substitutional N is deep in the bandgap of diamond, making it unsuitable for electronic applications. Less than 0.1% of natural diamonds belongs to type Ib.

Type II diamond

Type II diamond contains only small amounts of N, roughly $<10^{17} - 10^{18}$. cm^{-3} . Hence, they do not show any N-related IR absorption features. They are also further divided into subdivisions [Zai01];[Wil91].

Type IIa diamonds are considered the purest of all natural diamonds. They do not contain any impurities at all, hence they are optically the most transparent. $\sim 22\%$ of natural diamonds belong to type IIa, and are very much appreciated as a gemstone.

Type IIb diamonds contain no N, but they do contain boron (B). For this reason, they are naturally occurring p-type semiconductors (see section 1.2.2.1), containing a maximum B concentration of $10^{17}.\text{cm}^{-3}$. They absorb red, orange and yellow light, and therefore usually appear to be blue. They are also rare, making up 0.1% of all natural diamonds.

1.2.1.2 Synthetic diamond

Since the useful mechanical, electrical and chemical properties of diamond, which will be discussed in section 1.2.2, became known, numerous attempts were made to synthesise diamond. This was hoped to alleviate the high prices, scarcity and the inability to tailor the naturally occurring diamonds, limiting their use for technological applications. Moreover, the impurities that were present in 98% of all natural diamonds influenced and deteriorated the diamond properties, restricting the use for natural diamond in technology. In the course of history, two main procedures have been developed to synthesise diamond.

High Pressure – High Temperature (HPHT) is a technique that mimics the natural process that produces diamond from graphite. The technique has been perfected since 1955, providing a reliable way to produce synthetic diamond [Bun55]. However, since the procedure requires a metal solvent, traces in the diamond end product are not rare, leading to application-limiting defects in the diamond.

A more user-friendly and flexible method, allowing operation under lower pressure and temperature regimes, was obtained with the development of Chemical Vapour Deposition (CVD). Activation of a C-containing precursor gas mixture, most often consisting of methane (CH_4) and hydrogen gas (H_2), leads to the deposition of diamond onto a substrate [Lee99]. With this technique, it became possible to deposit thin films of diamond on a variety of substrates within reasonable time scales [May00].

Two basic forms of diamond can be synthesised, depending on certain diamond growth parameters: single-crystalline diamond (SCD) and polycrystalline diamond (PCD). The latter can be further subdivided according to the size of the crystals it is composed of: microcrystalline diamond (MCD), nanocrystalline diamond (NCD) and ultrananocrystalline diamond (UNCD).

Single-crystalline diamond (SCD)

SCD is grown using HPHT. Thin slices of natural or previously grown SCD are used as substrates or seed material for the graphite or feed material, making this a rather expensive procedure. Because there will be no lattice mismatch between the SCD seed material and the newly deposited diamond, a SCD layer will be formed. The diamond is said to have been grown homo-epitaxially. SCD growth has been optimised over the years to yield atomically smooth and defect-free diamond films [Liu93]. A Scanning Electron Microscope (SEM) image showing a SCD film is presented in figure 1.4.

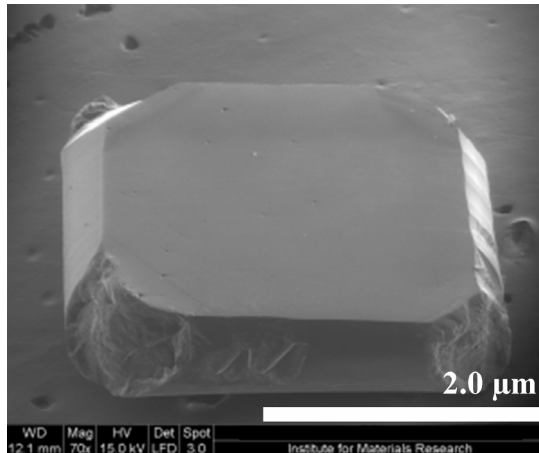


Figure 1.4: SEM image of a 600 μm thick freestanding homo-epitaxial SCD film grown at a 10% CH_4/H_2 ratio removed from the substrate by laser cutting (IMEC, *Wide Band Gap Materials*).

Polycrystalline diamond (PCD)

- *Microcrystalline diamond (MCD)*

MCD is synthesised on substrates with a lattice mismatch using CVD, and is therefore said to be grown hetero-epitaxially. The substrate is pre-treated by scratching the surface with diamond powder to roughen the surface and to act as seeds, or nucleation sites, for the diamond growth [Lee99]. Diamond growth starts simultaneously on every nucleation site, forming columnar structures, called grains, that increase in diameter as the growth proceeds. These grains eventually coalesce, leading to a surface consisting of grains in the μm -range delineated by their grain boundaries. These are rich in graphitic sp^2 -inclusions and defects. Depending on certain growth parameters, the orientation of the facets of the grains with respect to the surface can be controlled. MCD shows significant roughness, in the range of 1 to several tens of μm . For this reason, MCD is usually polished to obtain a smooth surface. However, this causes a thin and damaged surface, deteriorating its potential use in electronic applications [Neb07]. Figure 1.5 shows a SEM image of a MCD film.

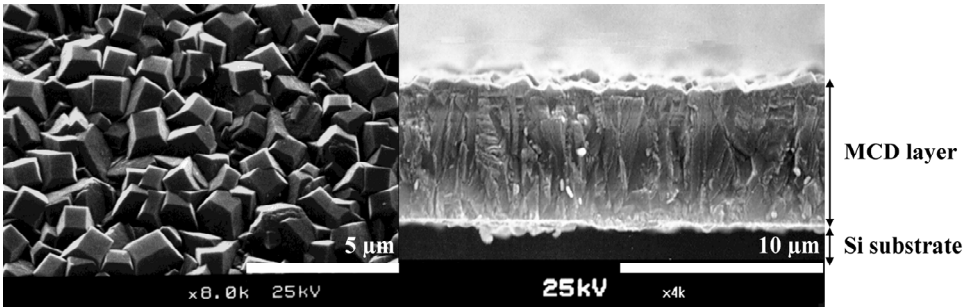


Figure 1.5: SEM images of a MCD film on Si. In a topographical view, the μm -sized grains on the surface are clearly visible (left panel). The cross-section shows the columnar growth nature of these grains (right panel) (*University of Bristol, CVD Diamond Film Group*).

- *Nanocrystalline diamond (NCD)*

NCD is grown identically to MCD, yet the density of nucleation sites is higher by increasing the concentration of the diamond powder during substrate pre-treatment. The result is a diamond film consisting of smaller (in the nm-range), and hence more, grains. This increases the amount of amorphous C and defects present in the grain boundaries. The grains facets are randomly oriented, resulting in a 'cauliflower'-like surface structure. The maximum attainable NCD film thickness is limited, since longer growth times cause the columnar crystals to become ever larger in diameter, eventually reaching MCD status. NCD and MCD are transparent and can be made semiconducting [Will06]. A SEM image is displayed in figure 1.6.

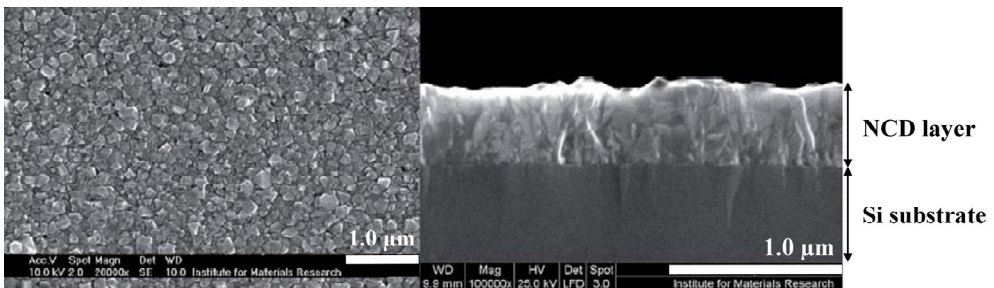


Figure 1.6: SEM images of a NCD film on Si. In a topographical view, the nm-sized grains on the surface are clearly visible (left panel). The cross-section shows the thinner diamond layer on top of the Si (right panel) (*Institute for Materials Research*).

- *Ultrananocrystalline diamond (UNCD)*

While the other PCD films are grown in a H-rich environment, UNCD is synthesised in an Argon-atmosphere. Instead of substrate nucleation before diamond growth, there is continuous re-nucleation during synthesis. This leads to even smaller grain sizes and to an even higher amount of non-diamond C phases in UNCD than in NCD, decreasing the optical transparency of UNCD films with respect to NCD. Also, UNCD is not semiconducting, but shows metallic conductivity governed by the grain boundaries at the surface [Will06]. This could create some difficulties in biosensor implementation. A UNCD SEM image is presented in figure 1.7.

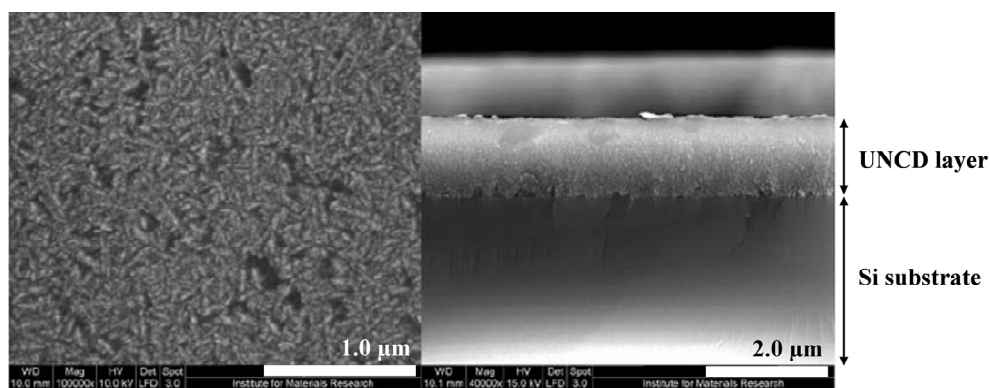


Figure 1.7: SEM images of a UNCD film on Si. In a topographical view, the even smaller grains on the surface are clearly visible (left panel). The cross-section is shown in the right panel (*Institute for Materials Research*).

1.2.2 Properties of diamond

1.2.2.1 Electronic properties

Large electrochemical potential window

When comparing diamond with other commonly used electrode materials, such as Pt, Au and glassy carbon, it has a significantly larger electrochemical potential window. As determined by cyclic voltammetry (CV, see section

1.3.1.1), the voltages at which oxidation (O_2 evolution) and reduction (H_2 evolution) occur are well separated by several volts. Oxidation reactions, occurring at a positive potential of ~ 1.8 V, produce positive currents. Reduction reactions produce negative currents and occur at different negative potentials for different kinds of diamond. For instance, by increasing the B-doping level from intrinsic (undoped) diamond to metallic diamond ($>10^{20} \text{ cm}^{-3}$), the onset of H_2 evolution can be switched on. Moreover, the background currents within this potential window are considerably smaller as compared to glassy carbon, Pt and Au. This is shown in figure 1.8 [Neb07].

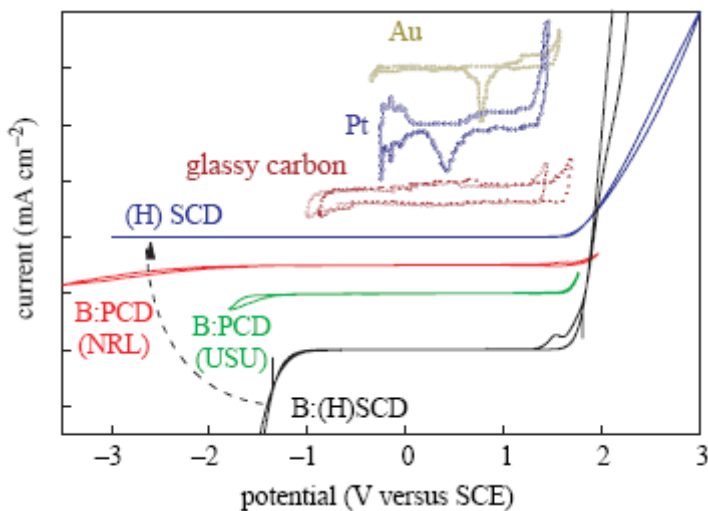


Figure 1.8: Cyclic voltammograms comparing various electrode materials. The graphs are shifted vertically for comparison. Two B-doped PCD films, B:PCD(NRL) containing $5 \times 10^{19} \text{ B.cm}^{-3}$ and B:PCD(USU) containing $5 \times 10^{20} \text{ B.cm}^{-3}$ [Gra99], are compared with a B-doped SCD film, B:(H)SCD, containing $3 \times 10^{20} \text{ B.cm}^{-3}$, and with an undoped SCD film, (H)SCD. Voltammograms of alternative electrodes such as Au, Pt and glassy carbon are also added for comparison. [Neb07]

Hydrogen (H)-induced surface conductivity

When H-terminated diamond is brought into contact with an electrolyte, a phenomenon called 'transfer doping' occurs. When the highest valence band energy level, or valence band maximum (VBM) of a material is higher than the chemical potential of the electrolyte (μ) in contact with that material, electrons can transfer from the valence band into the electrolyte, creating positively

charged holes in the valence band. These holes in the valence band cause surface conductivity. However, for most semiconductors, such as Si and Ge, their VBM is lower than the chemical potential of the electrolyte, μ .

H-termination of diamond creates a dense surface dipole layer because of the polar covalent bonds between C and H. The energy of this dipole varies over 1.6 eV, shifting all energy levels in the valence and conduction band of diamond upwards with this value. Figure 1.9 shows an overview of the energies of valence band and conduction band edges of several semiconductors, among which as-grown and H-terminated diamond.

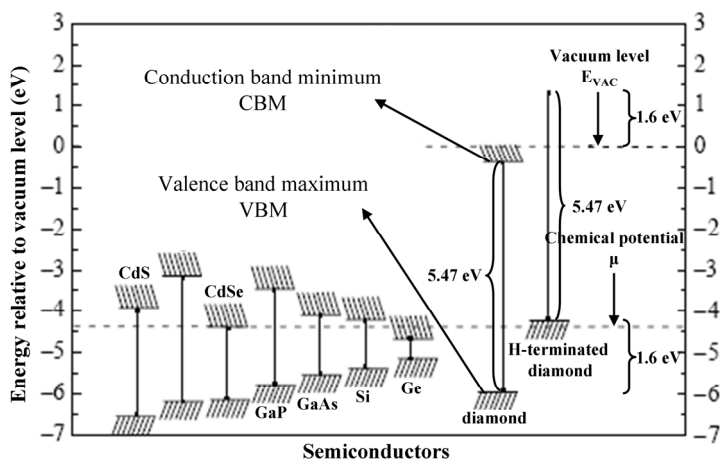


Figure 1.9: Energies of the valence and conduction band edges of several conventional semiconductors, including H-terminated and as-grown diamond relative to the vacuum level, E_{VAC} . The lower dashed line represents the chemical potential, μ , for electrons in an acidic electrolyte under the conditions of a standard hydrogen electrode. [Mai00]

Through the H-termination, the valence band energy level now surpasses the chemical potential of electrolytes, μ , allowing electrons to transcend into the electrolyte until the Fermi level (E_F) of the diamond and the chemical potential of the electrolyte, μ , align and reach thermodynamic equilibrium. This forms a hole accumulation layer in the diamond. This is illustrated in figure 1.10.

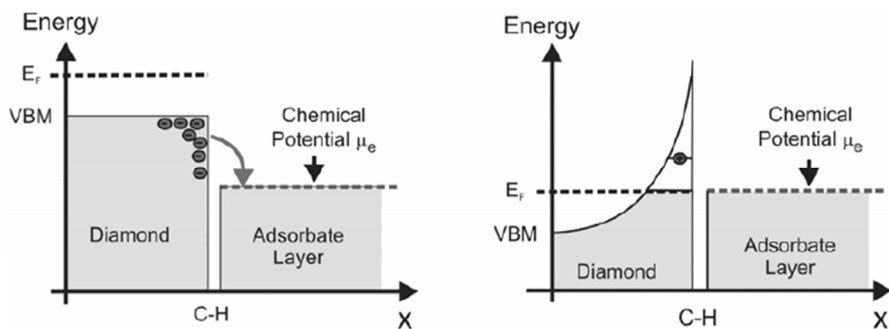


Figure 1.10: Schematic diagram of the diamond/electrolyte interface. Under non-equilibrated conditions (left panel), electrons from the valence band of the diamond tunnel into empty electronic states of the electrolyte. This continues until the E_f in the diamond and μ of the electrolyte align and reach thermodynamic equilibrium (right panel). [Neb07]

As the chemical potential of electrolytes, μ , is pH-dependent, the surface conductivity of H-terminated diamond also varies, as shown in figure 1.11. It can be predicted by the Nernst equation, showing a pH-dependency of 55 mV/pH [Neb06];[Mai00];[Cha07].

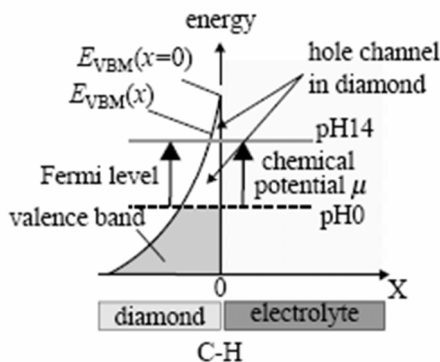


Figure 1.11: E_f and μ alignment at the diamond/electrolyte interface at pH 0 and pH 14. [Neb07]

Diamond doping

Intrinsic or undoped diamond has a very wide bandgap of 5.47 eV at room temperature, giving it near insulator-like characteristics. Diamond can be doped, however, into a semiconductor by the introduction of impurity atoms into the carbon lattice. As already mentioned, the major interest in semiconductors lies in the ability to control current flow through them by exposure to an external

energy source. Metals do not offer that option, since they almost always conduct electricity. Two types of diamond doping exist: p-type doping and n-type doping [Neb07].

- *p-type doping*

Introduction of impurity atoms of group III, for instance B atoms, into diamond results in p-type doping. In the diamond lattice structure, each C atom has 4 electrons in its outer, valence shell, that are shared with 4 other C atoms. The valence band, now containing 8 electrons per C atom, is completely filled, forming a very stable crystal. B has only 3 electrons in its valence shell. When B is introduced into the lattice, an electron deficiency, or a positively charged hole, is created in the energy level directly above the valence band of diamond, called the acceptor level. This hole can be filled by the movement of an electron from the valence shell of a neighbouring C atom into the hole of the B atom. B is thus called an acceptor atom. By filling the electron vacancy, a new hole is now created in the valence shell of the C atom that donated the electron, which itself can be filled by another neighbouring electron. The result is a movement of positively charged holes in the valence band of diamond. These holes are thus called the majority charge carriers.

In p-type diamond, the acceptor level lays 3.60 eV above the VBM, thus 1.87 eV below the conduction band minimum (CBM). This gap is too deep to be crossed at room temperature, a regime that has the most bio-electronic relevance. However, when the diamond is metallically doped with B, typically corresponding to $10^{20}.\text{cm}^{-3}$, enough holes will exist in the valence shell of diamond to propagate a current in the valence band without the need for thermal activation.

- *n-type doping*

Introduction of impurity atoms of group IV, such as phosphorous (P) atoms, into diamond results in n-type doping. P has 5 electrons in its valence shell. When P is incorporated into the diamond lattice, a situation is created where additional free electrons are supplied to the diamond lattice. Hence, P is called a donor

atom. These electrons are very loosely bound in the diamond crystal, and occupy an energy level directly (0.6 eV) below the conduction band, termed the donor level. Hence, only a small amount of energy is needed to promote excitation into the conduction band. The result is a movement of negatively charged electrons in the conduction band of diamond. These electrons are the majority charge carriers. In 1997, Koizumi *et al.* were the first to succeed in producing n-type doped SCD using phosphine [Koi97].

The difference between a p-type and an n-type semiconductor is graphically presented in figure 1.12.

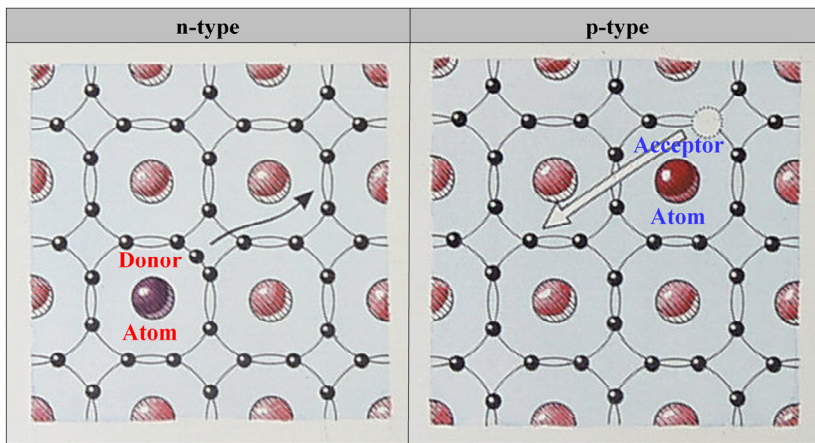


Figure 1.12: Schematic diagram of an n-type and p-type semiconductor material at the atomic level.

1.2.2.2 Physical properties

Hardness

Diamond is the hardest material found in nature. It scores a '10' on the Mohs scale. The Mohs scale, developed in 1822 by the Austrian Friedrich Mohs, ranks 10 minerals for their ability to scratch another mineral in the series. Another more quantitative scale, the Knoop scale, classifies materials according to the force needed to make indentations in them with a diamond. Again,

diamond ranks the highest. Diamond's hardness is not a constant quantity but varies even within a single diamond.

Because of the extreme hardness of diamond, tools can be coated with diamond for their use in the most important mechanical applications, such as sawing, drilling, cutting and polishing. Diamond coatings enhance their performance and prolong their lifetime. However, metals like manganese, iron, cobalt, nickel and Pt act as a solvent for carbon. For this reason, industrially important materials cannot be processed with diamond-coated tools [Davi92];[Mum93].

Thermal conductivity

Thermal conductivity indicates the ability of a material to conduct heat. In metals, thermal conductivity parallels electrical conductivity, as electrons transfer not only current but also heat energy. In other non-metal materials, this relationship between electric current and heat transfer fades. Phonons, quantised vibrational modes in a crystal lattice, are the major carriers of heat in these substances. Diamond has a very high thermal conductivity of 9 – 23 $\text{W.cm}^{-1}.\text{K}^{-1}$, exceeding that of, for instance, Si ($1.68 \text{ W.cm}^{-1}.\text{K}^{-1}$), copper (Cu) ($4.01 \text{ W.cm}^{-1}.\text{K}^{-1}$), silver (Ag) ($4.29 \text{ W.cm}^{-1}.\text{K}^{-1}$) and Au ($3.18 \text{ W.cm}^{-1}.\text{K}^{-1}$). Because atomic vibrations are controlled by temperature, thermal conductivity is usually temperature-dependent. This makes diamond an important material to be used in heat management. It can be used as a heat sink in computers, lenses, laser diodes, high-power integrated circuits and laser windows (see section 1.1.3.3, table 1.1) [Davi92].

Optics

Diamond is transparent over a large range of wavelengths [from the ultraviolet (UV) to the far-IR]. Moreover, its large bandgap (5.47 eV) prevents thermally generated conduction at elevated temperatures. Therefore diamond remains transparent even at very high temperatures and radiation intensities.

Diamond is thus an ideal material for optical applications, and can be used as X-ray and UV-transparent windows, and X-ray dosimeters.

The sparkling of a diamond is caused by an optical phenomenon called Total Internal Reflection (TIR). The light undergoes many internal reflections inside the diamond before it exits. When light crosses a boundary from a medium with a higher to one with a lower refractive index, the light will be partially refracted at the boundary surface, and partially reflected. At a certain critical angle, light is refracted such that it travels along the boundary. When the incidence angle is greater than the critical angle, all of the light will be reflected. This is called TIR. Total Internal Reflection Fluorescence (TIRF) spectroscopy makes use of this principle to study events at or close to the interface of two different media, for instance the analysis of cells on a coverslip in biological applications. The higher the refractive index of the material at the side of the incoming light beam with respect to the refractive index of the material at the other side of the boundary, the lower the critical angle at which TIR is obtained, and facilitating TIRF applications. The refractive index of diamond is 2.4, leading to a critical angle of 24.6°. This is much lower than for glass, having a refractive index of 1.5, and hence a critical angle of 40.5° [Davi92].

1.2.2.3 Biochemical properties

Another appealing feature of diamond, additional to the ones that are already described, is that the material is chemically inert. It does not degrade upon contact with aqueous electrolytes, as is the case with other well-known semiconductors used in the field of bio-electronics, such as Si. However, this inertness would form an obstacle to its use in biosensor-development, since biofunctionalisation cannot be achieved at an unreactive surface. Fortunately, in 2000, Takahashi *et al.* accomplished the activation of H-terminated diamond surfaces through a photochemical chlorination/amination/carboxylation [Tak00]. Hereby, they circumvented the barrier of diamond inertness, and paved the way towards the further modification of diamond with biomolecules, such as DNA and proteins (enzymes and antibodies). Together with the ability to be biofunctionalised, diamond is biocompatible, allowing for future *in vivo* electronic

applications. In the next section, a summary of the most important biofunctionalisation routes are given [Neb07].

Chemical biofunctionalisation

Ushizawa *et al.* reported the wet-chemical modification of diamond powder (1 – 2 μm) with thymidines [Ush02]. First, the surface of the diamond powder was oxidised to its surface oxides [carboxylic acid (COOH), hydroxyl (OH), acid anhydride] by immersion into a heated mixture of sulphuric acid (H_2SO_4) and nitric acid (HNO_3). Next, the carboxylated diamond was treated with thionyl chloride (SOCl_2) and thymidine, resulting in a thymidine-modified diamond surface. DNA molecules generated through Polymerase Chain Reaction (PCR) amplification could be covalently attached to the thymidine-modified surface via a simple ligation reaction. PCR has the interesting characteristic of adding an adenine (A) base to the 3' end of each amplified DNA molecule. These 3'A-overhangs were exploited in the ligation to the thymidine-modified substrate. Diffuse Reflectance Infrared Fourier-Transform spectroscopy (DRIFT) was used to verify the presence of DNA on the surface. A summary of their reaction process is given in figure 1.13.

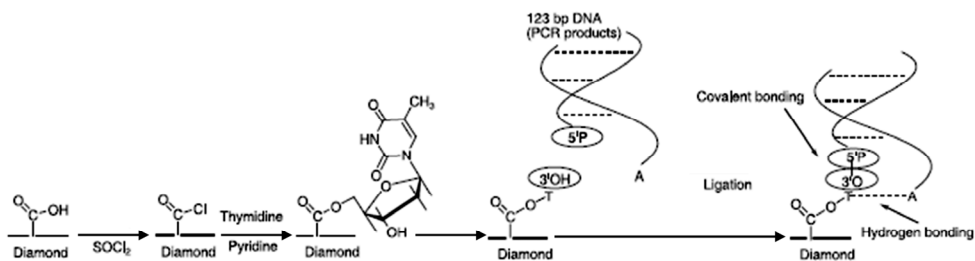


Figure 1.13: Reaction process used by Ushizawa for the covalent attachment of PCR-amplified dsDNA to thymidine-modified diamond powder. [Ush02]

Troupe *et al.* constructed a glucose sensor based on the modification of p-type diamond with the enzyme glucose oxidase through different mechanisms. Their most efficient sensor was prepared as follows. First, the B-doped diamond surface was oxidised and subsequently silanised with 3-aminopropyl-triethoxysilane (APTES), resulting in a NH_2 -modified diamond surface. This NH_2 -

modified diamond surface was modified with ferrocene-dicarboxylic acid. In parallel, glucose oxidase was modified with ferrocene-monocarboxylic acid. Lastly, the glucose oxidase-ferrocene-monocarboxylic acid complex was covalently bound to the ferrocene-dicarboxylic acid-modified diamond surface. The presence of glucose was detected amperometrically [Tro97]. Glucose is metabolised by glucose oxidase, causing the enzyme to become reduced and inactivated. Thus reactivation through oxidation of the enzyme is a prerequisite for the sensor to remain functional. This reduction-oxidation of glucose oxidase occurs through the redox couple ferrocene-monocarboxylic acid – ferrocene-dicarboxylic acid, transferring the electron current to be detected to the diamond electrode.

Clearly, chemical modification procedures are generally very tedious and labour-intensive multistep processes.

Electrochemical biofunctionalisation

SCD of p-type nature has been covalently modified with DNA molecules through an electrochemical procedure by Wang *et al.* They used a three-electrode configuration with a SCD working electrode, a Pt counter electrode and a silver/silver chloride (Ag/AgCl) reference electrode. The p-type SCD working electrode was treated with the diazonium salt 4-nitrobenzene-diazonium tetrafluoroborate. This salt was reduced in acetonitrile to nitrophenyl using CV and attached to the SCD surface in a nitrogen gas (N₂)-purged glove-box. The nitrophenyl groups were subsequently reduced to aminophenyl groups, resulting in a NH₂-modified SCD surface. This NH₂-modified SCD could then be modified downstream with the heterobifunctional cross-linker molecule sulphosuccinimidyl-4-(N-maleimido-methyl)cyclohexane-1-carboxylate (SSMCC). The N-hydroxy-succinimide (NHS)-ester group of SSMCC reacts with the NH₂-groups on the NCD to form amide (NH) bonds. SH-modified ssDNA could then be linked to the COOH-moiety of SSMCC at room temperature, resulting in a covalent bond. DNA functionality was confirmed with fluorescent hybridisation detection [Wa04]. However, this procedure involved a SSMCC crosslinker molecule between the surface and the attached biomolecules. This adds both complexity to the assay and distance between the molecule and the transducer.

The latter could negatively influence electronic read-out, since distance is inversely correlated with detection sensitivity. This procedure is outlined in figure 1.14.

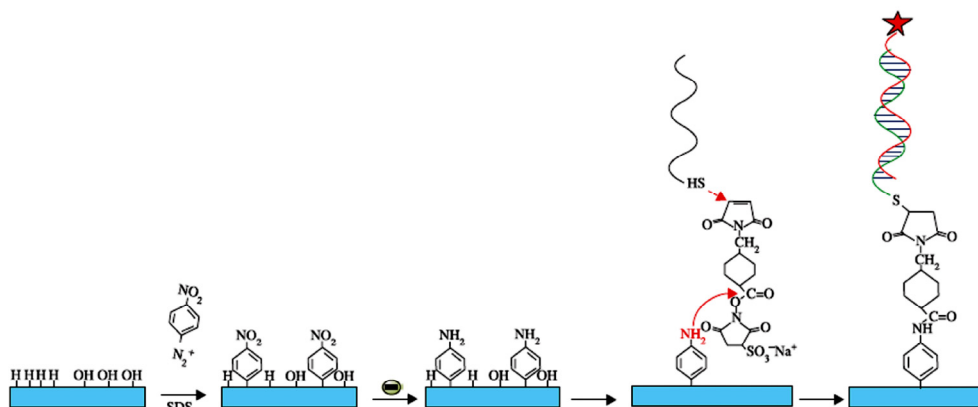


Figure 1.14: Reaction process used by Wang for the covalent attachment of thiolated ssDNA to aminophenyl-modified P-type SCD. [Neb07]

Gu *et al.* functionalised p-type diamond with a poly-aniline (PANI)/poly-acrylic acid (PAA) composite polymer films using CV. The p-type diamond working electrode was treated with the aniline and PAA monomeric solution, and by potential cycling the monomers were polymerised onto the electrode. In a final step, NH_2 -modified ssDNA was covalently attached to the exposed COOH -groups of the PANI/PAA polymeric film by 1-ethyl-3-(3-dimethylaminopropyl)-carbodiimide (EDC). The selective hybridisation was verified by fluorescence and impedance spectroscopy. The linear range of target ssDNA detection was 200 to 50 nM, with a detection limit of 20 nM [Gu05].

Photochemical biofunctionalisation

Undoped, H-terminated NCD surfaces were covered with trifluoro-acetamide acid (TFAAD) inside a nitrogen-purged Teflon reaction chamber by Yang *et al.* It is a 10-amino-dec-1-ene molecule, protected with a trifluoro-acetic acid group at one end. The other end is terminated by a $\text{C}=\text{C}$ double bond. The chamber was sealed with a quartz window, allowing the passage of UV-light from a low-pressure mercury lamp ($0.35 \text{ mW}\cdot\text{cm}^{-2}$ measured at the sample surface) for 12 h. This illumination process caused a covalent bond to be formed between the

TFAAD and the H-terminated NCD, exposing the trifluoro-acetic acid groups at the NCD surface. X-ray Photo-electron Spectroscopy (XPS) analysis confirmed the formation of a dense TFAAD monolayer [Yan02]. The exact mechanism of this photochemical reaction has not been completely elucidated, but Nichols *et al.* suggest two possible scenarios. Both of them involve the formation of TFAAD anions by UV-induced photo-emitted electrons from the NCD. In one scenario, these anions react directly with the H atoms on the NCD surface. In the other scenario, the anions abstract H atoms from the surface, creating surface C dangling bonds that can covalently bind with other TFAAD anions that are present [Nic05]. After TFAAD attachment, the trifluoro-acetic acid groups were removed by immersion into a hydrochloric acid (HCl)/methanol solution, forming NH₂-modified NCD surfaces. These were subsequently exposed to the heterobifunctional cross-linker molecule SSMCC. SH-modified ssDNA molecules could then be linked to the SSMCC in the same way as described above. Figure 1.15 represents the reaction steps that were employed. The functional activity of these ssDNA molecules was confirmed by the fluorescent detection of selective hybridisation with target ssDNA, and later, on p-type NCD, with impedance spectroscopy [Yan04]. However, the use of a permanent crosslinker allows the same remarks as with electrochemical biofunctionalisation.

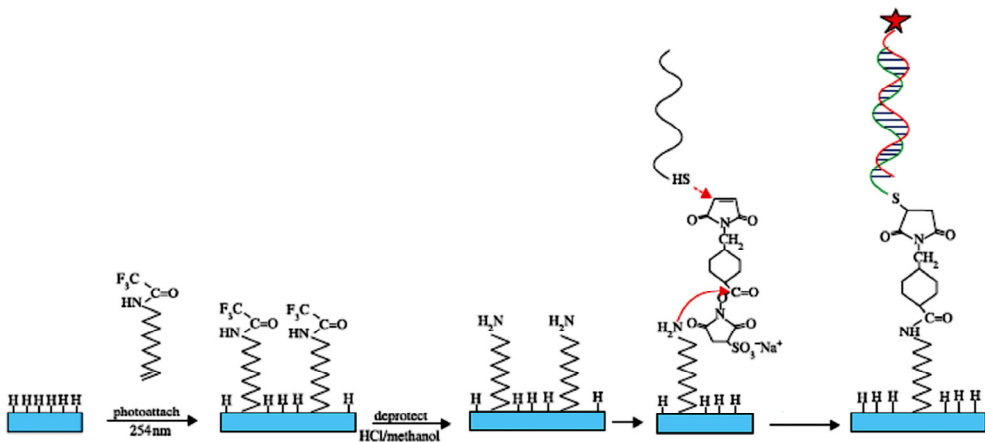


Figure 1.15: Reaction process used by Yang for the covalent attachment of thiolated ssDNA to photochemically activated NCD. [Neb07]

These same authors used this photochemical modification of p-type NCD and n- and p-type Si in 2007 to covalently attach human immunoglobulin G (IgG)

and IgM to the surface. The heterobifunctional cross-linker in this case was glutaraldehyde, consisting of two OH-groups on either end of the molecule, linked together by three C atoms. The NH₂-groups of IgG and IgM could easily be bound to the glutaraldehyde at room temperature. These covalently attached IgG and IgM antibodies served as antigens for anti-human IgG and anti-human IgM, and the selective recognition of the IgG's Fc region was confirmed in real-time with impedance spectroscopy. The detection limit was 42 nM in 12 minutes [Yan07].

Härtl *et al.* also used the same protocol to attach the enzyme catalase to n-type NCD. Since all proteins contain NH₂-groups, the catalase enzymes could easily be bound to the homobifunctional cross-linker glutaraldehyde. Using CV, the retention of the catalase enzymes' activity was confirmed amperometrically. After the addition of H₂O₂, the substrate of catalase, an increase in current was observed in the positive, anodic voltage range. This corresponded to the catalytic decomposition of H₂O₂ into water (H₂O) and O₂ by catalase. Also, current increased in the negative, cathodic voltage range, corresponding to the increased reduction of O₂ formed during the metabolism of H₂O₂. A linear response of the cathodic current to the H₂O₂ concentration was observed up to 150 mM, with a sensitivity of $\sim 70 \mu\text{A}\cdot\text{mm}^{-2}\cdot\text{M}^{-1}$. The detection limit was 0.3 mM [Här04].

Taken together, all of the above mentioned photochemical modification procedures involved crosslinker molecules between the surface and the attached biomolecules. Hence, the same remarks are valid as with electrochemical biofunctionalisation. Our group developed a **prototype of a DNA-sensor based on NCD**, being sufficiently flat to make **polishing unnecessary** and offering an **enlarged surface area** for biomodification due to the smaller grain structure. Moreover, the devised procedure for the covalent attachment of DNA was a **simple, two-step** photochemical method using a **flexible linker** and a **zero-length crosslinker**. Undoped, H-terminated NCD was immersed in a fatty acid molecule, 10-undecenoic acid (10-UDA), consisting of a reactive C=C double bond on one end, and a COOH-group on the other end. A 20 h illumination with UV-light ($2.5 \text{ mW}\cdot\text{cm}^{-2}$) also caused a covalent bond to be formed between the fatty acid and the H-terminated NCD, yielding a COOH-modified NCD surface. NH₂-modified DNA could then be reacted with these

COOH-groups via EDC, resulting in covalently bound DNA molecules to NCD through a NH bond. The presence of the fatty acid linker molecule offers **mobility** to the attached DNA, increasing their availability for hybridisation reactions. Moreover the EDC crosslinker did not remain present in the eventual amide bond, resulting in a **smaller distance** between NCD and DNA. The functional activity of this DNA was verified with PCR and gelelectrophoresis [Chr06] (see Chapter 3 and Aim 1), and later with impedance spectroscopy [Ver07] (see Chapter 5 and Aim 2).

1.3 CLASSIFICATION OF A BIOSENSOR

As already mentioned briefly, biosensors can be classified according to two systems. One can classify biosensors according to their biological selectivity for certain targets, inferred by their attached biological receptor molecules. The broad range of possible biological receptor molecules and the correlated biosensor types are summarised in table 1.2.

Table 1.2: Biosensor classification based on the type of biological receptor molecule.

Biomolecule	Type biosensor
Enzyme	Catalytic or enzyme biosensor
Affinity-complex forming biomolecules (membrane receptor, aptamer, protein, antibody, ...)	Affinity-based biosensor
→ antibody	→ immunosensor
→ DNA	→ DNA-based biosensor
Cell	Whole-cell biosensor

On the other hand, different transducer materials allow different physical signal transduction principles. Hence, another way to catalogue biosensors is according to the mode of signal transduction. The most frequently measured parameters accompanying the biological target recognition reaction and the concomitant transduction-based biosensor terminology are reviewed in table 1.3.

Table 1.3: Biosensor classification based on the transduction principle.

Measured parameter	Type biosensor
Electrochemistry	Electrochemical biosensor
→ current	→ amperometric biosensor
→ charge	→ coulometric biosensor
→ voltage	→ potentiometric biosensor
→ conductivity	→ conductometric biosensor
→ impedance	→ impedimetric biosensor
→ field-effect	→ Field-Effect Transistor-based biosensor
Optics	Optical biosensors
→ absorption	→ colorimetric biosensor
→ chemiluminescence	→ chemiluminescent biosensor
→ fluorescence (FRET*, reporter genes)	→ fluorescent biosensor (cell-based, array-based)
→ refractive index	→ Surface Plasmon Resonance biosensor
Mass	Piezo-electric biosensor

*FRET=Förster Resonance Energy Transfer

In the following subsections, both classification schemes will be used to catalogue biosensors. An overview of the principles used in literature is given in

table 1.4 on page 68 – 69. For a detailed discussion, the reader is referred to the text. The sensor platform developed in this thesis is compared with other types of sensing platforms and biofunctionalisation methods described in literature.

1.3.1 Electrochemical transduction

An electrochemical biosensor is a biosensor based on an electrochemical transducer. They are by far the most commonly used for clinical analysis and the most frequently cited in literature. These types of measurements are performed in an electrochemical cell equipped with a maximum of three electrodes. At the working electrode the recognition reaction of the analyte takes place. It can be constructed from a variety of materials, such as Pt, Au, glassy carbon, palladium, Si, and of course diamond, because of its favourable electronic properties even surpassing those of the popular Si (see table 1.1 and section 1.2.2.1). The reference electrode, usually Ag/AgCl or a saturated calomel electrode (SCE), has a known and constant potential. A counter electrode carries current flow away from the reference electrode. Electrochemical measurements can be subdivided into several categories [Gor05];[D'O03].

1.3.1.1 Amperometric

In amperometry, current generated in the electrochemical cell during the redox reaction of electro-active analytes is measured while the applied potential driving the redox reaction is kept constant. Usually a three-electrode setup is used. The reference electrode monitors fluctuations in voltage and hence, current, between the working and the counter electrode. A potentiostat then adjusts the current flow between these two electrodes to keep the voltage between them at a constant level. Because enzymes usually generate electro-active species, most amperometric biosensors are enzymatic biosensors. Moreover, amperometric enzyme biosensors were the first biosensors ever to be designed, as described in section 1.1.2. Hence, the following discussion about the working principles of amperometry is applied to enzymatic biosensors.

Enzymatic biosensors

A three-electrode electrochemical cell is used, consisting of the above mentioned working, reference and counter electrode. A schematic diagram of the amperometric measurement principle in an enzyme biosensor is shown in figure 1.16. The working electrode is modified with an enzyme of choice, suitable for the desired biosensor selectivity. The electrolyte contains the substrate of this enzyme that is to be quantified. When the substrate reaches the enzyme, it becomes metabolised into a product. In first-generation enzyme sensors, one of the generated products in the catalysed redox reaction diffuses to the working electrode surface. When the working electrode is set at a positive potential relative to the reference electrode, it will support an oxidation reaction of the product and it is referred to as the anode of the electrochemical cell. When the working electrode is set at a negative potential relative to the reference electrode, the product will be reduced and it is referred to as the cathode of the electrochemical cell. In second generation enzyme sensors, soluble electron mediators participate in the redox reaction of the immobilised enzymes together with the enzyme substrate. They, instead of one of the generated products, will become oxidised or reduced at the working electrode. The current flow in the electrochemical cell that accompanies this oxidation or reduction reaction of the product or mediators is measured, and is directly proportional to the substrate concentration. In a third generation enzyme sensor, the electrons that accompany the initial enzymatic reaction can be directly detected at the working electrode.

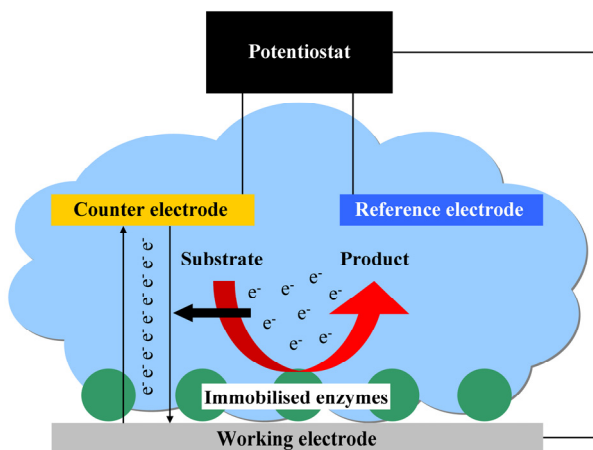


Figure 1.16: Schematic diagram of a third generation amperometric measurement principle. The enzymes immobilised onto the working electrode catalyse the metabolism of their substrate into a product. The electron flow between working and counter electrode accompanying this reaction is proportional to substrate concentration.

Fang *et al.* constructed a glucose biosensor based on the covalent immobilisation of glucose oxidase onto a Pt-sputtered indium-tin oxide (ITO) working electrode. Working potential was set at 0.5 V vs. SCE. Sensor signals were obtained from the anodic oxidation of H_2O_2 . A high sensitivity of $7 \mu\text{A}\cdot\text{cm}^{-2}\cdot\text{mM}^{-1}$ was obtained, and the dynamic range was situated between 0 and 10 mM. The detection limit was determined to be $50 \mu\text{M}$ [Fan03]. Since diabetic blood glucose concentrations fluctuate between 7 and over 11 mM, this was a clinically relevant result.

Stefan *et al.* constructed H_2O_2 -sensitive amperometric carbon paste biosensors for creatine and creatinine. A bi-enzyme sensor, based on immobilised creatinase and sarcosine oxidase, was constructed for the detection of creatine. A tri-enzyme sensor construction, based on immobilised creatinase, sarcosine oxidase and creatininase, was used for the detection of creatinine. For both assays, the dynamic range was in the pM- to nM-order, with very low detection limits [Stef03].

CV is a popular technique used to measure current in an electrochemical cell associated with the redox reaction of a certain analyte. It uses the same principle as described above, consisting of an enzyme-modified working electrode, a reference electrode and a counter electrode all in contact with the electrolyte containing the analyte to be measured. However, in contrast to the

general amperometric principle explained above, the potential of the working electrode relative to the reference electrode is not fixed, but varies linearly over time. The measurement starts at a potential where no redox reaction occurs. When the potential is swept to anodic values, the enzymatically generated electro-active species will become oxidised at a certain potential. When all of the species are oxidised and the potential is subsequently swept back to more cathodic voltages, the electro-active species will undergo a reduction at a certain voltage. The rate at which the voltages are swept is also an important parameter. CV rapidly provides considerable information on the thermodynamics of redox reactions and electron transfer processes, and offers a rapid localisation of redox potentials of the electro-active species.

Many amperometric enzyme biosensors are based on the enzymatic oxidation of a substrate and the concomitant reduction of O_2 to H_2O_2 . The electron-transfer during the re-oxidation of H_2O_2 back to O_2 is then amperometrically detected. However, as already mentioned previously in section 1.1.2, the oxidation of H_2O_2 requires a high potential, causing other substances present in the electrolyte to be oxidised more readily, and interfere with the detected signal. Therefore, amperometric enzyme biosensors using redox mediators became more widespread. The electron transfer that previously occurred through the redox reaction of O_2 to H_2O_2 and back to O_2 , now takes place through the redox reaction of the electron mediators. They have more favourable electron transfer kinetics, and allow operation of the sensor at much lower anodic potentials.

Jiali *et al.* developed a H_2O_2 -sensitive glucose biosensor based on a PCD film working electrode, a Pt counter electrode and a Ag/AgCl reference electrode. Glucose oxidase was covalently immobilised onto silanised PCD. The redox reaction of the enzyme was monitored using CV, in a potential range between 0 and 0.7 V vs. Ag/AgCl. The dynamic range of the sensor was from 0.5 mM to 15 mM using a Nafion membrane, and the sensitivity was determined to be 58.8 nA.mM^{-1} [Jia96].

Rao *et al.* fabricated an ethanol biosensor based on the oxidation of NADH to NAD^+ . PCD of p-type was used as a working electrode, a SCE electrode and a Pt foil were used as the reference and counter electrode, respectively. Alcohol dehydrogenase was covalently immobilised onto a nylon net on top of the p-type

PCD, and cyclic voltammograms were recorded from 0 to 0.9 V vs. SCE. The anodic NADH oxidation peak is situated at ~ 0.6 V vs. SCE. The anodic peak current increased monotonically upon addition of 0.2 to 1.5 mM of ethanol [Rao99].

Härtl *et al.*, as mentioned previously in section 1.2.2.3, attached the enzyme catalase to n-type NCD. Using CV, the retention of the catalase enzymes' activity was confirmed. After the addition of H_2O_2 , the substrate of catalase, an increase in current was observed in the positive, anodic voltage range. This corresponded to the catalytic decomposition of H_2O_2 into H_2O and O_2 by catalase. Also, current increased in the negative, cathodic voltage range, corresponding to the increased reduction of O_2 formed during the metabolism of H_2O_2 . A linear response of the cathodic current to the H_2O_2 concentration was observed up to 150 mM, with a sensitivity of $\sim 70 \mu A \cdot mm^{-2} \cdot M^{-1}$. The detection limit was 0.3 mM [Här04].

Enzyme biosensors profit from the intrinsic high sensitivity of enzymes. Using a diamond transducer material for the enzyme biosensor construction offers the additional benefits of biomolecule-diamond interface stability and, most importantly in CV, a wide potential window with no background current (see section 1.2.2.1). However, many of these reported diamond-based biosensors display a mere proof-of-principle but did not transcend into relevant clinical applicability.

Immunosensors

The above discussion is focused upon the largest group of amperometric biosensors, being enzymatic biosensors. However, amperometric immunosensors have also been developed. Because antibodies and antigens are usually not electro-active within the desired potential range, redox-active labels are required as indicators, making them indirect amperometric biosensors. In contrast to our approach (see Chapter 6 and Aim 4), these amperometric immunosensors are not label-free, complicating their operation significantly.

Alkaline phosphatase (AP) was used as an enzymatic label for the amperometric detection of digoxin and IgG. Anti-digoxin and anti-IgG monoclonal antibodies were immobilised on a carbon paste electrode. AP-

labelled digoxin and IgG and their unlabelled counterparts in samples competed for the anti-digoxin and anti-IgG binding sites, and the non-specifically bound digoxin and IgG was removed. The substrate for AP was added, and the current flow accompanying this enzymatic reaction was detected. They reached a detection limit of 64 pM for digoxin and 33 pM for IgG, mainly owing to the presence of the enzymatic label [Hei85].

DNA-based biosensors

Amperometric DNA-based biosensors have also been reported, making use of their intrinsically electro-active bases, guanine (G) and adenine (A). Probe ssDNA is attached to the working electrode surface, and hybridisation is detected by means of redox mediators. The G and/or A residues in the DNA and the redox mediators participate in a redox reaction, followed by the re-oxidation of the mediator at the anodic electrode. The current is proportional to the amount of G and/or A, being larger in dsDNA. Direct detection of the G and/or A bases without the use of a redox mediator is generally considered to be too insensitive.

Ye *et al.* constructed an electrochemical biosensor for the detection of Hepatitis B virus (HBV) DNA based on CV. They covalently immobilised ssDNA through their 3' OH-end to the COOH-groups of thioglycolic acid SAMs on a Au working electrode. Cyclic voltammograms were obtained from -0.3 V to 0.7 V vs. SCE, in the presence of the redox mediator ferrocenium hexafluorophosphate (FcPF₆). They reached a detection limit of 0.2 fM of PCR amplified HBV DNA. As a selectivity control, aspecific calf thymus DNA was used [Ye03].

Although the fact that a very high sensitivity is reached with DNA molecules that come straight out of PCR, some disadvantages are associated with the choice of transducer material. Gold causes substantial background current in CV [Neb07] and makes for a rather unstable biomolecule-gold interface [Yan02]. As opposed to our approach (see Chapter 5 and Aim 2), this approach can also not be termed label-free because of the requirement of an electron mediator.

1.3.1.2 Coulometric

Coulometry is an electrochemical technique related to amperometry. In this case, the amount of charge instead of the amount of current is measured between the electrodes, related to the oxidation and reduction reactions of the electro-active analytes at the working electrode.

1.3.1.3 Potentiometric

In potentiometry, the electrical potential difference between working and reference electrode in the electrochemical cell is measured when the current in the electrochemical cell is zero. This change in potential is directly correlated with the logarithmic analyte concentration. Usually, the potential of the working electrode varies depending on the concentration of charge or ions in the electrolyte. Hence, the most common potentiometric sensor is a pH-sensor. It is an ion-sensitive electrode (ISE) that is sensitive to the hydrogen ion (H^+) concentration in the electrolyte. However, since a pH-sensor does not make use of a biological receptor component, this type of sensor is referred to as a chemical sensor instead of a biosensor. The basis of a potentiometric biosensor is displayed in figure 1.17.

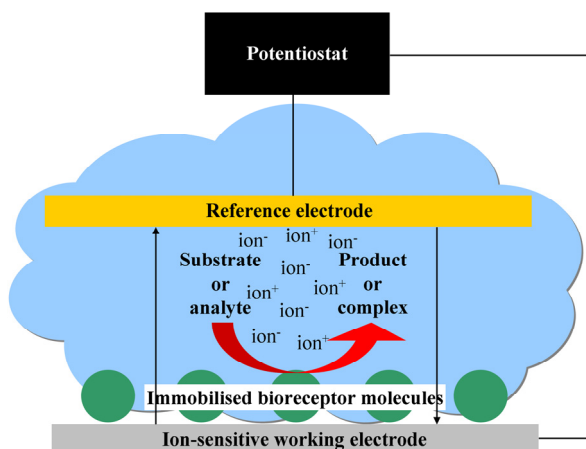


Figure 1.17: Schematic diagram of the potentiometric measurement principle. The biomolecules immobilised onto the working electrode catalyse or recognise their target. The generation of additional ions accompanying this reaction varies the potential, and is proportional to target concentration.

Enzymatic biosensors

Apart from potentiometric chemical sensors, such as the pH-sensor, potentiometric enzymatic biosensors also exist. Enzymatic biosensors generating an ionic product during the reaction can be used to potentiometrically measure the concentration of the substrate.

In literature, enzymatic potentiometric biosensors have been described for the detection of urea. The enzyme urease was immobilised at a polyvinyl chloride ISE and the detection was based on the production of the ammonium ion (NH_4^+). However, the linearity and sensitivity of these NH_4^+ -sensitive sensors was compromised by a rapid conversion of NH_4^+ back to ammonia (NH_3), to which the ISE was not sensitive [Gui70].

Immunosensors

In principle, potentiometric immunosensors should be feasible. Since antibodies and antigens usually contain a net electrical charge, the charge of the complex would be different than the charge of either the antibody or the antigen alone. Immobilising one of the immuno-agents could then result in a direct immunosensor. However, this has proven to be very difficult to realise. The potentiometric immunosensors described in literature have all been indirect, requiring most often enzymatic or ionophoric labels that are responsible for the generation of additional charge. None of them have been commercialised.

IgG detection was realised by Fonong *et al.* using the enzyme chloroperoxidase conjugated to anti-IgG immobilised onto a CO_2 electrode. Chloroperoxidase produces CO_2 from β -keto adipic acid. This enzymatic function is inhibited by the binding of IgG to anti-IgG, reducing the CO_2 -production. IgG-sensitivity in the nM- to μM -range was obtained [Fon84]. We obtained comparable sensitivity with a label-free approach (see Chapter 6 and aim 4).

DNA-based biosensors

Wang *et al.* utilised an enzyme-amplified method for hybridisation detection. Streptavidin-modified magnetic beads were functionalised with biotinylated ssDNA. Target ssDNA related to the BRCA1 breast cancer gene were modified with multiple copies of AP through a streptavidin-biotin bond, and exposed to the probe ssDNA-modified beads for hybridisation. After hybridisation, the AP substrate, α -naphthyl phosphate, was added and metabolised to α -naphthol. Finally, the complexes were magnetically separated from the supernatant, the latter containing the enzymatic product α -naphthol. This α -naphthol-containing supernatant was transferred to a three-electrode electrochemical cell with a carbon-nanotube working electrode, a Pt wire counter electrode and a Ag/AgCl reference electrode for potentiometric measurements of α -naphthol. A dynamic range of 3.3 – 20 nM was determined, and a detection limit of \sim 6.6 pM. As a selectivity control, random, non-complementary DNA was used [Wan04].

Again, the good sensitivity of this potentiometric DNA-sensor is overshadowed by the requirement of a label, complicating the setup. Moreover, no attempt was made to explore the sensitivity in terms of number of detectable mismatches. In this context of breast cancer, single nucleotide polymorphism (SNP) sensitivity in the BRCA1 gene is of utmost importance. In our research, we did focus on the establishment of SNP sensitivity (see Chapter 5 and Aim 2).

1.3.1.4 Conductimetric

Conductimetric devices detect changes in conductivity, or the ability to carry current, of the electrolyte between working and reference electrode in an electrochemical cell. Such changes in conductivity can arise due to changes in ionic strength of the electrolyte. Thus, it offers another way of determining the analyte concentration through the generation of ions.

Enzymatic biosensors

When an enzymatic reaction generates a change in the concentration of an ionised species, the conductivity of the electrolyte changes. For this reason, most of the conductimetric biosensors reported in the literature are enzymatic biosensors. However, measuring the conductivity is difficult, because of the variable ionic background of clinical samples, and the relatively small conductivity changes that occur in these solutions. This hinders the translation into commercial applications.

One commercial system (BUN analyzer, Beckman-Coulter) measures urea in plasma, blood and urine, but is limited to the measurement of high concentrations, due to the small conductivity changes associated with low concentrations [Eck82];[Chu76].

DNA-based biosensors

Park *et al.* presented an unusual setup for the conductimetric detection of DNA hybridisation. Probe ssDNA was covalently immobilised onto a silicon/silicon dioxide (Si/SiO₂) wafer, between two Au/tin electrodes. Longer target ssDNA was added and hybridisation occurred between probe ssDNA and one half of the target sequence. Subsequently, ssDNA-modified Au nanoparticles, complementary to the other half of the target ssDNA were added. Ag deposition to these Au nanoparticles leads to a measurable conductivity increase between the two electrodes. Target ssDNA was detected in the range of 50 nM to 500 fM. As a selectivity control, 3 types of 1-mismatch ssDNA were used [Par02].

The sensitivity obtained by these authors is due to the use of two signal amplification systems, complicating their procedure as a whole, but also the implementation of the platform into a lab-on-chip.

1.3.1.5 Impedimetric

Theory

In an ideally resistive electrical circuit, the elements such as the voltage (V), current (I), and resistance (R), behave independent of the voltage frequency, and are governed by Ohm's law:

$$R = \frac{V}{I} \quad (1)$$

Often, however, the electrical circuit is not purely resistive, but also contains inductive (L) and capacitive (C) components. If in this case an alternating (AC) voltage is applied, I and V become out of phase and are frequency-dependent. For this reason, the oscillating V and I will be written as complex entities, as a function of their magnitudes V_0 and I_0 , respectively, the phase shift φ of I with respect to V , and the frequency ω :

$$V(t) = V_0 \exp(j\omega t) \quad (2)$$

$$I(t) = I_0 \exp[j(\omega t - \varphi)] \quad (3)$$

Consequently, the simple R is replaced by the complex impedance, Z . Being a complex entity, Z is also defined by its magnitude, Z_0 , and its phase shift, φ :

$$Z = \frac{V(t)}{I(t)} = Z_0 e^{j\varphi} = Z_0 (\cos \varphi + j \sin \varphi) \quad (4)$$

where $Z_0(\cos \varphi)$ and $Z_0(\sin \varphi)$ are the real part, $\text{Re}(Z)$, and the imaginary part, $\text{Im}(Z)$, of the complex impedance, Z , respectively. In other words,

impedance signifies opposition to current flow in an alternating current (AC) electrical circuit.

Two popular ways exist to graphically represent the impedance data: a Bode plot and a Nyquist plot. A Bode plot depicts the magnitude of the complex impedance, Z , or the phase shift, φ , as a function of frequency, ω . Usually, a logarithmic scale is used for the magnitude and the frequency. Figure 1.18 shows an example of a Bode plot of the complex impedance, Z , and of the phase shift, φ , for a parallel RC circuit.

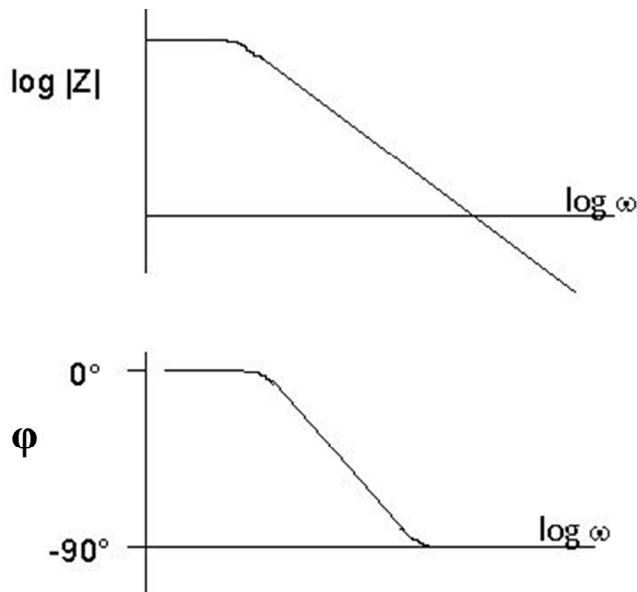


Figure 1.18: Bode plot of the complex impedance, Z (upper panel), and of the phase shift, φ (lower panel), versus frequency, ω , for a parallel RC circuit. Both the X-axis and the Y-axis are represented by a logarithmic scale.

A Nyquist plot displays the imaginary part and the real part which make up the complex impedance, Z . The negative form of $\text{Im}(Z)$ is plotted on the Y-axis, while $\text{Re}(Z)$ is presented on the X-axis. Figure 1.19 shows a Nyquist plot of the same parallel RC circuit as in figure 1.18.

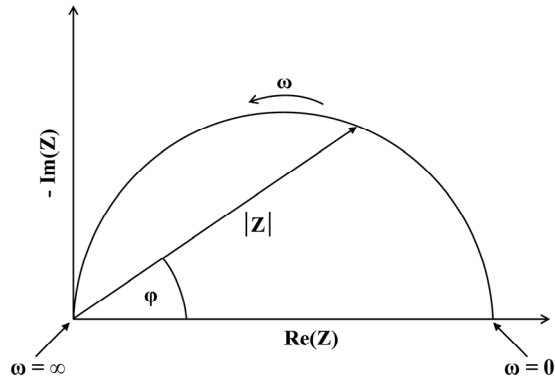


Figure 1.19: Nyquist plot, displaying $-\text{Im}(Z)$ versus $\text{Re}(Z)$, for a parallel RC circuit.

Each point in this Nyquist plot represents the complex impedance, Z , at one frequency, ω . When drawing a vector through the zero-point to this point, the magnitude, $|Z|$, and the phase shift, ϕ , can be deduced. The frequency, ω , decreases from right to left in the plot [You00].

Doping of semiconductors

Semiconductors are able to control current flow through them by exposure to an external energy source. As already mentioned in section 1.2.2.1, two types of doping exist [You00]:

- *p-type doping*

Introduction of impurity atoms of group III, with an electron deficiency in their valence shell, into the semiconductor material results in p-type doping. In this way, a positively charged hole is created in the energy level directly above the valence band of the semiconductor, called the acceptor level. This hole can be filled by the movement of an electron from the valence shell of a neighbouring atom into the hole of the impurity atom. This impurity atom is thus called an acceptor atom. By filling the electron vacancy, a new hole is now created in the valence shell of the atom that donated the electron, which itself

can be filled by another neighbouring electron. The result is a movement of positively charged holes in the valence band of the semiconductor. These holes are thus called the majority charge carriers.

- *n-type doping*

Introduction of impurity atoms of group IV, with an excess of electrons in their valence shell, into the semiconductor material results in n-type doping. In this way, a situation is created where additional free electrons are supplied. Hence, the impurity atom is called a donor atom. These electrons are very loosely bound, and only a small amount of energy is needed to promote their excitation into the conduction band. The result is a movement of negatively charged electrons in the conduction band of the semiconductor. These electrons are the majority charge carriers.

Semiconductor-liquid interface

As already touched upon in section 1.2.2.1, when a semiconductor electrode is placed into contact with an electrolyte, the E_F of the semiconductor and the chemical potential of the electrolyte, μ , are initially not in equilibrium. Two alternative events can occur to obtain the necessary thermodynamic equilibrium, depending on the type of semiconductor. These are shown in figure 1.20. When a p-type semiconductor is placed in contact with a liquid, electrons move from the electrolyte into the semiconductor, thereby depleting the positively charged holes in the material and creating a region just below the semiconductor surface where no majority charge carriers exist. This region is called the depletion zone or the space-charge region. When no more electrons move into the semiconductor, thermodynamic equilibrium is reached between the E_F and μ , resulting in a downward bending of the valence and conduction bands in the p-type semiconductor. When a n-type semiconductor is placed in contact with a liquid, electrons move from the semiconductor into the electrolyte, also decreasing the amount of majority charge carriers in the material and creating a depletion zone or space-charge region just below the semiconductor surface. At

thermodynamic equilibrium, the result is an upward band bending. These phenomena occurring in the semiconductor are called field-effects.

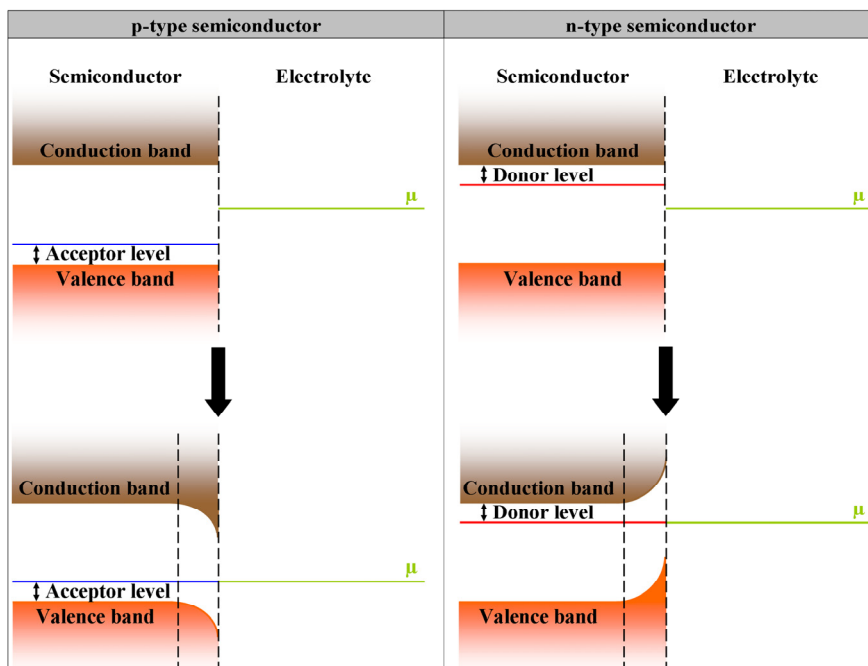


Figure 1.20: Generation of thermodynamic equilibrium in p-type (left panel) and n-type (right panel) semiconductors through downward and upward band bending, respectively.

Any chemical modification in the electrode-electrolyte interface, for instance the binding of an antigen to an antibody-modified electrode, or the hybridisation of target ssDNA to a ssDNA-modified electrode, will alter this equilibrium, and hence the degree of band bending. In other words, the depletion zone in the semiconductor can be made wider or narrower by external events. A narrowing of the depletion zone corresponds to a decrease in impedance, since the obstacle for charge carriers that want to cross this space-charge region decreases. A widening of the depletion zone corresponds to an increase in impedance, since the obstacle for charge carriers that want to cross this space-charge region increases. Since DNA is negatively charged, it will likely exert a field-effect in a semiconductor when bound to its surface. Electrochemical Impedance Spectroscopy (EIS) is therefore often used as a detection mechanism of hybridisation events. When ssDNA is attached to the surface of a p-type semiconductor, their negative charges attract the holes in the semiconductor to

the surface-DNA interface. The space-charge region becomes narrower, and the downward band bending becomes less steep. Moreover, additional negative charges brought about by hybridisation will increase this effect even more. The result is a decrease in impedance. When ssDNA is attached to the surface of a n-type semiconductor, their negative charges repel the electrons in the semiconductor. The space-charge region becomes wider, and the upward band bending becomes more pronounced. This effect is again amplified by hybridisation.

In EIS, an AC potential is generated over a range of frequencies between the biologically modified semiconductor working electrode and a counter electrode. The impedance is subsequently measured between these two electrodes, through the electrolyte, for each frequency in the analysed frequency range. By modelling the observed impedance effects with an electrical circuit, one can associate certain effects with changes in electrical elements, further elucidating the events at the molecular level. It is a useful tool for label-free and real-time target detection. In comparison, the previously summarised techniques, such as amperometry, conductimetry and potentiometry, very often required label-based signal amplification and detected their selective analytes in an endpoint configuration where 'before target addition' was compared to 'after target addition'. In contrast, we have chosen for a real-time approach, decreasing cost and analysis time [Neb06];[You00];[Mem00];[Cha07].

Immunosensors

Yang *et al.* used EIS to directly detect antigen-antibody binding on diamond and Si. A Pt foil and Ag/AgCl served as a counter and a reference electrode, respectively. They covalently modified n-type and p-type Si and p-type NCD with human IgG and IgM. The Fc regions of these covalently attached IgG and IgM antibodies served as antigens for anti-human IgG and anti-human IgM. They succeeded in real-time and label-free detection of selective antigen recognition, and observed an increase in impedance at frequencies $>10^4$ Hz for the p-type substrates, and a decrease in impedance in the same frequency region for n-type Si. This dependence on doping type indicates the involvement of a field-effect in the underlying semiconductor. Indeed, circuit modelling showed that

the frequency region sensitive for antigen recognition is dominated by the space-charge region of the electrode. When positively charged anti-IgG and anti-IgM approach a p-type surface, the holes are repelled and widen the depletion zone, increasing the impedance in the space-charge region. When positively charged anti-IgG and anti-IgM approach a n-type surface, the electrons are attracted, which narrows the depletion zone, decreasing the impedance in the space-charge region. The detection limit for real-time selective IgG detection was 42 nM in 12 minutes [Yan07].

This real-time, label-free immunosensor is unfortunately obscured by the fact that the manner of antigen recognition has questionable clinical relevance. The Fc regions of the immobilised antibodies serve as antigens while they do not explore the possibility of antigen detection through the Fab regions of immobilised antibodies.

In this PhD work, H-terminated NCD working electrodes were modified with anti-C-reactive protein (CRP) by simple physical adsorption. The detection of CRP, an acute phase protein serving as a marker for cardiovascular disease (CVD), occurred through the Fab regions of the immobilised antibodies. A Au wire in contact with the reaction fluid served as a counter electrode. The selective antigen recognition was analysed in real-time with EIS by monitoring the differences in frequency-dependent impedance change upon addition of CRP and fluorescein isothiocyanate (FITC)-labelled ssDNA. The detection limit was found to be 10 nM, which was in the physiologically relevant range, and could be discriminated within 10 minutes (see Chapter 6 and Aim 3 – 4).

DNA-based biosensors

Yang *et al.* monitored selective DNA hybridisation using EIS. H-terminated NCD working electrodes of p-type nature were covalently modified with thiolated ssDNA molecules. A Pt foil and a Ag/AgCl wire were used as counter and reference electrode, respectively. They showed that measurements at open-circuit potential displayed a significant decrease in impedance at frequencies of $>10^4$ Hz, even in real-time, when the NCD electrode was exposed to complementary target ssDNA, while 4-mismatch sequences were easily

discriminated. By electrical circuit modelling, they attributed this effect to a hybridisation-induced field-effect in the NCD film [Yan04].

Cai *et al.* performed analogous experiments on n-type Si working electrodes. They showed that hybridisation with complementary target ssDNA increased the impedance at frequencies $>10^3$ Hz, illustrating nicely the opposite effects of p- and n-type electrodes. The selectivity was demonstrated with 4-mismatch sequences. By electrical circuit modelling, they attributed the observed effect to a hybridisation-induced increase in the resistance of the Si film [Cai04].

Gu *et al.* covalently immobilised NH_2 -modified ssDNA onto p-type diamond with PANI/PAA composite polymer, as mentioned in section 1.2.2.3. A three-electrode system was used for EIS. The p-type diamond served as a working electrode, the counter electrode was a Pt wire and the reference electrode was Ag/AgCl. They observed an impedance decrease, this time in the lower frequency regions (10 – 100 Hz) upon complementary hybridisation, and a decrease in electron-transfer resistance to the electrode. Electric circuit modelling, using the same circuit model as Yang, attributed this lower frequency region to reflect the polymer/molecular double-layer. They suggest that hybridisation with complementary DNA decreases the resistance and increases the capacity of the polymer, both due to an increase in ionic density at the interface. The space-charge region of the p-type diamond electrode was reflected at frequencies of ~ 1000 Hz. They found that DNA hybridisation also altered the electrical response of the electrode through a field-effect, resulting in a decreased impedance in this space-charge region. The linear range of target ssDNA detection was 50 to 200 nM, with a detection limit of 20 nM. They obtained SNP sensitivity [Gu05].

Since these above mentioned publications either did not obtain SNP sensitivity [Yan04];[Cai04], did not report a real-time detection scheme [Cai04];[Gu05] or did not benefit from the advantages of diamond [Cai04], we devised a DNA-sensor covering all of these issues. In our study, we investigated the possibility of SNP detection on NCD using EIS. Probe ssDNA molecules were covalently attached to COOH-modified NCD working electrodes. The frequency-dependent change in impedance was analysed in real-time during hybridisation with complementary, 1-mismatch and non-complementary target ssDNA, and during the subsequent denaturation. SNP discrimination was possible in real-

time during hybridisation in a frequency region around 1000 Hz and during denaturation at the highest frequency of 1 MHz [Ver07] (see Chapter 5 and Aim 2).

1.3.1.6 Field-effect

Theory

Field-effect transistor (FET)-based biosensors offer an alternative approach for the label-free and real-time detection of changes in ionic charge concentrations in the electrolyte associated with the recognition and binding of target by electrode-immobilised biomolecules.

A FET is composed of four elements: a drain, a source, a gate and a semiconducting body. Depending on the materials used for certain of these elements, different FET configurations can be obtained. In a MOS(Metal-Oxide-Semiconductor)FET, the gate electrode is a metal, although more recently, semiconductor gate electrodes are most often used in MOSFETs, making the term more historic than correct. The gate electrode is also separated from the body by an electrical insulator, often SiO₂, to inhibit current flow through the gate. In a IS(Ion-Sensitive)FET, the gate voltage is determined by charges in the electrolyte, taking over the role of gate. The terms ENFET and IMFET are used to indicate that the gate has been modified by enzymes (EN) and antibodies (IM), respectively.

As already mentioned, two types of semiconductors can be distinguished. A n-type semiconductor contains an excess of negative electron carriers, whereas a p-type semiconductor contains an excess of positive holes. Depending on the type of semiconductor used as body electrode, also two types of FET structures can exist, which are graphically displayed in figure 1.21:

- PNP or p-channel FET
- NPN or n-channel FET

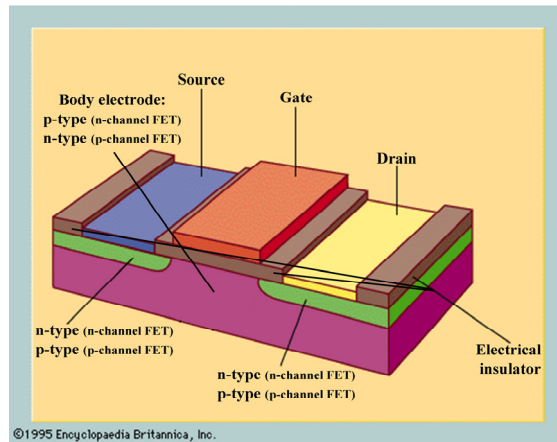


Figure 1.21: Schematic diagram of a FET structure.

When the semiconducting body electrode is n-type, the source and drain electrodes are p-type (PNP or p-channel FET). In the opposite configuration, the body electrode is p-type, the source and drain electrodes are n-type (NPN or n-channel FET).

The FET controls current flow from the source to drain by affecting the size and shape of the space-charge region in the semiconducting body electrode by applying a negative or positive voltage to the gate, as is shown in figure 1.22:

- *Applying a negative gate voltage to a n-channel FET (NPN FET)* causes the positive charge carriers in the p-type semiconducting body electrode to become attracted to the gate electrode. This positively charged channel blocks current flow between source and drain.

- *Applying a positive gate voltage to a n-channel FET (NPN FET)* will create a conductive channel from source to drain. By attracting electrons from source and drain to the gate electrode and repelling the positive charge carriers from the p-type semiconductor body electrode further into the bulk, the resistance in the space-charge region decreases and current flow between source and drain increases.

- *Applying a negative gate voltage to a p-channel FET (PNP FET)* will create a conductive channel from source to drain. By attracting positive holes from source and drain to the gate electrode and repelling the electrons from the n-type semiconductor body electrode further into the bulk, the resistance in the

space-charge region decreases and current flow between source and drain increases.

- Applying a positive gate voltage to a p-channel FET (PNP FET) causes the electrons in the n-type semiconducting body electrode to become attracted to the gate electrode. This negatively charged channel blocks current flow between source and drain.

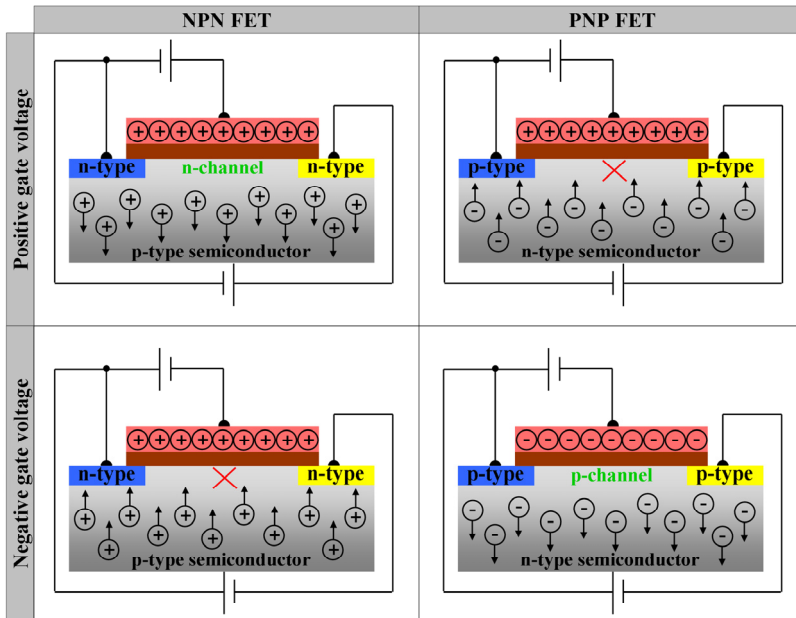


Figure 1.22: Schematic diagram of the varying source-drain current density as a function of semiconductor type and gate voltage.

From a biosensor perspective, hybridisation with target ssDNA to ssDNA immobilised onto the gate can influence the gate potential. Thus, one can measure the influence of the target recognition reaction directly on the source-drain current, or one can measure the compensatory change in gate potential necessary to keep the source-drain current at a constant level [You00].

Immunosensors

Nowadays, it has been generally accepted that the detection of antibody-antigen recognition by means of FET is problematic, to say the least. The

counter-ion screening effect is the main reason for this fact. Charged groups in the protein layer on top of the substrate will be neutralised by the surrounding counter-ions that are present in the buffer solution. This will result in net uncharged molecular layers, causing the biological recognition event to proceed undetected with FET-based devices. Furthermore, the density of the protein layer will determine greatly whether or not a measurable signal will result. The success or failure of FET-based immunosensors will therefore also depend on the specific conditions of the protein adsorption, which are often not really controlled [Pog05];[Ber03].

DNA-based biosensors

Ingebrandt *et al.* employed a FET-based technique to detect DNA-hybridisation in real-time and label-free, in a microarray setup. Si of n-type nature was used as a body electrode, and a reference electrode applied the gate voltage. The insulating gate oxide was SiO₂. The total transistor chip consisted of 16 of these PNP FET-units. A differential approach proved the most reliable, where one of two electrically identical chips, the reference chip, is covalently modified with a non-complementary ssDNA probe, while the other chip is modified with a probe complementary to the target ssDNA. A pronounced field-effect was detected when hybridising in low-ionic strength Tris/EDTA (TE) buffer, to minimise the counter-ion screening effect that blocks the effect of charge accumulation to the electrolyte-oxide interface. Such a low-ionic buffer is however not ideal to support hybridisation reactions. Complementary DNA hybridisation will increase the amount of negative charge at the n-type semiconductor surface. This will cause a repulsion of the majority charge carriers in the n-type semiconductor, and an attraction of the holes in drain and source towards to the interface, leading to the formation of a conductive channel in the space-charge region and an increase in current flow in the p-channel. The selectivity of their FET-biosensor was, however, not high enough for SNP identification [Ing06].

Song *et al.* devised a FET device for real-time DNA hybridisation detection based on a H-terminated diamond body electrode and a Ag/AgCl reference or gate electrode. The diamond was covalently functionalised with ssDNA

molecules. Like in the work by Ingebrandt, hybridisation was most pronounced in a low-ionic buffer. The additional negative charge accompanying complementary DNA hybridisation increased the hole density in the surface accumulation layer of H-terminated diamond (see section 2.1.2.2). This caused an increase in current flow through this p-type surface channel. They did succeed in SNP distinction from complementary target ssDNA at a concentration of 100 pM. However, their sensitivity decreased when monitoring hybridisation in real-time, because of the higher ionic strength of the buffer needed [Son06].

In summary, a FET-based detection technique is suitable for DNA hybridisation detection, but, just as with FET-based immunosensors, suffers from a rather high susceptibility to counter-ion screening effects as compared to impedimetric sensors. The solution, using hybridisation buffers of lower ionic strength, is sub-optimal for hybridisation promotion, often leading to decreased sensitivity.

1.3.2 Optical transduction principle

Optical sensors make use of optical principles for the transduction of biological reactions into a readable output signal. The biological event can be detected by a change in observable optical properties, such as absorption, fluorescence, chemiluminescence or refractive index. Roughly, optical biosensors can be classified as indirect optical biosensors, requiring labels that are responsible for the optical effect, and direct optical biosensors, requiring no label and exploiting the interference of the biological interaction with light [Gor05];[D'O03].

1.3.2.1 Indirect

The major advantage of indirect over direct sensing is the improvement of the sensitivity of the assay, because of the presence of the label. However, this same label also leads to increased complexity and cost of the assay. In the following, such label-requiring optical enzyme sensors, immunosensors and DNA-sensors are described.

Enzymatic biosensors

For enzymatic biosensors, the detection is often based on a colorimetric principle. Enzymes of choice are coupled onto a transducer and incubated with their substrate. An indicator dye is either co-immobilised onto the transducer or added together with the substrate. The product formed during the enzymatic reaction now participates in a redox reaction with the indicator dye. The result is a formation or change in colour, detectable by absorption spectroscopy. The intensity is a quantitative measure for substrate concentration.

The first example of an optical biosensor for a clinical application was a test strip for glucose in urine, commercialised in 1957 (Clinistix™, Miles Laboratories). Glucose oxidase, peroxidase and the dye orthotolidine were co-immobilised onto a cellulose pad. The H₂O₂ that is produced during the glucose oxidation participates in a redox reaction with orthotolidine. Oxidised orthotolidine was read out with the human eye for a semi-quantitative glucose measurement [Fre77]. The detection limit is 5.5 mM, which is in the normal blood glucose concentration range.

Another approach is the co-immobilisation of an enzyme and a fluorescent indicator dye. The fluorescence of the indicator dye is originally quenched by a substance present in the solution, for instance O₂. The enzymatic metabolisation of the substrate consumes that quencher substance, resulting in less quenching of the indicator dye. The increase in fluorescence is proportional to the concentration of the enzyme substrate.

The O₂-sensitive dye Ru(phen)₃²⁺ is co-immobilised with glucose oxidase on the surface of an optical fiber. A decrease in O₂, resulting from the enzyme-catalysed oxidation of glucose results in less quenching of the dye and an increase in luminescence. Glucose was detected in a range of 0.06 to 1 mM [Mor90]. Although sensitive, the elevated diabetic blood glucose concentrations are outside this dynamic range.

Immunosensors

Concerning immunosensors, the target antigen is often enzymatically labelled. After the antigen recognition reaction, the substrate of the enzymatic label is added. At this stage, two optical detection principles can be distinguished. The enzyme can catalyse the transformation of a substrate into a product that has a characteristic colour. The detection principle is therefore called colorimetry. The intensity is again determined with absorption spectroscopy, and is directly related to antigen concentration.

The enzyme label can also cause a chemiluminescent reaction. The emitted light intensity is also a measure for antigen concentration.

Yakovleva *et al.* covalently immobilised protein G onto silicon chips through polyethylenimine (PEI) and dextran (DEX). Atrazine recognition occurred via a competitive immuno-assay, injecting anti-atrazine IgG's together with a mixture of sample atrazine and horse radish peroxidase (HRP)-labelled atrazine into a microfluidic system. The formed immunocomplexes were then trapped by the protein G-modified sensor surface, and the HRP enzyme label transformed its substrate, luminol/p-iodophenol (PIP)/H₂O₂, into an intermediate that is in an excited energetic state. Upon relaxation to a more favourable low-energetic final product, light emission occurs. This process is called chemiluminescence. The emitted light intensity is also a measure for substrate concentration. They obtained detection limits of 40 – 66 fM, and were able to regenerate the immunosensor with 0.4 M glycine-HCl (pH 2.2) without any loss of activity [Yak02]. This reusability is a very desirable feature in biosensors.

DNA-based biosensors

In DNA-based biosensors, the target ssDNA is often fluorescently labelled. After the hybridisation reaction to the immobilised probe ssDNA, the presence, absence or degree of fluorescence emission upon illumination of the sample with laser light of a wavelength as close as possible to the absorption maximum of the label, indicates the selectivity of the hybridisation.

Since 1995, this principle has been put into use, miniaturised and expanded to the modification of surfaces such as glass with 1000 – 10000 ssDNA probes per cm² [Sch95]. This came to be known as the DNA microarray. Probe DNA can be immobilised through simple adsorption via spotting, or through on-chip synthesis via photolithography. The latter approach has been patented by Affymetrix. Based on the type of nucleic acids that are attached to the microarray, one can distinguish between oligonucleotide microarrays and complementary DNA (cDNA) microarrays.

In oligonucleotide microarrays, short genomic ssDNA fragments are spotted on the microarray, and all of the sequences on the array can cover an entire genome. Oligonucleotide microarrays are therefore mainly used for extensive genetic profiling and mutational analysis. The arrays are hybridised with fluorescently labelled genomic DNA and evaluated with a fluorescence microscope equipped with a CCD camera. These microarrays yield absolute values of the presence or absence of each particular gene sequence on the array and therefore, the comparison of two conditions, such as a healthy control and a cancerous patient, requires the use of two separate microarrays for the parallel genotyping or mutation analysis of multiple genes.

In cDNA microarrays, entire cDNA molecules are spotted on the microarray, and all of the sequences can cover the expressional activity of a certain cell or tissue type. cDNA microarrays are therefore mainly used for gene expression analysis. To compare two conditions, such as the gene expression level in a certain tissue of a healthy control and gene expression level in a certain tissue of a cancerous patient, mRNA is isolated from the tissue of the healthy control and from the tissue of the cancerous patient. Both mRNA sources are labelled with a different fluorescent dye, and the array is hybridised with a mixture of both mRNA sources. The fluorescence is again evaluated with a fluorescence microscope. These microarrays compare the expression level of the two conditions for each particular gene on the array. Hence, one microarray can be used for the expression analysis of two conditions.

A schematic representation of an oligonucleotide microarray and a cDNA microarray is shown in figure 1.23.

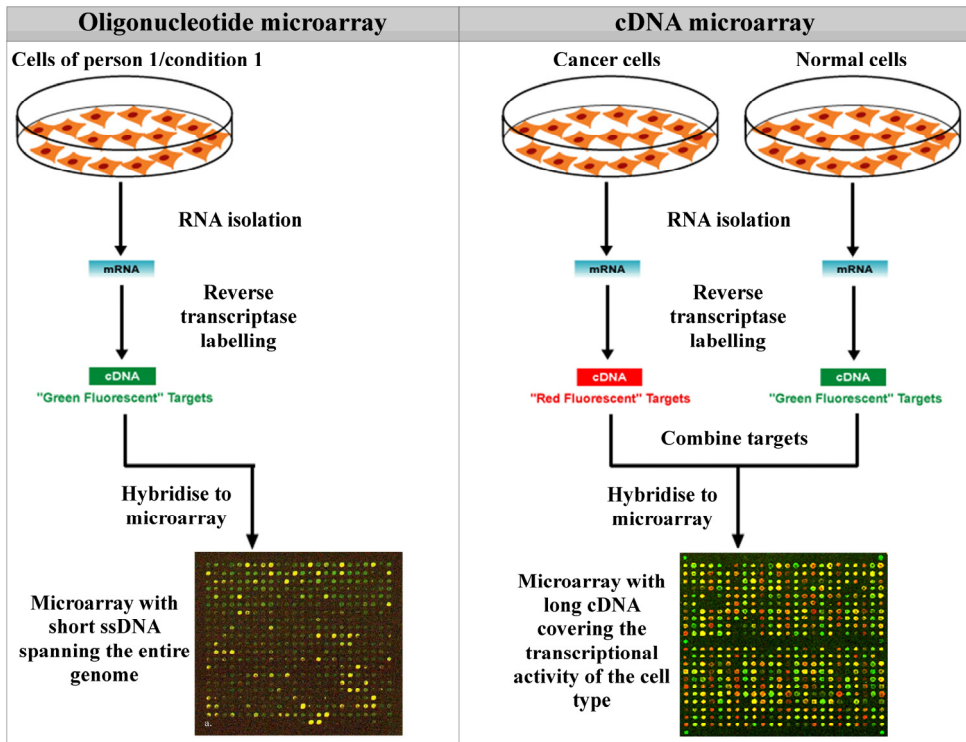


Figure 1.23: Schematic diagram of an oligonucleotide microarray (left panel) and a cDNA microarray (right panel). An oligonucleotide microarray, modified with short oligonucleotide sequences covering the entire genome, gives information about the presence and absence of certain gene fragments. Each microarray is hybridised with target material of 1 condition. A cDNA microarray, modified with longer cDNA sequences covering the expressional activity of a cell type, are used for gene expression analysis. Each microarray is hybridised with target material of 2 conditions.

Wu et al. developed an oligonucleotide microarray to distinguish between the Cyanine (Cy) 5-labelled pathogenic O157:H7 and Cy3-labelled non-pathogenic E. Coli strains [Wu03].

Schwonbeck *et al.* devised an alternative, reverse, method for oligonucleotide microarray construction, eliminating the disadvantage of a serial approach, i.e. the need for one chip per experimental condition or patient. They immobilised single-stranded and biotinylated PCR products of a well-known polymorphism of the gene for cytosolic sulfotransferase (SULT1A1*2) from 24 homozygotic individuals onto an avidin-coated microscope cover slip. Subsequently, they hybridised the array with fluorescently labelled target ssDNA, complementary to the wild-type. The final step after hybridisation involved a dissociation of the fluorescent strand from the immobilised strand.

The mismatched hybrids showed a higher dissociation rate than the complementary duplexes. They even succeeded in the discrimination of heterozygotes [Sch04].

Despite the enormous advances made in microarray technology and their widespread use in research and diagnostics because of its high-throughput construction, several disadvantages need to be mentioned. The requirement of target-labelling and the associated need for very expensive complex optics for detection make microarrays an extremely costly investment. The fact that the substrate material, usually Si, yields a rather unstable bond with biomolecules and hence allows only disposable applications only exacerbates this fact [Yan02];[Neb07]. Also, microarrays employ an endpoint manner of detection. This implies one hybridisation condition for all of the probes attached to the surface. However, many factors, such as the type of mismatch (involving pyrimidines or pyridines), influences the hybridisation efficiency. This sort of information could be lost after a significant hybridisation time, and incorrect conclusions will be drawn. Finally, many internal controls need to be included in the microarray design for statistical analysis, leading to increased complexity and a decrease in sample throughput.

As we will show in this work, all of these problems can be circumvented using our developed impedimetric sensor platform. No label and no expensive machinery is needed, which will have a significant impact on cost. Moreover, since the biomolecule-diamond interface is extremely stable, repeated use is possible, also positively influencing budget. Importantly, our impedimetric DNA-based biosensor allows real-time detection of hybridisation and denaturation, specifically focusing on the kinetic behaviour of different DNA molecules which is not possible with an endpoint detection. The advantage of high-throughput with microarrays is also relatively easily attainable with our setup in terms of array-functionalisation.

1.3.2.2 Direct

In direct optical transduction, no label is required. The biological reaction itself interferes with the optical properties of the system in one way or another, which becomes the subject of detection.

Since its development in the 1980s as a method for interrogation of thin films and biological and chemical interactions, Surface Plasmon Resonance (SPR) has become a powerful technique to measure biomolecular interactions in real-time in a label-free environment. As already mentioned briefly in section 1.2.2.2, when monochromatic polarised light hits an interface of two transparent media, such as a glass prism and a buffer solution, from the side of the media with the highest refractive index (glass prism), the light is partly reflected and partly refracted towards the plane of the interface. Above a certain incidence angle, all of the light is reflected and none of it is refracted. This phenomenon is called Total Internal Reflection (TIR).

In SPR, the glass prism is coated with a Au film. In conducting metals, such as Au, the free conduction electrons form periodic oscillations, called plasma waves. Like every periodic electromagnetic wave, this can also be described in a particle fashion. Like photons and phonons are the particle names for light and sound waves, respectively, a plasmon is the particle name for the plasma wave. Surface plasmons are those plasmons that are confined to the surface of the metal. They occur at the interface of the Au surface and the buffer. These plasmons create an electric field that extends about 100 nm both into the buffer solution and into the Au film and glass prism. This electrical field is called an evanescent wave, because it decays exponentially with distance. When the incident light beam has the correct incidence angle within TIR, surface plasmon resonance occurs. At this so-called 'resonance angle', θ , the photons in the light beam have a momentum (vector with magnitude and direction) equal to the momentum of the surface plasmons, and the photons are converted into plasmons. In other words, optical energy is coupled into the Au surface. As a result, reflection is decreased at this resonance angle.

Any change in the composition of the material at the interface between the Au and the buffer will alter the momentum of the surface plasmons, and their associated evanescent wave. As a consequence, SPR no longer occurs at the previous incidence angle, and a SPR shift takes place. The shift in the resonance angle is directly proportional to the change in mass at the Au surface, for instance during an antigen-antibody recognition event, or during DNA hybridisation [Ber78];[Fla84]. A well known commercial system employing SPR

is the BIAcore™. A graphical display of an antibody-based SPR biosensor is presented in figure 1.24.

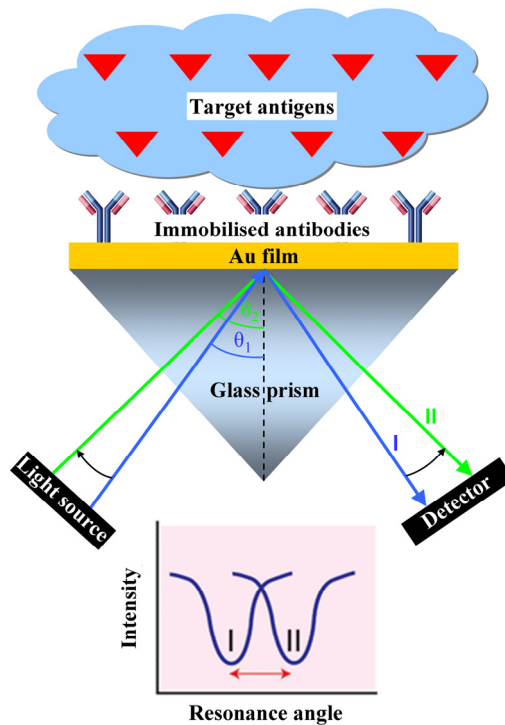


Figure 1.24: Schematic diagram of SPR. At the resonant angle θ_1 , the incident light is no longer completely reflected, due to energy coupling into the Au surface. Upon target recognition by the Au-associated biomolecular layer, this resonant angle shifts to θ_2 .

Immunosensors

Wei *et al.* devised a real-time SPR-based immunosensor for measuring cardiac troponin I (cTnI), a specific indicator for heart damage, in sera. They immobilised biotinylated monoclonal anti-cTnI to an avidin-modified Au film on top of a glass prism. Two setups were devised. In a direct, label-free measurement protocol, they observed a change immediately after addition of cTnI-containing serum. In a second, amplified approach a secondary antibody was added to sandwich the cTnI. The detectable range was between 0.1 and 1.7 nM for the direct approach and between 22 pM and 0.8 nM with a detection limit of 11 pM for the amplified approach [Wei03].

Hu *et al.* detected the pentameric and monomeric form of CRP in real-time using SPR. They attached three monoclonal anti-CRP antibodies (C8, 8D8 and 9C9) to a Au film through protein G. C8 is able to recognise both pentameric and monomeric forms of CRP. 8D8 is reactive to the pentameric form, while 9D9 recognises the monomeric form. No false signals caused by non-specific binding were observed, and selective recognition occurred within 10 minutes. For C8, a detection limit of 8.7 nM was determined for the pentameric CRP recognition, and can thus be used in a clinical setting, since the physiologically relevant range lies between 8 nM and higher [Hu06].

DNA-based biosensors

Wang *et al.* investigated the selectivity of covalently immobilised thiolated ssDNA probes onto the Au films of two commercially available SPR-based biosensors: SPREETA™ and BIAcore™. For the BIAcore™ system, complementary target ssDNA was efficiently detected in real-time in a range between 0 and 500 nM, with a linear range up to 25 nM. The limit of detection was determined to be 2.5 nM. With the SPREETA™ system, complementary target ssDNA was efficiently detected in real-time in a range between 0 and 1000 nM, with a limit of detection of 10 nM. However, the effect of non-complementary DNA was not studied [Wang04].

In summary, although SPR is another method for real-time and label-free detection of molecular interaction, be it hybridisation or antibody-antigen recognition, the restraint for Au substrates could collide with the requirement of interface stability. Moreover, implementation of SPR sensing into a point-of-care application will be unlikely in the short term.

1.3.3 Piezo-electric transduction principle

Since the antigen-recognition by immobilised antibodies, and the DNA hybridisation to immobilised ssDNA molecules increases the mass of the attached complex, mass-sensitive transducers were developed for biosensing.

Although SPR also exploits the change in mass during a biological recognition event, that detection principle relies on an optical technique.

In 1917, it was shown that quartz crystals could be used as transducers of ultrasound, sounds with a higher frequency than the upper limit of human hearing. Since 1934, AT-cut quartz crystals have been used in the construction of Quartz Crystal Microbalances (QCM). Such an AT-cut quartz plate is sandwiched between two Au electrodes. Because of this mechanical compression, or stress, the quartz obtains an electrical charge due to the piezo-electric effect. When the electrodes are connected to an oscillator and an AC voltage is applied, the quartz crystal starts to oscillate and resonates at a frequency proportional to the piezo-electric thickness. It was observed that the resonant frequency of the quartz decreases upon addition of mass. In 1959, Sauerbrey demonstrated that this frequency shift is proportional to the added mass, and formulated this relationship in the Sauerbrey equation, given in (5) [Sau59]:

$$\Delta F = -\frac{2F_0^2 \Delta m}{A\sqrt{\mu_q \rho_q}} \quad (5)$$

In this equation, Δm is the added mass, F_0 is the resonant frequency of the crystal, A is the active area of the crystal between the electrodes, ρ_q is the density of quartz, and μ_q is the shear modulus of quartz. Frequency measurements are easily made with high precision, making it an ideal tool to measure small masses, such as antigen binding or DNA hybridisation in real-time and in a label-free fashion [<http://www.pharmaceutical-int.com/categories/qcm-technology/quartz-crystal-microbalance-qcm.asp>]. But, the prerequisite of a quartz, being Si, could compromise interface stability. Also, its temperature sensitivity and difficult miniaturisation limit its widespread use.

Immunosensors

Ferreira *et al.* immobilised either single-chain variable fragments or single-domain fragment antibodies onto Au-coated 5 MHz AT-cut quartz crystals through a mixed SAM of hydroxylated and carboxylated alkanethiols. Single-

chain variable fragments are molecular assemblies of the two functional heavy-chain and light-chain variable domains of an antibody, covalently linked by a polypeptide. Single-domain fragments are composed of two heavy-chains with no light-chain. Both types of antibody derivatives were directed against the HIV1 virion infectivity factor (HIV1-Vif), a protein present in the cytoplasm of infected cells and indispensable for viral replication and spread. The immobilised receptors were capable of selectively detecting HIV1-Vif in real-time, and the lowest amount detected was 0.3 and 0.47 μM for the single-chain variable fragments (scFv-4BL) and the single-domain fragments (4BL-V_HD), respectively. Selective recognition occurred within 20 minutes. The single-domain fragments were even capable of detecting 2 μM HIV1-Vif in a complex mixture of either bovine serum albumin (BSA), cytochrome C and ribonuclease A or cell extracts expressing HIV1-Vif [Fer07].

DNA-based biosensors

Feng *et al.* immobilised thiolated ssDNA molecules onto Au-coated 9 MHz AT-cut quartz crystals in a mixed self-assembly process together with the thiolated spacer molecule, mercaptopropionic acid. Hybridisation comprised two steps. First, target ssDNA was hybridised, with one half fully complementary to the immobilised probe ssDNA and the other half fully complementary or displaying one mismatch to a biotinylated detection probe. Secondly, the biotinylated detection probe was hybridised to the remaining single-stranded part of the target DNA. When the target ssDNA does not perfectly match the detection probe, the nick between the detection probe and the immobilised probe will not be sealed by the high-fidelity E. Coli ligase. In case of a perfectly matched complex, this ligase will form a proper duplex. Subsequent denaturation by heating resulted in a biotinylated, immobilised ssDNA probe in the complementary condition. When HRP conjugated to streptavidin was added, the streptavidin bound to the biotin label. HRP oxidised 3,3-diaminobenzidine (DAB) to an insoluble product in the presence of H₂O₂. This product precipitated onto the QCM and caused a mass amplification. However, in the case of one mismatch, the target ssDNA and the biotinylated detection probe both detached from the immobilised ssDNA probe during denaturation. The downstream

amplification reaction hence did not take place. This approach proved applicable for quantification of the target ssDNA. The frequency response was linear in the range between 0.7 – 100 nM, with a detection limit of 100 pM [Fen07]. Although sensitive, this method is rather complex and not real-time nor label-free.

In conclusion, let it be clear that biosensor research is a vast topic. The options for transduction principles and construction concepts are widespread, and depend largely on the type of target recognition and research questions involved. However, since a significant application area for biosensors is clinical diagnostics, this poses certain desires and constraints concerning construction and detection principles. An ideal biosensor to be used in clinical applications would offer a universal platform for the detection of all analytes of interest. Enzymatic sensors for instance, in contrast to immunosensors, are not an option for every analyte. They also need to be fast, relatively cheap, portable, sensitive, specific and stable to allow a point-of-care application. Nevertheless, many biosensor concepts described in this overview do not comply with one or more of these features. Optical techniques require expensive machinery and operate in an endpoint setting. This increases size, cost and analysis time, preventing their use in bedside diagnostics. QCM is a very sensitive mass-detection technique that can be used to detect proteins and DNA. However, despite the fact that the technique can operate in real-time, which decreases analysis time greatly, it is quite sensitive to temperature fluctuations and poses limitations for miniaturisation and arraying. Electrical transduction however, such as impedance spectroscopy, is sensitive, it can detect DNA and proteins in real-time, and it does not require expensive equipment. Often, semiconducting electrode materials such as Si are used, allowing the devices to be miniaturised. But the interface between Si and biomolecules suffers greatly from environment, condemning them to a disposable use. Diamond can replace Si in an otherwise very promising detection technique. Its wide electrochemical window makes it an ideal electrode, doping options give it semiconducting properties, its inertia makes it resistant to the most harsh environments, and the attachment of biomolecules through C-C-bonds create a stable bio-interface. Because of these reasons, the body of this thesis is dedicated to the exploration of diamond as a substrate material in impedimetric immunosensors and DNA-sensors.

Table 1.4: Literary overview of the types of biosensors, classified according to transduction principle and biological receptor molecule, including key measurement parameters.

Bioreceptor molecule	Transduction	Substrate	Target	Dynamic range	LOD*	Ref.
Enzyme	Electrochemical					
→ glucose oxidase	→ amperometric	ITO	glucose	0–10 mM	0.05 mM	[Fan03]
→ - creatinase - sarcosine oxidase		carbon paste	creatinine	pM–nM	pM	[Stef03]
→ - creatinase - sarcosine oxidase - creatininase			creatinine	pM–nM	pM	
→ glucose oxidase	(CV)	PCD	glucose	0.5 mM–12 mM	-	[Jia96]
→ alcohol dehydrogenase	(CV)	PCD (p)	ethanol	0.2–1.5 mM	-	[Rao99]
→ catalase	(CV)	NCD (n)	H ₂ O ₂	up to 150 mM	0.3 mM	[Här04]
→ urease	→ potentiometric	polyvinyl chloride ISE	urea	problematic	problematic	[Gui70]
→ urease	→ conductimetric	NH ₄ ⁺ electrode (BUN Analyzer)	urea	-	high	[Chu76]
	Optical					
→ - glucose oxidase - peroxidase	→ colorimetric	cellulose pad (Clinistix™)	glucose	-	5.5 mM	[Fre77]
→ - glucose oxidase - Ru(phen) ₃ ²⁺	→ fluorescent	optical fiber	glucose	0.06 mM–1 mM	-	[Mor90]
Antibody	Electrochemical					
→ - anti-digoxin	→ amperometric	carbon paste	- AP-labelled digoxin	-	64 pM	[Hei85]
→ - anti-IgG			- AP-labelled IgG	-	33 pM	
→ chloroperoxidase- labelled anti-IgG	→ potentiometric	CO ₂ electrode	IgG	-	nM–μM	[Fon84]
→ - anti-IgG	→ impedimetric	- PCD (p)	- IgG	-	PCD: 42 nM IgG	[Yan07]
→ - anti-IgM		- Si (n+p)	- IgM		(real-time, 12 min.)	
→ anti-CRP		NCD	CRP	-	10 nM (real-time, 10 min.)	
	Optical					
→ anti-atrazine	→ chemiluminescent	Si	HRP-labelled atrazine	-	40–66 fM	[Yak02]
→ biotinylated anti-cTnI	→ SPR	Au	- direct: cTnI in serum - amplified: cTnI + anti-cTnI secondary antibody	- direct: 0.1–1.7 nM - amplified: 22 pM–0.8 nM	- amplified: 11 pM	[Wei03]
→ - C8 → - 8D8 → - 9C9		Au	- C8: monomeric + pentameric CRP - 8D8: pentameric CRP - 9C9: monomeric CRP	-	C8: 8.7 nM (pentameric) (real-time, 10 min.)	[Hu06]

Piezo-electric						
→ - scFv-4BL → - 4BL-V _H D	→ QCM	Au coated quartz	HIV1-Vif		- scFv-4BL: 0.3 µM - 4BL-V _H D: 0.47 µM (real-time, 20 min.)	[Fer07]
DNA Electrochemical						
→ HBV ssDNA	→ amperometric (CV)	Au	HBV dsDNA amplicons	-	- calf thymus DNA: no SNP detection - complement: 2 fM	[Ye03]
→ biotinylated BRCA 1 ssDNA	→ potentiometric	magnetic beads	AP-labelled BRCA 1 ssDNA	3.3–20 nM	- random DNA: no SNP detection - complement: 6.6 pM	[Wan04]
→ SH-ssDNA	→ conductimetric	Si/SiO ₂	Au-labelled ssDNA	50 nM–500 fM	- 1-mm*: SNP detection - complement: 50 nM	[Par02]
→ SH-ssDNA	→ impedimetric	NCD (p)	ssDNA	-	4-mm: no SNP detection (real-time)	[Yan04]
→ SH-ssDNA		Si (n)	ssDNA	-	4-mm: no SNP detection	[Cai04]
→ NH ₂ -ssDNA		diamond (p)	ssDNA	- complement: 50–200 nM	- 1-mm: SNP detection - complement: 20 nM	[Gu05]
→ NH ₂ -ssDNA		NCD	- hybridisation - denaturation	-	1-mm: SNP detection at 4 µM (real-time)	[Ver07]
→ NH ₂ -modified ssDNA	→ field-effect	Si (n)	ssDNA	-	No SNP detection (real-time)	[Ing06]
→ NH ₂ -modified ssDNA		PCD (p)	ssDNA	-	1-mm: SNP detection at 100 pM (real-time)	[Son06]
Optical						
→ E. Coli ssDNA	→ fluorescent	oligonucleotide array	Cy5-ssDNA (O157:H7) Cy3-ssDNA (nonpathogenic)	-	Discrimination possible	[Wu03]
→ ssDNA amplicons of SULT1A1*2		oligonucleotide array	SULT1A1*2 ssDNA	-	Discrimination of heterozygotes possible	[Sch04]
→ SH-ssDNA	→ SPR	Au	ssDNA	complement: - BIAcore™: 0–500 nM - SPREETA: 0–100 nM	complement: - BIAcore™: 2.5 nM - SPREETA: 10 nM random DNA: no SNP detection (real-time)	[Wang04]
Piezo-electric						
→ SH-ssDNA	→ QCM	Au coated quartz	ssDNA + detection probe	0.7 – 100 nM	- 1-mm: SNP detection - complement: 100 pM	[Fen07]

*LOD = limit of detection
*mm = mismatch

1.4 AIM OF THE STUDY

As mentioned in the introduction, the field of bio-electronics has been developing since the 1950s. Since this time, many accomplishments have been attained in biosensor construction. These advances are based upon major corner stones.

Almost all types of biological recognition molecules can be attached to a solid substrate through a very wide variety of attachment mechanisms, ranging from physical adsorption to an array of covalent binding procedures. This of course guarantees an enormous diversity in biosensor specificity. Also, the manners of signal transduction are just as widespread, offering a suitable detection mechanism for every application, be it optical, mass-sensitive or electrochemical. The type of transducer substrate offers yet another degree of freedom, since many materials can be functionalised with molecules using the correct attachment chemistry. However, not all transducer materials are reconcilable with every type of transduction mechanism. A fluorescence detection strategy, for instance, requires a substrate with an intrinsically low background, such as glass, while the electrical properties of the material are of lesser importance. For SPR-based biosensors, a glass-Au or glass-Ag platform is mandatory. If electrochemical read-outs are preferred, substrates with a semiconducting nature are necessary.

Choosing a specific transduction principle depends largely on the type and purpose of the experiment. Since we are aiming at point-of-care applications, desirable assets of every experiment are speed, reliability and cost. Reaction speed can be attained by eliminating the need for target labelling and offering the possibility of monitoring the recognition reaction in real-time instead of before and after analyte addition. A frontline requirement for test reliability is the generation of a dense and stably attached molecular layer on top of the substrate. Finally, cost is largely reflected by the required equipment, and this certainly influences the possible integration of the platform in a point-of-care application.

When focusing on a fast, label-free, and real-time detection scheme, this immediately eliminates any indirect optical transduction principle (colorimetric,

chemiluminescent, fluorescent). Moreover, the required infrastructure for fluorescent detection usually represents a vast investment. Similarly, amperometry, potentiometry and conductimetry usually require enzymatic labels generating electro-active species that amplify the response. EIS, FET-based transduction, SPR and QCM are generally considered to be capable of real-time and label-free analyte detection. However, SPR sets very clear restrictions for the type of transducer material to be used. In this approach, Au or Ag will need to be biofunctionalised. QCM is temperature sensitive and can not readily be miniaturised and modified into a simultaneous detection scheme for many analytes. In EIS and FET-based transduction, semiconductors are used as substrate material, such as Si. However, the chemical linkage between these materials, Au (SPR) and Si (EIS, FET), and biomolecules has been known to be rather weak and unstable, which unavoidably has a negative impact on the stability and hence reliability of the sensor. The recognition of diamond as a promising semiconductor alternative, and the paper by Yang *et al.* in 2002 demonstrating that the bond between biomolecules and diamond is extremely stable, has led to new opportunities for diamond to be used as a substrate in impedimetric and FET-based biosensors. Moreover, the fact that diamond can be synthetically grown and efficiently cleaned and reused, combined with inexpensive equipment needed for signal read-out in an impedimetric setup, undoubtedly has an effect on the overall cost of impedimetric and FET-based diamond biosensors. Once established, such a platform is the most appropriate to be introduced in both lab-on-chip or point-of-care applications. For these reasons, efforts to devise these types of biosensors have been elaborate, as reflected by the many publications in the field of diamond-based impedimetric and FET-DNA- and immunosensors.

At the start of this PhD project in 2003, biofunctionalisation of diamond for biosensor fabrication purposes was still in its infancy. Most of the milestones that have been mentioned in this overview, including the work that has been done in our laboratory, were not yet attained. Because of this, real-time diamond-based impedimetric DNA-sensors did not reach SNP sensitivity [Yan04];[Cai04], and real-time diamond-based impedimetric immunosensing did not show a sensitivity for clinically relevant targets [Yan07]. The most important publications concerning FET-based DNA-sensors employ a real-time detection

scheme, but suffer from the counter-ion screening effect. This imposes the use of low-ionic buffers, which are not ideal for the support of hybridisation reactions [Ing06];[Son06]. FET-based immunosensors have even been deemed unattainable because of this same counter-ion screening effect [Pog05];[Ber03].

Keeping in mind, and taking together all of the above-mentioned accomplishments and problems in this area, our laboratory wished to develop a generic diamond-based impedimetric biosensing platform for the real-time detection of DNA hybridisation and denaturation events and of antibody-antigen recognition, tackling the current issues still commonly associated with this type of transduction principle. Important objectives in this setup were to obtain a DNA-sensor offering SNP sensitivity, and a selective immunosensor capable of measuring targets in a physiologically relevant concentration range. Both prototypes should also be operable in real-time. In order to reach these ambitious goals, landmarks were set for this research project, as formulated in the following research questions:

1) How can we attach DNA to NCD in order to get an optimal surface coverage and an optimal functionality in subsequent impedimetric sensor platforms? Can our immobilisation approach be adapted in such a way that we can introduce it into an array format?

2) Is it possible to extend this optimal approach for covalent and functional attachment of DNA molecules to the development of a prototype of a real-time electrochemical DNA-based biosensor reaching SNP sensitivity? Can this sensor be used to study both hybridisation and denaturation processes in real-time?

3) Can NCD function as a kind of generic sensor platform? Is it also a suitable substrate for antibody immobilisation, and do these molecules retain their functional activity?

4) Can a prototype of an electrochemical immunosensor be developed to measure clinically relevant targets in a concentration-dependent manner and in physiologically appropriate concentrations?

To answer these research questions, the following strategies were undertaken. These also delineate the outline of the Chapters in this thesis.

A) We needed to develop a modified photochemical attachment method, and we did this based on the procedure published by Yang *et al.* [Yan02] as described in Chapter 3. Our photochemical attachment method was further optimised in terms of increasing the functional DNA binding capacity and decreasing the amount of non-covalently attached DNA. This fine tuning was needed in order to use this approach in a real-time biosensing device allowing SNP sensitivity. Chapter 4 thoroughly addresses this optimisation process.

B) A prototype of a DNA-based biosensor needed to be developed in which the selective target hybridisation was demonstrated using EIS. The sensitivity of this DNA-based biosensor was judged on its ability to discriminate fully complementary target DNA from mismatched target DNA. SNP discrimination, being the highest sensitivity attainable, should be possible. Moreover, we wanted to study both hybridisation and denaturation processes in real-time, possibly giving additional sequence-dependent information. This topic is dealt with in Chapter 5.

C) Physically adsorbed anti-CRP antibodies onto H-terminated NCD were used to prove their functional activity by an Enzyme-Linked Immunosorbent Assay (ELISA)-procedure. Selective CRP antigen detection was colorimetrically evaluated at 405 nm. This way, NCD was shown to be a suitable substrate for antibody attachment.

D) The clinically relevant CRP was chosen to create a prototype of an immunosensor using EIS. The immunosensor sensitivity was assessed by determining the detection limit of the attached anti-CRP antibodies, such that physiologically relevant concentrations could be measured in a concentration-dependent manner. Chapter 6 is dedicated to the research tasks described in **C)** and **D)**.

Chapter 2:

Materials and methods common to all Chapters

2.1. BUFFERS AND SOLUTIONS

In the following, a summary is given entailing the source of purchased solutions and the composition of homemade buffers that are used throughout this thesis.

2.1.1 Homemade

2.1.1.1 Coating buffer

0.014 M Na_2CO_3

0.035 M NaHCO_3

0.003 M NaN_3

2.1.1.2 Conjugation buffer

1× PBS, containing:

0.05% Tween 20

2.1.1.3 CRP buffer

20 mM TRIS buffer, pH 8, containing:

0.28 M NaCl

0.09% NaN_3

5 mM CaCl_2

2.1.1.4 Hybridisation buffer

5× SSC

5× Denhardt

5% Dextran sulphate

5 mM Na₂HPO₄
0.1% SDS
7.5 µg herring sperm DNA

2.1.1.5 10× Phosphate buffered saline (PBS), pH 7.2

1.29 M NaCl
0.05 M Na₂HPO₄·2H₂O
0.015 M KH₂PO₄

2.1.1.6 Sodium chloride/sodium citrate (SSC), pH 7.5

3 M NaCl
0.3 M C₆H₈O₇·3Na

2.1.1.7 10× Tris-buffered saline (TBS), pH 7.6

0.5 M Tris base
1.5 M NaCl

2.1.2 Purchased

H₂SO₄, ethanol (analytical grade) and sodium dodecyl sulphate (SDS) were obtained from VWR International (Zaventem, Belgium). 10-UDA was bought from Sigma-Aldrich (Bornem, Belgium). EDC and 2-(N-morpholino)-ethanesulphonic acid (MES) were purchased from Perbio Science (Erembodegem, Belgium). PCR buffer and Taq-DNA polymerase (5 U.µl⁻¹) were bought from Roche Diagnostics (Vilvoorde, Belgium). Sodium hydroxide (NaOH), potassium nitrate (KNO₃) and acetic acid (99-100% pure) were acquired from Merck (Overijse, Belgium). Phenol:Chloroform:Isoamyl Alcohol (25:24:1, v/v) and MicroHyb™ hybridisation buffer were synthesised by Invitrogen (Merelbeke, Belgium).

2.2 EXPERIMENTAL PROCEDURES

In this section, certain experimental procedures are described that play a pivotal role throughout this thesis.

2.2.1 Synthesis, cleaning and hydrogenation of NCD

2.2.1.1 *Homemade*

IMO grown CVD diamond layers were deposited as follows. Doped (1 – 20 Ω .cm) p-type Si (100) was seeded with ultra-dispersed detonation diamond powder in an ultrasonic bath. In Chapter 3, a thin titanium (Ti) layer with a thickness of \pm 50 nm was sputtered on top to act as a seeding enhancement. In Chapters 4 – 6, this step was omitted. Next, undoped NCD films with a thickness of 200 – 300 nm and a grain size of 50 – 200 nm were grown on this pre-treated substrate using Microwave Plasma Enhanced Chemical Vapour Deposition (MPECVD) in an ASTeX[®] 'AX6550' reactor (Seki Technotron Corp., Tokyo, Japan) equipped with a 2.45 GHz microwave generator. The NCD thin films in Chapter 3 were deposited from a standard mixture of 25 standard cubic centimetre (sccm) per minute at STP CH₄ and 475 sccm H₂. The standard mixture for the NCD synthesis in Chapters 4 – 6 was composed of 15 sccm CH₄ and 485 sccm H₂. Microwave power in Chapter 3 was set at 3000 W, with a process pressure of 53 hPa (40 torr). For the NCD used in Chapters 4 – 6, microwave power was set at 3500 W, with a process pressure of around 43.9 hPa (33 torr). Substrate temperature was around 667 – 695°C in Chapter 3, and around 710°C in Chapters 4 – 6. The growth rate was approximately 600 nm/hr.

After growth, the wafer was cut in 1 cm² pieces using a diamond scribe and cleaned for 30 minutes in an oxidising mixture of hot H₂SO₄ and KNO₃. This procedure was followed by washing in an ultrasonic bath with distilled, ultra-pure water at room temperature. Afterwards, the samples were thoroughly rinsed with heated distilled, ultra-pure water and dried with N gas. The final hydrogenation was performed at 700°C during 30 s at 3500 W, 120 hPa (90

torr) and 1000 sccm H₂ in Chapter 3. The hydrogenation in Chapters 4 – 6 was performed at 700°C during 60 s at 3000 W, 46.6 hPa (35 torr) and 1000 sccm H₂.

2.2.1.2 Purchased

In Chapters 4 – 6, IMO NCD samples were compared with commercially available H-terminated NCD samples grown by Hot Filament Chemical Vapour Deposition (HFCVD) from rho-BeSt (Innsbruck, Austria). This was done to investigate the robustness of either the DNA-attachment method (Chapter 4), the impedimetric interrogation of covalently attached DNA (Chapter 5) or the impedimetric interrogation of physisorbed antibodies (Chapter 6). The rho-BeSt samples consisted of a 2 – 4 µm thick NCD film with a grain size of 5 – 15 nm, grown on p-type Si.

2.2.2 Synthesis of NH₂-modified and fluorescently labelled dsDNA

A 250 bp amplicon of the Small Tandem Repeat (STR)-region of the Phenylalanine Hydroxylase (PAH) gene was obtained using a GenAmp PCR System 9600 (Perkin-Elmer, Massachusetts, USA) in Chapter 3, and a MyCycler Personal Thermal Cycler (Bio-Rad Laboratories, Eke, Belgium) in Chapter 4. In Chapter 3, FITC-labelled dsDNA was generated using a FITC-labelled forward primer (22 b: 5'-FITC-C₆H₁₂-TCA-AAT-TGC-CAG-AAC-AAC-TAC-T-3') and an NH₂-labelled reverse primer (26 b: 5'-NH₂- C₆H₁₂-CTT-CTC-ACA-GTA-ATC-ATA-AGT-GTT-CC-3'). In Chapter 4, Alexa Fluor® 488-labelled dsDNA was generated using an Alexa Fluor® 488-labelled version of the previously mentioned forward primer and the same reverse primer.

Standard 100 µl-PCR reactions contained 200 nmol of each dNTP, 50 pmol of each primer, 5 U Taq DNA polymerase, genomic template DNA and PCR buffer. The PCR consisted of a preliminary denaturation for 5 minutes at 95°C, followed by 35 cycles of a subsequent three-step reaction: denaturation for 20 seconds at

95°C, annealing for 20 seconds at 52°C and extension for 30 seconds at 72°C. Finally, the PCR amplicons were subjected to a final extension for 6 minutes at 72°C.

Amplified dsDNA was purified using phenol-chloroform extraction and concentrated to $\sim 40 \text{ ng} \cdot \mu\text{l}^{-1}$ ($\sim 0.8 \text{ pmol} \cdot \mu\text{l}^{-1}$) in Chapter 3 and to $\sim 100 \text{ ng} \cdot \mu\text{l}^{-1}$ ($\sim 2 \text{ pmol} \cdot \mu\text{l}^{-1}$) in Chapter 4 through ethanol precipitation.

2.2.3 Impedance spectroscopy

Impedance spectroscopy was performed using a Hewlett Packard 4194A Impedance/Gain-Phase Analyzer (Agilent, Diegem, Belgium) which has a frequency range from 100 Hz to 40 MHz. The impedance is measured by applying an AC potential (U) of 10 mV to the measurement cell. The response to this potential is an AC current signal (I). The complex impedance (Z), calculated from the ratio $\frac{U}{I}$, was measured for 50 frequencies, equidistant on a log scale, in a frequency range from 100 Hz to 1 MHz. The duration of one frequency sweep was 8 seconds. For simultaneous measurements, a Keithley 7001 switch card (Keithley Instruments, B.V., Sint-Pieters-Leeuw, Belgium) was used to switch between the channels after each frequency sweep. The impedance spectra were analysed using equivalent circuit models using the ZSimpWin software from Princeton Applied Research (Massachusetts, USA). The goodness of the fit is determined by the χ^2 value:

$$\chi^2 = \sum_{i=1}^n \left[W_i' \cdot (Z_i'(\omega_i, \vec{p}) - a_i)^2 + W_i'' \cdot (Z_i''(\omega_i, \vec{p}) - b_i)^2 \right] \quad (6)$$

a_i and b_i are the experimental, while $Z_i'(\omega_i, \vec{p})$ and $Z_i''(\omega_i, \vec{p})$ are the calculated $\text{Re}(Z)$ and $\text{Im}(Z)$ for each data point, respectively. ω_i is the frequency and \vec{p} represents the model parameters. W_i' and W_i'' are the weighting factors correcting for the higher impedances at lower frequencies:

$$W_i' = W_i'' = \frac{1}{(a_i^2 + b_i^2)} \quad (7)$$

Chapter 3:

EDC-mediated DNA attachment to nanocrystalline CVD diamond films

Based on:

EDC-mediated DNA attachment to nanocrystalline CVD diamond films
Biosensors & Bioelectronics (2006); 22; 170 – 177.

P. Christiaens^{a*}, V. Vermeeren^{b*}, S. Wenmackers^a, M. Daenen^a, K. Haenen^{a,c},
M. Nesládek^{a,c,d}, M. vandeVen^b, M. Ameloot^b, L. Michiels^b, P. Wagner^a

^a Hasselt University and transnationale Universiteit Limburg, School for Life Sciences, Institute for Materials Research, Wetenschapspark 1, B-3590 Diepenbeek, Belgium

^b Hasselt University and transnationale Universiteit Limburg, School for Life Sciences, Biomedical Research Institute, Agoralaan, Bldg. A, B-3590 Diepenbeek, Belgium

^c IMEC vzw, Division IMOMECE, Wetenschapspark 1, B-3590 Diepenbeek, Belgium

^d CEA/Saclay, LIST (CEA-Recherche Technologique)/DETECS/SSTM/LTD, Bât 451, F-91191, Gif-sur-Yvette, France

* P. Christiaens and V. Vermeeren contributed equally to this publication.

ABSTRACT

CVD diamond is a very promising material for biosensor fabrication owing both to its chemical inertness and the ability to make it electrically semiconducting which allows for connection with integrated circuits. For biosensor construction, a biochemical method to immobilise nucleic acids to a diamond surface has been developed. NCD is grown using MPECVD. After hydrogenation of the surface, 10-UDA, a ω -unsaturated fatty acid, is tethered by 254 nm photochemical attachment. This is followed by EDC-mediated attachment of NH_2 -modified dsDNA. The functionality of the covalently bound dsDNA molecules is confirmed by fluorescence measurements, PCR and gel electrophoresis during 35 denaturation and rehybridisation steps. The linking method after the fatty acid attachment can easily be applied to other biomolecules like antibodies and enzymes.

3.1. INTRODUCTION

Over the past couple of years, one of the frontiers of micro-electronics technology and biotechnology integration is biosensor development based on artificially grown diamond by CVD. The development of diamond-based biosensors for durable, long-term implantation is a new and very interesting area of research. This substrate pairs biocompatibility [Tan95];[Bak02] with semiconductor characteristics when properly doped [Koi97];[Nes05]; [Yam00];[Ter05] or using H-terminated surfaces [Ama02]. Artificially grown diamond has unequalled properties. It is the hardest material known, chemically inert with high thermal conductivity [Car04], and it is transparent to UV and far-IR (FIR) light [May00].

When a hydrogenated layer is exposed to air, surface conduction occurs [Mai00];[Can01];[Gar05];[Neb06]. Patterning of hydrogenated and oxidised regions, makes it possible to fabricate transistors based on this p-type surface conductivity [Ban02];[Gar03].

Tethering biomolecules is indispensable for the fabrication of biosensors. Yang *et al.* were the first to describe the attachment of DNA to diamond using UV illumination (0.35 mW.cm^{-2} , 254 nm). In their approach, vinyl groups of organic molecules were UV-linked to the H-terminated diamond surface. Applying a SSMCC crosslinker, SH-modified DNA was subsequently tethered to the H-terminated NCD films [Yan02]. Advantages of this method are the formation of a strong C-C bond, the possibility of photopatterning and the high stability of the resulting covalent functionalisation [Str00]. This approach also allows the prevention of non-specific protein adsorption by an analogous photochemical modification of diamond films with triethylene glycol [Las04]. Immobilising molecules allows the construction of affinity biosensors that can monitor molecular interactions like DNA hybridisation [Cai04] or antibody-antigen interaction [Coo05] with great sensitivity using impedance spectroscopy.

Our previous work on DNA attachment to CVD diamond, making use of standard PCD with grain sizes ranging between tens to several hundreds of μm , was based on a method developed for diamond powder (see section 1.2.2.3) [Ush02]. The SOCl_2 -mediated reaction of surface oxides with thymidine was

followed by enzymatic attachment of dsDNA molecules. However, this method appeared hard to reproduce on PCD films [Wen03]. This is possibly due to an insufficient availability of COOH-groups on the PCD surface.

Here, we investigate an alternative DNA-tethering method based on photochemical attachment of ω -unsaturated fatty acids onto NCD. The deprotection step of Yang *et al.* can be discarded by utilising ω -unsaturated fatty acids to introduce COOH-groups and a carbodiimide-mediated coupling method for NH₂-modified dsDNA which will leave no linker molecule behind in the bond. This technique will also overcome the problem of insufficient carboxylation by attaching fatty acid chains to the diamond surface and will create a universal coupler for NH₂-groups.

3.2. MATERIALS AND METHODS

3.2.1 Materials

FITC-labelled forward primer (22 b: 5'-FITC-C₆H₁₂-TCA-AAT-TGC-CAG-AAC-AAC-TAC-T-3') and NH₂-labelled reverse primer (26 b: 5'-NH₂-C₆H₁₂-CTT-CTC-ACA-GTA-ATC-ATA-AGT-GTT-CC-3') were purchased from Applied Biosystems (Lennik, Belgium).

SMART ladder was obtained from Eurogentec (Seraing, Belgium). Dynabeads[®] MyOne[™] Carboxylic Acid were bought from Dynal Biotech (Oslo, Norway).

3.2.2 NCD functionalisation

The surface of the diamond samples was covered with 10-UDA and subsequently illuminated for 20 h with 254 nm light from a Philips TUV G4T4 4W lamp (2.5 mW.cm⁻²), mounted in an EPROM eraser box from Lawtronics (ME5, Edenbridge, UK) under a protective N atmosphere inside a glove box (figure 3.1). The samples were rinsed with 10% SDS, an anionic detergent, and with distilled water.

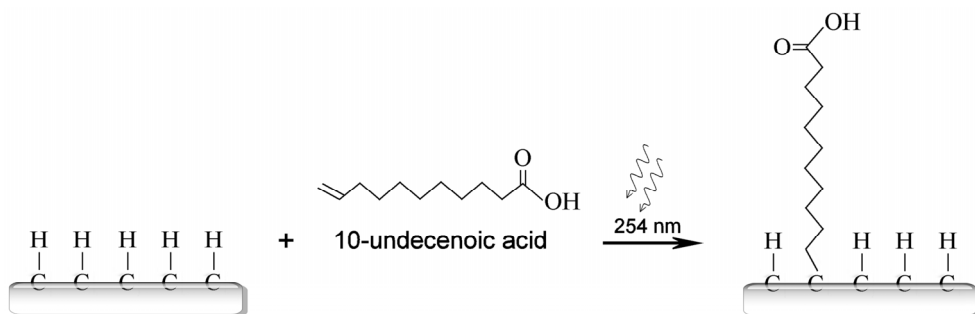


Figure 3.1: Photoattachment of 10-UDA acid to the NCD surface through irradiation with 254 nm UV light.

The COOH-groups on the diamond surface are transformed using EDC into intermediates that readily react with the NH₂-groups on the FITC-labelled PCR

amplicons [Gra90]. The OH-moiety of the COOH-group, which is a bad leaving group, is transformed into a better leaving group using the EDC reagent, that forms an unstable O-acylisourea intermediate. Afterwards, an acid-catalysed nucleophilic substitution with NH₂-modified DNA results in a net amide bond formation between the fatty acid and the dsDNA (figure 3.2).

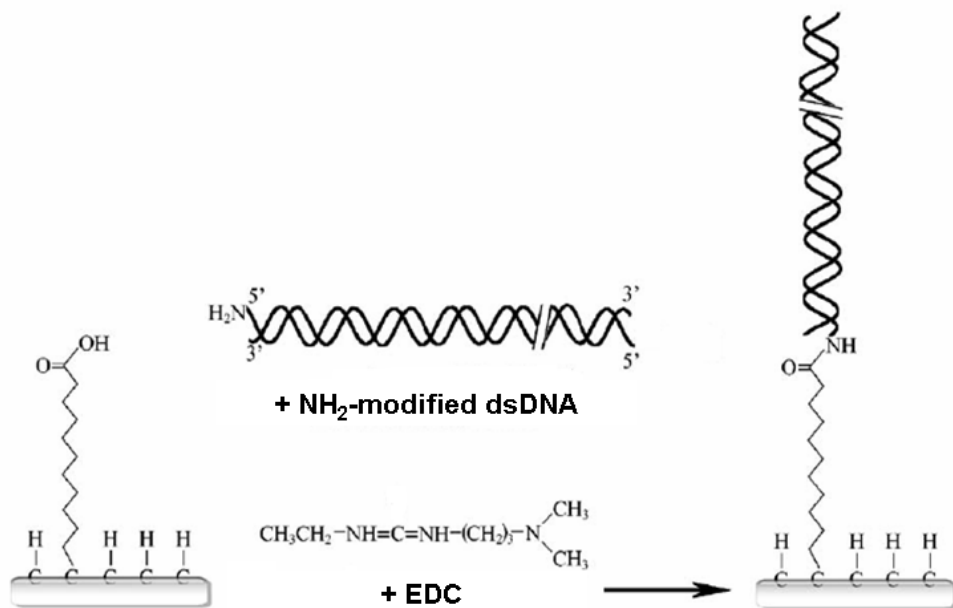


Figure 3.2: Covalent attachment of FITC-labelled NH₂-modified dsDNA to 10-UDA on an NCD substrate using an EDC-mediated reaction.

The NCD surfaces were incubated with a 50 μ l droplet of a mixture of 1.2 μ g (\sim 8 pmol) PCR-amplified FITC-labelled NH₂-modified dsDNA (250 bp) and 1 mg EDC (\sim 5 μ mol, \sim 0.1 M) in a 25 mM MES solution, pH 6, for 2 h at 4°C. The NCD samples were placed in a closed container with a droplet of water enclosed, to avoid evaporation. As a negative control, other COOH-modified NCD samples were treated with a similar mixture in which EDC was replaced by 25 mM MES, pH 6. Non-covalently bound DNA was removed from the diamond samples by thoroughly washing with 1 \times PBS buffer. The washing steps were performed as follows. The NCD samples were submerged in 1 \times PBS buffer and were continuously shaken for 5 minutes. This was repeated 11 times. For the 12th and last washing step, 50 μ l of 1 \times PBS was introduced onto the surface and was removed and collected after 5 minutes.

In an analogous experiment, FITC-labelled NH₂-modified dsDNA was also EDC-linked to COOH-modified paramagnetic beads. Again, COOH-modified beads treated with FITC-labelled NH₂-modified dsDNA without EDC served as a control.

3.2.3 Denaturation-rehybridisation

These COOH-modified NCD samples that were treated with an FITC-labelled NH₂-modified dsDNA solution, either with or without EDC, were used in a denaturation and rehybridisation experiment. To denature the immobilised dsDNA, 50 µl of 0.1 M NaOH was placed on the treated diamond surfaces at room temperature for 5 minutes. This NaOH, now containing the FITC-labelled denatured strands, was collected by simply pipetting the drop of NaOH from the surface and was neutralised with 0.1 M HCl. Samples were subsequently submerged in boiling water for 1 minute, to make sure all of the surface-bound dsDNA would be denatured.

Rehybridisation of the ssDNA still remaining on the diamond surfaces was carried out by submerging the samples for 30 minutes at 59°C in hybridisation buffer containing an excess of complementary DNA, which was previously denatured for 5 minutes at 95°C. The samples were then thoroughly washed with 1× PBS, as described previously, and 50 µl of the last washing step was also collected.

This cycle of denaturation-rehybridisation-washing (d-r-w), which is outlined in figure 3.3, was repeated 35 times, and for each cycle the fluids corresponding to the last washing step and the denaturation step were collected from the EDC-positive and EDC-negative sample batches for further analysis.

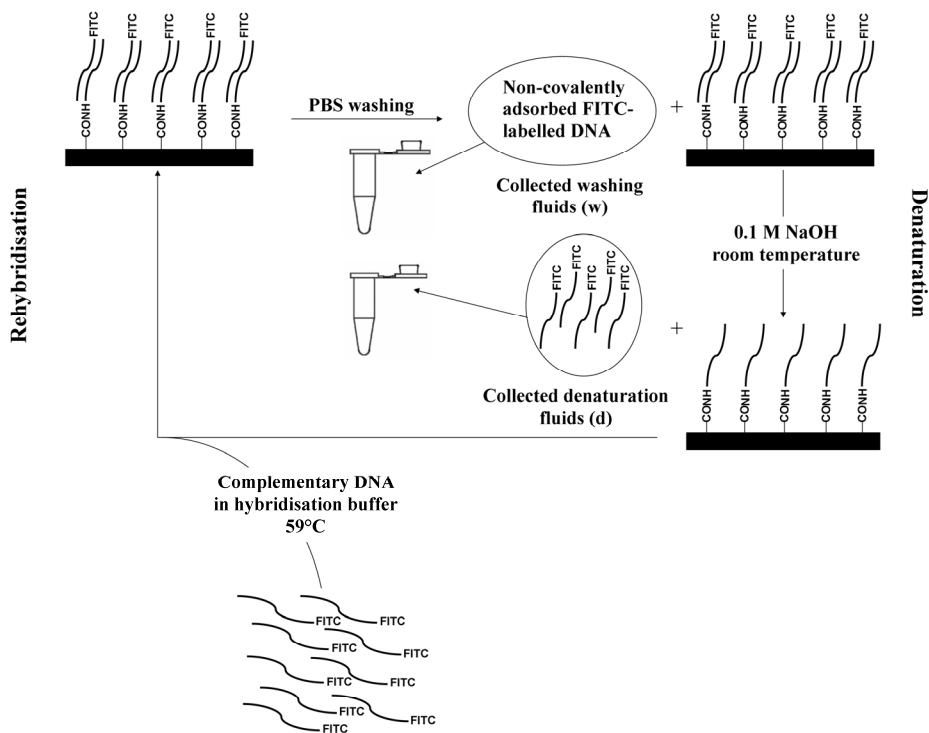


Figure 3.3: Denaturation-rehybridisation-washing (d-r-w) cycle on COOH-modified NCD. FITC-labelled NH₂-modified dsDNA was immobilised onto the surface. After thoroughly washing the non-covalently bound DNA away, the sample was denatured. Rehybridisation was obtained by incubating the sample with new FITC-labelled complementary ssDNA. In every cycle, fluids from the last washing (w) step and the denaturation step (d) were collected for further analysis.

3.2.4 Fluorescence measurements

Fluorescence signals from all of the collected fluids were measured with the fluorescence module of the Lightcycler (Roche Diagnostics, Vilvoorde, Belgium). Both denaturation and washing steps of EDC-positive as well as EDC-negative NCD and paramagnetic bead samples were measured. An emission filter of 530/20 nm Full Width at Half Maximum (FWHM) was used. Of each collected denaturation and washing volume, 10 μ l from both diamond sample batches and both bead samples was analysed. As a blank, 10 μ l of deionised water was used.

Sensitivity calibration of the fluorimeter used for FITC detection was carried out by measuring the fluorescence signal in a dilution series of FITC-labelled dsDNA. These measurements were performed at 30°C.

3.2.5 PCR and gel electrophoresis

In parallel to the fluorescence measurements, PCR reactions were performed on the fluids collected from the last washing steps and the denaturation steps from the EDC-positive and EDC-negative NCD sample batches. In a parallel experiment performed on the dsDNA-treated EDC-positive and EDC-negative paramagnetic beads, a PCR reaction was performed on the beads after each denaturation reaction. Subsequent to the PCR, the PCR amplicons were checked on a 2% agarose gel.

3.3 RESULTS

3.3.1 FITC sensitivity determination of Lightcycler fluorescence module

FITC-labelled DNA was prepared as described in Chapter 2 and brought to a concentration of $40 \text{ ng} \cdot \mu\text{l}^{-1}$. A dilution series was prepared in triplicate from this FITC-labelled dsDNA. Concentrations were 1.5 , 0.8 , 0.4 , 0.2 and $0.1 \text{ ng} \cdot \mu\text{l}^{-1}$. Deionised water was used as blank. Of each dilution, $10 \mu\text{l}$ was analysed with the Lightcycler fluorescence module using a $530/20 \text{ nm}$ FWHM emission filter. The sensitivity calibration curve is shown in figure 3.4A. The detection limit for the FITC label is 2 ng ($0.2 \text{ ng} \cdot \mu\text{l}^{-1} \times 10 \mu\text{l}$).

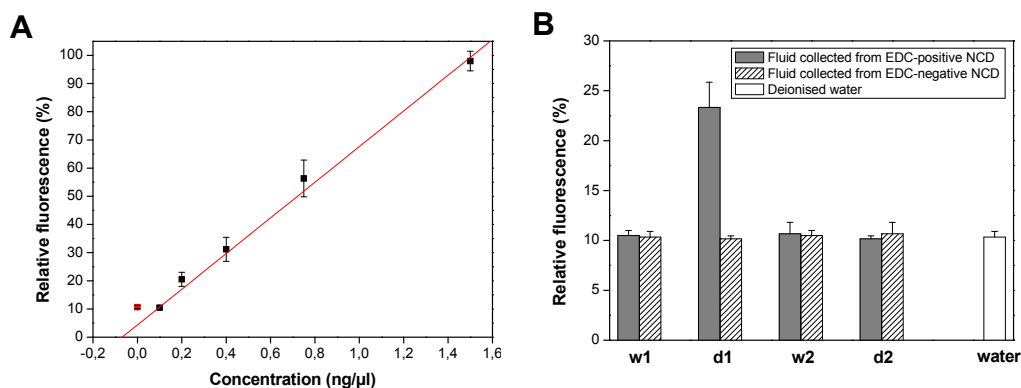


Figure 3.4: Fluorescence detection of FITC-labelled DNA. **A)** Sensitivity curve of Lightcycler fluorimeter for FITC detection. The measurements are expressed as relative values to an internal calibrator. The red line indicates the linear regression fit ($y = A + Bx$). **B)** Fluorescence graph obtained from the analysis of the fluids collected from the washing and denaturation steps of cycle 1 and 2 (w1-2 and d1-2, respectively) of the EDC-positive and the EDC-negative NCD sample batches.

3.3.2 Denaturation and rehybridisation monitored by fluorescence measurements

The presence of FITC fluorescence in $10 \mu\text{l}$ of each of the fluids collected from the successive washing and denaturation steps from the EDC-positive and EDC-negative NCD sample batches was analysed with the Lightcycler

fluorescence module. The results, which are based on three separate experiments, are shown in figure 3.4B.

For the EDC-positive as well as the EDC-negative NCD sample batch, the fluorescence signal from the last PBS washing step after the dsDNA incubation reaction (w1) did not differ from that in water. Also, the fluid obtained from the last washing step after the first rehybridisation reaction (w2) remained negative for both sample batches.

In the EDC-positive samples, there was a significant rise in fluorescence in the fluid obtained from the first denaturation step (d1), consistent with the release of the fluorescently labelled ssDNA strand during the alkaline denaturation. However, this rise in fluorescence could not be detected in the fluid corresponding to the second denaturation step (d2), or in any of the subsequent denaturation volumes (data not shown). In the EDC-negative samples, no increase in fluorescence was detected.

Comparable results were obtained from the fluids obtained from the last washing steps and the denaturation steps from the EDC-positive and EDC-negative paramagnetic beads (data not shown).

3.3.3 Denaturation and rehybridisation monitored by PCR and gel electrophoresis

PCR reactions (15 cycles) were performed on 2 µl of dsDNA-treated EDC-positive and EDC-negative paramagnetic beads after 2 subsequent denaturation-rehybridisation reactions. They showed clear bands for the EDC-treated sample, but no signal for the EDC-negative sample (figure 3.5).

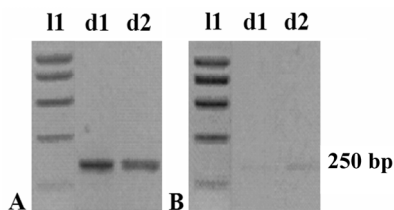


Figure 3.5: Results obtained for paramagnetic beads after the first and the second denaturation-rehybridisation reaction via 2 % agarose gel electrophoresis. **A)** EDC-positive beads. **B)** EDC-negative beads. I1 = SMART Ladder; d1 = after the denaturation step of cycle 1; d2 = after the denaturation step of cycle 2.

For the EDC-positive and EDC-negative NCD samples, 2 μ l of the fluids from the collected last washing steps and the denaturation steps of the first 26 cycles from both batches were used in a 27 cycle PCR reaction. PCR conditions for the fluids of the last 9 cycles from both batches were modified into a 30 cycle PCR reaction while using 3 μ l of sample volume. Equal volumes of PCR product for the EDC-positive and EDC-negative samples were loaded on a 2 % agarose gel. Figure 3.6 shows results of 10 out of 35 hybridisation cycles that are representative of the entire data set.

As shown in figure 3.6A, the bands corresponding to fluids collected during the denaturation steps remain visible throughout the entire 35 cycles for the EDC-positive NCD sample. However, the bands have low intensity. Also, a band corresponding to the fluid collected from the last washing step of cycle 17 can be detected (w17). This indicates that not all non-covalently adsorbed DNA was removed from the NCD surface during the last washing step of cycle 17. This attached DNA, however, would certainly have been removed during the boiling step in between hybridisation cycles. In the EDC-negative sample, shown in figure 3.6B, cycle 2, 5, 11, 17, 24 and 33 also show the presence of weak bands corresponding to the fluids collected during the associated denaturations (d2, d5, d11, d17, d24 and d33). This suggests that a low amount of DNA is also non-covalently attached to the COOH-modified NCD surface. Also a slight positive signal could be detected in the fluid collected from the last washing steps from cycles 32 and 33 (w32 and w33).

Control experiments performed on other NCD samples in the EDC-positive and EDC-negative batch gave comparable results.

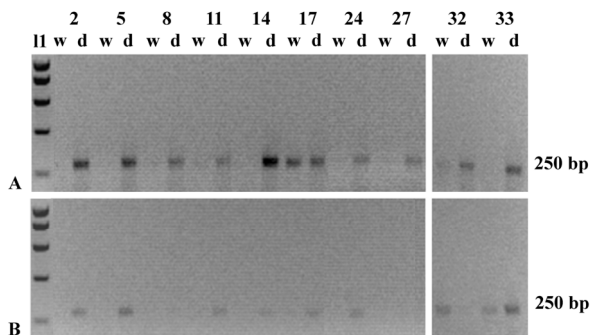


Figure 3.6: Analysis of the denaturation-rehybridisation cycles on NCD samples via 2 % agarose gel electrophoresis. **A)** EDC-positive NCD. **B)** EDC-negative NCD. l1 = SMART Ladder; w2-33 = fluids collected from the last washing steps of cycles 2-33; d2-33 = fluids collected from the denaturation steps of cycles 2-33.

3.4. DISCUSSION

In the present study, an EDC-mediated reaction was used to covalently attach dsDNA molecules to NCD surfaces through the formation of an amide bond between the COOH-groups that were photochemically introduced on the diamond surface and the NH₂-modified dsDNA molecules.

To analyse the attached dsDNA molecules in terms of their functional activity, they were subjected to a series of 35 denaturations, rehybridisations and washings. The fluids of the denaturation steps and the last washing steps were analysed for the presence of DNA.

Fluorescence measurements appeared to be not sensitive enough to detect the FITC-labelled DNA in the fluid samples after the various washing and denaturation steps, so a PCR and gel electrophoresis-based approach was used. From the PCR reaction that was performed on the collected last washing steps and the denaturation steps, it was clear that repeated denaturations and rehybridisations remained possible for more than 30 times for the EDC-treated diamond sample (figure 3.6A), which confirms the results obtained by Yang *et al.*, who were able to perform more than 30 denaturation/rehybridisation cycles with a DNA attachment method on diamond employing an SSMCC crosslinker, as detected by fluorescence measurements [Yan02].

For the EDC-negative sample the denaturation signals appeared much weaker and sporadic (figure 3.6B). These results indicate that the NH₂-modified DNA was indeed covalently bound to the COOH-modified diamond surface in an EDC-mediated reaction, besides a low amount of DNA that was aspecifically adsorbed to the diamond surface.

To confirm our findings from the denaturation reactions performed on the NCD-immobilised dsDNA, a PCR reaction was also performed on analogously treated paramagnetic beads immediately after the first and the second denaturation cycle. The results indicate that DNA was covalently bound using the EDC-attachment protocol. Indeed, ssDNA was present on the surface of the EDC-treated beads after successive denaturation steps. No DNA appeared to be present on the surface of beads that were treated without EDC.

The above results indicate a covalent bond between the DNA and NCD. The initial binding capacity of functionally active dsDNA appears acceptable, as the denatured ssDNA of the EDC-positive NCD-sample was directly visible with fluorescence measurements in the first cycle. No signal could be detected for the sample without EDC. However, amplification of the DNA present in the collected denaturation and washing fluids by PCR became necessary after this first denaturation-rehybridisation-cycle. Denaturation and rehybridisation of NCD-bound DNA thus appeared to occur with a rather low efficiency. This can be attributed to the physical properties of the DNA itself. The length and nature of the DNA molecules that were linked onto the diamond determines their conformation. Conformation is one of the most important parameters affecting surface coverage and hybridisation efficiency. Longer molecules, as were used in this study (250 bp) are dynamic, flexible coils that attach themselves aspecifically to the surface on multiple locations. This could lead to a lower DNA surface density and an inaccessibility of various DNA molecules to subsequent hybridisations and denaturations. This implies a lower hybridisation efficiency, resulting in low or even no denaturation signals [Ste00]. dsDNA molecules are more rigid in structure, thereby assuring the accessibility of a considerable amount of DNA-molecules for the first denaturation. ssDNA molecules of the same length, however, as produced during this denaturation, are much more flexible and display a greater tendency towards multiple attachment sites on the surface. This might explain the lower hybridisation efficiencies in cycles 2 to 35.

Moreover, the signal intensity was even lower for the last 9 cycles of denaturation-rehybridisation in comparison to the first 26 cycles. This can be explained by the use of the same hybridisation buffer containing the complementary hybridisation DNA for the entire 35 cycles, and the degradation effects that are surely associated with this.

Although no non-covalently attached DNA was visible with paramagnetic beads, a sporadic, non-specific denaturation signal was present with the EDC-negative NCD sample, corresponding with some non-covalently adsorbed DNA to the NCD surface. The fact that this signal did not appear in every cycle also displays the dynamic nature of this non-covalently attached DNA. Depending on the conformation and orientation of these adsorbed molecules, they become either available or unavailable for denaturation reactions themselves.

When the functionalisation procedure was tested on PCD no evidence of covalent DNA attachment was found for these samples. The exact mechanism of the UV-induced reaction between the diamond surface (with respect to poly- or nanocrystalline structure) and the ω -unsaturated fatty acid therefore remains unclear. However, as already mentioned in section 1.2.2.3, Nichols *et al.* suggest that UV-induced photo-emitted electrons from the diamond surface transform the molecules to be attached into anions. These anions then react directly or indirectly with the H atoms on the diamond surface [Nic05].

3.5. CONCLUSIONS

Our goal is to develop a prototype biosensor, based on covalently attached DNA, for diagnostic purposes with the same sensitivity and specificity as the commonly used methods, such as blotting techniques, microarrays and PCR-ELISA.

In this work, we described a DNA-attachment method with ω -unsaturated fatty acids and EDC on an NCD surface.

Compared to other procedures for the attachment of biomolecules to diamond surfaces, this method has several advantages. First of all, there are many molecules with NH_2 -groups. Proteins (enzymes, antibodies...) contain NH_2 -groups both at the NH_2 -terminus, as well as at some aminoacid residues. When using the EDC crosslinker with these molecules, inter- and intramolecular linking of the proteins can be prevented by using NHS in a two-step reaction. Moreover, no deprotection step is necessary. The method provides a short and simple link between the DNA and the diamond surface, since no part of EDC is left in the final bond. In the SSMCC approach, part of the crosslinker remains in the final linkage. Therefore, the EDC-based method prevents unwanted side reactions. This approach also maintains the proximity-to-the-surface criterion, which is required for the electrical detection sensitivity during impedance measurements.

An EDC-mediated attachment of dsDNA to NCD leads to a covalent bond between this DNA and the diamond. However, the binding capacity and/or the denaturation/rehybridisation efficiency of the functionally active DNA still remains low, and some non-covalently adsorbed DNA can be detected. Adjustments to the method to increase the binding capacity, to improve the denaturation/rehybridisation efficiency, and to reduce the non-specificity are currently being investigated.

Further down the line, this sensitive and specific DNA-based biosensor will be integrated in an electrical read-out system, which will facilitate and speed up measurements.

ACKNOWLEDGEMENTS

The research was performed in the framework of the IWT-project #030219 '*CVD Diamond: a novel multifunctional material for high temperature electronics, high power/high frequency electronics and bioelectronics*' funded by the Institute for the Promotion of Innovation by Science and Technology in Flanders (IWT) , the OSTC-IUAP V programme '*Quantum Size Effects in Nanostructured Materials*', and the Scientific Research Community WO.035.04N '*Hybrid Systems at Nanometer Scale*' of FWO Flanders. M. Daenen (Assistant) and Dr. K. Haenen (Postdoctoral Fellow) are supported by the Fund for Scientific Research – Flanders (FWO-Vlaanderen). We would like to thank Prof. Dr. D. Vanderzande of the Chemistry Department of Hasselt University and Dr. J.A. Garrido of the Walter Schottky Institut at the Technische Universität München for helpful discussions. Also many thanks to W. Deferme, K. Vanstreels, Dr. G. Vanhoyland and Dr. J. D'Haen of the Institute for Materials Research (IMO) for their practical assistance.

Chapter 4:

Topographical and functional characterisation of the ssDNA probe layer generated through EDC-mediated covalent attachment to nanocrystalline diamond using fluorescence microscopy.

Based on:

Topographical and functional characterisation of the ssDNA probe layer generated through EDC-mediated covalent attachment to nanocrystalline diamond using fluorescence microscopy.

Submitted

V. Vermeeren^{a*}, S. Wenmackers^{b*}, M. Daenen^b, K. Haenen^{b,c}, O.A. Williams^{b,c}, M. Ameloot^a, M. vandeVen^a, P. Wagner^b, L. Michiels^a

^a Hasselt University and transnationale Universiteit Limburg, School for Life Sciences, Biomedical Research Institute, Agoralaan, Bldg. A, B-3590 Diepenbeek, Belgium, Hasselt

^b University and transnationale Universiteit Limburg, School for Life Sciences, Institute for Materials Research, Wetenschapspark 1, B-3590 Diepenbeek, Belgium and IMEC vzw,

^c Division IMOMECE, Wetenschapspark 1, B-3590 Diepenbeek, Belgium

* V. Vermeeren and S. Wenmackers contributed equally to this publication.

ABSTRACT

The covalent attachment method for DNA on NCD, involving the introduction of COOH-functionalities on the surface by photoattachment of 10-UDA, followed by the EDC-mediated coupling to NH₂-labelled ssDNA, is evaluated in terms of stability, density, and functionality of the resulting biological interface. This is of crucial importance in DNA-biosensor development. The covalent nature of DNA attachment will infer the necessary stability and favourable orientation to the ssDNA probe molecules. Using confocal fluorescence microscopy, the influence of buffer type for the removal of excess 10-UDA and ssDNA, the probe ssDNA length, the probe ssDNA concentration, and the presence of the COOH-linker on the density and functionality of the ssDNA probe layer was investigated. It was determined that the most homogeneously dense and functional DNA layer was obtained when 300 pmol of short ssDNA was applied to COOH-modified NCD samples, while H-terminated NCD was resistant for DNA attachment. Exploiting this surface functionality-dependence of the DNA attachment efficiency, a shadow mask was applied during the photochemical introduction of the COOH-functionalities, leaving certain regions on the NCD H-terminated. The subsequent DNA attachment resulted in a fluorescence pattern corresponding to the negative of the shadow mask. Finally, NCD surfaces covered with mixtures of the 10-UDA linker molecule and a similar molecule lacking the COOH-functionality, functioning as a lateral spacer, were examined for their suitability in preventing non-specific adsorption to the surface, and in decreasing steric hindrance. However, purely COOH-modified NCD samples, patterned with H-terminated regions and treated with a controlled amount of probe DNA proved the most efficient in fulfilling these tasks.

4.1. INTRODUCTION

Increasing interest in the combination of molecular biology and micro-electronics has led to the dawn of a new field, called bio-electronics. An important corner stone in the development of this field is the design of interfaces that are both compatible with micro-electronic processing methods, and modification with biomolecules. This way, the biological reaction, such as a target recognition event, and the associated sensing and signal processing can be integrated into a single platform. A successful combination of biomolecules with solid substrates was first established in Southern blotting [Sou75], and has since become the basis of the widely used and commercialised microarrays, or gene chips, used for expression profiling or mutational analysis [Sch95]. Probe ssDNA molecules are covalently attached to Si or glass, which are materials that are compatible with micro-electronics. Hybridisation of the probe ssDNA molecules with target ssDNA is usually detected fluorimetrically. However, degradation of these interfaces in aqueous solutions limits their use to that of disposable biosensors [Yan02];[Neb07].

CVD diamond has become an attractive alternative substrate for biosensors because of several very appealing physical, optical, chemical and electrical characteristics [Fie87];[Swa93]. It is transparent in a wide spectrum of optical wavelengths, is chemically inert, has a wide electrochemical window and can be made semiconductive by doping [Koi97];[Will06]. At relatively low temperatures, diamond can also be deposited on substrates such as Si and quartz that are compatible with micro-electronics processing. In addition, various procedures have been developed to covalently attach biomolecules to diamond, such as chemical [Ush02], photochemical [Yan02];[Här04] and electrochemical methods [Uet07];[Wa04]. These linkages were proven to be more stable than those with other commonly used semiconductors such as Si, allowing for reusable diamond-based biosensors. Furthermore, the biocompatibility of diamond permits *in vivo* applications [Tan95].

We developed a simple but efficient two-step process to covalently bind NH₂-modified DNA to COOH-modified thin NCD films using EDC [Chr06] (see Chapter 3). It was shown that the attached DNA remained functionally active. However,

since DNA of 250 bp was used, the probe density was rather low, and some physisorbed DNA was present. These results clearly demonstrated that several reaction parameters in the covalent attachment procedure are of critical importance in order to achieve biological activity combined with high density and specificity of the sensor surface. Elucidating these parameters is crucial for the fabrication of functional biosensors. First of all, covalency is to be preferred as a means of biomolecule attachment because of the associated stability of the resulting molecular interface, the favourable probe orientation that is brought about by a terminal attachment, and the ability to predetermine the location of the probes on the surface. Secondly, a high probe density should be attained in order to achieve a high sensitivity. However, the dense probe layer must remain biologically active, i.e., the DNA molecules must still be accessible for hybridisation. Finally, the amount of non-specifically adsorbed DNA should be minimised, especially in the case of DNA attachment in an array format.

The current study was performed to address these issues. Several reaction parameters associated with the EDC-mediated covalent DNA attachment were evaluated in terms of their effect on probe density and functionality, such as the washing buffers after 10-UDA and DNA attachment, DNA probe length, DNA probe concentration, surface functionality and sample type. These experiments served to offer a detailed understanding of the process of attachment and to establish the conditions for optimal functionality of the DNA-sensor surface.

4.2. MATERIALS AND METHODS

4.2.1 Materials

The probe ssDNA molecules used for the EDC-mediated attachment protocol were purchased from Eurogentec (Seraing, Belgium). They were labelled at the 5' end with an NH₂-modifier, while the 3' end carried an Alexa Fluor® 488 label (8 b: 5'-NH₂-C₆H₁₂-CCC-CTG-CA-Alexa 488-3'). Probe ssDNA molecules used for the hybridisation experiments were purchased from Invitrogen (Merelbeke, Belgium), and were labelled at the 5' end with an NH₂-modifier (36 b: 5'-NH₂-C₆H₁₂-AAA-AAA-ACC-CCT-GCA-GCC-CAT-GTA-TAC-CCC-CGA-ACC-3'). Target ssDNA molecules bought from Invitrogen (Merelbeke, Belgium), were modified at the 5' end with an Alexa Fluor® 488 label, allowing to monitor hybridisation using confocal fluorescence microscopy. This target ssDNA contained a sequence that was either completely complementary to the probe ssDNA (29 b: 5'-Alexa 488-C₆H₁₂-GGT-TCG-GGG-GTA-TAC-ATG-GGC-TGC-AGG-GG-3'), carried a 1-base mismatch to the probe ssDNA (29 b: 5'-Alexa 488-C₆H₁₂-GGT-TCG-GGG-GTA-TAC-ATG-GGC-TCC-AGG-GG-3'), or was completely non-complementary (29 b: 5'-Alexa 488-C₆H₁₂-TCA-AAT-TGC-CAG-AAC-AAC-TAC-TGA-CTG-AA-3'). A 250 bp NH₂-modified and Alexa 488-labelled dsDNA fragment from the PAH gene was generated through a PCR reaction, making use of a 5'-Alexa 488-labelled forward primer (5'-Alexa 488-C₆H₁₂-TCA-AAT-TGC-CAG-AAC-AAC-TAC-T-3') and a NH₂-modified reverse primer (5'-NH₂-C₆H₁₂-CTT-CTC-ACA-GTA-ATC-ATA-AGT-GTT-CC-3').

9-decen-1-ol (9-DO; >97% pure) and 1-undecene (1-UD; ≥99.5% pure) were purchased from Sigma-Aldrich (Bornem, Belgium).

4.2.2 NCD functionalisation

The surfaces of the IMO and rho-BeSt NCD samples were covered with either pure 10-UDA, containing a COOH-functionality, or a mixture of 10-UDA and 9-DO, containing an OH-functionality. To prevent evaporation and to obtain more

reproducible liquid film thicknesses, a quartz glass of 1 mm thickness was placed on top of the samples. The samples were subsequently illuminated for 20 h with 254 nm light from a Philips TUV G4T4 4W lamp ($> 2.5 \text{ mW.cm}^{-2}$), mounted in an EPROM eraser box from Lawtronics (ME5, Edenbridge, UK) under a protective N atmosphere inside a glove box, as described previously [Chr06] (see Chapter 3). The samples were subsequently rinsed either with 10% SDS and distilled water, or with hot acetic acid and distilled water.

To establish the effect of different washing buffers on the DNA binding, IMO NCD samples were treated with 5 μmol (0.1 M) EDC and 30 pmol of NH_2 -modified and Alexa 488-labelled probe ssDNA (8 b) in a 25 mM MES buffer (pH 6) for 2 h at 4°C.

To investigate the effect of the DNA length on the attachment efficiency, photochemically modified rho-BeSt surfaces were incubated with a mixture of 5 μmol (0.1 M) EDC and ~ 60 pmol of either NH_2 -modified and Alexa 488-labelled dsDNA (250 bp) or NH_2 -modified and Alexa 488-labelled probe ssDNA (8 b) in a 25 mM MES buffer (pH 6) for 2 h at 4°C.

For the determination of the most efficient probe DNA concentration, rho-BeSt samples were covalently modified with different amounts of NH_2 -modified and Alexa 488-labelled probe ssDNA (8 b) (300 pmol, 30 pmol, 3 pmol, 300 fmol, 30 fmol or 3 fmol) using 5 μmol (0.1 M) EDC in a 25 mM MES buffer (pH 6) for 2 h at 4°C.

For the mixed functionality-experiments, 300 pmol of Alexa 488-labelled probe ssDNA (8 b) was covalently bound to rho-BeSt samples using 5 μmol (0.1 M) EDC in a 25 mM MES buffer (pH 6) for 2 h at 4°C.

For the hybridisation experiments, 300 pmol of NH_2 -modified unlabelled probe ssDNA (36 b) was attached to rho-BeSt samples with 5 μmol (0.1 M) EDC in a 25 mM MES buffer (pH 6) for 2 h at 4°C.

As a negative control, photochemically modified IMO and rho-BeSt surfaces were treated with similar mixtures in which EDC was replaced by an equal volume of 25 mM MES (pH 6). Non-covalently bound DNA was removed from the IMO and rho-BeSt samples either by thoroughly washing with 1 \times PBS buffer, as described previously [Chr06] (see Chapter 3), or by washing with 1 \times PBS buffer followed by 2 \times SSC buffer containing 0.5% SDS.

4.2.3 DNA hybridisation

Hybridisation of the ssDNA molecules (36 b) attached to the NCD was performed by incubating ssDNA-modified IMO NCD samples for 2 h at different temperatures with 600 pmol Alexa 488-labelled target ssDNA (29 b), either complementary to the probe ssDNA or containing a 1-base mismatch, in MicroHyb™ hybridisation buffer. After hybridisation, the samples were rinsed in 2× SSC buffer containing 0.5% SDS for 30 minutes at room temperature, followed by two 5 minute rinsing steps in 0.2× SSC buffer, at a few degrees below the hybridisation temperature and at room temperature, respectively.

To determine the effect of various surface functionalities on the hybridisation efficiency, the ssDNA molecules (36 b) attached to rho-BeSt surfaces were hybridised with 600 pmol Alexa 488-labelled target ssDNA (29 b), either complementary or non-complementary to the probe ssDNA, for 2 h at 70°C. Next, the samples were rinsed in 2× SSC buffer containing 0.5% SDS for 30 minutes at room temperature, followed by two 5 minute rinsing steps in 0.2× SSC buffer: at 65°C and at room temperature, respectively.

During hybridisation, the samples were placed in a closed container under a saturated water vapour atmosphere, to avoid evaporation of the reaction fluid.

4.2.4 Confocal fluorescence microscopy and software

The EDC-mediated covalent attachment of the Alexa 488-labelled ssDNA (8 b) and the hybridisation efficiency were evaluated by measuring the fluorescence of the sample surfaces in 1× PBS buffer solution with a Zeiss LSM 510 META Axiovert 200M laser scanning confocal fluorescence microscope (Zeiss, NV/SA, Zaventem, Belgium), using 488 nm Argon-ion laser excitation with a maximum intensity at the sample surface of 1.00 ± 0.05 mW. Apart from better refractive index matching resulting in a significantly brighter fluorescence signal, measuring biological layers in buffer solution allows to study them under physiological conditions. To obtain this, a 1 mm thick, glass microscope slide, with a 1 cm wide hole, sealed at the bottom with a thin cover glass was placed on the stage of the inverted microscope. The samples were positioned over this

hole, the functionalised side facing downwards. The hole then formed a sealed compartment, and was entirely filled with buffer solution, making sure that no air bubbles were present at the sample surface. Spurious 514 nm light passing through the Acousto Optic Tuning Filter (AOTF) was blocked by a 488/10 nm interference filter placed in front of the coupling fiber optic. Confocal optics included a 490 nm dichroic and BP 500-550 nm emission filter.

All images were collected with a 10×/0.3 Plan Neofluar air objective with a working distance of 5.6 mm. Image size was 512×512 pixels corresponding with $\sim 900 \mu\text{m}^2$, unless stated otherwise. Pinhole size was 150 μm . Pixel dwell time was 25.6 μs . The settings that were varied in different measurements were the laser illumination (2 or 10% of the previously mentioned maximum, to avoid detector saturation between various measurements) and the detector gain (800, 850, 931 or 1200). The latter is a measure for the photomultiplier voltage in arbitrary units. For photobleaching experiments, laser illumination was set to 100% for 3 min. Fluorescence images were processed and the average fluorescence intensities retrieved using the ImageJ software v. 1.37c (National Institute of Health, Bethesda, MD, USA).

4.3. RESULTS AND DISCUSSION

4.3.1 Optimisation of EDC-mediated covalent DNA attachment

In our previous work, we introduced an efficient, two-step procedure to covalently bind 250 bp dsDNA to NCD. In a first step, the NCD samples were covered with 10-UDA and illuminated with UV (254 nm) for 20 h, yielding a COOH-modified NCD surface. Subsequently, NH₂-modified DNA was attached to these COOH-groups through the formation of a peptide bond, using the zero-length cross-linker EDC [Chr06] (see Chapter 3). However, the DNA binding capacity and the adsorption of non-specific DNA remains a major concern in biosensor development. Both of these aspects are addressed in this study. The parameters that were evaluated in this respect were the washing buffers used to remove the excess 10-UDA and probe DNA, the length of the probe DNA, the most efficient probe concentration to be immobilised, and the effect of 10-UDA as a functionalisation layer on the NCD.

4.3.1.1 Effect of washing buffers

A particular problem encountered in this procedure is a less than optimal removal of excess, non-covalently attached 10-UDA appearing as a vertically stacked multilayer of molecules, held firmly in place by strong hydrogen bonding between COOH-dimers [Sch76]. Only the top layer will present available COOH-functionalities for the attachment of NH₂-modified ssDNA. However, since many of the 10-UDA molecules in this top layer will not be covalently attached to the underlying NCD surface, they will gradually desorb in the subsequent processing steps, leading to bright fluorescent patches, corresponding to regions of covalently attached ssDNA through bound 10-UDA molecules, alternating with less intense regions where most of the 10-UDA and the associated DNA were lost (figure 4.1A and B).

Hot acetic acid was described to efficiently remove COOH-terminated alkyl monolayers from H-Si(111) surfaces by breaking the hydrogen bonds between the COOH-dimers [Fau06]. To verify if this could also be transferred to NCD

surfaces, four IMO NCD samples were photochemically modified with 10-UDA, of which two were subjected to washing steps in 10% SDS and distilled water. The two remaining samples underwent washing steps in heated acetic acid and distilled water. One sample of each condition was subsequently modified with 30 pmol of NH₂-modified Alexa 488-labelled ssDNA (8 b) using EDC, while the other served as a negative control, in which EDC was omitted from the reaction and replaced with an equal volume of 25 mM MES buffer (pH 6). Removal of excess ssDNA still occurred by thoroughly rinsing in 1× PBS. Figures 4.1C and D show the remaining fluorescence. The positive control sample (figure 4.1C) showed a dramatic increase in fluorescence intensity as compared to figure 4.1A. Rinsing with hot acetic acid after photochemical modification thus succeeded in removing most of the non-covalently attached 10-UDA molecules, leaving only the covalently bound monolayer of COOH-functionalities that are all available for ssDNA binding.

The dark region highlighted in figure 4.1D was obtained by regional photobleaching. When an excitation wavelength hits a flat sample surface, part of it is absorbed by the fluorophores and the biggest part is reflected off the surface. Appropriate filters and beam splitters inside the microscope will allow only the fluorescence emission wavelength to pass to the detector. However, in spite of these filters and beam splitters, a fraction of very intense reflection will still reach the detector. Photobleaching is an efficient technique to distinguish between this residual reflection and real fluorescence due to the presence of a fluorescent label. Hitting the sample surface containing the fluorescent molecules with a high intensity excitation wavelength will photobleach these fluorescent molecules: their chemical structure will become permanently changed, and this structure cannot be fluorescently excited. In the image, the fluorescence in that region will have disappeared because of the bleached molecules. Reflection will not be reduced after this intense illumination: it does not bleach. The obvious destruction of fluorescence in Figure 4.1D indicated the presence of non-specifically attached ssDNA.

To overcome this, the same two samples as in figure 4.1C and D were subjected to different washing buffers, and a fluorescence image was taken after each rinse. Upon washing with 2× SSC buffer containing 0.5% of the anionic detergent SDS, there was no longer any evidence of non-specifically bound

ssDNA (figure 4.1F), while the fluorescence intensity of the positive control remained unaffected (figure 4.1E). These conditions yielded reproducibly superior attachment efficiencies. The mean fluorescence intensity value after EDC-mediated ssDNA attachment was $68.0 \pm 5.5\%$, while that of the negative control amounted to only $9.5 \pm 1.5\%$ (N=3). In all further experiments described below, the excess 10-UDA and ssDNA were therefore removed by washing with hot acetic acid and $2\times$ SSC/0.5% SDS, respectively. Because the fluorescence intensities measured at gain 1200 now caused detrimental saturation of the detector, preventing certain fluorescence images from being distinguishable from each other in terms of their absolute intensities (figure 4.1C and E), subsequent images were collected with the detector gain set at lower, non-saturating values.

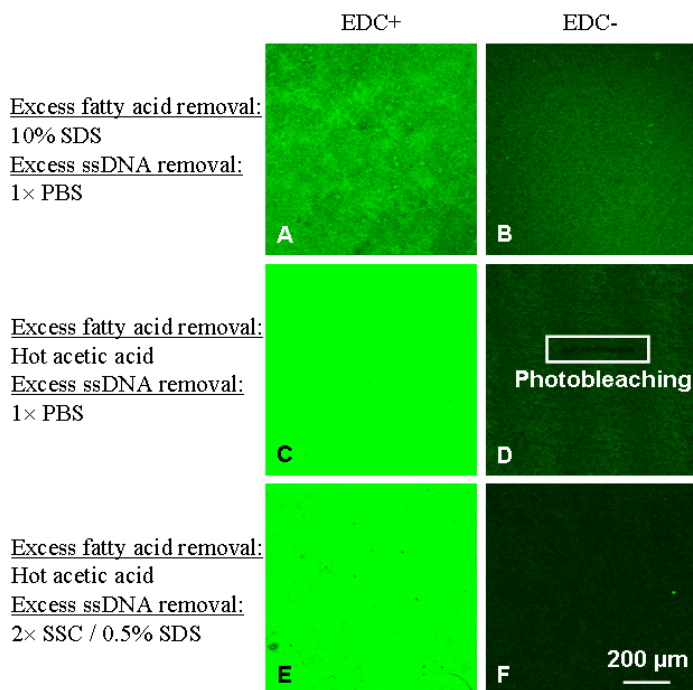


Figure 4.1: Comparison of fluorescence intensity of IMO NCD samples after treatment with 30 pmol of NH_2 -modified and Alexa 488-labelled ssDNA (8 b) using different washing steps.

A) Washed with 10% SDS after photochemical modification and with $1\times$ PBS after covalent attachment.

B) Negative control sample treated under the same conditions as **A)**, but having omitted EDC in the DNA attachment procedure.

C) Washed with hot acetic acid after photochemical modification and with $1\times$ PBS after covalent attachment.

- D)** Negative control sample treated under the same conditions as **C)**, but having omitted EDC in the DNA attachment procedure. A photobleached area, indicating the presence of adsorbed ssDNA, is highlighted.
- E)** Washed with hot acetic acid after photochemical modification and with 2× SSC/0.5% SDS after covalent attachment.
- F)** Negative control sample treated under the same conditions as **E)**, but having omitted EDC in the DNA attachment procedure.
Laser illumination 2% and detector gain 1200.

4.3.1.2 Effect of probe ssDNA length

Next, the effect of probe length on the attachment efficiency was evaluated. It has been published by Steel *et al.* that surface coverage of Au substrates with DNA is strongly dependent on DNA probe length [Ste00]. For probes shorter than 24 bases, the attachment occurs mainly through the end anchoring group, yielding highly extended ssDNA configurations. For longer probes, the surface coverage begins to decrease notably. This decrease was presumed to be associated with a less ordered arrangement of the ssDNA chains, reflecting a more flexible and polymeric ssDNA configuration. Again, to examine if this effect is also valid under our experimental settings, four rho-BeSt samples were modified with two types of DNA. One sample was functionalised with ~60 pmol of NH₂-modified Alexa 488-labelled dsDNA with a length of 250 bp in an EDC-mediated reaction. A second sample was treated with ~60 pmol of NH₂-modified Alexa 488-labelled ssDNA with a length of 8 b. The two remaining samples served as negative controls, in which the EDC was omitted from the reaction. The confocal fluorescence images of these samples are shown in figure 4.2.

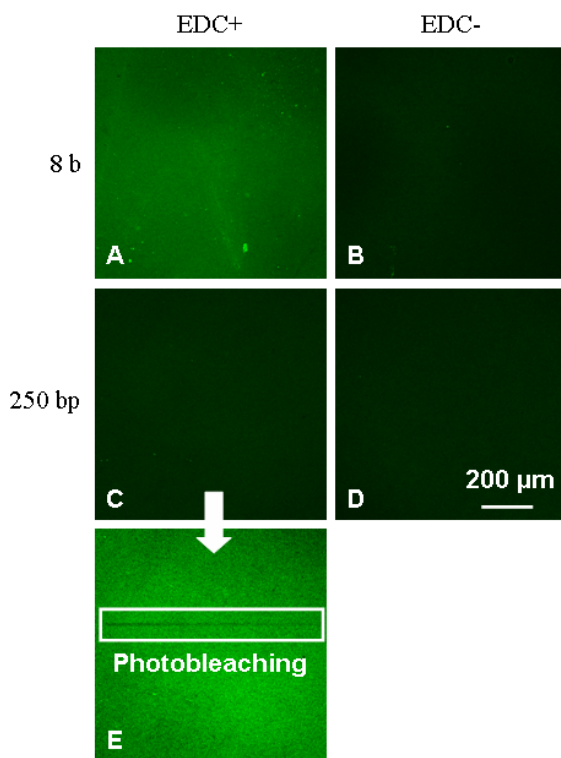


Figure 4.2: Comparison of fluorescence intensity of rho-BeSt NCD samples after covalent attachment of DNA molecules of different lengths.

- A)** Covalent attachment of ~ 60 pmol of NH_2 -modified and Alexa 488-labelled ssDNA (8 b).
- B)** Negative control sample treated with ~ 60 pmol of NH_2 -modified and Alexa 488-labelled ssDNA (8 b), but having omitted EDC in the DNA attachment procedure.
- C)** Covalent attachment of ~ 60 pmol of NH_2 -modified and Alexa 488-labelled dsDNA (250 bp).
- D)** Negative control sample treated with ~ 60 pmol of NH_2 -modified and Alexa 488-labelled dsDNA (250 bp), but having omitted EDC in the DNA attachment procedure.
- E)** The same image as in **C)**, but with a photobleached area.

In **A-D)**: laser illumination 10% and detector gain 800.

In **E)**: laser illumination 10% and detector gain 1200.

It is clear that the density of the short ssDNA probes (figure 4.2A) is much higher than that obtained with long dsDNA molecules (figure 4.2C). The negative controls in both cases showed no fluorescence (figure 4.2B and D). To verify that there was indeed some covalently attached dsDNA present in figure 4.2C, the fluorescence was bleached, and the resulting image is shown in figure 4.2E. For clarity, the latter image was collected at a higher gain. This indicates that the observations made by Steel *et al.* are also applicable to NCD-bound DNA. The 8 b ssDNA remains more upright and highly ordered as compared to the 250 bp dsDNA. The latter will obtain the conformation of flexible coils, despite the

additional straightening effect associated with a duplex [Moi06]. In this manner, the dsDNA molecules attach themselves to the diamond surface on multiple locations along their length, thereby blocking large regions of adjacent surface space. In all following experiments, short ssDNA probes of 8 and 36 b were used for the EDC-mediated covalent attachment.

4.3.1.3 Effect of probe ssDNA concentration

In order to determine the optimal ssDNA probe density on the surface of the NCD, eight rho-BeSt samples were modified with eight varying amounts of NH₂-modified Alexa 488-labelled ssDNA (8 b) (3 nmol, 300 pmol, 30 pmol, 3 pmol, 300 fmol, 30 fmol and 3 fmol) using EDC. Figure 4.3 shows the resulting fluorescence images.

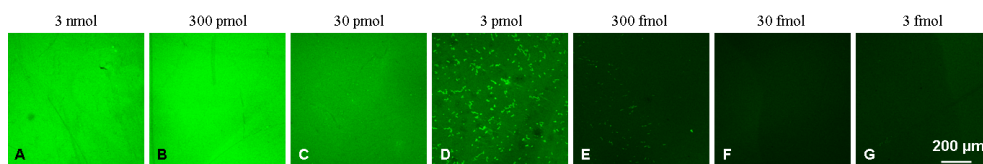


Figure 4.3: Comparison of fluorescence intensity between rho-BeSt NCD samples treated with varying amounts of NH₂-modified Alexa 488-labelled probe ssDNA. **A)** 3 nmol. **B)** 300 pmol. **C)** 30 pmol. **D)** 3 pmol. **E)** 300 fmol. **F)** 30 fmol. **G)** 3 fmol. Laser illumination 10% and detector gain 931.

The fluorescence intensity becomes weakly visible at 300 fmol and rises until a plateau is reached for the sample treated with 300 pmol, which translates into 10^{14} molecules. The plateau is not due to saturation of the detector, since a lower gain gave the same results (data not shown). This amount yields the highest ssDNA probe density on a NCD sample of $\sim 1 \text{ cm}^2$. Increasing the applied amount of DNA further has no effect on fluorescence intensity, which confirms the saturation of the NCD surface. Below 30 pmol, the homogeneity of the DNA layer becomes compromised, resulting in brightly fluorescing DNA clusters on a darker background. It should be noted that the EDC-mediated reaction does not bind 100% of the probe DNA that is offered to the NCD surface. It has been shown that the DNA is not perpendicular to the surface, but present under an angle of $\sim 45^\circ$ to the surface normal [Wen07]. This will decrease the binding

density slightly, likely resulting in the value most cited in literature, 10^{12} molecules.cm⁻².

To evaluate the dependency of the EDC-mediated attachment procedure of DNA on the origin of the NCD sample, 3 nmol and 300 pmol of NH₂-modified Alexa 488-labelled probe ssDNA were also covalently bound to IMO NCD samples. Figure 4.4 shows that the procedure yields comparable results when applied to a NCD substrate from a different source: Figure 4.4A shows a similar fluorescence intensity as figure 4.3A, and figure 4.4B is comparable to figure 4.3B. In all subsequent experiments, probe amounts of 300 pmol DNA were used, and IMO and rho-BeSt samples were employed interchangeably.

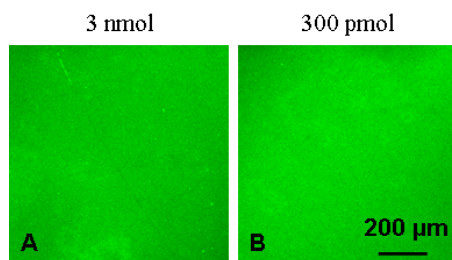


Figure 4.4: Comparison of fluorescence intensity between IMO NCD samples treated with varying amounts of NH₂-modified Alexa 488-labelled probe ssDNA. **A)** 3 nmol. **B)** 300 pmol.

Laser illumination 10% and detector gain 931.

4.3.1.4 Effect of 10-undecenoic acid (10-UDA)

To examine if the attachment method was truly proceeding through the expected formation of a peptide bond between the NH₂-group of a ssDNA molecule and the COOH-group of a 10-UDA molecule on the surface, the fluorescence intensities of H-terminated, oxidised and COOH-terminated diamond samples were compared after EDC-mediated reactions with 300 pmol of NH₂-modified Alexa 488-labelled ssDNA (8 b). H-termination of the samples was obtained inside the ASTeX[®] reactor at 700°C during 60 s at 3000 W, 35 torr and 1000 sccm H₂. Oxidation of the samples was achieved by immersing the samples in a heated H₂SO₄/KNO₃ solution, resulting in a surface covered with various oxygen-containing groups. These are mostly -OH and =O, and to a lesser extent -O- and -COOH [Wen05]. These oxidised NCD samples are

hereafter referred to as O-terminated. For each condition, a negative control was included, in which the EDC was omitted.

Figure 4.5 shows the fluorescence images of H-, COOH-, and O-terminated surfaces to investigate their suitability for functional ssDNA attachment. It is clearly visible that H-terminated diamond samples are resistant to EDC-mediated ssDNA attachment (figure 4.5A and B). O-terminated samples, however, show a significant fluorescence intensity after EDC-mediated ssDNA attachment (figure 4.5F and G). Nevertheless, when an analogous O-terminated sample was covalently modified with 300 pmol unlabelled ssDNA (36 b), and subsequently hybridised with 600 pmol Alexa 488-labelled complementary target ssDNA (29 b) under conditions that will be described in section 4.3.3, the ssDNA molecules attached during the EDC-reaction appear to be non-functional (figure 4.5H). In contrast, hybridisation of the COOH-modified sample was successful (figure 4.5E).

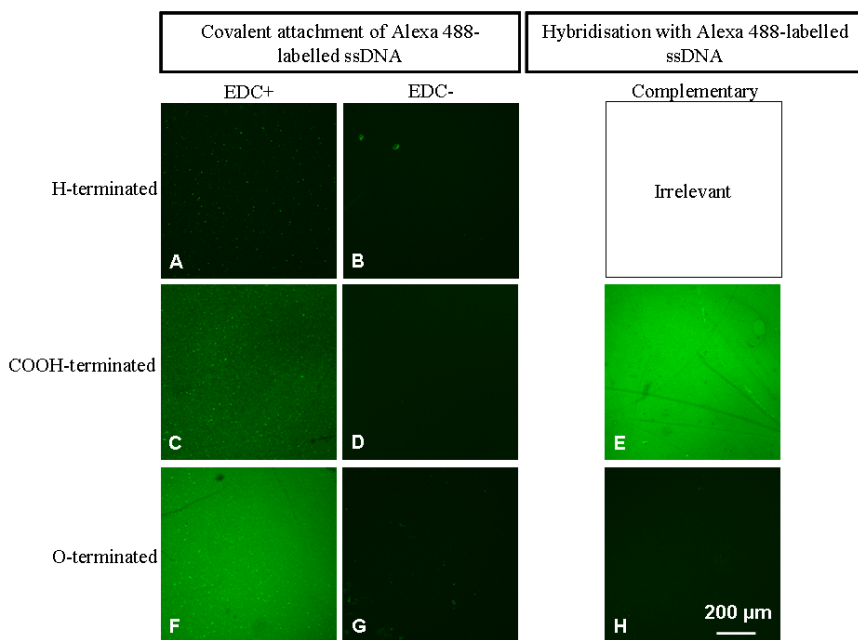


Figure 4.5: Comparison between differently functionalised diamond samples for their suitability for functional ssDNA attachment. In each condition, 300 pmol of ssDNA was used.

- A)** H-terminated sample after covalent attachment of NH₂-modified Alexa 488-labelled ssDNA (8 b).
- B)** Negative control sample treated under the same conditions as **A)**, but having omitted EDC in the DNA attachment procedure.

- C)** COOH-terminated sample after covalent attachment of NH₂-modified Alexa 488-labelled ssDNA (8 b).
- D)** Negative control sample treated under the same conditions as **C)**, but having omitted EDC in the DNA attachment procedure.
- E)** COOH-terminated sample after covalent attachment of NH₂-modified ssDNA (36 b) and hybridisation with 600 pmol of complementary Alexa 488-labelled target ssDNA (29 b).
- F)** O-terminated sample after covalent attachment of NH₂-modified and Alexa 488-labelled ssDNA (8 b).
- G)** Negative control sample treated under the same conditions as **F)**, but having omitted EDC in the DNA attachment procedure.
- H)** O-terminated sample after covalent attachment of NH₂-modified ssDNA (36 b) and hybridisation with 600 pmol of complementary Alexa 488-labelled target ssDNA (29 b).
Laser illumination 10% and detector gain 800.

These results can be explained as follows. First of all, the preferred substrate for EDC is COOH, the highest available amount being situated on the photochemically modified samples. However, DNA molecules also contain internal NH₂-groups along their length. Hence, to some extent, each EDC-reaction will also cause cross-linking of DNA into a network of intertwined strands. As previously mentioned, oxidation of the NCD samples with hot H₂SO₄/KNO₃ will also generate a small amount of COOH-groups on the surface, which can then serve as anchor points to covalently link the entangled and cross-linked DNA strands. Secondly, it is known that EDC can also catalyse esterification reactions, for instance between OH-groups on the NCD surface and the phosphate backbone of the DNA. Oxidation of the NCD surface produces a large amount of these OH-groups that can lend themselves for these esterification reactions. These two processes cause the DNA molecules to bind to the surface through multiple sites along their lengths. The result is a surface-attachment of entangled DNA molecules, making them largely unavailable for hybridisation. These side-effects of cross-linking and esterification of the DNA strands play a minor role when the amount of surface-associated COOH-groups is significantly higher, as is the case with the 10-UDA-modified NCD samples, and when the DNA is modified with a terminal NH₂-group. The ssDNA molecules will be covalently attached to these COOH-groups through their 5' NH₂-terminus, taking preference over their internal functionalities. The H-terminated diamond surface contains no COOH- or other oxygen-containing groups. Even though the cross-linking between the DNA strands probably still occurs, these clusters find no anchor points on the sample surface. Hence, they will not be covalently attached to the surface and can be washed away easily.

It is noteworthy that the fluorescence intensity of the COOH-modified sample appears higher after hybridisation than after covalent binding of ssDNA. This is the same effect as was observed by Rant *et al.*, when comparing the fluorescent intensity of Cy3-labelled ssDNA and Cy3-labelled dsDNA. Time-resolved measurements indicated that cyanine dyes exist in two distinct stereoisomers: a trans-isomer with a relatively short lifetime, and a cis-isomer with a longer lifetime. The relative contributions of these stereoisomers differed when comparing ssDNA with dsDNA. Cy3 appeared to adopt the cis-configuration with a higher probability when interacting with dsDNA, leading to a higher fluorescence quantum yield associated with this isomer [Ran07]. We believe that the observations made by Rant also apply in this case.

4.3.1.5 Patterning

Since H-termination appears to be an efficient barrier for EDC-mediated DNA attachment as compared to COOH-groups, this phenomenon can be exploited for patterning purposes. Using shadow masks during photochemical attachment of 10-UDA that obstruct the UV-light from reaching the surface in some areas, but allow the passage of UV-light in other regions, the location of the probe ssDNA can be easily controlled. This can prove to be a very useful way to array the sensor surface in the framework of high-throughput biosensor development.

A Cu TEM grid of ~ 3 mm in diameter and forming $45 \mu\text{m}^2$ open squares, separated by $20 \mu\text{m}$ wide bars, was placed on top of a diamond sample during the photochemical modification. The UV-light was only able to reach and covalently attach the 10-UDA molecules through the open squares. The subsequent NH_2 -modified Alexa 488-labelled ssDNA (8 b) attachment could therefore only occur at these same regions (figure 4.6).

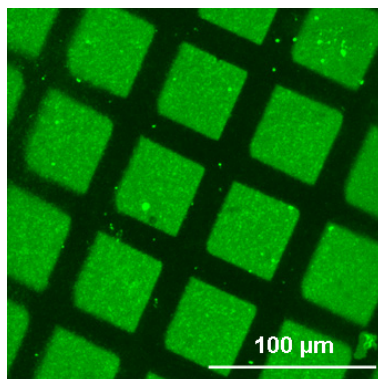


Figure 4.6: Fluorescence image of a diamond sample with covalently attached NH₂-modified and Alexa 488-labelled ssDNA (8 b) after patterning with a Cu TEM grid (~3 mm in diameter, 45 μm² open squares, 20 μm wide bars) during photochemical modification. Laser illumination 10% and detector gain 850.

This surface functionality-dependent DNA attachment efficiency is an important observation. The H-terminated regions can suffer from oxidation in several processing steps, leading to an increase in the alternative, internal, attachment of DNA probes to O-terminated regions. However, as described in the previous section, this will not lead to an increased background signal, since these probes are not functionally active.

4.3.2 Optimisation of DNA hybridisation

After the covalent attachment of short ssDNA molecules to COOH-modified NCD, the functional activity of these bound probes needed to be investigated. Different NCD samples covalently modified with 300 pmol unlabelled probe ssDNA (36 b) were hybridised at different temperatures with 600 pmol of either complementary or 1-mismatch Alexa 488-labelled target ssDNA (29 b) in MicroHyb™ hybridisation buffer. This buffer, containing BSA and aspecific DNA for blocking purposes, is used traditionally in general hybridisation experiments. After the hybridisation reaction, stringency washings at different temperatures were evaluated.

For each condition, figure 4.7 shows the relative fluorescence intensity values of the sample hybridised with complementary target ssDNA (full circles) and the sample hybridised with 1-mismatch target ssDNA (open circles). Each

fluorescence intensity value is the average intensity of an image of 512^2 pixels, corresponding to a surface of $900 \mu\text{m}^2$, and normalised to the intensity value of a fully saturated image, corresponding to 100% intensity. It can be seen that hybridisation at 80°C , followed by two stringency washings in $0.2\times$ SSC, at 75°C and at room temperature, respectively, gave the best contrast between the sample hybridised with complementary target ssDNA and the sample hybridised with 1-mismatch target ssDNA. This could be reliably reproduced. Hybridisation with complementary DNA at 80°C , followed by stringency washing at 75°C gave a mean fluorescence intensity of $98.2 \pm 0.7\%$ ($N=6$). Hybridisation with 1-mismatch DNA at 80°C , followed by stringency washing at 75°C gave a mean fluorescence intensity of $62.4 \pm 19.7\%$ ($N=3$). The probe ssDNA molecules bound to the NCD surface via EDC thus retain their biological ability to selectively recognise and hybridise their targets.

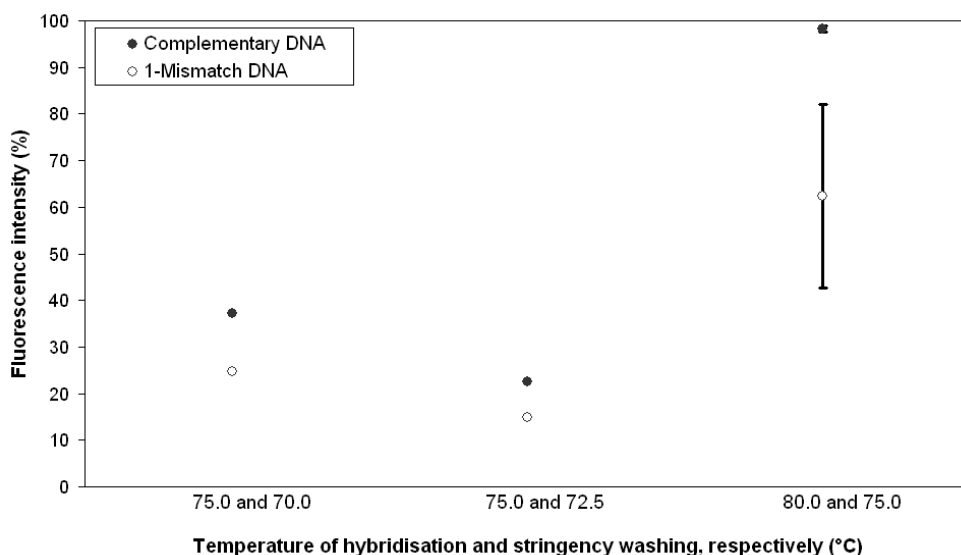


Figure 4.7: Relative fluorescence intensity values of ssDNA (36 b)-modified IMO NCD samples after hybridisation with complementary (full circles) and 1-mismatch (open circles) target ssDNA (29 b) at different hybridisation and stringency washing temperatures.

Laser illumination 10% and detector gain 800.

4.3.3 Effect of COOH/OH mixed surface functionalities

In the work of Huang *et al.*, it was demonstrated that SAMs of thiolated COOH- and OH-modified alkanes, yielding mixed functionalities on Au, enhanced the binding capacity of an antibody against prostate-specific antigen (anti-PSA) and its target recognition capability. Moreover, these mixed monolayers minimised non-specific binding by distributing the suitable functional groups over the surface while covering the remaining surface with an inert functionality [Hua05]. It was examined whether this phenomenon could be transferred to binding and hybridisation of DNA molecules on NCD. This could present a simple and easy method to 'dilute' the reactive 10-UDA molecules in order to control the ssDNA probe density on the surface.

The surfaces of ten NCD samples were photochemically modified with 5 different ratios of 10-UDA and 9-DO: 100%-0%, 80%-20%, 50%-50%, 20%-80% and 0%-100%. 300 pmol of NH₂-modified Alexa 488-labelled ssDNA (8 b) was covalently attached via EDC. For each condition, a negative control was included, in which EDC was omitted.

Figure 4.8 shows the relative fluorescence intensity values of each sample after an EDC reaction in the presence of 300 pmol of NH₂-modified and Alexa 488-labelled ssDNA (8 b), normalised to the intensity value of a fully saturated image. It appears that all of the examined combinations of 10-UDA and 9-DO yield comparable fluorescence intensities to the reproducible 100% COOH-modified surface (mean fluorescence intensity of $68 \pm 5.5\%$ for EDC+ and $9.5 \pm 1.5\%$ for EDC-, both N=3). This suggests that DNA attachment via internal esterifications becomes more important with increasing fraction of 9-DO.

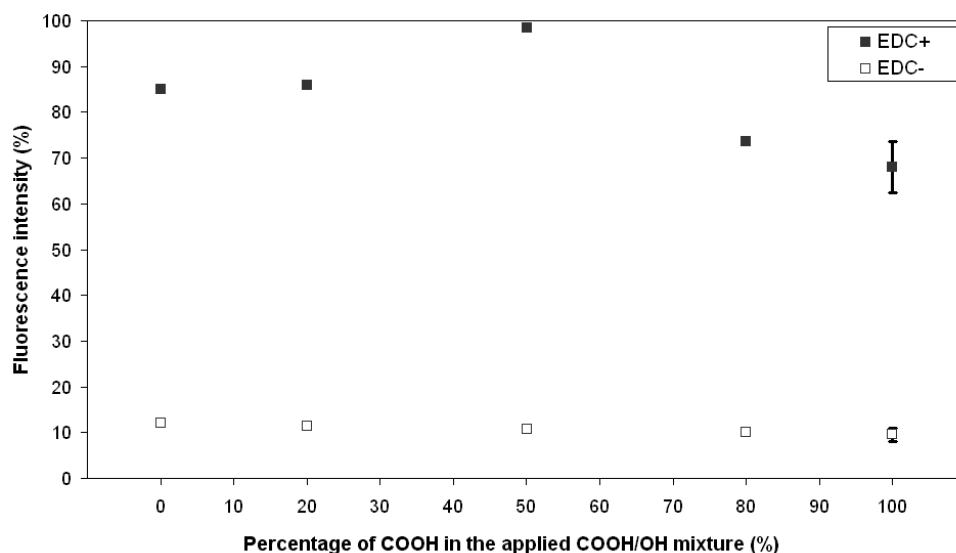


Figure 4.8: Relative fluorescence intensity values of NCD samples with different ratios of mixed COOH- and OH-functionalities after covalent attachment of 300 pmol of NH₂-modified and Alexa 488-labelled ssDNA (8 b) (full squares) and their corresponding negative controls (open squares). Laser illumination 10% and detector gain 931.

This effect can be explored by investigating the functional activity of this bound ssDNA. Ten samples analogous to the ones in figure 4.8 were produced, but with 300 pmol of unlabelled ssDNA (36 b) instead. Hybridisation occurred with 600 pmol of either Alexa 488-labelled complementary or non-complementary target ssDNA (29 b) for 2 h at 70°C, followed by two stringency washings in 0.2× SSC: at 65°C and at room temperature, respectively. The greater degree of mismatch for the non-complementary target ssDNA as compared to the 1-mismatch target ssDNA used in section 4.3.2 allowed the use of less stringent hybridisation conditions in this experiment.

Figure 4.9 shows the relative fluorescence intensity values of each sample after hybridisation. On the 0% 10-UDA sample, no functional ssDNA probes were present, in spite of the rather high fluorescence intensity after direct covalent attachment of Alexa 488-labelled ssDNA (figure 4.8). This can be explained in the same way as for the O-terminated sample (figure 4.5F, G, H). The ssDNA molecules become anchored at multiple locations along their lengths to the OH-surface groups through esterification reactions by EDC, limiting their availability

for hybridisation in comparison to the ssDNA probes that are attached to the surface through their 5' NH₂-terminus.

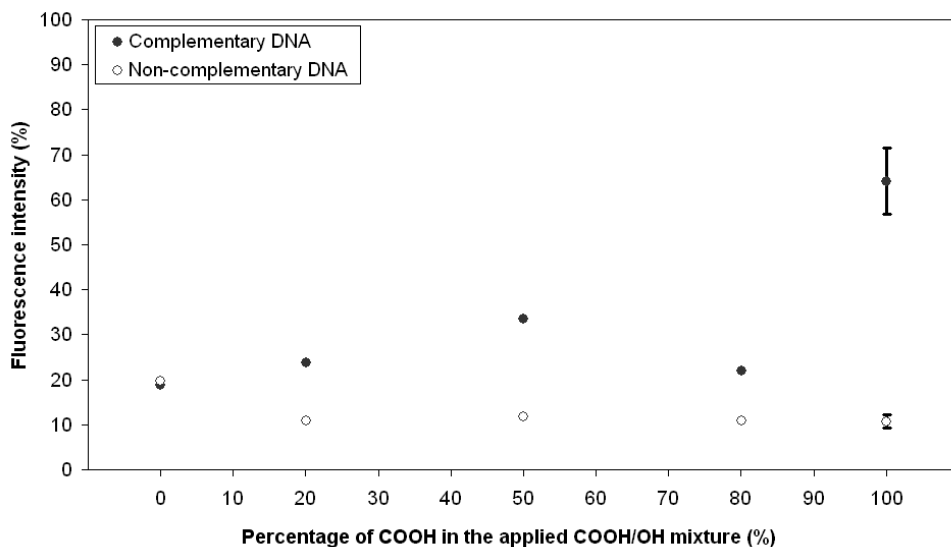


Figure 4.9: Relative fluorescence intensity values of NCD samples with different ratios of mixed COOH- and OH-functionalities after covalent attachment of 300 pmol of NH₂-modified ssDNA (36 b) and hybridisation with 600 pmol of Alexa 488-labelled complementary (full circles) and non-complementary target ssDNA (open circles) (29 b). Laser illumination 10% and detector gain 800.

The NCD samples carrying the mixed functionalities did show some hybridisation due to the presence of few functional probe ssDNA molecules attached to the dispersed COOH-functionalities in the mixed layer. However, an explanation for the low variability in hybridisation efficiency in all of these mixed samples as compared to the 100% COOH-modified sample could be that the ratio of 10-UDA/9-DO in the treatment mixture does not reflect the final ratio of COOH/OH on the NCD surface [Clar05]. Because of the shorter length, 9-DO could be preferentially attached through photochemical modification, leading to less distinct surface compositions than expected. Ultimately, the highest hybridisation efficiency was still obtained with samples modified with 100% COOH-groups. This was again a reproducible result, with a mean fluorescence intensity for the complementary hybridisation of $64.1 \pm 7.3\%$ (N=3), and a mean fluorescence intensity for the non-complementary hybridisation of $10.7 \pm 1.5\%$ (N=3).

Because of the obvious reactivity of EDC towards the surface-bound OH-moieties of 9-DO, controlling the ssDNA probe density with this alcohol is inadequate. Attempts were made to repeat this experiment using mixtures of 10-UDA and 1-UD, containing a simple methyl (CH₃)-functionality. However, the latter substance led to difficulties with the UV-illumination procedure due to its volatile nature. The 1-UD evaporated and adsorbed onto the lamp, reducing the UV output.

A much simpler way to control the surface probe density was achieved by varying the probe concentration, as shown in figure 4.3. To investigate if a decrease in surface probe ssDNA improved the hybridisation efficiency, four samples were covalently modified with 300 pmol, 30 pmol, 3 pmol and 300 fmol of NH₂-modified and unlabelled ssDNA (36 b). Next, these samples were hybridised with 600 pmol of Alexa 488-labelled complementary target ssDNA (29 b) under the conditions as described above. The results are shown in figure 4.10.

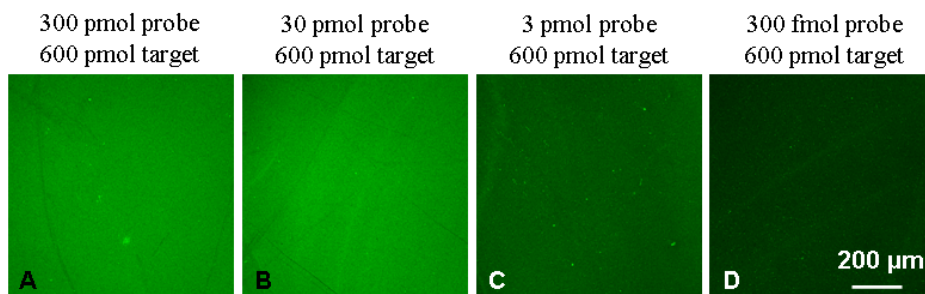


Figure 4.10: Comparison of hybridisation efficiencies on NCD samples modified with different amounts of NH₂-modified unlabelled probe ssDNA. **A)** 300 pmol. **B)** 30 pmol. **C)** 3 pmol. **D)** 300 fmol. Hybridisation occurred with 600 pmol of Alexa 488-labelled complementary target ssDNA. Laser illumination 10% and detector gain 931.

The hybridisation efficiency increases from 300 fmol, 3 pmol and 30 pmol probe ssDNA, but no strong additional improvement could be detected with 300 pmol probe ssDNA. Given that the area of a ssDNA molecule is $\sim 1 \text{ nm}^2$, the 10^{14} molecules (300 pmol) that were presented to the NCD surface during the EDC reaction yield a geometrical upper limit for the probe density on a 1 cm^2 sample. This would leave no room for hybridisation. However, since the hybridisation efficiency for this condition is significant, the final amount of probe ssDNA that was attached to the surface is lower than the amount present in the reaction

mixture. Decreasing the probe DNA concentration in the reaction solution by a factor of 10 (30 pmol or 10^{13} molecules), which resulted in a clear reduction of the eventual probe density on the surface (see figure 4.3), gave a comparable hybridisation efficiency, indicating that the same amount of probe molecules were available for hybridisation. The hybridisation efficiency for even lower probe densities was significantly reduced. We therefore postulate that the highest hybridisation efficiency would be obtained with a presented probe content of 10^{14} to 10^{13} molecules. An efficiency lower than this optimal value will be achieved with more and less probe molecules, either because of the slight steric hindrance of a too tightly packed probe layer, or because of a less than optimal probe density, respectively. However, the hybridisation efficiency obtained with a DNA probe content in the 10^{13} - $10^{14}/\text{cm}^2$ range was quite acceptable. These presented amounts will likely yield an eventual probe density on the surface close to the density value most often cited in literature: $10^{12}/\text{cm}^2$.

4.4. CONCLUSIONS

In this work, we evaluated the two-step EDC-mediated DNA-attachment method that was introduced in a previous report in terms of stability, density, and functionality of the resulting DNA probe layer. In the first step, 10-UDA is covalently bound to the NCD through a photochemical reaction with UV (254 nm), resulting in COOH-functionalised NCD. The excess 10-UDA was most efficiently removed with hot acetic acid. In the second step, NH₂-modified DNA is attached to these COOH-groups through the formation of a peptide bond. Efficient removal of non-specifically attached DNA was accomplished with 2× SSC/0.5% SDS. Short, highly organised ssDNA revealed to be more suitable for a maximal binding capacity to NCD as compared to long, dsDNA, which indicated that the results obtained by Steel *et al.* could be transferred from the Au to the NCD setting [Ste00]. The highest ssDNA probe density was obtained with an applied amount of ~300 pmol.cm⁻², correlating to a maximum of 10¹⁴ molecules.cm⁻². The thus obtained surface density was still suitable for efficient hybridisation, and a clear distinction could be made between fully complementary and 1-mismatch target DNA. It was also determined that purely COOH-terminated NCD was the most suitable substrate for the functional end-mediated attachment of NH₂-modified DNA. The DNA that was covalently attached to O-terminated NCD samples and samples carrying mixed functionalities was non-functional. The EDC-mediated DNA attachment to H-terminated NCD samples was not possible. This result can be turned into a major advantage in straightforward photopatterning reactions. Hence, in this study, we succeeded in generating a stable, dense, functionally active and patterned biological interface on NCD, which can be exploited in the fabrication of high-throughput DNA-based biosensors in array formats.

ACKNOWLEDGEMENTS

The research was performed in the framework of the project #030219 '*CVD Diamond: a novel multifunctional material for high temperature electronics, high power/high frequency electronics and bioelectronics*' funded by the Institute for the Promotion of Innovation by Science and Technology in Flanders (IWT), the IUAP VI program '*Quantum Effects in Clusters and Nanowires*', and the Scientific Research Community WOG WO.035.04N '*Hybrid Systems at Nanometer Scale*' of the Research Foundation – Flanders (FWO-Vlaanderen). M. Daenen (Assitant) and K. Haenen (Postdoctoral Fellow) are funded by the Research Foundation – Flanders (FWO-Vlaanderen). We also gratefully acknowledge tUL impulse financing and dr. W. Rasband for making ImageJ available as freeware.

Chapter 5:

Towards a real-time, label-free diamond-based DNA-sensor

Based on:

Towards a real-time, label-free diamond-based DNA sensor
Langmuir (2007); 23; 13193 – 13202.

V. Vermeeren^{a*}, N. Bijmens^{b*}, S. Wenmackers^b, M. Daenen^b, K. Haenen^{b,c}, O.A. Williams^{b,c}, M. Ameloot^a, M. vandeVen^a, P. Wagner^b, L. Michiels^a

^a Hasselt University and transnationale Universiteit Limburg, School for Life Sciences, Biomedical Research Institute, Agoralaan, Bldg. A, B-3590 Diepenbeek, Belgium

^b Hasselt University and transnationale Universiteit Limburg, School for Life Sciences, Institute for Materials Research, Wetenschapspark 1, B-3590 Diepenbeek, Belgium

^c IMEC vzw, Division IMOMECE, Wetenschapspark 1, B-3590 Diepenbeek, Belgium

* V. Vermeeren and N. Bijmens contributed equally to this publication.

ABSTRACT

Most challenging in the development of DNA-sensors is the ability to distinguish between fully complementary target ssDNA and 1-mismatch ssDNA. To deal with this problem, we performed impedance spectroscopy on DNA-functionalised NCD layers during hybridisation and denaturation. In both reactions, a difference in behaviour is observed for 1-mismatch target DNA and complementary target DNA in real-time. During real-time hybridisation, a decrease of the impedance is observed at lower frequencies when complementary target DNA is added, while the addition of 1-mismatch target ssDNA causes no significant change. Fitting these results to an electrical circuit demonstrates that this is correlated with a decrease of the depletion zone in the space-charge region of the diamond. During real-time denaturation, differentiation between 1-mismatch and complementary target DNA was possible at higher frequencies. Denaturation of complementary DNA showed the longest exponential decay time of the impedance, while the decay time during 1-mismatch denaturation was the shortest. The real-time hybridisation and denaturation experiments were carried out on different NCD samples in various buffer solutions at temperatures between 20°C and 80°C. It was revealed that the best results were obtained using Microhyb™ hybridisation buffer at 80°C and 10× PCR buffer at 30°C for hybridisation, and 0.1 M NaOH at temperatures above 40°C for denaturation. We demonstrate that the combination of real-time hybridisation spectra and real-time denaturation spectra yield important information on the type of target. This approach may allow a reliable identification of the mismatch sequence, which is the most biologically relevant.

5.1. INTRODUCTION

Detection of DNA molecules is the basis of many applications in molecular diagnostics. Mutation analysis and gene expression studies rely on the selective hybridisation of target ssDNA or RNA to complementary probe ssDNA molecules, usually immobilised on a surface. Classical methods based on this principle of DNA hybridisation are Southern [Sou75] and Northern blotting [Alw77], Denaturing Gradient Gel Electrophoresis (DGGE) [Fis79];[Bor88] and microarray-based gene analysis [Sch95]. In these cases, detection of the hybridisation event usually involves labelling of the target DNA molecules with a radioactive or fluorescent label. Combined with long reaction times (hours to days) and the need for expensive equipment, this results in an overall high cost of these techniques. Recently, methods such as SPR [Pet01] and QCM [Su04] have received increased attention. These eliminate the need for target labelling and show a high sensitivity. However, a major drawback remains the requirement of skilled and trained staff. This explains a general interest in the development of fast and low-cost DNA-based biosensors in literature [Tur95];[Don02];[Mal03];[Mor04];[Davi05].

Because of very appealing physical, optical, chemical and electrical characteristics [Fie87];[Swa93], synthetic diamond has been studied extensively as a transducer material for biosensor fabrication. Diamond has a high thermal conductivity, is transparent in a wide region of wavelengths, is chemically inert, has a wide electrochemical window and can be made electrically semiconductive by chemical doping [Koi97];[Will06]. Moreover, diamond is biocompatible [Tan95], allowing *in vivo* applications. The electrical properties of diamond have been exploited in the construction of diamond-based FETs using technologies that are compatible with lithographic methods [Ban02];[Rez02]. Chemical [Ush02], photochemical [Yan02];[Här04] and electrochemical [Uet07];[Wa04] methods have been developed to covalently immobilise biomolecules to a diamond surface, forming linkages that are more stable than those with other commonly used semiconductors, such as Si [Yan02].

In this work we will construct a NCD-based DNA-biosensor with an electronic detection of real-time hybridisation and denaturation events using impedance

spectroscopy. Using the protocol we recently introduced, ssDNA will be attached to NCD [Chr06] (see Chapter 3). Only two surface-chemical steps are required to covalently bind NH₂-modified DNA to COOH-modified NCD films using EDC. This DNA-NCD construct will be employed in an impedimetric setup. The electronic properties of the NCD surface interface are expected to change during hybridisation and denaturation, mainly due to the charge of the target DNA molecules inducing a field-effect in the semiconductor substrate [Mem00]. Several field-effect based biosensor setups have been reported in literature using different kinds of semiconducting substrates [Sout97];[Fri02];[Usl04], including diamond [Yan04]. The results depend sensitively on the details of the experimental setup, as reviewed by Poghossian *et al.* [Pog05]. Several specific factors have been identified that jeopardise a reproducible and sensitive field-effect based DNA-sensor: (a) the drift of the measured signal, (b) the variable distance of the DNA molecules from the surface due to the attachment via long linker molecules, and (c) the effect of counter-ions screening the DNA charge-effect [Schö06];[Ing06]. The latter problem can be avoided by measuring in a low-ionic buffer [Ing06];[Ing07]. However, hybridisation requires cations in the buffer so that only endpoint measurements can be performed using low-ionic buffers. In this work, we investigate the possibility of real-time impedimetric detection of both DNA hybridisation as well as denaturation. Moreover, the ability to discriminate between complementary target DNA, non-complementary target DNA and 1-mismatch target DNA using this real-time impedance spectroscopy will be studied. The experiments will be performed on IMO NCD and commercially available NCD samples in different buffer solutions and at different temperatures.

5.2. MATERIALS AND METHODS

5.2.1 Materials

The probe ssDNA molecules were purchased from Eurogentec (Seraing, Belgium), and were modified at the 5' end with a NH₂-modifier (36 b: 5'-NH₂-C₆H₁₂-AAA-AAA-ACC-CCT-GCA-GCC-CAT-GTA-TAC-CCC-CGA-ACC-3'). The target ssDNA molecules bought from Invitrogen (Merelbeke, Belgium), were modified at the 5' end with an Alexa Fluor® 488 label, allowing to monitor hybridisation and denaturation using confocal fluorescence microscopy. Target ssDNA contains a sequence that is either completely complementary to the probe ssDNA (29 b: 5'-Alexa 488-C₆H₁₂-GGT-TCG-GGG-GTA-TAC-ATG-GGC-TGC-AGG-GG-3'), carries a 1-base mismatch to the probe ssDNA (29 b: 5'-Alexa 488-C₆H₁₂-GGT-TCG-GGG-GTA-TAC-ATG-GGC-TCC-AGG-GG-3'), or is completely non-complementary (29 b: 5'-Alexa 488-C₆H₁₂-TCA-AAT-TGC-CAG-AAC-AAC-TAC-TGA-CTG-AA-3').

5.2.2 NCD functionalisation

SEM images of the IMO and the rho-BeSt NCD samples are shown in figure 5.1.

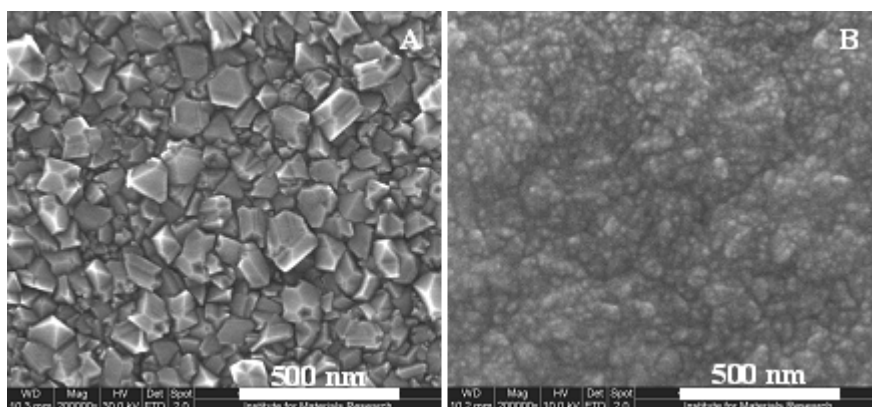


Figure 5.1: SEM images of a **A**) IMO and a **B**) rho-BeSt NCD sample. The white scale bar indicates 500 nm.

300 pmol of probe ssDNA was covalently immobilised onto the NCD according to the procedure described in Christiaens *et al.* [Chr06] (see Chapter 3). Hereby, 10-UDA was first photochemically attached to H-terminated NCD. In a second step, NH₂-modified ssDNA was covalently linked to the COOH-group of this 10-UDA using an EDC-mediated coupling.

5.2.3 Sensor setup

The NCD sample, functioning as a working electrode, was mounted on an aluminium (Al) back contact using Ag paste. A rubber O-ring with a diameter of 7 mm and a Teflon lid containing a circular opening of equal size were pressed onto the sample to create a reaction well above the NCD. The well was filled with 100 to 200 µl of reaction fluid. A Au wire, placed ~1 mm above the NCD surface in contact with the reaction fluid, was used as a counter electrode. Working and counter electrode were connected to the impedance analyser with shielded cables. The reported sequential measurements were performed with this type of reaction well.

In order to measure the hybridisation and denaturation of two different DNA targets simultaneously and under identical conditions, a double-cell sensor setup was constructed. In this case, an NCD sample of twice the size of that for the sequential measurements described above, was mounted onto a Cu plate (figure 5.2). Two rubber O-rings, each with a diameter of 6 mm, and a Teflon lid containing two circular holes of equal size created two reaction wells above the NCD. Two Au wires, one for each reaction well, were placed in contact with the reaction fluid. Hence, two signals were recorded simultaneously, using one common working electrode, but different counter electrodes.

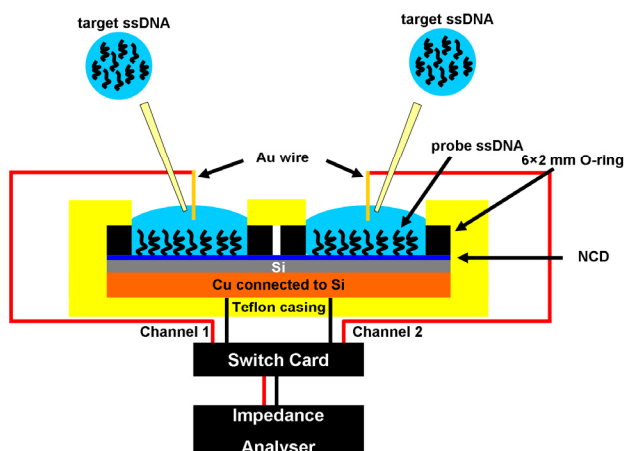


Figure 5.2: Schematic representation of the double-cell setup for the simultaneous measurements. A single-cell setup of comparable construction was also used for the sequential measurements.

5.2.4 Impedance spectroscopy

Real-time impedance curves were recorded continuously during stabilisation, hybridisation and denaturation on a ssDNA-modified NCD sample mounted into the above described setups. They were collected using two different measurement protocols. In a first protocol, DNA hybridisation and denaturation experiments were performed inside the measurement setup. Both setups were first filled with buffer, and the device was allowed to stabilise until no further change in Z was detected throughout the entire frequency range. For hybridisation, 600 pmol of either complementary, 1-mismatch or non-complementary target ssDNA was added to the buffer, and allowed to react for 1 h. After this hybridisation reaction, the wells were rinsed and refilled with buffer and the signal was allowed to stabilise for at least 10 minutes before denaturation. The DNA strands were denatured by filling the wells with 100 μ l of 0.1 M NaOH. This was done twice, for 10 minutes each. Finally, the device was again stabilised with buffer.

The influence of parameters such as buffer composition and temperature on Z was also investigated. Experiments were performed using MicroHyb™ hybridisation buffer at 80°C and 60°C, 1× PBS buffer at 60 and 40°C and 10×

PCR buffer at room temperature. The sensor setup was put in a humidity-controlled hybridisation oven, which also resulted in electromagnetic shielding.

In a second protocol, real-time impedance curves were recorded during denaturation of NCD samples that were previously exposed to one of the three different ssDNA targets outside of the measurement setup. In this case, hybridisation occurred for 2 h in a hybridisation oven at 80°C. The samples were then rinsed for 30 minutes with 2× SSC buffer containing 0.5% SDS at room temperature and subsequently with 0.2× SSC buffer, first at 75°C for 5 minutes, then at room temperature for 5 minutes.

5.3. RESULTS

5.3.1 Impedance changes during hybridisation

5.3.1.1 Sequential measurements in a single-cell setup

For the sequential measurements, IMO NCD samples were used. Figure 5.3A shows a Bode plot of a sequential measurement. The sample was hybridised at 80°C using 600 pmol complementary target DNA in MicroHyb™ hybridisation buffer. As a selectivity control, the sample was hybridised with 600 pmol 1-mismatch target DNA in a subsequent experiment. The curves show the impedance in the total frequency range at the moment of target DNA addition to the buffer (solid lines), and after 40 minutes of hybridisation. While the 1-mismatch DNA curve shows a small increase (dashed line), the complementary DNA curve has decreased with more than 20% in the low frequency region (100 Hz – 1500 Hz) (dotted line). This decrease was most pronounced at around 1000 Hz. In figure 5.3B, the real and the imaginary part of the impedance at the previously mentioned reaction stages are represented in a Nyquist plot. It can be observed that the largest effect occurs during complementary hybridisation.

Figure 5.3C shows the real-time impedance curves at 1150 Hz for both kinds of target DNA. The impedance has been normalised to the value immediately after target DNA addition to the buffer. The complementary DNA curve (dotted line) shows a decrease of 25% after 40 minutes, while the impedance of the 1-mismatch DNA (solid line) remains stable within 5%.

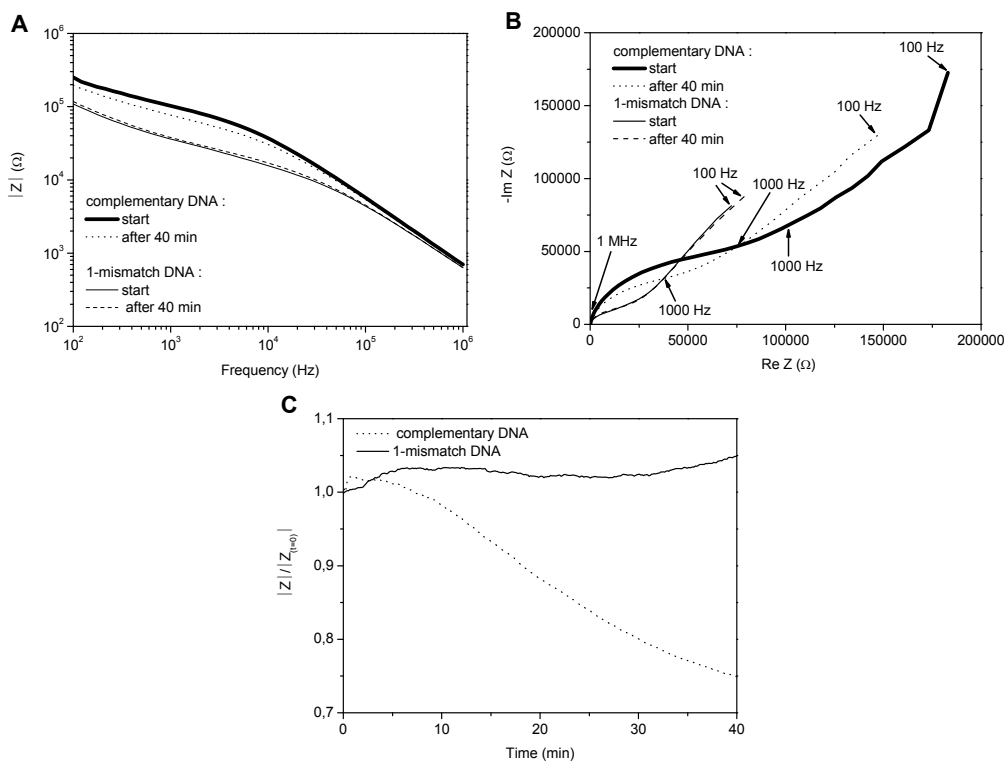


Figure 5.3: Sequential impedance measurement of a hybridisation reaction with complementary and 1-mismatch target DNA. **A)** Bode plot showing the impedance in the total frequency range immediately after complementary and 1-mismatch target DNA addition to MicroHyb™ hybridisation buffer, and after 40 minutes of hybridisation. **B)** Nyquist plot showing the real and imaginary part of the impedance immediately after complementary and 1-mismatch target DNA addition to MicroHyb™ hybridisation buffer, and after 40 minutes of hybridisation. **C)** Real-time hybridisation curves at 1150 Hz. The modulus of Z is normalised to the value immediately after adding the target DNA.

5.3.1.2 Simultaneous measurements in a double-cell setup

Simultaneous measurements were performed in the double-cell setup (see figure 5.2), using NCD samples from rho-BeSt. In this setup, complementary and 1-mismatch DNA were each added simultaneously to two different reaction wells on one NCD sample during hybridisation. Subsequently, the sample was denatured by adding 0.1 M NaOH in both measurement cells. In order to prove the robustness of the results and the reusability of the sensor, a second round was performed, where both kinds of target DNA were swapped. Figure 5.4A shows the Bode plot of round one at the start of the hybridisation and after 40

minutes. In agreement with the sequential measurements, the complementary DNA curve has decreased with more than 10% (dotted line), while the 1-mismatch DNA curve has hardly changed at all (dashed line). This can also be observed in the Nyquist plot, shown in figure 5.4B. The semi-circle becomes significantly smaller during complementary hybridisation only.

Figure 5.4C gives the real-time hybridisation curves of round one at 1150 Hz. A decrease of more than 10% was observed during complementary hybridisation, while the 1-mismatch DNA had no effect on the impedance. The second reaction round was comparable, showing a decrease of 6% during complementary hybridisation (data not shown). This experiment was performed at 30°C and 10× PCR buffer was used.

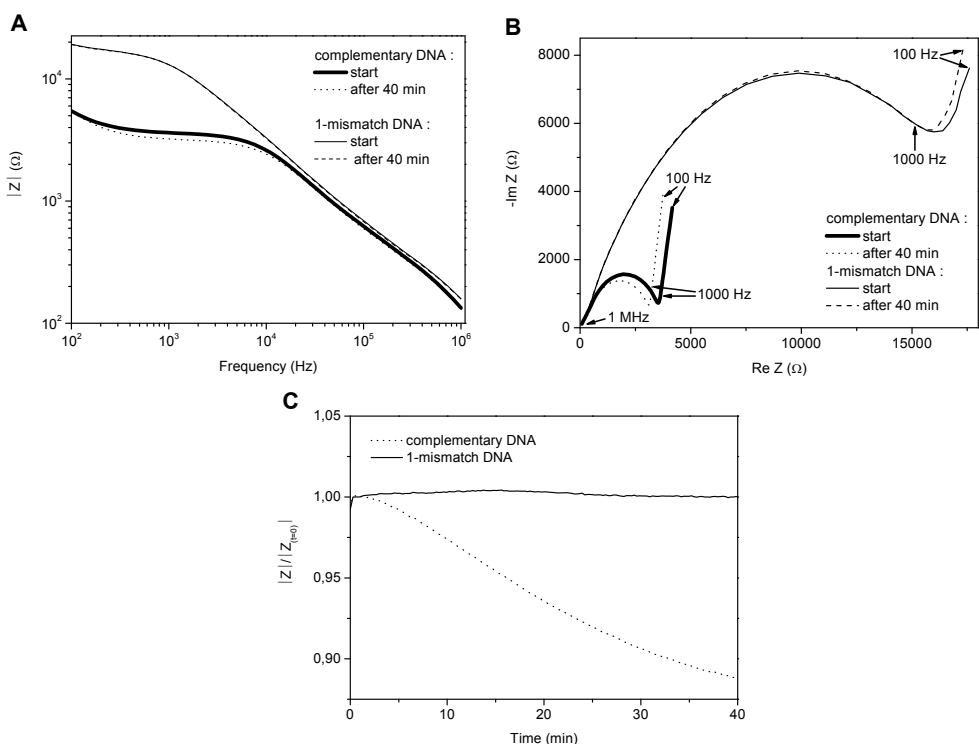


Figure 5.4: Simultaneous impedance measurement of a hybridisation reaction with complementary and 1-mismatch target DNA. **A)** Bode plot of round one showing the impedance in the total frequency range immediately after complementary and 1-mismatch target DNA addition to 10× PCR buffer, and after 40 minutes of hybridisation.

Complementary target DNA was added to one reaction well and 1-mismatch target DNA was added to the other reaction well on the same sample. **B)** Nyquist plot showing the real and imaginary part of the impedance immediately after complementary and 1-mismatch target DNA addition to 10× PCR buffer, and after 40 minutes of hybridisation. **C)** Real-time hybridisation curves at 1150 Hz. The modulus of Z is normalised to the value immediately after adding the target DNA.

5.3.1.3 Effect of buffer composition and temperature

The presence of a sufficient amount of salt in the hybridisation buffer appeared crucial in order to obtain clear real-time hybridisation curves. Hybridisation in 1× PBS buffer was unsuccessful, while the separation between the complementary and 1-mismatch hybridisation curves was very clear and reproducible when using either 10× PCR buffer at 30°C or MicroHyb™ hybridisation buffer at 80°C. Under these conditions, after 40 minutes, the impedance decreased with 5 – 30% with respect to the starting value of the complementary DNA, while the effect of 1-mismatch DNA was negligible.

5.3.2 Impedance changes during denaturation

Before denaturation, the cell was rinsed and refilled with the same buffer used for the hybridisation. When a stable signal was obtained, the DNA was denatured by filling the cell with 100 µl of 0.1 M NaOH.

5.3.2.1 Sequential measurements in a single-cell setup

For the sequential measurements, Bode plots are shown for complementary DNA (figure 5.5A) and for non-complementary DNA (figure 5.5C). The corresponding Nyquist plots are shown in figure 5.5B and 5.5D, respectively. The preceding hybridisation step was performed at 80°C using MicroHyb™ hybridisation buffer inside the measurement cell. When the cell is filled with 0.1 M NaOH during denaturation (also at 80°C), this is immediately visible in the impedimetric signal at higher frequencies (dashed line). After 20 minutes of denaturation, the signal has increased with more than 50% over the total frequency range (dotted line). After rinsing and refilling the cell with the MicroHyb™ hybridisation buffer, the signal immediately returns to the starting value at higher frequencies (thin solid line). At lower frequencies (100 Hz – 1500 Hz) a difference can be observed between complementary DNA (figure 5.5A) and non-complementary DNA (figure 5.5C). While for non-complementary DNA the signal shows a small increase of ~5% relative to the starting value (figure

5.5C), the signal for complementary DNA (figure 5.5A) has increased with $\sim 30\%$. This is also noticed in the Nyquist plots, where the semi-circle becomes much larger after denaturation of the complementary DNA (figure 5.5B) than after the addition of NaOH to the sample that was previously treated with non-complementary DNA (figure 5.5D). This increase, observed after denaturation, is opposite to the decreasing behaviour observed during hybridisation.

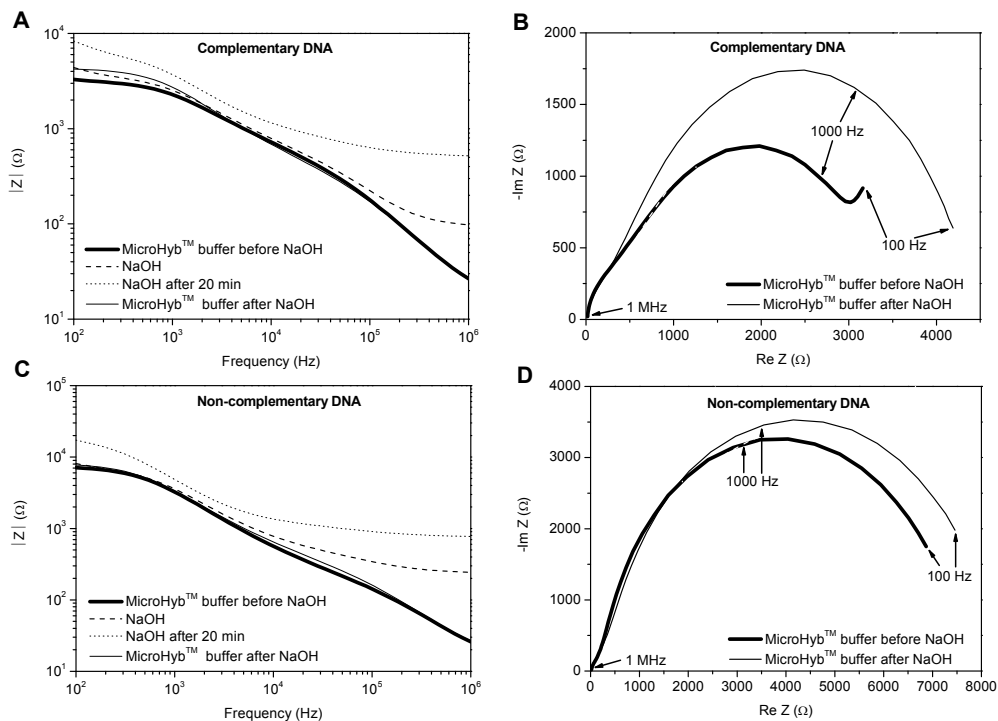


Figure 5.5: Sequential impedance measurement of a denaturation reaction of complementary and non-complementary DNA. **A)** Bode plot showing the impedance in the total frequency range after hybridisation in MicroHyb™ buffer, immediately after filling the cell with NaOH, after 20 minutes of denaturation in NaOH and after rinsing and refilling the cell with MicroHyb™ buffer for the sample previously hybridised with complementary DNA and **C)** for the sample previously treated with non-complementary DNA. The corresponding Nyquist plots are shown in **B)** for the complementary case and in **D)** for the non-complementary case.

The most significant changes in the impedance were observed in real-time during the first 10 minutes of denaturation, at the lowest frequencies (100 Hz – 500 Hz) as well as at the highest frequency (1 MHz). Figure 5.6 shows results that were obtained during denaturation at 60°C after previous hybridisation of the NCD samples at 80°C outside the measurement cell. The signal was first allowed to stabilise in 1× PBS. Then, the cell was filled with 100 μl 0.1 M NaOH.

Figure 5.6A shows real-time denaturation curves at 100 Hz that were recorded after previous hybridisation with either complementary (open squares), 1-mismatch (open dots) or non-complementary (open triangles) target DNA. The impedance has been normalised to the value at the moment of NaOH addition. The non-complementary DNA curve shows the strongest effect upon NaOH addition. After 10 minutes in NaOH, the signal has increased with more than 40%. The smallest impedance increase occurs with the samples previously hybridised with 1-mismatch DNA (less than 10%). The complementary DNA curve always showed the slowest rise. These were typical trends in all experiments, indicating a high reproducibility. In figure 5.6B, the impedance at the highest frequency (1 MHz) is depicted. Again, the impedance has been normalised to the value at the moment of NaOH addition. The curves reveal a decay in the first minutes of denaturation. These decay curves could be fitted to an exponential decay as indicated by the solid lines. This resulted in a decay time of 1.49 ± 0.03 minutes for the complementary curve and a much shorter decay time of 0.49 ± 0.02 minutes for the 1-mismatch DNA curve. For the non-complementary DNA curve, when starting with the fourth data point, a good exponential decay fit could also be obtained, revealing a decay time of 1.37 ± 0.03 minutes.

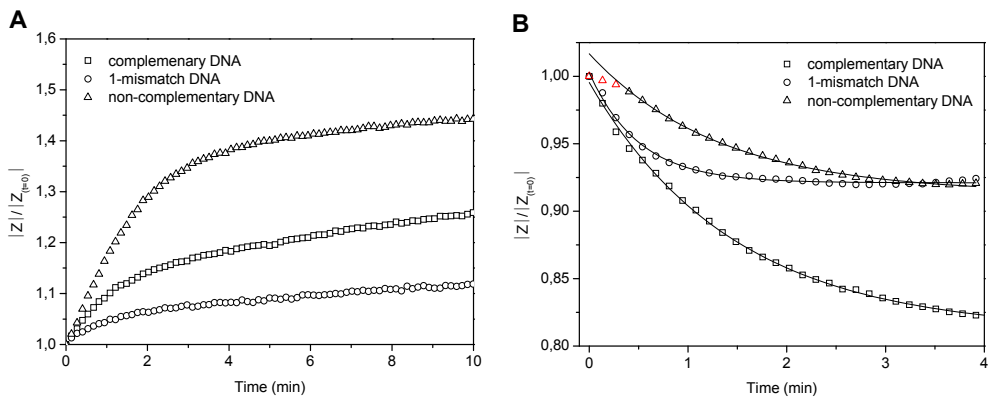
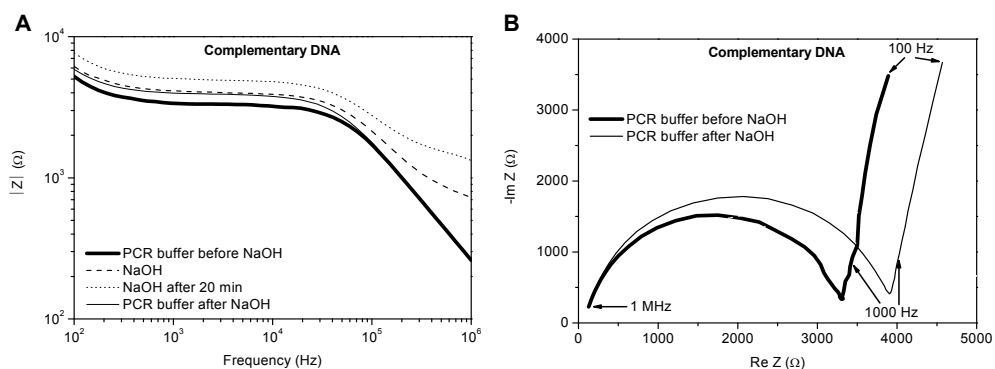


Figure 5.6: Real-time denaturation curves at **A)** 100 Hz and **B)** at 1 MHz for complementary, 1-mismatch or non-complementary target DNA. The modulus of Z is normalised to the value immediately after NaOH addition. The solid lines in **B)** indicate fits using an exponential decay [$y = A_1 \times \exp(-x/t_1) + y_0$].

5.3.2.2 Simultaneous measurements in a double-cell setup

Similar denaturation results were obtained using the rho-BeSt samples in the double-cell setup. After a preceding hybridisation at 30°C in 10× PCR buffer inside the measurement cell, the oven was heated to 50°C for a thorough denaturation. Bode plots are given in figure 5.7 where the sample in one cell was previously hybridised with complementary DNA (figure 5.7A) and the sample in the other cell was previously hybridised with 1-mismatch DNA (figure 5.7C). In the low frequency region, the effect of NaOH (dashed line) is much larger in figure 5.7A than in figure 5.7C. After 20 minutes in NaOH (dotted line), the signal has increased for 50% in the complementary case, as compared to 10% for the 1-mismatch target DNA. After rinsing and refilling the cell with PCR buffer (thin solid line), the signal in figure 5.7C almost returns to its starting value, while in figure 5.7A the signal in the low frequency region shows an increase of ~18%. This can also be observed from the corresponding Nyquist plots. The semi-circle becomes much larger after denaturation of the complementary DNA (figure 5.7B) than after denaturation of the 1-mismatch DNA (figure 5.7D). Switching the target DNA yields a similar contrast between 1-mismatch and complementary DNA curves at 100 Hz and 1 MHz (data not shown).



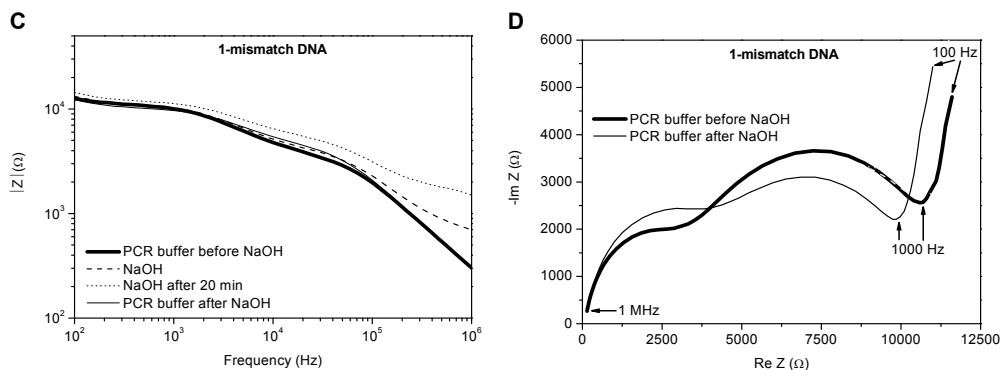


Figure 5.7: Simultaneous impedance measurement of a denaturation reaction of complementary and 1-mismatch DNA. **A)** Bode plot showing the impedance in the total frequency range after hybridisation in 10× PCR buffer, immediately after filling the cell with NaOH, after 20 minutes of denaturation in NaOH and after rinsing and refilling the cell with 10× PCR buffer, for the sample previously hybridised with complementary DNA and **C)** for the sample previously treated with 1-mismatch target DNA. The corresponding Nyquist plots are shown in **B)** for the complementary case and in **D)** for the non-complementary case.

5.3.2.3 Effects of temperature

The presented denaturation effects were no longer visible when the denaturation was performed at temperatures lower than 40°C (data not shown). Denaturing in 0.1 M NaOH at different temperatures above 40°C gave consistent results regarding the impedance change at 1 MHz. Table 5.1 summarises the exponential decay time of the impedance obtained using different NCD samples (IMO or rho-BeSt) that were previously hybridised at temperatures ranging from 20°C to 80°C in different hybridisation buffer solutions. The denaturation of the complementary DNA consistently showed the longest exponential decay time. In comparison, the denaturation of 1-mismatch DNA showed exponential decay times that reach only 41 – 61% of that of the complementary denaturation curve. The denaturation of non-complementary DNA showed an exponential decay of 66 – 76% of that of the complementary denaturation curve.

Table 5.1: Exponential decay time during the first minutes of denaturation, summarised according to hybridisation and denaturation parameters.

Sample source	Hybridisation temperature (°C)	Hybridisation buffer	Denaturation temperature (°C)	Exponential decay time (min)		
				Complementary DNA	1-mismatch DNA	Non-complementary DNA
Homemade	80	MicroHyb™	80	2.13 ± 0.02 [†]		1.40 ± 0.04
Homemade	60	MicroHyb™	60	2.65 ± 0.04		2.02 ± 0.09
Homemade	40	1× PBS	40	1.28 ± 0.09		0.84 ± 0.02
rho-BeSt	20	10× PCR	50	0.97 ± 0.02	0.40 ± 0.02	
rho-BeSt	30	10× PCR	50	4.64 ± 0.09	2.66 ± 0.07	
rho-BeSt	25	10× PCR	70	1.55 ± 0.02	0.96 ± 0.05	
Homemade*	80*	MicroHyb™*	60*	1.49 ± 0.03*	0.49 ± 0.02*	1.37 ± 0.03*

*hybridisation occurred outside of the measurement cell

[†]reported uncertainties are standard deviations as obtained from the data fits

5.4. DISCUSSION

5.4.1 Hybridisation

In this work, we report the real-time electronic detection of hybridisation using impedance spectroscopy. We are able to discriminate clearly between the hybridisation with complementary and 1-mismatch DNA, even within the first 5 minutes after target DNA addition, demonstrating SNP sensitivity. Furthermore, blocking reagents to prevent non-specific adsorption of DNA to the NCD surface [Ing07], are not required in our approach.

As expected, the buffer composition plays an important role in the electronic detection of hybridisation. MicroHyb™ hybridisation buffer at 80°C and 10× PCR buffer at 30°C, containing the highest concentration of ions, were the most suitable for hybridisation. Despite their high ionic strength, which can lead to an increase of the counter-ion screening effect [Pog05];[Ing06], it was possible to measure real-time hybridisation using impedance spectroscopy. The highest sensitivity, i.e. the largest discrepancy between the complementary and the 1-mismatch ssDNA, was observed in the 1000 Hz – 1500 Hz frequency region. Hybridisation with 1× PBS buffer was unsuccessful. Its low ionic content did not favour hybridisation. The suitability of 10× PCR buffer as a hybridisation buffer has an important advantage over MicroHyb™. Because it is the same buffer that is used for PCR reactions, it facilitates the lab-on-a-chip integration of DNA-extraction, PCR and real-time hybridisation. Keeping in mind the need for easy operation and possible point-of-care application, hybridisation in 10× PCR buffer at room temperature is to be preferred as a standard procedure.

In order to get more insight in the effect of charged DNA molecules on the electrical properties of the semiconducting layer, the impedance spectra were analysed using equivalent circuit models. This was done using the ZSimpWin software from Princeton Applied Research (Massachusetts, USA). The fits were performed over the total frequency range from 100 Hz to 1 MHz. The data were fitted according to the circuit given in figure 5.8 ($\chi^2 \sim 10^{-4}$).

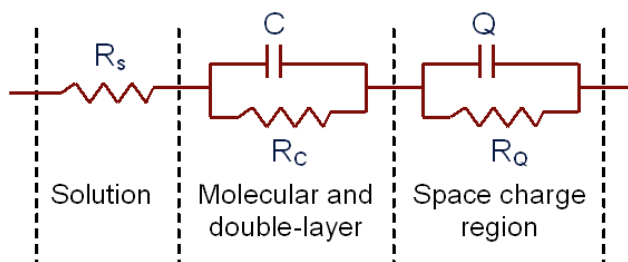


Figure 5.8: The electrical circuit model used for fitting the impedance data.

This circuit has previously been proposed by Yang *et al.* to explain the hybridisation-induced changes in electrical properties of DNA-modified diamond surfaces [Yan04]. It can be divided into three components: (a) the solution resistance R_s , between the Au electrode and the NCD surface, (b) a resistance R_c and a capacitor C in parallel, attributed to the molecular layer and double-layer, and (c) a resistance R_Q and a constant phase element Q in parallel, physically corresponding to the space-charge region in the diamond substrate [Yan04]. The impedance of the Q element is defined by $Z = [Q(i\omega)^n]^{-1}$. For our data, n varied between 0.6 and 1. A value of $n = 1$ is equivalent to the 'perfect' capacitor. Lower values of n have been attributed to depth-dependent variations in the charge carrier concentration [Kon03]. A value of $n = 0.5$ corresponds with the Warburg impedance [Gri00].

In figure 5.9, the real and the imaginary part of the complex impedance before (full squares) and after (open squares) hybridisation with complementary DNA in 10× PCR buffer at 30°C, are represented in a Nyquist plot. The fits of these data to the given electrical circuit are indicated by solid lines. It can be seen that the decrease of the impedance during hybridisation at lower frequency values corresponds with a reduction of the typical semi-circle.

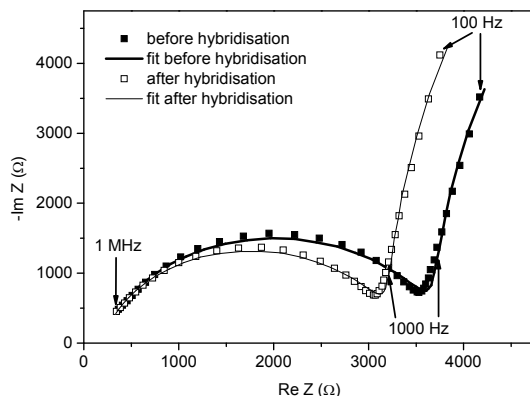


Figure 5.9: Nyquist plot of the complex impedance before and after hybridisation with complementary target DNA in 10× PCR buffer. Fits to the equivalent circuit are indicated with solid lines.

Table 5.2 gives the values of the electrical elements after fitting these data to the electrical circuit. Uncertainties on the parameter estimates are given in terms of their standard deviation, σ . The value of the elements R_s , R_C , Q and n do not change significantly upon hybridisation given the uncertainty on the recovered values. A smaller semi-circle upon hybridisation results from a decrease of R_Q from $\sim 3500 \Omega$ to $\sim 3000 \Omega$. The capacity C decreases with 15%. Combining the fit results and the Nyquist plots reveals that the impedance at the lowest frequencies (100 Hz – 500 Hz) is determined by the $R_C C$ element. These data points form the start of a second semi-circle at frequencies lower than 100 Hz. At the highest frequency (1 MHz), mainly the resistance of the solution, R_s , determines the impedance. This becomes obvious when changing the reaction fluid from MicroHyb™ hybridisation buffer to NaOH and vice versa (figure 5.5A and C).

Table 5.2: Results of fitting the impedance spectra before and after hybridisation with complementary DNA at 30°C in 10× PCR buffer

Element	Before hybridisation	After hybridisation
R_s (Ω)	$222 \pm 14^*$	205 ± 12
C (nF)	436 ± 10	369 ± 6
R_C (k Ω)	26 ± 6	30 ± 5
Q (nS.s ⁿ)	14.4 ± 1.5	13.6 ± 1.0
n	0.888 ± 0.009	0.896 ± 0.008
R_Q (k Ω)	3.49 ± 0.04	3.02 ± 0.03

*reported uncertainties are standard deviations as obtained from the data fits

The samples used during the low-temperature (20°C – 30°C) hybridisation experiments, were heated for denaturation at 50°C or 70°C. The change of the impedance during heating has been used to get more insight in the physical relevance of the fitted circuit elements. In figure 5.10, the real and the imaginary part of the complex impedance before and after heating the total setup from 30 to 50°C are represented in a Nyquist plot. The cell was filled with 10× PCR buffer. The fits of these data to the electrical circuit are indicated by solid lines. It can be seen that the semi-circle at higher frequencies (1000 Hz – 1500 Hz) has become much smaller.

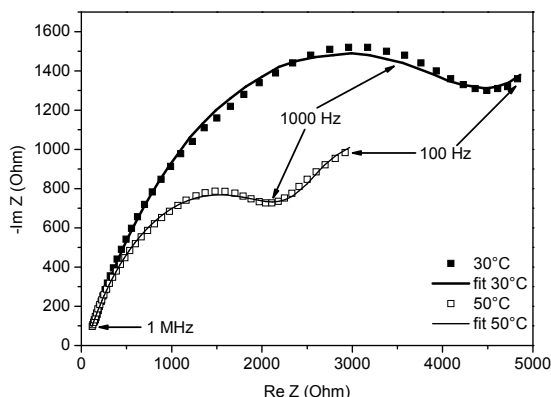


Figure 5.10: Nyquist plot of the complex impedance before and after heating the setup from 30°C to 50°C in 10× PCR buffer. Fits to the equivalent circuit are indicated with solid lines.

The results of fitting these data to the equivalent circuit are given in table 5.3. These results reveal that the semi-circle corresponds with the R_Q element of the circuit. The value R_Q decreases with more than 50% upon heating the sample (from 5300 Ω to 2600 Ω). The Q value shows an increase of 18%. The observed decreasing R_Q value and increasing Q value can be rationalised in terms of the depletion zone in the space-charge region of a semiconductor during heating. This depletion zone is a result of the exchange of charges at a semiconductor-solution interface. For a p-type semiconductor, when equilibrium is reached, the resulting electric field at the interface corresponds to a downward band bending of the conduction and the valence band [Mem00]. Heating the semiconductor will increase the amount of charge carriers, resulting in a smaller depletion zone, and thus in a lower resistance R_Q , and a higher Q

value. The fit results indicate that the resistance of the $R_C C$ element, R_C , is the largest and determines the impedance in the low frequency range (100 Hz – 500 Hz). In the literature, the largest resistance in the circuit has been attributed to the layer of molecules and ions at the surface [UsI04]. This resistance R_C as well as its parallel capacity C , show a decrease of $\sim 35\%$ upon heating the sample.

Table 5.3: Results of fitting the impedance spectra before and after heating the setup from 30°C to 50°C in 10× PCR buffer

Element	Before heating	After heating
R_s (Ω)	$59 \pm 3^*$	51.3 ± 1.7
C (μF)	2.2 ± 0.3	1.48 ± 0.06
R_C ($k\Omega$)	2.8 ± 1.3	1.7 ± 0.1
Q ($nS.s^n$)	670 ± 30	786 ± 3
n	0.630 ± 0.004	0.639 ± 0.003
R_Q ($k\Omega$)	5.28 ± 0.08	2.62 ± 0.03

*reported uncertainties are standard deviations as obtained from the data fits

From the previous discussion, it can be concluded that the $R_Q Q$ element, responsible for the decrease of the impedance at higher frequencies (1000 Hz – 1500 Hz) during hybridisation, can be attributed to the depletion zone in the diamond substrate, confirming the results obtained by Yang *et al.* and Gu *et al.* [Yan04];[Gu05]. It should be remarked that any field-effect in the heavily doped Si substrate will be negligible, because of its nearly metallic behaviour. During hybridisation, the amount of negative charges near the diamond surface will increase and will reduce the electric field at the interface. As a result, the band bending will be less pronounced and the depletion zone will be smaller for samples with dsDNA, as illustrated in figure 5.11. This will result in a decrease of the resistance R_Q (in this case from $3490 \pm 40 \Omega$ to $3020 \pm 30 \Omega$) and possibly in a higher Q value. From the fitted Q values in table 5.2 and 5.3 and using a dielectric constant of 5 for diamond, widths of the depletion zones between 3 and 125 nm can be deduced, in agreement with values found in literature [Koid04];[Mai01].

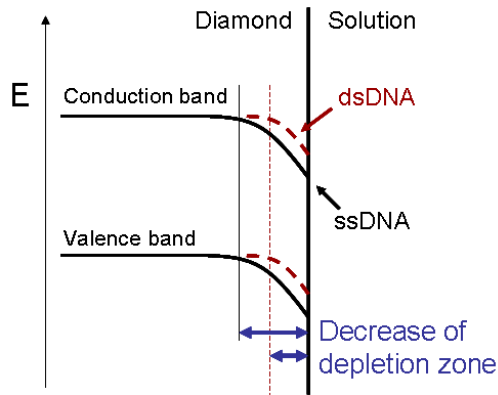


Figure 5.11: Schematic representation of the energy diagram at the diamond-solution interface. Extra negative charges, located at the surface during hybridisation, will decrease the electric field and reduce the band bending in the space-charge region.

5.4.2 Denaturation

We present the value of real-time denaturation as a reliable tool for the discrimination between target DNA/mRNA. Analogous to the real-time hybridisation, denaturation can discriminate between complementary and 1-mismatch DNA. During real-time denaturation, differences can be observed within 5 minutes in the lower frequency region (100 Hz – 15 kHz) and the highest frequency (1 MHz).

At low frequencies, denaturation of complementary DNA with 0.1 M NaOH causes an impedance increase during the first 10 minutes, which is opposite to the effects observed during hybridisation. In the previous section it is shown that the largest part of this frequency region (500 Hz – 15 kHz) is dominated by the R_QQ element of the circuit, attributed to the depletion zone of the semiconductor. An increase of the impedance of the depletion zone is explained in figure 5.11. When transferring from dsDNA to ssDNA, negatively charged DNA strands are released from the NCD surface, and as a result, the depletion zone will become larger. Only in the lowest frequency region, from 100 to 500 Hz, the $R_C C$ element influences the impedance. This $R_C C$ element has been attributed to the layer of molecules and ions at the surface. When the cell is filled with buffer, there will be numerous ions located at the surface, either forming a double-layer, or being attracted by the dsDNA molecules. When the cell is subsequently filled with 0.1 M NaOH, a new equilibrium will be formed. Negatively charged

ssDNA molecules and their associated counter-ions will leave the double-layer (figure 5.12). It has also been reported in literature that ssDNA is less conductive than dsDNA [Kel99]. Both factors can explain an increase of the impedance in the double-layer region.

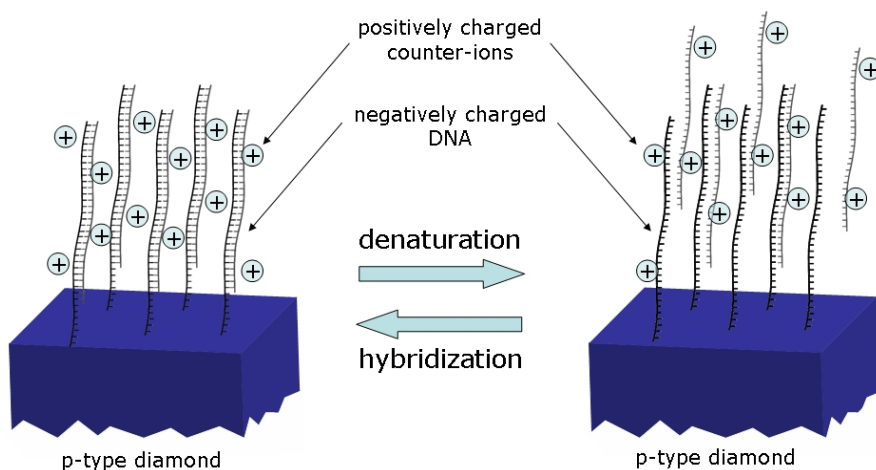


Figure 5.12: Formation of a new equilibrium during denaturation. Negatively charged ssDNA molecules and their associated positively charged counter-ions will leave the double-layer and will enter the buffer solution, causing a decrease in R_s .

The extent of impedance increase differs when comparing the denaturation of complementary DNA with that of 1-mismatch and non-complementary DNA. The smallest increase in impedance appears to occur during the denaturation of NCD samples previously hybridised with 1-mismatch DNA. The samples treated with non-complementary DNA display the largest increase in impedance upon treatment with NaOH.

Denaturation effects are also visible at the highest frequency, which is dominated by the resistance of the buffer solution. At this frequency, the addition of NaOH causes an initial rise in impedance, because of its low ionic strength as compared to the hybridisation buffers that were used. This initial rise is followed by a gradual decrease in impedance. This decrease of impedance can be interpreted as follows. During the formation of a new equilibrium upon addition of 0.1 M NaOH, the ssDNA molecules and their associated counter-ions that leave the double-layer, as explained above, are expected to enter the solution, resulting in a decrease of R_s (figure 5.12).

Our approach offers an alternative and reliable way to distinguish between the denaturation of complementary DNA, 1-mismatch DNA and non-complementary DNA. In all experiments, independent of temperatures above 40°C, the exponential decay time of the impedance during the denaturation of complementary DNA is the longest. This can be explained by the fact that, during complementary hybridisation, the highest density of dsDNA molecules are formed on the surface. Releasing the ssDNA molecules and ions into the solution during the denaturation will hence take the longest time. The ~50% shorter exponential decay times obtained during denaturation of 1-mismatch DNA can be explained by the fact that imperfect duplexes are more easily denatured because of their intrinsic instability. The denaturation of non-complementary DNA shows an exponential decay of ~70 % of that of the complementary denaturation curve. The different kinetic properties of the 'denaturation' of non-complementary DNA infer a different kind of discharge from the NCD surface. Instead of the release from a duplex structure into the solution, non-complementary ssDNA molecules are probably attached in a non-specific manner to the NCD surface. Removal of these non-complementary ssDNA molecules most likely occurs differently than denaturation of complementary or 1-mismatch DNA.

This work demonstrates that the given measurement platform can be expanded from lab-made diamond to commercial diamond. Moreover, the reproducible and sensitive real-time denaturation spectra are a valuable addition to the real-time hybridisation spectra. Therefore, it is recommended that both techniques should be combined to complement each other during data analysis.

5.5. CONCLUSIONS

This paper demonstrates the potential of impedance spectroscopy on diamond substrates for the development of a label-free DNA-based biosensor with SNP-sensitivity. Our approach proves to be robust, since NCD samples from both sources (IMO and rho-BeSt) gave consistent results. It was possible to detect hybridisation of probe ssDNA covalently attached to NCD samples with target ssDNA in real-time. More importantly, complementary and 1-mismatch target DNA could be discriminated in the low frequency region (100 Hz- 1500 Hz), even in the first 10 minutes after target DNA addition. Furthermore, blocking reagents to prevent non-specific adsorption of DNA to the NCD surface appeared unnecessary with our approach. The ionic content of the hybridisation buffer used was crucial to allow efficient hybridisation, the most suitable being MicroHyb™ hybridisation buffer at 80°C and 10× PCR buffer at 30°C. The suitability of 10× PCR buffer facilitates the lab-on-a-chip integration of DNA-extraction, PCR and real-time hybridisation.

Furthermore, we demonstrated the value of real-time denaturation as a tool for the reliable and fast discrimination between complementary, 1-mismatch and non-complementary target DNA within the first 5 minutes. It was possible to distinguish between the different ssDNA targets on the basis of their real-time impedance kinetics. Temperatures above 40°C yielded consistent results, allowing clear target discrimination.

These findings were reproducibly confirmed in two independent measurement setups: a single-cell and a double-cell setup, the latter being the least time consuming and the most useful for future applications in routine diagnostics. A double-cell setup, made up of a reference cell being exposed to complementary DNA as an internal standard, and a measurement cell being exposed to patient material, can be used in a clinical laboratory setting. This leads to a fast and reusable biosensor. The combination of both the real-time hybridisation spectra as well as the real-time denaturation spectra gives important information on the type of target DNA/mRNA and can be used for a reliable identification of target DNA/mRNA, possibly allowing SNP-identification in the future.

ACKNOWLEDGEMENTS

The research was performed in the framework of the project #030219 '*CVD Diamond: a novel multifunctional material for high temperature electronics, high power/high frequency electronics and bioelectronics*' funded by the Institute for the Promotion of Innovation by Science and Technology in Flanders (IWT), the IUAP VI program '*Quantum Effects in Clusters and Nanowires*', and the Scientific Research Community WOG WO.035.04N '*Hybrid Systems at Nanometer Scale*' of the Research Foundation – Flanders (FWO-Vlaanderen). M. Daenen (Assitant) and K. Haenen (Postdoctoral Fellow) are funded by the Research Foundation – Flanders (FWO-Vlaanderen). We also gratefully acknowledge tUL impulse financing. The assistance of J. Bacchus and J. Soogen in the development of the measurement setups and of J. D'Haen in SEM imaging is greatly appreciated.

Chapter 6:

Towards a real-time, label-free diamond-based immunosensor

Based on:

**Towards a real-time, label-free diamond-based immunosensor
*In preparation***

N. Bijnens^{a*}, V. Vermeeren^{b*}, S. Wenmackers^a, M. Daenen^a, K. Haenen^{a,c}, O.A. Williams^{a,c},
M. Ameloot^b, M. vandeVen^b, L. Michiels^b, P. Wagner^a

^a Hasselt University and transnationale Universiteit Limburg, School for Life Sciences, Institute for Materials Research, Wetenschapspark 1, B-3590 Diepenbeek, Belgium

^b Hasselt University and transnationale Universiteit Limburg, School for Life Sciences, Biomedical Research Institute, Agoralaan, Bldg. A, B-3590 Diepenbeek, Belgium

^c IMEC vzw, Division IMOMEC, Wetenschapspark 1, B-3590 Diepenbeek, Belgium

* N. Bijnens and V. Vermeeren contributed equally to this publication.

ABSTRACT

In the framework of developing a fast and label-free immunosensor for CRP detection, H-terminated NCD was functionalised with anti-CRP antibodies that were physically adsorbed to the surface. Impedance spectroscopy was used to electronically detect CRP recognition, in a frequency range of 100 Hz – 1 MHz. At low frequencies (100 Hz), different impedance behaviours were observed in real-time after CRP addition as compared to after FITC-labelled ssDNA addition. After fitting the data, the strong increase in impedance during CRP incubation indicated a decrease in capacitance of the molecular layer due to specific CRP recognition. The impedance signal during FITC incubation remained stable. At high frequencies (1 MHz), the impedance level after rinsing with 0.1× PBS was higher for the wells treated with CRP than for the wells treated with FITC, indicating a withdrawal of buffer ions to the CRP-loaded surface. Sensitivity experiments in real-time showed a clear discrimination between 1 μM, 100 nM, and 10 nM of CRP after 10 minutes at 100 Hz. Moreover, 10 nM of CRP was still clearly distinguishable from buffer, enabling the development of a CRP-immunosensor reaching physiologically relevant concentrations.

6.1. INTRODUCTION

CRP is an acute phase protein that is produced in the liver. In its native form, it is a pentamer of 126 kDa, consisting of five identical monomers of 25 kDa each. Its levels increase rapidly during systemic inflammation, where it is thought to assist in complement binding to foreign and damaged cells. Through this mechanism, phagocytosis is enhanced by macrophages, which express a receptor for CRP. The protein is also believed to increase the expression of ICAM-1, VCAM-1, and E-selection in cultured endothelial cells [Pas00]. Therefore, CRP has traditionally been used as a reliable marker for tissue injury, infection, and inflammation. More recently however, studies have shown that CRP is also implicated in the development of cardiovascular diseases (CVD), such as atherosclerosis, angina, coronary heart disease, peripheral artery disease, myocardial infarction, and stroke. Not only can elevated blood levels of CRP predict the recurrence of coronary events in patients with stable or unstable angina [Hav97], but it can even determine an increased risk for hypertension [Ses03] and CVD in healthy controls [Rid97];[Dan00]. As a result, apart from being a general inflammation marker, CRP can also function as an important risk assessment factor for the development of CVD.

The most recent statistics from the American Heart Association report that in 2004, 79.4 million Americans suffered from CVD, of whom 871,500 actually died. Hence, the need for reliable and sensitive risk assessment is obvious. During the course of history, many assay methods for the detection of CRP have been developed and improved, such as latex agglutination, nephelometry, turbidimetry, and fluorescent polarisation [Hok87]. Currently, an ELISA-based blood test called the 'high sensitivity C-reactive protein (hs-CRP) assay' is available to determine CVD risk (Dade Behring, Inc., Illinois, USA). With this test, a result of less than 8 nM of CRP indicates a low risk for CVD, a serum CRP concentration between 8 and 25 nM indicates a moderate risk, while a level of over 25 nM is a sign of high risk. However, a common disadvantage of ELISA is the false-positivity due to non-specific binding [Hu06], the long reaction times, and the expensive reagents involved.

With the field of bio-electronics progressing at the speed that it is, an electronic antigen detection system could allow for a faster and a real-time collection of results. Moreover, an electronic, real-time antigen detection system will become indispensable as a point-of-care diagnostic tool in the doctor's office. In this framework, both the method for the detection of protein-protein interactions and the manner of protein immobilisation have been widespread over the years. In the early 1990s, John *et al.* developed the first label-free electrochemical method for the detection of antibody-antigen recognition. They entrapped the antibodies in a polypyrrole membrane on an electrode surface by electrodepositing the polypyrrole in the presence of the antibody. The recognition was detected amperometrically [Joh91]. Dill *et al.* devised a Si-based micro-electrode array for multiple simultaneous immunoassays. The antibodies were adsorbed to the surface, and the antigen detection was based on a HRP-amplified amperometric method [Dil04]. Rick *et al.* molecularly imprinted thin films of aminophenylboronic acid (APBA) with template proteins on glass slides. Micro-calorimetry was used to relate changes in enthalpy with the binding of the correct template protein into the Molecularly Imprinted Polymer (MIP) [Ric05]. A SPR biosensing platform for CRP has also been developed by Hu *et al.*, where anti-CRP antibodies were bound to a Au surface through protein G [Hu06]. Yang *et al.* used EIS to directly detect antigen-antibody binding [Yan07].

Diamond has been studied extensively as a transducer material for biosensor fabrication because of very appealing physical, optical, chemical, and electrical characteristics that have been described in previous Chapters [Fie87];[Swa93]. In our previous work, we demonstrated that real-time differentiation between fully complementary and 1-mismatch DNA was possible on undoped NCD substrates using EIS [Ver07] (see Chapter 5 and Aim 2). In this study, this NCD-based impedimetric biosensor setup will be transferred to an immunological setting. In the above mentioned work of Yang *et al.*, human IgG and IgM that served as antigens were covalently immobilised via their antigen-recognition moieties to NH₂-terminated p-type diamond and Si surfaces. Their Fc regions were recognised in real-time by anti-IgG and anti-IgM antibodies. In contrast, we will adsorb monoclonal anti-CRP antibodies onto hydrophobic H-terminated NCD, in order for CRP recognition to occur through a typical antigen-antibody

interaction via the Fab regions of anti-CRP, giving our immunosensor setup a greater clinical relevance. The experiments will be performed on NCD samples grown at IMO and commercially available NCD samples in different buffer solutions.

6.2. MATERIALS AND METHODS

6.2.1 Materials

BSA was bought from Roche Diagnostics (Vilvoorde, Belgium). An ELISA amplification system based on the cyclic redox reaction of NADH/NAD⁺ was obtained from Invitrogen (Merelbeke, Belgium). Anti-CRP monoclonal antibodies (unlabelled and AP-labelled) and their specific antigen CRP were synthesised by Scipac (Kent, United Kingdom).

FITC-labelled ssDNA (22 b: 5'-FITC-C₆H₁₂-TCA-AAT-TGC-CAG-AAC-AAC-TAC-T) was purchased from Applied Biosystems (Lennik, Belgium) and used to test the specificity of the immunosensor.

6.2.2 NCD functionalisation

Unlabelled anti-CRP monoclonal capture antibodies were diluted in coating buffer until a concentration of 20 nM was reached. The H-terminated NCD samples (IMO and rho-BeSt) were immersed in this anti-CRP solution and incubated for 2 h at 37°C to allow physisorption of the antibodies. The anti-CRP-coated NCD samples were subsequently incubated overnight in a 6% BSA solution in 1× TBS at 4°C to block the remainder of the NCD surface that was not coated with anti-CRP.

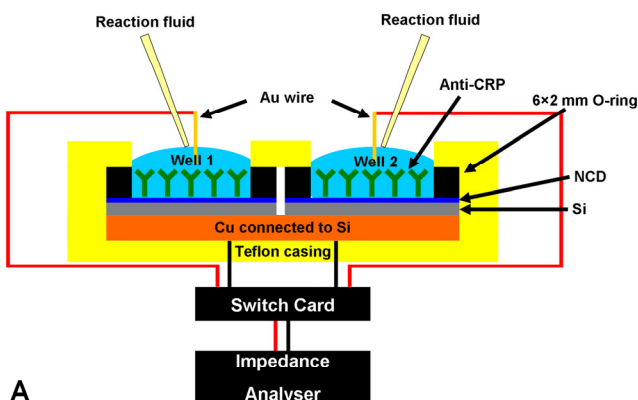
6.2.3 Reference ELISA procedure to verify formation of antibody/antigen-complex on NCD

As a control reaction, to verify the formation of the anti-CRP/CRP-complex, 20 nM unlabelled anti-CRP antibodies and 6% BSA were coated on two H-terminated NCD samples using the method described above. One was subsequently incubated with 2.4 μM CRP, while the other was treated with CRP buffer. After 2 h of reaction, detection occurred through the incubation with 70

nM AP-labelled anti-CRP detection antibodies in conjugation buffer for 1 h, and a subsequent substrate reaction using an ELISA amplification system based on NADPH. This substance is transformed by AP to NADH, which is the substrate for a secondary enzymatic redox cycle. Diaphorase oxidises NADH to NAD^+ while reducing a tetrazolium salt to an intensely coloured formazan dye. Subsequently, while ethanol is oxidised by alcohol dehydrogenase, NAD^+ is again reduced to NADH, driving the cyclic behaviour of the amplification reaction. Absorption of the coloured product is measured at 405 nm. To examine the amount of adsorbed CRP molecules and anti-CRP detection antibodies to unmodified NCD, two H-terminated samples that were not coated with anti-CRP but only blocked with 6% BSA were also treated with CRP and CRP buffer, respectively.

6.2.4 Sensor setup

Two sensor setups were devised for the development of a CRP-sensitive immunosensor, and are displayed in figure 6.1A and B.



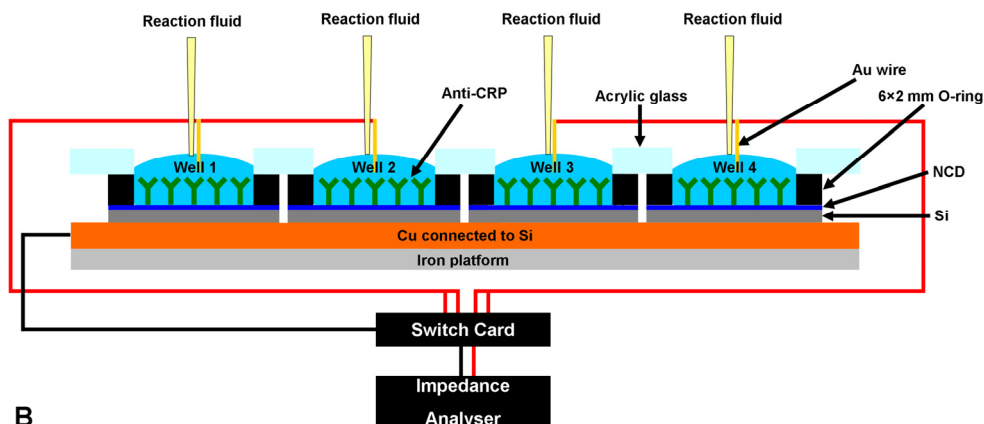


Figure 6.1: Graphical diagrams of the immunosensor setups used in the experiments. **A)** Teflon encased sensor setup allowing simultaneous measurement of 2 conditions. **B)** Sensor setup housing 4 NCD samples, allowing simultaneous measurement of 4 conditions.

In the first setup (figure 6.1A), two separate rho-BeSt NCD samples of 1 cm^2 coated with anti-CRP antibodies, functioning as working electrodes, were mounted on a Cu back contact using Ag paste. Rubber O-rings with a diameter of 6 mm and a Teflon lid containing circular openings of equal size were pressed onto the samples to create a reaction well above each NCD sample. The entire setup was incased in Teflon to prevent leaking from one reaction well to the other.

In the second setup (figure 6.1B), four separate IMO NCD samples of 1 cm^2 coated with anti-CRP antibodies, functioning as working electrodes, were mounted on a Cu back contact using Ag paste. Rubber O-rings with a diameter of 6 mm and an acrylic glass lid containing circular openings of equal size were pressed onto the samples to create four reaction wells above the NCD samples.

In both setups, the wells were filled with $140 \mu\text{l}$ of reaction fluid. Au wires, placed $\sim 1 \text{ mm}$ above each NCD surface in contact with the reaction fluid, were used as counter electrodes. Working and counter electrodes were connected to the impedance analyser with shielded cables. Hence, two and four signals, respectively, were recorded simultaneously.

6.2.5 Impedance spectroscopy

Real-time impedance curves from anti-CRP-modified NCD samples mounted into the above described setups were recorded continuously during stabilisation, antigen addition and rinsing. The reaction wells were first filled with 140 μl of pure PBS buffer (1 \times or 0.1 \times), and the device was allowed to stabilise until the difference in Z between two successive frequency sweeps was negligible throughout the entire frequency range. Regarding the physiological concentrations of CRP (8 nM and higher), concentrations of 10 nM – 1 μM were used in our experiments. For the specificity experiments, either CRP or FITC-labelled ssDNA was then added to the buffer in separate wells so that their final concentration was 1 μM , and allowed to react for 1 h. For the sensitivity analysis, CRP was diluted in CRP buffer, so that the final concentrations in the wells were 1 μM , 100 nM, and 10 nM, and allowed to react for 1 h. Pure CRP buffer served as a negative control. Finally, the reaction wells were rinsed and refilled with pure PBS buffer.

Experiments were performed using at 37°C, by placing the sensor setup inside a humidity-controlled hybridisation oven, which also resulted in electromagnetic shielding.

6.3. RESULTS

6.3.1 Reference ELISA procedure to verify formation of antibody/antigen-complex on NCD

To verify the suitability of H-terminated NCD as a substrate for the physisorption of anti-CRP, as well as the functionality of these adsorbed antibodies, two H-terminated NCD samples were coated with 20 nM unlabelled anti-CRP antibodies and 6% BSA. To examine the amount of aspecifically adsorbed CRP and AP-labelled anti-CRP antibodies to bare diamond, two additional H-terminated samples were only coated with 6% BSA. For both NCD couples, one sample was treated with CRP, while the other was incubated with CRP buffer. Detection occurred with an AP-labelled anti-CRP antibody and an AP-based substrate reaction. The absorption of the coloured product was determined at 405 nm. Figure 6.2 shows the results of this experiment. It is clear that the absorption is the highest for the sample allowing the formation of the antibody/antigen-complex, with minimal contributions due to aspecific bonding.

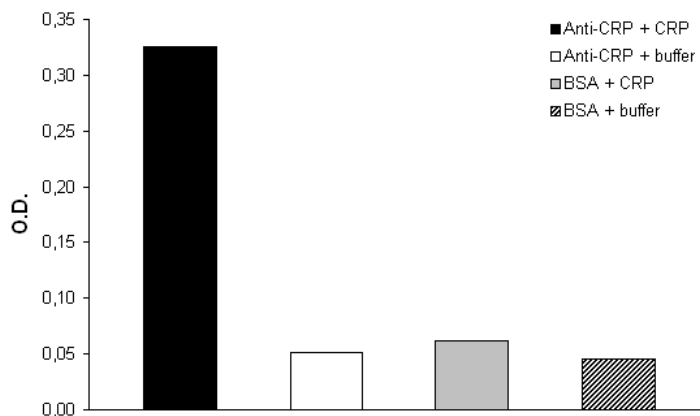


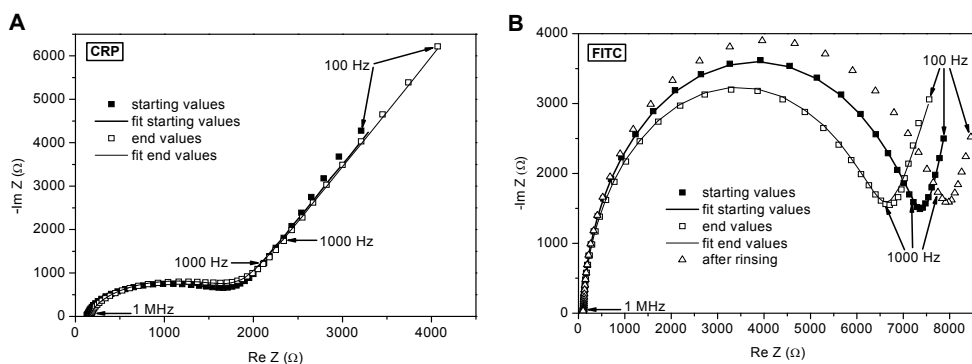
Figure 6.2: Colorimetric measurements of differently functionalised NCD samples, displaying the efficiency of the antibody/antigen-complex formation and the amount of aspecific adsorption of CRP and AP-labelled anti-CRP.

6.3.2 Specificity of the immunosensor

Specificity experiments were performed using both experimental setups indicated in figure 6.1A and B. For the two-well setup only 1× PBS solution was used for the pre-antigen stabilisation and the post-antigen rinsing phase, while for the four-well setup the concentration of the buffer solution was also lowered to 0.1× PBS. Lowering the buffer concentration was done in order to monitor any variation in the solution resistance before, during, and after the antigen recognition experiments. The specificity of the immunosensor was investigated by comparing the impedimetric influence of 1 μM CRP with that of 1 μM FITC on an anti-CRP functionalised NCD surface.

6.3.2.1 Low frequency

Figure 6.3 gives a typical result of an experiment performed by using the two-well setup (figure 6.1A). The wells were first filled with 140 μl of 1× PBS, after which the impedance was allowed to stabilise. Next, CRP was added to well 1, while FITC was added to well 2, ensuring that both final concentrations were 1 μM .



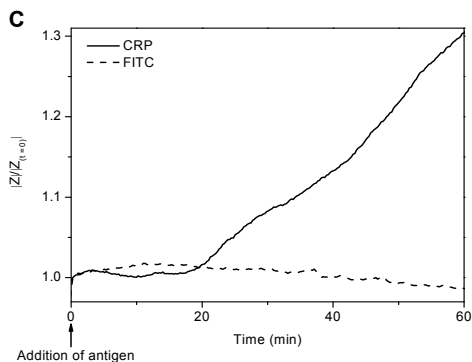


Figure 6.3: Nyquist plots showing the effect of antigen addition on the impedance. **A)** Immediately after (■) and 1 h after (□) CRP addition, and **B)** immediately after (■) and 1 h after (□) non-specific FITC addition, and after rinsing (Δ). The full lines indicate fits to an equivalent circuit. **C)** The corresponding real-time behaviour at 100 Hz during recognition.

Figure 6.3A and B show the Nyquist plots at the start (full squares) and 1 h after (open squares) CRP and FITC addition, respectively. Note that the start of antigen addition can be regarded as an internal reference point, corresponding to a condition where none of the antibodies are occupied by antigen. This allows the events in each channel to be evaluated relative to this point. It is obvious that the impedance at low frequencies has increased during the CRP recognition (figure 6.3A). In the well where the FITC was added (figure 6.3B), a completely different behaviour is observed. During incubation, the impedance has decreased over a large frequency range from ~ 1000 Hz to $\sim 5 \times 10^4$ Hz, corresponding to the semi-circle (open and full squares). This effect is reversed after rinsing with $1 \times$ PBS (open triangles). At lower frequencies, only a slight, negligible effect is observed. The real-time behaviour of the impedance at 100 Hz during recognition is given in figure 6.3C. The impedance has been normalised to the internal reference point, i.e., the value immediately after antigen addition to the buffer, corresponding to $t=0$. After 1 h, the impedance has increased with 30% in the well treated with CRP (solid line), while a decrease of less than 2% was observed in the well where FITC was added (dashed line).

6.3.2.2 High frequency

Differential behaviour between the samples treated with CRP and FITC can also be observed at high frequency. To increase the sample capacity and thus the throughput and information gathering of the immunosensor, a setup was developed in which four NCD samples could be housed and measured simultaneously. A graphical representation of this sensor setup is given in figure 6.1B.

First, the wells were filled with 140 μl of 0.1 \times PBS, after which the impedance was allowed to stabilise. Next, CRP was added in wells 1 and 2, while FITC was added in wells 3 and 4, ensuring that their final concentrations were 1 μM . The anti-CRP on the surface of the NCD samples was allowed to react with the added antigens for ~ 110 minutes. Finally, the reaction fluid in the wells was again replaced with 0.1 \times PBS.

Figure 6.4 shows the effects of these events on the impedance at 1 MHz. On the Y-axis, the impedance is normalised to its value after stabilisation in 0.1 \times PBS before the moment of CRP or FITC addition.

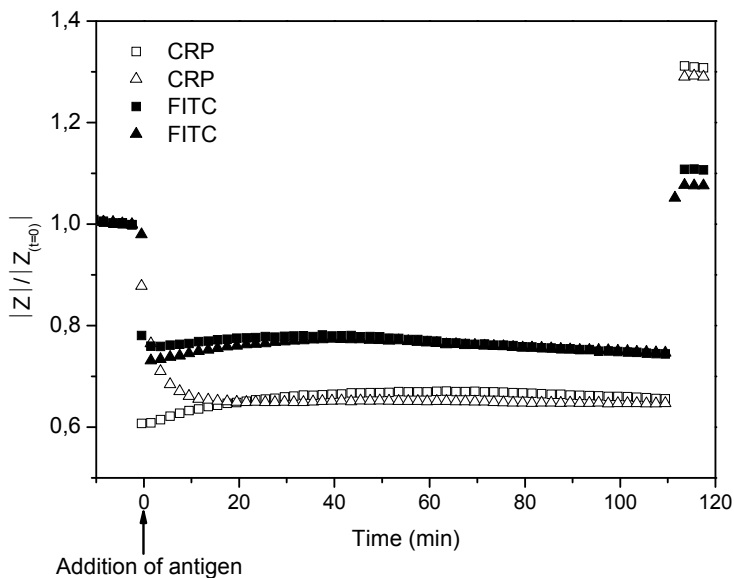


Figure 6.4: Effect of 0.1 \times PBS after CRP (□ and Δ) and non-specific FITC addition (■ and ▲) on the impedance at 1 MHz.

At $t=0$, CRP (open symbols) or FITC (full symbols) was added, causing a decrease in the impedance. After 10 minutes, the impedance has reached a stable level, indicating a fast response and fast generation of results. Also, after these 10 minutes, the two samples treated with each type of antigen arrive at the same level of the impedance, pointing towards a high reproducibility and reliability of the results. However, the stabilisation level is different for the CRP- and the FITC-treated samples. After ~ 110 minutes, the antigen was removed from the wells, and $140\ \mu\text{l}$ of $0.1\times$ PBS was again added after a short rinse. Although this is the same buffer as was used during the pre-antigen stabilisation phase, the two samples that were treated with CRP immediately obtain significantly higher values than the samples treated with the non-specific FITC.

6.3.3 Sensitivity of the immunosensor

In order to investigate the sensitivity of the sensor setup, different CRP concentrations were added to the $140\ \mu\text{l}$ of $0.1\times$ PBS buffer in the four-well setup. Figure 6.5 and 6.6 illustrate an experiment where CRP with final concentrations of $1\ \mu\text{M}$, $100\ \text{nM}$, and $10\ \text{nM}$, and pure CRP buffer was added to well 1, 2, 3, and 4, respectively. Real-time impedance spectra were taken at $100\ \text{Hz}$ and at $1\ \text{MHz}$.

6.3.3.1 Low frequency

Figure 6.5 shows the effects of different CRP concentrations on the impedance at $100\ \text{Hz}$ in real-time.

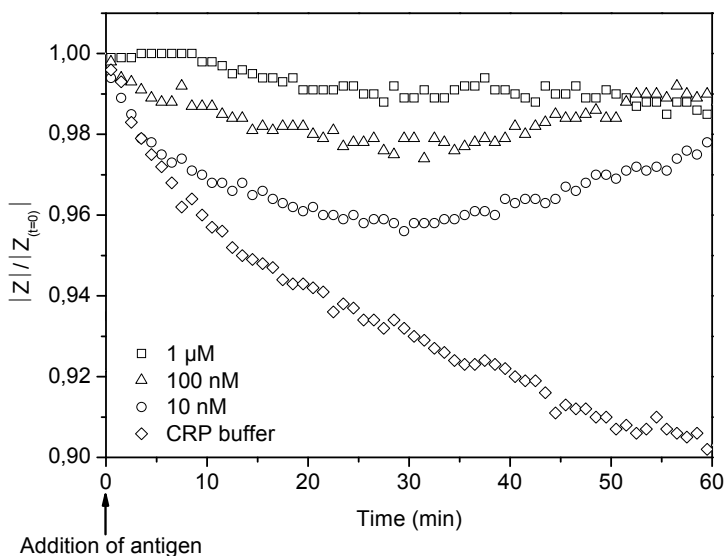


Figure 6.5: Real-time impedance spectra at 100 Hz illustrating the concentration sensitivity of the sensor for CRP. The CRP concentrations used were 1 μM (\square), 100 nM (Δ), 10 nM (\circ), and 0 nM (\diamond).

The impedance course at 100 Hz changes in a concentration-dependent manner. Each curve, corresponding to a specific CRP concentration can be clearly distinguished from each other within 10 minutes. While the impedance of the reference channel (well 4, open diamonds) is continually decreasing, the impedance of the channels with a CRP concentration of 100 nM (open triangles) and 10 nM (open circles), clearly start increasing after 30 minutes, and show a comparable behaviour to the effect shown in figure 6.3C. The impedance of the channel with the highest CRP concentration (open squares) doesn't show an increase at all. After 1 h, the impedance of all of the channels treated with CRP are at least 10% higher than that of the reference channel. It should be remarked that the sharp impedance increase of 30% for the 1 μM CRP channel observed in figure 6.3C is not reproduced here.

6.3.3.2 High frequency

Figure 6.6 shows real-time impedance spectra taken at 1 MHz, where the impedance is most sensitive to the solution resistance R_s .

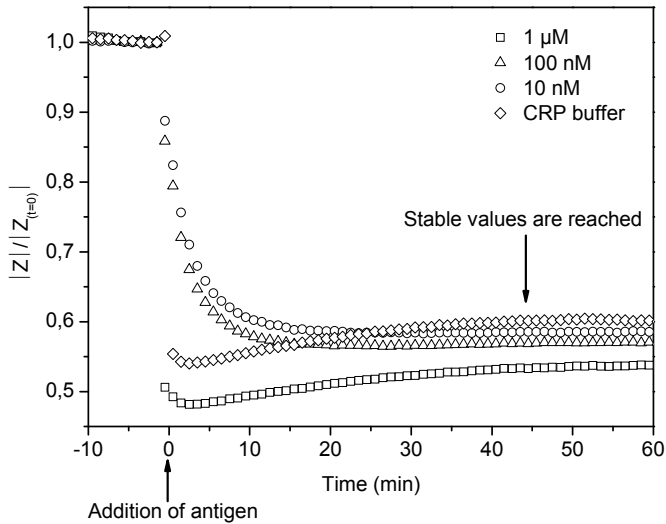


Figure 6.6: Real-time impedance spectra at 1 MHz illustrating the concentration sensitivity of the sensor for CRP. The CRP concentrations used were 1 μM (□), 100 nM (Δ), 10 nM (○), and 0 nM (◇).

As in figure 6.4, the impedance decreases immediately after the antigen addition. Only after 45 minutes, the impedance reaches clearly distinguishable stable values in the four wells: 53% of the pre-antigen impedance level for 1 μM (open squares), 55% for 100 nM (open triangles), 59% for 10 nM (open circles), and 60% in the well where no antigen was added (open diamonds).

6.4. DISCUSSION

In this study, the real-time electronic detection of antibody-antigen recognition on NCD is reported using impedance spectroscopy. H-terminated NCD surfaces prove to be suitable substrates for the adsorption of functionally active anti-CRP capture antibodies (figure 6.2). Impedance variations indicating selective recognition of CRP by the adsorbed anti-CRP antibodies were observed at low and high frequencies, and consistent results were obtained using two types of measurement setups.

6.4.1 Specificity

Specificity of the immunosensor was investigated by the incubation of anti-CRP-functionalised NCD with either CRP or FITC-labelled ssDNA with a final concentration of 1 μM using both the two-well and the four-well setup. At low frequencies, the impedance during CRP treatment showed a clear rise, while remaining nearly constant during FITC incubation. Instead, the effect of the latter antigen on the impedance was visible in the frequency region of 1 – 50 $\times 10^3$ Hz.

In order to get more insight in the physical meaning of these impedance variations at low frequencies, the impedance spectra were analysed using equivalent circuit models. This was done using the ZSimpWin software from Princeton Applied Research (Massachusetts, USA), as in Chapter 5. The fits were performed over the total frequency range from 100 Hz to 1 MHz. For most of the data obtained with the two-well setup, excellent fits ($\chi^2 \sim 10^{-4}$) could be obtained by using the model given in figure 6.7, which are illustrated by the full lines in figure 6.3A and B.

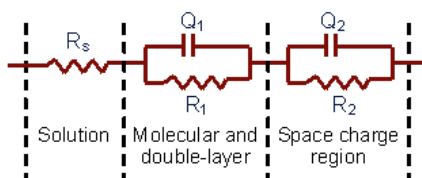


Figure 6.7: The electrical circuit model used for fitting the impedance data.

The circuit can be divided into three components: (a) the solution resistance R_s , between the gold electrode and the NCD surface, (b) a resistance R_{Q_1} and a constant phase element Q_1 in parallel, corresponding to the molecular layer and its associated double-layer on the surface, (c) and a resistance R_{Q_2} and a constant phase element Q_2 in parallel corresponding with the space-charge region in the NCD. The impedance of the Q elements is defined by $Z = [Q(i\omega)^n]^{-1}$. For our data, n varied between 0.6 and 1. A value of $n = 1$ is equivalent to the 'perfect' capacitor. As already mentioned, a value of $n = 0.5$ corresponds with the Warburg impedance [Gri00]. The parameter values obtained for the fits shown in figure 6.3 are indicated in table 6.1.

Table 6.1: Results of fitting the impedance spectra before and after addition of CRP and FITC.

Element	CRP			FITC		
	Start	End	Effect (%)	Start	End	Effect (%)
R_s (Ω)	127.3 ± 1.3	162.2 ± 1.3	+ 27	99.8 ± 0.6	105.7 ± 1.1	+ 6
Q_1 ($\mu S \cdot s^n$)	1.6 ± 0.2	1.1 ± 0.1	- 31	2.0 ± 1.1	2.7 ± 0.9	-
n	0.76 ± 0.02	0.76 ± 0.01	-	0.83 ± 0.08	0.74 ± 0.05	-
R_1 (Ω)	uncertain	uncertain	-	uncertain	uncertain	-
Q_2 ($nS \cdot s^n$)	17.8 ± 1.3	18.4 ± 1.4	-	7.1 ± 0.2	6.8 ± 0.3	-
n	0.92 ± 0.01	0.92 ± 0.01	-	1.00 ± 0.01	1.00 ± 0.01	-
R_2 ($k\Omega$)	1.52 ± 0.03	1.52 ± 0.03	-	7.17 ± 0.10	6.23 ± 0.09	- 14

*reported uncertainties are standard deviations as obtained from the data fits

From the fit results of the data in figure 6.3A, it can be observed that the increase of the tail at low frequencies corresponds to a significant decrease of the Q_1 value of 31%. This indicates a smaller capacity for the molecular layer after CRP recognition at the surface. The additional layer of CRP antigens on top of the anti-CRP antibodies increases the thickness of the molecular layer, decreasing its capacitance. This is illustrated in figure 6.8.

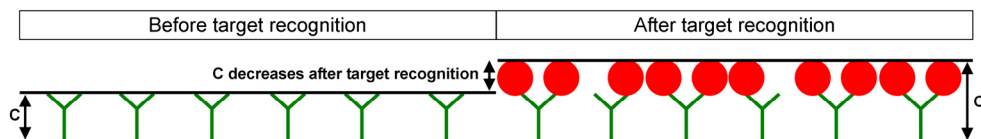


Figure 6.8: Decrease in capacitance of the molecular layer due to its increased thickness by the CRP antigens that have been recognised by anti-CRP.

However, in the well where FITC-labelled ssDNA was added, only the second parallel element R_2Q_2 shows significant changes. The decrease of the semi-circle

observed in figure 6.3B corresponds to a strong decrease of the resistance R_2 (14%). This effect persisted through all of the experiments, giving a strong indication that the negatively charged ssDNA attached to the FITC-label is adsorbed at the surface inducing a field-effect in the space-charge region of the NCD. The field-effect in NCD substrates, caused by negatively charged DNA at the surface, has been reported in our previous work on real-time impedimetric DNA detection [Ver07] (see Chapter 5 and Aim 2) as well as in other publications [Yan04];[Gu05] and will not be discussed here. This decrease of the semi-circle disappeared after rinsing and refilling the well with 1× PBS. As is shown in figure 6.3C, the Nyquist spectrum returned to its starting values before FITC-labelled ssDNA addition. This was not the case in the aforementioned publications, where ssDNA was covalently bound to the NCD samples and hybridisation occurred with complementary target ssDNA added to the buffer. The return of the semi-circle to its starting values indicates that after rinsing, the FITC-labelled ssDNA molecules were removed from the surface. A negligible field-effect in the NCD substrate was observed during CRP treatment, reflected by the lack of impedance variations in the semi-circle. This is in correspondence to the observations made by Poghossian et al. and Bergveld et al., that antibody-antigen recognition detection by means of FET is seriously compromised by the counter-ion screening effect [Pog05];[Ber03].

A relevant increase of the parameter R_s can also be remarked in table 6.1, with more than 27% for CRP, but with only 6% for FITC. In both cases, this increase of the solution resistance during the recognition experiment can be explained by the elimination of the CRP and FITC antigens and associated ions from the buffer solution due to their migration to the surface. It should be noted, however, that these effects, visible mainly at high frequencies, were not always observed.

At 1 MHz, an impedance decrease is observed upon addition of both types of antigen to the 0.1× PBS buffer. This can be explained by the ionic content of the buffers in which both antigens were diluted. CRP buffer and 1× PBS both contain a higher salt concentration than the stabilising 0.1× PBS buffer. Stabilisation is obtained within 10 minutes, after which each sample couple, treated with each type of antigen, reaches a similar impedance value. This indicates a fast generation and a high reproducibility and reliability of the results. The difference

in stabilisation level between the CRP- and FITC-treated samples probably reflects the difference in their respective buffers. After the antigen incubation phase, 0.1× PBS was again added after a short rinse. Although this is the same buffer as was used during the pre-antigen stabilisation phase, the two samples that were treated with CRP immediately obtain significantly higher values than the samples treated with the non-specific FITC. This can not be explained by remnants of the previous buffers in the wells since this would result in a lower impedance for CRP as compared to FITC. However, it gives an indication that during the antigen treatment phase, specific CRP recognition took place in wells 1 and 2, causing significant rearrangement of the molecular layer at the corresponding NCD samples with respect to the period before antigen addition. When replacing the reaction fluid with 0.1× PBS, this causes an immediate withdrawal of ions from the buffer solution towards this molecular layer, increasing the resistance of the buffer. Any FITC adsorbed onto the NCD would have been removed during the rinsing step, as discussed before. Hence, the molecular layer, and thus the impedance level after 0.1× PBS addition remain comparable to the level of before antigen addition. This phenomenon appeared consistent and reproducible over several independent experiments.

6.4.2 Sensitivity

A clear effect on the impedance is also observed in real-time when exposing the anti-CRP-modified H-terminated NCD samples to different concentrations of CRP. At low frequencies, the impedance decreased with decreasing CRP concentration, as shown in figure 6.5. A distinction is already possible within 10 minutes. However, the 30% impedance increase for the 1 μ M CRP channel observed in figure 6.3C is not reproduced. This can be explained by a shift of the Nyquist spectra with one frequency order of magnitude. In this case, almost the entire frequency range is occupied by the semi-circle, while only a short tail is left as shown in figure 6.9.

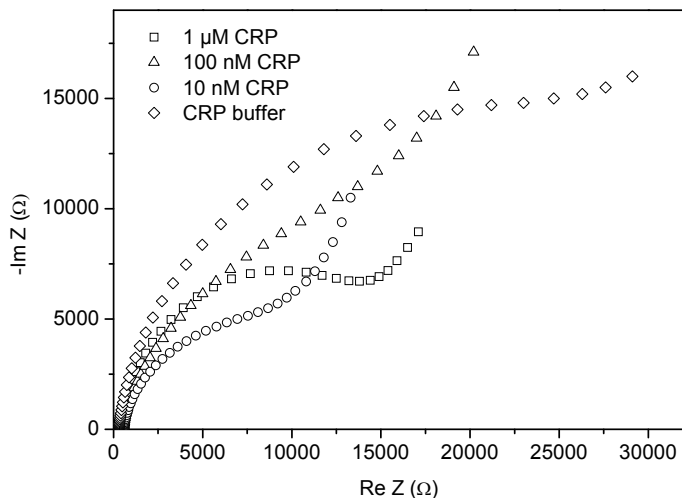


Figure 6.9: The shapes of the Nyquist plots for the samples in the four-well setup. The CRP concentrations used were 1 μM (\square), 100 nM (Δ), 10 nM (\circ), and 0 nM (\diamond).

At frequencies below 100 Hz, this tail will become more pronounced, likely resulting in an even more clearly distinguishable impedance signal between different concentrations of CRP or between CRP and a non-specific reference.

There is still a clear separation between the curves corresponding to the lowest concentration used (~ 10 nM) and the pure buffer. This indicates that the detection limit of the immunosensor could lie beneath this value.

At 1 MHz, the impedance is most sensitive to the solution resistance R_s . As mentioned before, the decrease of the impedance at this frequency immediately after CRP addition can be attributed to the higher ionic concentration of the CRP buffer as compared to the $0.1\times$ PBS buffer. This initial fast process is followed by a slow stabilisation phase. Only after 45 minutes, the impedance stabilised at clearly distinguishable levels, after which it gradually started to increase again. This stabilised level decreased with increasing CRP concentration, with the lowest impedance level associated with the highest CRP concentration, and the highest level of impedance associated with buffer. Because of the much faster generation of results (10 minutes) and the more straightforward association with the molecular layer, impedance spectra at lower frequencies are preferred to make antibody-antigen recognition evaluations.

In comparison to our impedimetric experiments on ssDNA functionalised NCD samples [Ver07] (see Chapter 5 and Aim 2), the stabilisation of the immunosensor impedance signal after the disturbance of the system by pipetting manipulations takes longer. This increased stabilisation time can be attributed to the fact that the antibodies were physically adsorbed to a H-terminated NCD instead of covalently bound to the NCD through fatty acid linker molecules. Some degree of dissociation of the antibodies from the surface can therefore not be excluded. The adsorbed antibodies and BSA molecules also form a coating on top of the NCD, restricting the counter-ions in the double-layer to a region above this coating. This ionic layer can thus easily be disturbed by pipetting. In the case of covalently bound DNA, the location of the ions near the NCD surface is physically separated from the site of hybridisation. Hence, rinsing only slightly disturbs the distribution of ions in the molecular and double-layer.

Miniaturisation of the sensor setup will be a useful development for improvement of reaction time through its effects on diffusion and double-layer disturbances. First of all, it will significantly decrease the diffusion time of the antigens to the surface by decreasing the reaction volume. Secondly, this smaller reaction volume will likely shorten the reformation time of the double-layer after disturbances.

6.5. CONCLUSIONS

In this work the potential of impedance spectroscopy on H-terminated diamond is investigated for the development of a real-time and label-free immunosensor. Specific discrimination between CRP and FITC was obtained, by physically adsorbed antibodies on NCD substrates. This was observed in real-time at low frequencies (100 Hz) and after rinsing the samples in 0.1× PBS at 1 MHz. The sensitivity of the immunosensor was analysed in real-time by incubation of the NCD samples with different concentrations of CRP. At 100 Hz, clear discrimination was obtained within 10 minutes. Moreover, the lowest concentration of CRP used in our experiments (10 nM) was still clearly distinguishable from the reference channel. This indicates the possibility of an immunosensor with a sensitivity in the range of the physiologically relevant concentrations (8 nM and higher). These findings were reproducibly confirmed in two independent measurement setups: a two-well and a four-well setup, the latter being the least time consuming and the most useful for future applications in routine diagnostics.

For future experiments however, it is imperative to expand this immunosensor research to the investigation of its impedimetric behaviour upon addition of a CRP-like antigen, having comparable charge and molecular weight. Moreover, it is recommended to look at frequencies lower than 100 Hz where an impedance increase of even more than 30% can be expected. Also, a covalent attachment between antibody and NCD is advised to decrease the stabilisation time of the impedance signal. Another point of improvement is the miniaturisation of the setup, which will diminish the diffusion process, and therefore decrease the detection time. All of these aspects will be tackled in future experiments.

ACKNOWLEDGEMENTS

The research was performed in the framework of the project #030219 '*CVD Diamond: a novel multifunctional material for high temperature electronics, high power/high frequency electronics and bioelectronics*' funded by the Institute for the Promotion of Innovation by Science and Technology in Flanders (IWT), the IUAP VI program '*Quantum Effects in Clusters and Nanowires*', and the Scientific Research Community WOG WO.035.04N '*Hybrid Systems at Nanometer Scale*' of the Research Foundation – Flanders (FWO-Vlaanderen). M. Daenen (Assitant) and K. Haenen (Postdoctoral Fellow) are funded by the Research Foundation – Flanders (FWO-Vlaanderen). We also gratefully acknowledge tUL impulse financing. The assistance of J. Bacchus, J. Soogen, and B. Coninx in the development of the measurement setups is greatly appreciated.

Chapter 7 :

Discussion and concluding remarks

7.1 DISCUSSION

The evolution from micro-science into nano-science has prompted the blossoming of the field of bio-electronics. More and more, the functional activity of biomolecules, i.e. the recognition and/or metabolisation of their targets, is exploited and interrogated by electronics to increase the detection speed and sensitivity of certain pathogens, pollutants, and genetic mutations. To enable the electronic interrogation of these biomolecules, they need to be attached to or embedded into a solid support or transducer with a favourable orientation and density, ensuring the retention of their biological functionality. The resulting analytical device is called a biosensor. Semiconductors are the preferred transducer material, since their conductivity can be controlled and cheap production methods are available. Metal electrodes, however, are constitutively conductive, and may hamper the detection of a biological signal. However, leaching of biomolecules from the semiconductor surface when placed in aqueous media is a serious disadvantage associated with popular and established semiconductors such as Si. This inadvertently leads to a decrease in sensitivity and a lack of reproducibility over time. Diamond on the other hand has proven to be an attractive alternative. It can be made electrically semiconducting, it is chemically inert in a wide range of solutions, and it can be modified with a battery of functionalised alkenes, inferring the desired functionality for the covalent attachment of biomolecules. Yang *et al.* and Nebel *et al.* have also shown that this tethering of biomolecules to diamond is much more stable than that to other commonly used electrode materials [Yan02];[Neb07]. Moreover, diamond is biocompatible, paving the way for future *in vivo* and continuous measurements when high sensitivity can be successfully coupled with miniaturisation.

In this work, we assessed the applicability of NCD both as a substrate for biomolecule attachment, and as a transducer material for the development of label-free and electronic DNA- and immunosensors. As mentioned in the general introduction, this study was based on four research questions. In this last Chapter, the results will be discussed based upon these same four pillars.

1) How can we attach DNA to NCD in order to get an optimal surface coverage and an optimal functionality in subsequent impedimetric sensor platforms? Can our immobilisation approach be adapted in such a way that we can introduce it into an array format?

In Chapter 3, we developed an efficient two-step reaction to covalently attach DNA to NCD, as an improvement and a significant simplification of the procedure that was suggested by Yang *et al.* [Yan02]. In a first step, a ω -unsaturated fatty acid molecule, 10-UDA, was photochemically attached to H-terminated NCD by illumination with UV (254 nm) for 20 h. The resulting COOH-modified NCD was then ideally functionalised for the subsequent attachment of NH₂-modified DNA. The crosslinker molecule EDC joined the COOH-group of the NCD to the NH₂-group of the DNA into a peptide bond. The DNA that was used in this study was a 250 bp double-stranded PCR amplicon, modified with the necessary NH₂-group and an FITC-label for fluorescent detection.

This chosen length of the DNA (250 bp) immediately brought about some practical difficulties. The binding capacity to the NCD was low, because of the disorganised orientation of the attached DNA molecules. According to Steel *et al.*, DNA molecules that surpass a length of 24 bases, adopt a conformation resembling entangled flexible coils instead of well-organised stiff rods. In this way, fewer molecules will geometrically fit onto the surface, and the ones that are, lie flat on the NCD surface [Ste00]. This low DNA density on the NCD surface combined with the rather low quantum yield of FITC, made it impossible to directly detect the DNA using fluorescence microscopy. However, PCR and gel electrophoresis performed on the reaction fluids obtained from repeated denaturation and rehybridisations did prove, on the one hand, the EDC-mediated covalent attachment of DNA to NCD, and, on the other hand, the functionality of this DNA. Nevertheless, the negative control showed the presence of some non-covalently adsorbed DNA.

The low DNA density and the presence of non-covalent DNA prompted the need for improvement of the technique. In Chapter 4, all parameters involved in this improvement process were evaluated. In this study, the procedure was fine tuned to remove the adsorbed DNA, and it was shown, using fluorescence microscopy, that the use of short ssDNA (8 – 36 bases) offered a huge

enhancement of the attachment efficiency, indicating that the findings of Steel *et al.*, making use of Au substrates, could be extended to our work on NCD. An amount of 300 pmol, corresponding to 10^{14} molecules, yielded the highest DNA density on NCD samples obtained from independent sources. This proved the robustness of our improved DNA attachment procedure. Furthermore, the attached ssDNA molecules still displayed a high functionality, as was determined by the efficient hybridisation of the same amount of attached ssDNA molecules to fluorescently labelled target ssDNA. Under optimised conditions, discrimination between complementary and 1-mismatch target ssDNA was well detectable. Although we did not perform single-molecule experiments to determine the exact amount of DNA molecules that was covalently coupled to the surface, hybridisation of NCD samples modified with a decreasing amount of probe DNA did give us semi-quantitative information about the probe availability, which is even more important in view of sensor functionality. A probe content in the EDC-reaction mixture between 10^{13} (30 pmol) and 10^{14} molecules (300 pmol) will likely yield an optimal probe surface density in terms of functionality and availability for hybridisation reactions.

The COOH-termination of the NCD was also proven to be crucial for EDC-mediated NH_2 -DNA attachment, since functional DNA attachment did not occur on O- and H-terminated NCD. Moreover, as we showed in Chapter 4, the anti-adsorptive effect of H-termination is a very attractive feature, and can be exploited for patterning purposes. Making use of shadow masks in pre-designed shapes, areas on the diamond surface covered with the mask are protected from the UV-illumination and concomitant photochemical 10-UDA functionalisation, while on the non-covered areas the UV-mediated COOH-modification is allowed to proceed. This way, the location of DNA probes, and hence the location of signal generation on the surface can be easily and reproducibly controlled. This holds great promise for applications in the field of micro-electronics because one needs to be sure that the DNA molecules are not attached to the locations of the electrodes on the surface. Furthermore, the attachment of biomolecules to the surface of the NCD can be arrayed, allowing for high-throughput analyses. At the same time, the surface conductivity properties of H-terminated diamond can still be taken advantage of. We note that H-termination could become compromised by O_2 during exposure to several downstream processing steps.

This could jeopardise the above described advantages offered by H-termination. However, since O-terminated NCD only creates a platform for non-functional DNA probes, the H-terminated regions will still determine the signal-generating regions on the DNA-sensor. Therefore, the platform we developed in this thesis will lay the groundwork for the creation of a real-time, electronic DNA microarray.

Huang *et al.* proposed an alternative approach, simultaneously resulting in blocking of non-specific adsorption and diluting the amount of biomolecules to be attached, hereby reducing steric hindrance and increasing binding efficiency. They formed mixed SAMs on Si substrates with different ratios of thiolated alkanes carrying either a COOH- or an OH-functionality. The modified surfaces were subsequently analysed in terms of fouling and binding efficiency, the surface carrying the 90% OH- and 10% COOH-SAM turning out to be the most favourable [Hua05]. We undertook a similar experiment, photochemically functionalising NCD samples with mixtures containing different ratios of COOH-carrying and OH-carrying alkenes and covalently attaching ssDNA to these mixed surface chemistries. Although the EDC-mediated DNA attachment on every NCD surface containing a fraction or even pure OH-functionalities appeared as efficient as that on purely COOH-terminated NCD, functional ssDNA was only present on the latter. Possibly, EDC also catalyses a secondary esterification reaction between the OH-functionalities on the NCD and the phosphate backbone throughout the DNA. This results in DNA molecules being bound to the surface at multiple locations along their length, instead of through their end-functionalisation, making them unavailable for hybridisation. To circumvent the issue of causing secondary reactions, the OH-alkene spacer molecules were replaced by CH₃-alkenes. However, these molecules caused undesirable side-effects during the photochemical attachment, and were considered unmanageable.

Taken together, our approach yields a very versatile, robust, and efficient technique to covalently bind functional DNA to NCD. Importantly, our EDC-mediated strategy offers the following advantages. It is a simple and reproducible **two-step procedure**, in which EDC is a **zero-length crosslinker**. This means that the molecule will not be present in the eventual peptide bond between the DNA and the 10-UDA on the NCD. For this reason, the DNA

molecules will be closer to the surface, which is beneficial for electronic detection of hybridisation. Furthermore, the ω -unsaturated fatty acid molecule is a **flexible linker**. It will thus offer some mobility to the attached DNA molecules, mimicking their behaviour in solution and thereby increasing their hybridisation efficiency. Moreover, regional COOH- and H-termination of the NCD is an easy and efficient way to **pattern** the diamond surface with DNA probes. All of these aforementioned advantages make our approach very promising to be used in a prototype of a DNA-based biosensor. This was the subject of Chapter 5.

2) Is it possible to extend this optimal approach for covalent and functional attachment of DNA molecules to the development of a prototype of a real-time electrochemical DNA-based biosensor reaching SNP sensitivity? Can this sensor be used to study both hybridisation and denaturation processes in real-time?

Although fluorescent DNA detection and identification systems are promising, the gain in speed and information associated with electrical transduction is undeniable. This was the main incentive for the extension of the observations in Chapter 4 concerning the EDC-mediated DNA attachment procedure and the endpoint fluorescence-based mutation analysis into the development of a real-time and fast electronic DNA-sensor based on impedance spectroscopy, as outlined in Chapter 5. A prototype device was constructed with sufficient sensitivity to allow for the simultaneous measurement of the effect of either complementary or 1-mismatch target DNA on the impedance of a DNA-modified NCD sample.

First of all, similar to studies performed by Yang *et al.* and Gu *et al.*, changes in the impedance were measured during the hybridisation reactions of complementary and 1-mismatch DNA [Yan04];[Gu05]. However, our work also investigated the influence of certain buffer types and temperatures on the sensitivity of the read-out. Traditional hybridisation buffers contain aspecific DNA, such as salmon sperm DNA, and BSA to reduce background signal due to non-specifically adsorbed DNA. This prompted the initial decision of using MicroHyb™ hybridisation buffer for the impedimetric measurements. Very good results were obtained while hybridising in this MicroHyb™ hybridisation buffer at

80°C. The observation that H-terminated NCD was an efficient barrier for non-specific adsorption of DNA, however, prompted the search for more practical solutions. Hybridisation in 10× PCR buffer at room temperature gave excellent results comparable to those of MicroHyb™ hybridisation buffer. Considering the importance of practicality and easy implementation, 10× PCR buffer at room temperature is preferred. It could allow for the 'lab-on-chip' integration of a DNA extraction unit, a DNA amplification unit, and a mutation analysis unit using a minimal amount of buffer systems. In table 7.1, the effects observed with the DNA-sensor are summarised.

Table 7.1: Summary of effects observed with a prototype DNA-sensor during hybridisation and denaturation.

Hybridisation	Denaturation	
Low frequency (1000 – 1500 Hz)	Low frequency (100 – 15000 Hz)	High frequency (1 MHz)
<i>Real-time decrease in Z for complementary DNA</i> → reduction of semi-circle = decrease in R_Q = narrowing of NCD depletion zone by field-effect	<i>Intermediate real-time increase in Z for complementary DNA</i> → increase of semi-circle = increase in R_Q ($1 - 15 \times 10^3$ Hz) = widening of NCD depletion zone by field-effect → change in $R_C C$ (100 – 500 Hz) = effect on molecular and double-layer	<i>Slowest real-time decrease in Z for complementary DNA</i> → slowest decrease in R_S = release of ssDNA into solution
	<i>Largest real-time increase in Z for non-complementary DNA</i>	<i>Intermediate decrease in Z for non-complementary DNA</i>
<i>No real-time effect on Z for 1-mismatch DNA</i>	<i>Smallest real-time increase in Z for 1-mismatch DNA</i>	<i>Fastest real-time decrease in Z for 1-mismatch DNA</i>

In the frequency range of 1000 – 1500 Hz, a large decrease in impedance was observed in real-time only during the hybridisation with complementary DNA, while the effect of 1-mismatch hybridisation on the impedance was negligible in 10× PCR buffer at room temperature. This decrease of the complex impedance was reflected in a significant reduction of the size of the semi-circle in the Nyquist plot at the end of hybridisation with respect to the plot at the start of hybridisation. To explain the observations, the Nyquist plots, displaying the real and the imaginary values of the measured complex impedance, were fitted with the same equivalent circuit as was used by Yang *et al.* [Yan04]. The circuit was composed of a series connection of a solution resistance R_S , a capacitor C and an associated resistance R_C in parallel, and a constant phase element Q and its associated resistance R_Q in parallel. This allowed us to attribute the observed changes in impedance to actual circuit elements, offering

a detailed understanding of the effect of DNA hybridisation on the diamond and the immobilised probe layer. The reduction of the semi-circle during hybridisation with complementary DNA was caused by the significant decrease of R_Q . Heating experiments, showing the largest impedance effect in the reduction of this semi-circle, could assign the R_Q element in the circuit to the space-charge region in the NCD. Upon heating of semiconductors the amount of charge carriers increases, thereby decreasing the resistance inside the semiconductor. Therefore, our observations suggest that hybridisation of NCD-bound DNA with complementary target has the largest effect on the space-charge region of the NCD. Since the NCD contains a low amount of B, making it slightly p-type, downward band bending occurs at the NCD-solution interface upon reaching thermodynamic equilibrium. A depletion zone is formed because of the exchange of charges at this interface. Upon the increase of negatively charged DNA during hybridisation, positive charge carriers from the NCD bulk are attracted to the surface, narrowing the depletion zone and decreasing its resistance. On an energy scale, the downward band bending is reduced by a slight upward direction. Yang *et al.* also attributed their observed impedance decrease to events in the depletion zone of the diamond, although the frequency range where this effect occurred was different [Yan04].

No significant effect of hybridisation was observed at low frequencies, which are dominated by the $R_C C$ element. According to the literature, this element reflects the molecular layer and its associated double-layer [Yan04]. Gu *et al.* postulated that the use of highly insulating alkane linkers for the attachment of DNA makes it impossible to detect variations in resistance in this region. These authors, however, did observe the largest effect of DNA hybridisation in the molecular layer, reflected at low frequencies. The PANI/PAA-copolymer on top of the diamond used to attach the DNA appeared to undergo most of the ionic redistributions upon hybridisation, leading to a dramatic decrease in resistance and increase in capacitance in this molecular layer [Gu05].

Our approach for real-time detection of DNA hybridisation offers specific advantages when compared to the work of Yang *et al.* and Ingebrandt *et al.* It was possible to discriminate between complementary and 1-mismatch target DNA within 10 minutes, while using a buffer system with a rather high ionic content, favouring hybridisation. The counter-ion screening effect usually

associated with high-ionic buffers was not observed here. Moreover, blocking of the surface to avoid interference of non-specific DNA was unnecessary, greatly simplifying the approach [Yan04];[Ing06];[Pog05].

While most other authors have up to now focused on the development of hybridisation-based impedimetric DNA-sensors, we also included real-time denaturation as an additional feature for mutation detection. Traditional techniques are also available that make use of this principle, such as DGGE [Fis79];[Bor88] and melting curve analysis during real-time PCR. In these procedures, the melting behaviour of DNA is used as a source of sequence-dependent information. In a second part of our study, we investigated whether this type of additional information could also be retrieved from our real-time NCD-based impedimetric DNA-sensor. In fact, discrimination between complementary, 1-mismatch and non-complementary DNA was also accomplished in real-time during denaturation with 0.1 M NaOH. To our knowledge, this is completely new in biosensor research. In comparison to DGGE, this approach offers the added benefit of a dramatically decreased reaction time. During the first ten minutes of denaturation, an increase of the complex impedance in the 100 – 15000 Hz frequency range is observed, corresponding to the molecular and double-layer (100 – 500 Hz) and the space-charge region (500 – 15000 Hz). At the highest frequency, corresponding to the solution resistance, a decrease of the impedance occurs.

Addition of 0.1 M NaOH will denature the hybridised DNA strands, causing them and their associated counter-ions to be removed from the NCD surface. This explains the observed impedance increase in the molecular layer. Since more duplexes were probably formed during complementary hybridisation than during hybridisation with 1-mismatch DNA, the rise in impedance is larger in the former condition. However, non-complementary DNA will not have hybridised into a duplex but will probably have adsorbed onto the NCD surface to some degree. Since proximity to the electrode surface is positively correlated with efficiency of signal detection, a field-effect is also generated during non-complementary 'hybridisation' (data not shown). Removal of some of these adsorbed molecules therefore also shows the largest impedance increase. The reason why an effect of denaturation is seen at the molecular level, in contrast to hybridisation, lies probably in the lower ionic content of 0.1 M NaOH as

compared to 10× PCR buffer. Variations in ionic distributions caused by actual biological events become more obvious when buffer interference effects are minimised. The intrinsically high ionic content of 10× PCR buffer shielded the actual hybridisation event from being detected at the molecular level, but the effects on the depletion zone were not affected. The denaturation events also have an influence on the NCD substrate itself. Removing negatively charged DNA during denaturation will completely reverse the effects seen in the space-charge region during hybridisation. The depletion zone will become wider, resulting in an increase in resistance.

At the highest frequency, the system is most sensitive to the resistance of the solution, R_s . Initially, the decrease in ionic content of 0.1 M NaOH with respect to 10× PCR buffer causes a steep rise in impedance. For the complementary, the 1-mismatch, and the non-complementary condition, this is followed by a gradual impedance decrease, correlated with the release of the denatured DNA and associated ions into the solution. Discrimination between the three cases was possible after fitting this gradual decrease to an exponential decay, and attributing decay times to this decrease. Relative to each other, the longest decay time is associated with complementary denaturation, while the shortest time correlates with 1-mismatch DNA. When adding 0.1 M NaOH to a sample previously treated with non-complementary DNA, the decay time lies in between. As already mentioned, the different manner of capturing non-complementary DNA will inadvertently lead to differences in removal kinetics into the solution. Discrimination of the three types of DNA was possible within 5 minutes. Up to now, we are not yet able to attribute reproducible absolute decay values to each type of DNA that are representative of each type's kinetic behaviour. However, relative decay times with respect to the complementary condition were highly reliable. Simultaneous measurements are therefore advised, including at least one reference cell.

Taken together, we have developed a **fast and real-time impedimetric DNA-biosensor** based on NCD, displaying **SNP sensitivity**. Currently, the state-of-the-art techniques for mutation analysis are the oligonucleotide and the cDNA microarrays, and DGGE. However, we believe our approach can offer some definite benefits with respect to certain practical difficulties associated with these alternatives. They are summarised in table 7.2.

Table 7.2: Overview comparing typical features between three different methods of mutation analysis.

Current DNA-sensor	Microarray	DGGE
Price		
No fluorescent labelling	Expensive fluorescent labelling	No fluorescent labelling
Relatively cheap impedance analyser	Fluorimetric optics system	Electrophoresis system
Possibility for high-throughput	High-throughput	Low-throughput
Reusable	Not reusable	Not reusable
→ Rather cheap	→ Expensive	→ Expensive
Biological relevance of detected parameter(s)		
Real-time detection of hybridisation/denaturation kinetics	Endpoint detection of hybridisation	Endpoint detection of denaturation
Detection based upon real biological event	Detection based upon over-generalised yes/no principle	Detection based upon real biological event
→ Possible identification of new mutations based on real-time kinetics behaviour	→ No identification of new mutations	→ Possible identification of new mutations based on endpoint behaviour
Reaction time		
<One hour	>Hours	>Hours
→ Fast	→ Slow	→ Slow

First of all, the requirement of fluorescently labelled target DNA and the corresponding need for highly specialised equipment for signal detection and data processing make commercially available microarrays an expensive investment. Moreover, the rather unstable bond between the biomolecules and the platforms used for microarray development, often Si, as already mentioned in the work of Yang *et al.* and Nebel *et al.*, limits them to one-use purposes [Yan04];[Neb07]. The synthetic manufacturing of diamond, the stable bonds formed between diamond and biomolecules, the label-free approach, and the possibility of regeneration, either of the functional sensor surface by simple denaturation, or of the diamond surface by cleaning in strong acid, make our approach much more **budget-friendly**. Furthermore, while microarrays only offer the option of endpoint detection, wrongly implying one hybridisation condition for all probes present on the array, we believe that additional valuable information can be obtained with a real-time approach. This time-resolved detection exploits exactly these **kinetic hybridisation and denaturation differences** that cannot be made use of in an endpoint detection. For this reason, we recommend to include the real-time hybridisation spectra as well as the real-time denaturation spectra in the data analysis. While discrimination of a 1-mismatch sequence from complementary and non-complementary sequences is already possible during the real-time hybridisation phase, correct

differentiation between complementary and non-complementary DNA will be achieved during the real-time denaturation, making use of their different surface removal kinetics. Moreover, we expect that not only SNP detection, but also SNP identification will be possible during this phase, exploiting their different denaturation kinetics. Taking less than one hour to execute the entire experiment, including hybridisation and denaturation, our presented prototype DNA-biosensor is much **faster** than the current technologies, for instance DGGE. Furthermore, because of the requirement of a simplified impedance analyser fixed at one low and one high frequency setting, each being sensitive to another phase of the experiment, our approach will also be much cheaper than microarray analysis.

3) Can NCD function as a kind of generic sensor platform? Is it also a suitable substrate for antibody immobilisation, and do these molecules retain their functional activity?

To examine if NCD could also serve as a platform for antibody attachment, a traditional reference method was used as a starting point in Chapter 6. Comparable conditions were subsequently used to transfer this technique from a standard ELISA microtiterplate to NCD surfaces.

Two H-terminated NCD samples were incubated with 20 nM anti-CRP for 2 h at 37°C. These, and two other H-terminated NCD samples were subsequently incubated overnight in 6% BSA at 4°C. One sample in each group was treated with 2.4 µM of CRP. The other was merely incubated with CRP-buffer. Detection of antibody recognition and possible non-specific adsorption of CRP and/or detection antibody occurred through incubation with 70 nM AP-labelled anti-CRP detection antibodies and a subsequent substrate reaction based on the cyclic redox reaction of NADH and formazan dye. The colour formation was read out at 405 nm.

Only the positive control sample, modified with anti-CRP and BSA, and treated with CRP showed a significant colour reaction, indicating antigen recognition. The three remaining negative controls instead indicated the absence of interference from non-specifically adsorbed CRP or detection antibodies. Hence, H-terminated NCD proved to be an appropriate substrate for non-

covalent antibody modification. Silin *et al.* also investigated the influence of several surface chemistries on the adsorption efficiency of human IgG, and found a CH₃-surface modification to be the most suitable. They postulated that the protein adsorption to this surface was a multistep process, probably initiated by interaction of hydrophobic residues, that have temporarily become exposed at the surface of the protein, with the hydrophobic substrate. This initial interaction is then followed by multipoint interactions due to various degrees of protein denaturation, making desorption from the surface extremely difficult [Sil97]. Our experiments indicate that these various degrees of antibody denaturation do not hamper their biological activity. Using these H-terminated NCD surfaces for antibody adsorption also allows the exploitation of the electronic benefits of this surface, i.e. its surface conductivity.

4) Can a prototype of an electrochemical immunosensor be developed to measure clinically relevant targets in a concentration-dependent manner and in physiologically appropriate concentrations?

After having determined the suitability of H-terminated NCD for the modification with anti-CRP, we set out to transfer the colorimetric immunoassay into an electronic NCD-based immunosensor using impedance spectroscopy as the transduction principle. Two measurement setups were constructed, for double-simultaneous and quadruple-simultaneous analyses, respectively. The observed effects are summarised in table 7.3.

First of all, the selectivity of the anti-CRP immunosensor was investigated by analysing the effect of either CRP or FITC addition on the course of the complex impedance.

Table 7.3: Summary of effects observed with the immunosensor during selectivity and sensitivity testing.

Selectivity		Sensitivity
Low frequency (100 Hz)	High frequency (1 MHz)	Low frequency (100 Hz)
<i>Real-time increase in Z during CRP treatment (100 Hz)</i> → increase in Nyquist 'tail' = decrease in Q_1 = decrease in molecular layer C by thickness increase	<i>Endpoint increase in Z after CRP treatment</i>	<i>Real-time decrease in Z during CRP treatment</i> → lower stabilisation levels for decreasing [CRP]
<hr/> <i>Real-time decrease in Z during FITC treatment ($1 - 50 \times 10^3$ Hz)</i> → reduction in semi-circle = decrease in R_{Q2} = narrowing of NCD depletion zone by field-effect		

At low frequencies, a significant rise of the impedance is observed in real-time during CRP addition, while the effect of FITC was negligible. In the corresponding Nyquist plots, showing the real and the imaginary parts of the complex impedance at the start and end of the CRP addition, this increase was observed as an increase in the 'tail' region to the right of the semi-circle. FITC, however, showed an effect on the impedance at a higher frequency region, i.e. $1 - 50 \times 10^3$ Hz. The Nyquist plots indicate that this effect is largely visible as a decrease in the semi-circle. However, rinsing with $1 \times$ PBS buffer caused the semi-circle to return to its starting position. To explain these observations, the Nyquist plots corresponding to the start and end of CRP and FITC addition were fitted to an equivalent circuit. This circuit was composed of a series connection of a solution resistance R_S , a constant phase element Q_1 and an associated resistance R_{Q1} in parallel, and a constant phase element Q_2 and its associated resistance R_{Q2} in parallel. Just as with the DNA-based biosensor, this allowed us to attribute the observed changes in impedance to actual circuit elements. Since the addition of the ssDNA-linked FITC caused the same decrease in R_{Q2} , associated with the reduction in the semi-circle, as was the case with the DNA-biosensor, we were able to assign the $R_{Q2}Q_2$ element to the space-charge region in the NCD. The negatively charged DNA bound to the FITC-label caused a field-effect inside the slightly p-type NCD, narrowing the depletion layer and decreasing its resistance. The low-frequency $R_{Q1}Q_1$ element was therefore attributed to the molecular layer on the surface and its associated double-layer, which only experienced an influence during CRP addition. The increase in

impedance that was observed during CRP treatment was reflected in a decrease of Q_1 . This can be rationalised by the fact that the addition of antigen on top of the antibody film will increase the thickness of the molecular layer on the NCD surface. This increase in thickness will cause a decrease of molecular layer capacitance.

A differential effect was also observed at the highest frequency, when comparing the pre-antigen stabilisation phase and the post-antigen rinsing phase of CRP and FITC. This highest frequency is most sensitive to the solution resistance R_s . Since both pre- and post-antigen phase occurred in $0.1\times$ PBS buffer, they could be directly compared in terms of R_s . The solution impedance level of the post-antigen rinsing phase consistently resided higher than the level during the pre-antigen stabilisation phase for the CRP treated sample. For the FITC treated sample, the solution impedance level of the post-antigen rinsing phase did not differ much from the pre-antigen stabilisation phase. This could be explained by the fact that substantial ionic redistribution took place during specific CRP recognition. This caused a withdrawal of the ions after addition of $0.1\times$ PBS buffer. No specific antigen recognition occurred during FITC treatment, and the few adsorbed FITC molecules would have been removed from the surface during the short rinsing step before the post-antigen stabilisation phase. For this reason, no significant ionic redistribution took place, and hence no major discrepancies were observed between the impedance level of the pre- and post-antigen phase.

Secondly, the sensitivity of the CRP-directed immunosensor was investigated by the incubation of anti-CRP-coated NCD samples with different final concentrations of CRP ($1\ \mu\text{M}$, $100\ \text{nM}$, and $10\ \text{nM}$), including one sample that was incubated with pure CRP buffer. The different CRP concentrations exhibited differential effects on the complex impedance, making them clearly distinguishable from each other and from pure CRP buffer at low ($100\ \text{Hz}$) frequencies.

At these low frequencies, addition of the different concentrations of CRP and the buffer caused a decrease in complex impedance in real-time. However, the degree of impedance decrease differs among the concentrations added, increasing with decreasing CRP concentration. Within 10 minutes, a clear discrimination could be made, and the lowest concentration of $10\ \text{nM}$ was still

clearly distinguishable from buffer. The impedance increase during CRP treatment that was observed during the selectivity experiments was not reproduced. This was probably due to the fact that the Nyquist plots in this case were almost entirely occupied by semi-circle, leaving no tail region to be discerned. Even though all frequencies were included in the Nyquist plot, physically, the region most sensitive to the events in the molecular and double-layer is not represented. If we had been able to analyse the frequencies lower than 100 Hz, this tail region would have appeared in the Nyquist plots, together with its characteristic impedance increase and its associated effect on the molecular layer capacitance. For this reason, the exact physical interpretation of the observed effects on the impedance in terms of electrical circuit elements caused by the different CRP concentrations is still in progress.

At the highest frequency, the addition of the different CRP concentrations and the CRP buffer caused an immediate impedance decrease. This initial effect is due to the higher ionic content with respect to the pre-antigen 0.1× PBS buffer, since this frequency is most sensitive to the solution resistance R_s . However, after about 45 minutes, new stabilisation levels were reached, with a higher impedance level associated with lower CRP concentrations. Because of the much faster generation of results (10 minutes) and the more straightforward association with the molecular layer, impedance spectra at lower frequencies are preferred to make antibody-antigen recognition evaluations.

In Chapter 6, we were able to introduce the groundwork for the development of a **real-time impedimetric CRP-selective immunosensor**. Preliminary experiments showed a **sensitivity** (10 nM) approaching that of the **physiologically relevant** concentrations (<10 nM). However, this work will be expanded and improved on several levels.

First of all, as compared to the impedimetric DNA-biosensor (Chapter 5), the stabilisation time of the immunosensor is significantly longer. This can be explained by the fact that the anti-CRP antibodies and the BSA were physically adsorbed to the NCD surface, forming a dense molecular layer on top of the NCD. This causes the counter-ions of the double-layer to be located above this molecular layer, making them easily accessible for disturbances caused by pipetting. In the DNA-sensor, the DNA molecules were covalently attached to the NCD through a fatty acid linker molecule. The counter-ions in the double-

layer were thus physically separated from the region of biological interaction and less susceptible to disturbances. Miniaturisation of the setup will likely improve reaction time through effects on diffusion and disturbances of the double-layer. A smaller sample volume will, on the one hand, decrease the diffusion time of the antigens to the surface, and, on the other hand, likely result in a more easily reformed double-layer after any disturbance.

Secondly, the use of two very distinct antigens, FITC-labelled ssDNA and CRP, exhibiting very distinct electronic behaviour, allowed us to be introduced to the effects of CRP on the impedance. However, it is of course required to explore the ability to distinguish CRP from a non-specific antigen of comparable molecular weight and charge. Thirdly, we will transfer to an approach based on covalently bound antibodies. This will avoid the additional variable associated with the possible loss of antibodies from the surface, and create a more rigid and reliable system. However, notwithstanding this increase in system stability, this immunosensor will be restricted to a disposable use. Since high-affinity antibodies are preferred in immunosensors because of their strong binding energies towards their specific antigens, it is exactly this property that hinders their regeneration. The harsh conditions that will be used to separate the antigen-antibody bond, will most likely also destroy the antibody. Hence, as a final point, extensive research will also be performed into this area to achieve this goal of immunosensor regeneration. It will again drastically decrease the cost of such immunosensor applications, in comparison to the currently widely used and commercially available ELISA kits.

A final aspect of improvement applies to both the NCD-based DNA-sensor and immunosensor. Sensitivity could be significantly improved by the use of interdigitated electrodes (IDEs). These are electrodes shaped into a finger-like pattern. Two electrodes of opposing polarity are oriented in such a way that the fingers of each electrode are interlacing. A thin, functionalised NCD transducer layer will isolate these electrodes from the buffer solution. The electric field between these opposing electrode fingers will mainly be confined to the transducer layer and the molecular layer. Hence, this approach will be less sensitive to interfering buffer effects and more sensitive to molecular layer effects.

7.2 CONCLUDING REMARKS AND FUTURE PROSPECTS

In this project, we developed a prototype of a real-time impedimetric NCD-based DNA-biosensor with SNP sensitivity. What is important to note, is that no blocking methods were needed in our approach to prevent the non-specific DNA from adsorbing to the surface. Moreover, our method allows to identify DNA sequences from two complementary points of view, i.e. hybridisation and denaturation behaviour, making use of the real-time kinetics during these reaction phases. The created sensor platform will be extended from a proof-of-principle into a clinical setting. On the one hand we will be performing mutational analysis where the hybridisation and denaturation kinetics will be evaluated between short immobilised DNA molecules bearing the polymorph DNA sequence to be studied and longer, purified PCR amplicons of patient material. On the other hand, we wish to accomplish gene expression analysis, requiring the immobilisation of much longer gene fragments. This implies the development of an efficient way to construct a dense layer of long DNA strands without the associated quandaries described in Chapters 3 and 4.

Two basic aspects need to be mentioned here concerning our DNA-biosensor. In the presented approach, a multiple-simultaneous array setup is advised, offering at least one reference cell, where the complete affinity cycle can be executed with complementary target DNA. The other measurement cells can be treated with sample target material. This way, relative comparisons in terms of kinetic behaviour can be made with the wild-type. Furthermore, the method requires PCR amplification of the desired gene fragment in the patient material. Nevertheless, considering that the same buffer plays a large role in PCR and real-time hybridisation, both experimental phases of the genetic analysis can be implemented into a 'lab-on-chip', greatly simplifying laboratory manipulations. This rather innovating approach, combining low cost, system stability and reliability, holds promise to grow into a valuable complementary technique for the widely applied endpoint microarrays.

We have also laid the groundwork for the development of a prototype of a real-time and label-free impedimetric NCD-based immunosensor. Although we

made use of two antigens of intrinsically different nature, their respective effects on the impedance introduced us to the fundamental events that occur during antigen recognition in an electronic setting. This will be developed further into a prototype of an immunosensor with the ability to discriminate between two antigens comparable in molecular weight and charge. Eventually, the sensitivity and specificity of the sensor will be challenged with patient whole serum.

It should be noted, however, that two limitations plague the development of a high-throughput routine-based immunosensor. First of all, cross-reactivity of the antibodies towards other antigens present in patients whole serum or blood is a very common but in many cases to be avoided issue. It negatively affects the specificity and hence, the sensitivity of the immunosensor. However, there are applications where some degree of cross-reactivity is desired, for instance when searching for similar members of a protein family. Secondly, as already mentioned, any attempt to regenerate the active, antibody-modified sensor surface will often result in the destruction of the antibodies themselves. Thirdly, but equally important, the production of monoclonal antibodies is a very complicated and tedious procedure. It can take months to select suitable high-affinity antibodies. For these reasons, alternative biosensor setups will be explored in an attempt to address these needs, for instance cell-based and aptamer-based biosensors.

Cells are nature's version of biosensors. They detect and react to environmental changes through the action of ligand-membrane receptor interaction, intracellular signal transduction, and response. The latter can, for instance, be in the form of the transcriptional activation of several relevant genes, or operation of the membrane channels for (de)polarisation. Exploitation of these natural phenomena could lead to exciting new possibilities in biosensor research.

Four goals need to be fulfilled: sensitivity, flexibility, regeneration, and transduction. Since a whole-cell sensor setup will make use of the cell's natural task, it will also ensure a high specificity and a sensitivity in the physiologically relevant ranges. Furthermore, our laboratory has extensive experience in the genetic engineering of antibody and T-cell receptor genes. Through this genetic engineering, the antigen-recognising region of any antibody of choice can be combined with the transmembrane and intracellular parts of the T-cell receptor,

conferring a vast array of possible target specificities, and hence flexibility, to these engineered cells [Mot96]. Also, a natural cellular response to receptor activation is receptor internalisation, enabling the creation of a self-regenerating sensor system [Dava05].

The transduction principle can be embodied in an impedimetric read-out system. This can be achieved by immobilising these engineered whole cells onto a diamond electrode. This mode of sensor design is certainly worth exploring, which will be tackled in an ensuing research project. Of course, one must keep in mind that in order to achieve this form of transduction, cells must be immobilised onto a surface while retaining their functional conformation and viability. However, not all cell types, especially not T-cells, are adherent. One way to circumvent this issue, is to realise a cell-capturing approach after the biological recognition event, instead of immobilising the cells as part of the sensor assembly. Upon receptor activation due to recognition of its target, an intracellular signalling cascade will cause the transcriptional activation of several genes. One of these genes can be modified by joining it to the gene sequence coding for a cell surface protein, leading to the production of a specific protruding surface marker upon target recognition. When the biological recognition event is allowed to proceed in solution, over a sensor surface modified with antibodies directed against this induced membrane marker, activated cells will be selectively captured onto the surface. This can then be detected with impedance spectroscopy.

Since the discovery of its remarkable features in 1990, interest has significantly grown in the possible exploitation of another molecular tool for biosensor development, the aptamer. Aptamers, derived from the Latin 'aptus', meaning 'to fit', are artificial oligonucleotides, DNA or RNA, with the ability to recognise target molecules such as peptides, proteins, drugs, organic and inorganic molecules or even whole cells, with high affinity and specificity. This specific recognition ability is conferred to these oligonucleotides by virtue of their primary sequence that folds into a 3D globular shape. Consequently, they have the chemical structure of DNA or RNA, but behave functionally as antibodies [Mair07].

Aptamers that are able to bind to the desired target molecules are selected and amplified *in vitro* with a relatively simple procedure called Systematic

Evolution of Ligands by EXponential Enrichment (SELEX). After the SELEX selection procedure, the aptamer sequences, being nucleic acids, can be produced in sizeable quantities using chemical synthesis [Mair07].

Aptamers are an interesting alternative to the widely used biological components, such as antibodies, in terms of application in diagnostics, therapeutics, and bioanalytical research. They are readily available, since SELEX can be entirely carried out *in vitro*, avoiding the need for animals, in contrast to the tedious hybridoma-technology for monoclonal antibody production. Moreover, the technique can be executed in non-physiological conditions, yielding aptamers that will also function in these conditions. Aptamers show an affinity for their targets comparable to, and sometimes even better than, monoclonal antibodies. They can also be selected against non-immunogenic and toxic targets, because the SELEX process does not rely on the induction of an animal's immune response, as is the case with antibody generation. Aptamers are also very flexible. They can be easily labelled with reporter molecules, such as fluorophores or enzymes, and can be immobilised onto a surface, provided that the affinity for its target is not affected [Mair07].

When an aptamer is used as the biological recognition element of a biosensor, it is termed an aptasensor. The small size of aptamers allows efficient surface immobilisation and formation of high-density monolayers. Hence, improved sensitivity can be expected, which is of vital importance for techniques whose signal is enhanced with closer proximity to the transducer surface (EIS) and for future miniaturisation. Subsequent target recognition can be transduced in the same way as the more traditional biosensors. For instance, a label-free sensor platform can be created using impedance spectroscopy as a transduction system. Detection will be achieved simply upon target recognition, either by a field-effect in the electrode material or changes in the electrical properties of the molecular layer. Very importantly also, apart from their high target affinity and the advantages described above, aptamers provide reusable affinity-based biosensors, which was the major obstacle for the routine implementation of immunosensors. They can be easily regenerated by treatment with a chaotropic agent to break the aptamer-target complex [Mair07].

This thesis has provided a suitable biosensing platform with sufficient flexibility to implement these alternative setups. Thanks to our interdisciplinary expertise, these new inroads towards biosensor development allow the establishment of new and exciting research initiatives.

All together, the groundwork was laid for obtaining a reliable and sensitive impedimetric sensing scheme for DNA as well as proteins. However, many demands will need to be met and many factors taken into consideration in order to be applicable in routine clinical diagnostics. A prerequisite for both types of sensors for use in routine diagnostics and research is their compatibility with 'real-life' samples. The impedimetric DNA-sensor will need to be expanded from a proof-of-principle into a sensor that retains its sensitivity and specificity when challenged with patient PCR material. The impedimetric immunosensor must remain functionally active in physiologically relevant ranges even when treated with patient whole serum. Both of them will need to be miniaturised in order to be portable and easy to handle, but also to decrease analysis time into the minute-scale. For the immunosensor, this miniaturisation will also ensure a point-of-care or bedside application. For the DNA-sensor, a co-integration with a PCR-unit into a lab-on-chip will speed up SNP detection and identification while circumventing the problem posed by low target amounts. In order to comply with all of these demands, the first task at hand is the optimisation and pinning down the role of crucial parameters, such as probe density, target concentration, NCD thickness, NCD size, and doping degree, in order to obtain a specific, sensitive and reliable impedance response at one chosen frequency. These issues will form the subjects of subsequent research projects and challenges that lay before us.

REFERENCE LIST

Physical properties of semiconductors, www.ioffe.ru/SVA/NSM/Semicond/index.html

- [Alw77] Alwine, J. C., Kemp, D. J., Stark, G. R., 1977. Method for detection of specific RNAs in agarose gels by transfer to diazobenzyloxymethyl-paper and hybridization with DNA probes. *Proc.Natl.Acad.Sci.U.S A* 74, 5350-5354.
- [Ama02] Amaratunga, G. A. J., 2002. A dawn for carbon electronics. *Science* 297, 1657-1658.
- [Bak02] Bakowicz, K., Mitura, S., 2002. Biocompatibility of NCD. *J.Wide Bandgap Mater.* 9, 261-272.
- [Ban02] Banno, T., Tachiki, M., Seo, H., Umezawa, H., Kawarada, H., 2002. Fabrication of diamond single-hole transistors using AFM anodization process. *Diamond Relat.Mater.* 11, 387-391.
- [Ber03] Bergveld, P., 2003. Thirty years of ISFETOLOGY - What happened in the past 30 years and what may happen in the next 30 years. *Sens.Actuators, B* 88, 1-20.
- [Ber78] Bernhard, B., Lengeler, B., *Electronic structure of noble metals and polariton-mediated light scattering*, Springer-Verlag, Berlin, 1978
- [Bor88] Borresen, A. L., Hovig, E., Brogger, A., 1988. Detection of base mutations in genomic DNA using denaturing gradient gel electrophoresis (DGGE) followed by transfer and hybridization with gene-specific probes. *Mutat.Res.* 202, 77-83.
- [Bun55] Bundy, F. B., Hall, H. T., Strong, H. M., Wentorf, R. H. Jr., 1955. Man made diamonds. *Nature* 176, 51-55.
- [Cai04] Cai, W., Peck, J. R., van der Weide, D. W., Hamers, R. J., 2004. Direct electrical detection of hybridization at DNA-modified silicon surfaces. *Biosens.Bioelectron.* 19, 1013-1019.
- [Can01] Cannaerts, M., Nesládek, M., Haenen, K., Stals, L. M., De Schepper, L., Van Haesendonck, C., 2001. Reversible switching of the surface conductance of hydrogenated CVD diamond Films. *Phys.Stat.Sol.(a)* 186, 235-240.
- [Car04] Carlisle, J. A., 2004. Precious biosensors. *Nat.Mater.* 3, 668-669.
- [Cas84] Cass, A. E., Davis, G., Francis, G. D., Hill, H. A., Aston, W. J., Higgins, I. J., Plotkin, E. V., Scott, L. D., Turner, A. P., 1984. Ferrocene-mediated enzyme electrode for amperometric determination of glucose. *Anal.Chem.* 56, 667-671.
- [Cha07] Chakrapani, V., Angus, J. C., Anderson, A. B., Wolter, S. D., Stoner, B. R., Sumanasekera, G. U., 2007. Charge transfer equilibria between diamond and an aqueous oxygen electrochemical redox couple. *Science* 318, 1424-1430.

- [Chr06] Christiaens, P., Vermeeren, V., Wenmackers, S., Daenen, M., Haenen, K., Nesladek, M., vandeVen, M., Ameloot, M., Michiels, L., Wagner, P., 2006. EDC-mediated DNA attachment to nanocrystalline CVD diamond films. *Biosens.Bioelectron.* 22, 170-177.
- [Chu76] Chua, K. S., Tan, I. K., 1976. Serum urea analysis using the Beckman BUN Analyzer. *J.Clin.Pathol.* 29, 517-519.
- [Clar05] Clare, T. L., Clare, B. H., Nichols, B. N., Abbott, N. L., Hamers, R. J., 2005. Functional monolayers for improved resistance to protein adsorption: Oligo(ethylene glycol)-modified silicon and diamond surfaces. *Langmuir* 21, 6344-6355.
- [Cla56] Clark, L. C., Jr., 1956. Monitor and control of blood and tissue oxygen tensions. *Trans.Am.Artif.Intern.Organs* 2, 41-48.
- [Cla62] Clark, L. C., Jr., Lyons, C., 1962. Electrode systems for continuous monitoring in cardiovascular surgery. *Ann.N.Y.Acad.Sci.* 102, 29-45.
- [Coo05] Cooreman, P., Thoelen, R., Manca, J., vandeVen, M., Vermeeren, V., Michiels, L., Ameloot, M., Wagner, P., 2005. Impedimetric immunosensors based on the conjugated polymer PPV. *Biosens.Bioelectron.* 20, 2151-2156.
- [D'O03] D'Orazio, P., 2003. Biosensors in clinical chemistry. *Clin.Chim.Acta* 334, 41-69.
- [Dan00] Danesh, J., Whincup, P., Walker, M., Lennon, L., Thomson, A., Appleby, P., Gallimore, J. R., Pepys, M. B., 2000. Low grade inflammation and coronary heart disease: prospective study and updated meta-analyses. *BMJ* 321, 199-204.
- [Dava05] Davanture, S., Leignadier, J., Milani, P., Soubeyran, P., Malissen, B., Malissen, M., Schmitt-Verhulst, A. M., Boyer, C., 2005. Selective defect in antigen-induced TCR internalization at the immune synapse of CD8 T cells bearing the ZAP-70(Y292F) mutation. *J.Immunol.* 175, 3140-3149.
- [Dav94] Davidson, J. L., *Synthetic diamond: Emerging CVD science and technology*, Spear, K. E., Dismukes, J. P., Wiley-Interscience, New York, 1994
- [Davi05] Davis, F., Nabok, A. V., Higson, S. P., 2005. Species differentiation by DNA-modified carbon electrodes using an ac impedimetric approach. *Biosens.Bioelectron.* 20, 1531-1538.
- [Davi92] Davis, R. F., *Diamond films and coatings: Development, properties and applications*, Davis, R. F., Noyes Publications, New Jersey, 1992
- [Dil04] Dill, K., Montgomery, D. D., Ghindilis, A. L., Schwarzkopf, K. R., Ragsdale, S. R., Oleinikov, A. V., 2004. Immunoassays based on electrochemical detection using microelectrode arrays. *Biosens.Bioelectron.* 20, 736-742.
- [Div75] Divis, C., 1975. *Annals of Microbiology* 126A, 175-186.
- [Don02] Dong, S., Chen, X., 2002. Some new aspects in biosensors. *J.Biotechnol.* 82, 303-323.

- [Eck82] Eckfeldt, J., Levine, A. S., Greiner, C., Kershaw, M., 1982. Urinary urea: Are currently available methods adequate for revival of an almost abandoned test? *Clin.Chem.* 28, 1500-1502.
- [Fan03] Fang, A., Ng, H. T., Li, S. F., 2003. A high-performance glucose biosensor based on monomolecular layer of glucose oxidase covalently immobilised on indium-tin oxide surface. *Biosens.Bioelectron.* 19, 43-49.
- [Fau06] Faucheux, A., Gouget-Laemmel, A. C., Henry, d., V, Boukherroub, R., Ozanam, F., Allongue, P., Chazalviel, J. N., 2006. Well-defined carboxyl-terminated alkyl monolayers grafted onto H-Si(111): Packing density from a combined AFM and quantitative IR study. *Langmuir* 22, 153-162.
- [Fen07] Feng, K., Li, J., Jiang, J. H., Shen, G. L., Yu, R. Q., 2007. QCM detection of DNA targets with single-base mutation based on DNA ligase reaction and biocatalyzed deposition amplification. *Biosens.Bioelectron.* 22, 1651-1657.
- [Fer07] Ferreira, G. N., Encarnacao, J. M., Rosa, L., Rodrigues, R., Breyner, R., Barrento, S., Pedro, L., Ires da, S. F., Goncalves, J., 2007. Recombinant single-chain variable fragment and single domain antibody piezoimmunosensors for detection of HIV1 virion infectivity factor. *Biosens.Bioelectron.* 23, 384-392.
- [Fie87] Field, J. E., 1987. Mechanical and physical properties of diamond. *Inst.Phys.Conf.Ser.* 75, 181-205.
- [Fis79] Fischer, S. G., Lerman, L. S., 1979. Length-independent separation of DNA restriction fragments in two-dimensional gel electrophoresis. *Cell* 16, 191-200.
- [Fla84] Flanagan, M. T., Pantell, R. H., 1984. Surface plasmon resonance and immunosensors. *Electron.Lett.* 20, 968-970.
- [Fon84] Fonong, T., Rechnitz, G. A., 1984. Homogeneous potentiometric enzyme immunoassay for human immunoglobulin G. *Anal.Chem.* 56, 2586-2590.
- [Fre77] Free, A. H., 1977. Analytical applications of immobilized enzymes. *Ann.Clin.Lab Sci.* 7, 479-485.
- [Fri02] Fritz, J., Cooper, E. B., Gaudet, S., Sorger, P. K., Manalis, S. R., 2002. Electronic detection of DNA by its intrinsic molecular charge. *Proc.Natl.Acad.Sci.U.S.A* 99, 14142-14146.
- [Gar05] Garrido, J. A., Heimbeck, T., Stutzmann, M., 2005. Temperature-dependent transport properties of hydrogen-induced diamond surface conductive channels. *Phys.Rev.B:Condens.Matter* 71,
- [Gar03] Garrido, J. A., Nebel, C. E., Todt, R., Rosel, G., Amann, M. C., Stutzmann, M., Snidero, E., Bergonzo, P., 2003. Fabrication of in-plane gate transistors on hydrogenated diamond surfaces. *Appl.Phys.Lett.* 82, 988-990.
- [Gey85] Geyssant, A., Dormois, D., Barthelemy, J. C., Lacour, J. R., 1985. Lactate determination with the lactate analyser LA 640: a critical study. *Scand.J.Clin.Lab Invest* 45, 145-149.

- [Gor05] Gorton, L. O., *Comprehensive analytical chemistry*, Elsevier Science, Amsterdam, 2005
- [Gra90] Grabarek, Z., Gergely, J., 1990. Zero-length crosslinking procedure with the use of active esters. *Anal.Biochem.* 185, 131-135.
- [Gra99] Granger, M. C., Xu, J., Strojek, J. W., Swain, G. M., 1999. Polycrystalline diamond electrodes: basic properties and applications as amperometric detectors in flow injection analysis and liquid chromatography. *Anal.Chim.Acta* 397, 145-161.
- [Gri00] Grimnes, S., Martinsen, O. S., *Bioimpedance & Bioelectricity*, Academic Press, London, 2000
- [Gu05] Gu, H., Su, X., Loh, K. P., 2005. Electrochemical impedance sensing of DNA hybridization on conducting polymer film-modified diamond. *J.Phys.Chem.B* 109, 13611-13618.
- [Gui73] Guilbault, G. G., Lubrano, G. J., 1973. An enzyme electrode for the amperometric determination of glucose. *Anal.Chim.Acta* 64, 439-455.
- [Gui70] Guilbault, G. G., Montalvo, J. G., 1970. An enzyme electrode for the substrate urea. *J.Am.Chem.Soc.* 92, 2533-2538.
- [Här04] Härtl, A., Schmich, E., Garrido, J. A., Hernando, J., Catharino, S. C. R., Walter, S., Feulner, P., Kromka, A., Steinmuller, D., Stutzmann, M., 2004. Protein-modified nanocrystalline diamond thin films for biosensor applications. *Nat.Mater.* 3, 736-742.
- [Has94] Hashimoto, K., Ito, K., Ishimori, Y., 1994. Sequence-specific gene detection with a gold electrode modified with DNA probes and an electrochemically active dye. *Anal.Chem.* 66, 3830-3833.
- [Hav97] Haverkate, F., Thompson, S. G., Pyke, S. D., Gallimore, J. R., Pepys, M. B., 1997. Production of C-reactive protein and risk of coronary events in stable and unstable angina. European Concerted Action on Thrombosis and Disabilities Angina Pectoris Study Group. *Lancet* 349, 462-466.
- [Hei85] Heineman, W. R., Halsall, H. B., 1985. Strategies for electrochemical immunoassay. *Anal.Chem.* 57, 1321A-1331A.
- [Hok87] Hokama, Y., Nakamura, R. M., 1987. C-reactive protein: Current status and future perspectives. *J.Clin.Lab.Anal.* 1, 15-27.
- [Hu06] Hu, W. P., Hsu, H. Y., Chiou, A., Tseng, K. Y., Lin, H. Y., Chang, G. L., Chen, S. J., 2006. Immunodetection of pentamer and modified C-reactive protein using surface plasmon resonance biosensing. *Biosens.Bioelectron.* 21, 1631-1637.
- [Hua05] Huang, L., Reekmans, G., Saerens, D., Friedt, J.-M., Frederix, F., Francis, L., Muyldermans, S., Campitelli, A., Van Hoof, C., 2005. Prostate-specific antigen immunosensing based on mixed self-assembled monolayers, camel antibodies and colloidal gold enhanced sandwich assays. *Biosens.Bioelectron.* 21, 483-490.

- [Ing07] Ingebrandt, S., Han, Y., Nakamura, F., Poghossian, A., Schöning, M. J., Offenhäusser, A., 2007. Label-free detection of single nucleotide polymorphisms utilizing the differential transfer function of field-effect transistors. *Biosens.Bioelectron.* 22, 2834-2840.
- [Ing06] Ingebrandt, S., Offenhäusser, A., 2006. Label-free detection of DNA using field-effect transistors. *Phys.Stat.Sol.(a)* 203, 3399-3411.
- [Jia96] Jiali, W., Jianzhong, Z., Guoxiong, Z., Xinru, L., Nianyi, C., 1996. Fabrication and application of a diamond-film glucose biosensor based on a H₂O₂ microarray electrode. *Anal.Chim.Acta* 327, 133-137.
- [Joh91] John, R., Spencer, M., Wallace, G. G., Smyth, M. R., 1991. Development of a polypyrrole-based human serum albumin sensor. *Anal.Chim.Acta* 249, 381-385.
- [Kel99] Kelley, S. O., Barton, J. K., 1999. Electron transfer between bases in double helical DNA. *Science* 283, 375-381.
- [Koid04] Koide, Y., 2004. Depletion layer in pn-junction of diamond with phosphorus donor and boron acceptor. *Diamond Relat.Mater.* 13, 1963-1966.
- [Koi97] Koizumi, S., Kamo, M., Sato, Y., Ozaki, H., Inuzuka, T., 1997. Growth and characterization of phosphorous doped (111) homoepitaxial diamond thin films. *Appl.Phys.Lett.* 71, 1065-1067.
- [Kon03] Kondo, T., Honda, K., Tryk, D. A., Fujishima, A., 2003. AC impedance studies of anodically treated polycrystalline and homoepitaxial boron-doped diamond electrodes. *Electrochim.Acta* 48, 2739-2748.
- [Kre87] Kremsky, J. N., Wooters, J. L., Dougherty, J. P., Meyers, R. E., Collins, M., Brown, E. L., 1987. Immobilization of DNA via oligonucleotides containing an aldehyde or carboxylic acid group at the 5' terminus. *Nucleic Acids Res.* 15, 2891-2909.
- [Las04] Lasseter, T. L., Clare, B. H., Abbott, N. L., Hamers, R. J., 2004. Covalently modified silicon and diamond surfaces: Resistance to nonspecific protein adsorption and optimization for biosensing. *J.Am.Chem.Soc.* 126, 10220-10221.
- [Lee99] Lee, S.-T., Lin, Z., Jiang, X., 1999. CVD diamond films: Nucleation and growth. *Mater.Sci.Eng.* 25, 123-154.
- [Lie83] Liedberg, W., Nylander, C., Lundström, I., 1983. Surface plasmon resonance for gas detection and biosensing. *Sens.Actuators, A* 4, 299-304.
- [Liu93] Liu, H., Dandy, D. S., *Diamond chemical vapour deposition: Nucleation and early growth stages*, Noyes Publications, Park Ridge, 1993
- [Lüb75] Lübbers, D. W., Opitz, N., 1975. The pCO₂-pO₂-optode: A new probe for measurement of pCO₂ or pO in fluids and gases (authors transl). *Z.Naturforsch.[C.]* 30, 532-533.
- [Mai01] Maier, F. 2001. Electronic properties of diamond interfaces.

- [Mai00] Maier, F., Riedel, M., Mantel, B., Ristein, J., Ley, L., 2000. Origin of surface conductivity in diamond. *Phys.Rev.Lett.* 85, 3472-3475.
- [Mair07] Mairal, T., Cengiz, O., V, Lozano, S. P., Mir, M., Katakis, I., O'sullivan, C. K., 2007. Aptamers: molecular tools for analytical applications. *Anal.Bioanal.Chem.*
- [Mal03] Malhotra, B. D., Chaubey, A., 2003. Biosensors for clinical diagnostics industry. *Sens.Actuators, A* 91, 117-127.
- [May00] May, P. W., 2000. Diamond thin films: A 21st-century material. *Phil.Trans.R.Soc.Lond.A* 358, 473-495.
- [Mem00] Memming, R., *Semiconductor electrochemistry*, Wiley-VCH, Weinheim, 2000
- [Mil92] Millan, K. M., Spurmanis, A. J., Mikkelsen, S. R., 1992. Covalent immobilization of DNA into glassy-carbon electrodes. *Electroanalysis* 4, 929-932.
- [Moi06] Moiseev, L., Unlu, M. S., Swan, A. K., Goldberg, B. B., Cantor, C. R., 2006. DNA conformation on surfaces measured by fluorescence self-interference. *Proc.Natl.Acad.Sci.U.S.A* 103, 2623-2628.
- [Mor90] Moreno-Bondi, M. C., Wolfbeis, O. S., Leiner, M. J., Schaffar, B. P., 1990. Oxygen optrode for use in a fiber-optic glucose biosensor. *Anal.Chem.* 62, 2377-2380.
- [Mor04] Moreno-Hagelsieb, L., Lobert, P. E., Pampin, R., Bourgeois, D., Remacle, J., Flandre, D., 2004. Sensitive DNA electrical detection based on interdigitated Al/Al₂O₃ microelectrodes. *Sens.Actuators, B* 98, 269-274.
- [Mos74] Mosbach, K., Danielsson, B., 1974. An enzyme thermistor. *Biochim.Biophys.Acta* 364, 140-145.
- [Mot96] Motmans, K., Raus, J., Vandevyver, C., 1996. Quantification of cytokine messenger RNA in transfected human T cells by RT-PCR and an automated electrochemiluminescence-based post-PCR detection system. *J.Immunol.Methods* 190, 107-116.
- [Mum93] Mumm, D. R., Faber, K. T., Drory, M. D., Gardinier, C. F., 1993. High-temperature hardness of chemically vapor-deposited diamond. *J.Am.Ceram.Soc.* 76, 238-240.
- [Neb06] Nebel, C. E., Rezek, B., Shin, D., Watanabe, H., 2006. Surface electronic properties of H-terminated diamond in contact with adsorbates and electrolytes. *Phys.Stat.Sol.(a)* 203, 3273-3298.
- [Neb07] Nebel, C. E., Shin, D., Rezek, B., Tokuda, N., Uetsuka, H., Watanabe, H., 2007. Diamond and biology. *J.R.Soc.Interface* 4, 439-461.
- [Nes05] Nesladek, M., 2005. Conventional n-type doping in diamond: State of the art and recent progress. *Semicond.Sci.Technol.* 20, R19-R27.
- [Nic05] Nichols, B. M., Butler, J. E., Russell, J. N., Jr., Hamers, R. J., 2005. Photochemical functionalization of hydrogen-terminated diamond surfaces: a structural and mechanistic study. *J.Phys.Chem.B* 109, 20938-20947.

- [Par02] Park, S. J., Taton, T. A., Mirkin, C. A., 2002. Array-based electrical detection of DNA with nanoparticle probes. *Science* 295, 1503-1506.
- [Pas00] Pasceri, V., Willerson, J. T., Yeh, E. T., 2000. Direct proinflammatory effect of C-reactive protein on human endothelial cells. *Circulation* 102, 2165-2168.
- [Pet01] Peterson, A. W., Heaton, R. J., Georgiadis, R. M., 2001. The effect of surface probe density on DNA hybridization. *Nucleic Acids Res.* 29, 5163-5168.
- [Pie93] Pierson, H. O., *Handbook of carbon, graphite, diamond and fullerenes*, Noyes Publications, New Jersey, 1993
- [Pog05] Poghossian, A., Cherstvy, A., Ingebrandt, S., Offenhäuser, A., Schöning, M. J., 2005. Possibilities and limitations of label-free detection of DNA hybridization with field-effect-based devices. *Sens.Actuators, B* 111-112, 470-480.
- [Ran07] Rant, U., Arinaga, K., Scherer, S., Pringsheim, E., Fujita, S., Yokoyama, N., Tornow, M., Abstreiter, G., 2007. Switchable DNA interfaces for the highly sensitive detection of label-free DNA targets. *Proc.Natl.Acad.Sci.U.S.A* 104, 17364-17369.
- [Rao99] Rao, T. N., Yagi, I., Miwa, T., Tryk, D. A., Fujishima, A., 1999. Electrochemical oxidation of NADH at highly boron-doped diamond electrodes. *Anal.Chem.* 71, 2506-2511.
- [Ras91] Rasmussen, S. R., Larsen, M. R., Rasmussen, S. E., 1991. Covalent immobilization of DNA onto polystyrene microwells: The molecules are only bound at the 5' end. *Anal.Biochem.* 198, 138-142.
- [Rez02] Rezek, B., Garrido, J. A., Stutzmann, M., Nebel, C. E., Snidero, E., Bergonzo, P., 2002. Local oxidation of hydrogenated diamond surfaces for device fabrication. *Phys.Stat.Sol.(a)* 193, 523-528.
- [Ric05] Rick, J., Chou, T. C., 2005. Enthalpy changes associated with protein binding to thin films. *Biosens.Bioelectron.* 20, 1878-1883.
- [Rid97] Ridker, P. M., Cushman, M., Stampfer, M. J., Tracy, R. P., Hennekens, C. H., 1997. Inflammation, aspirin, and the risk of cardiovascular disease in apparently healthy men. *N.Engl.J.Med.* 336, 973-979.
- [Sau59] Sauerbrey, G., 1959. Verwendung von Schwingquarzen zur Wägung dünner Schichten und zur Mikrowägung. *Z.Phys.* 155, 206-222.
- [Sch95] Schena, M., Shalon, D., Davis, R. W., Brown, P. O., 1995. Quantitative monitoring of gene expression patterns with a complementary DNA microarray. *Science* 270, 467-470.
- [Schö06] Schöning, M. J., Poghossian, A., 2006. Bio FEDs (field-effect devices): State-of-the-art and new directions. *Electroanalysis* 18, 1893-1900.

- [Sch76] Schuster, P., Zundel, G., Sandorfy, C., The hydrogen bond: Recent developments in theory and experiment, Schuster, P., Zundel, G., Sandorfy, C., North-Holland Publishing Co., Amsterdam, 1976
- [Sch04] Schwonbeck, S., Krause-Griep, A., Gajovic-Eichelmann, N., Ehrentreich-Forster, E., Meinel, W., Glatt, H., Bier, F. F., 2004. Cohort analysis of a single nucleotide polymorphism on DNA chips. *Biosens.Bioelectron.* 20, 956-966.
- [Ses03] Sesso, H. D., Buring, J. E., Rifai, N., Blake, G. J., Gaziano, J. M., Ridker, P. M., 2003. C-reactive protein and the risk of developing hypertension. *JAMA* 290, 2945-2951.
- [Sil97] Silin, V., V. Weetall, H., Vanderah, D. J., 1997. SPR Studies of the Nonspecific Adsorption Kinetics of Human IgG and BSA on Gold Surfaces Modified by Self-Assembled Monolayers (SAMs). *J.Colloid Interface Sci.* 185, 94-103.
- [Son06] Song, K. S., Zhang, G. J., Nakamura, Y., Furukawa, K., Hiraki, T., Yang, J. H., Funatsu, T., Ohdomari, I., Kawarada, H., 2006. Label-free DNA sensors using ultrasensitive diamond field-effect transistors in solution. *Phys.Rev.E.Stat.Nonlin.Soft.Matter Phys.* 74, 041919-
- [Sout97] Souteyrand, E., Cloarec, J. P., Martin, J. R., Wilson, C., Lawrence, I., Mikkelsen, S., Lawrence, M. F., 1997. Direct detection of the hybridization of synthetic homooligomer DNA sequences by field effect. *J.Phys.Chem.B* 101, 2980-2985.
- [Sou75] Southern, E. M., 1975. Detection of specific sequences among DNA fragments separated by gel electrophoresis. *J.Mol.Biol.* 98, 503-517.
- [Ste00] Steel, A. B., Levicky, R. L., Herne, T. M., Tarlov, M. J., 2000. Immobilization of nucleic acids at solid surfaces: Effect of oligonucleotide length on layer assembly. *Biophys.J.* 79, 975-981.
- [Stef03] Stefan, R. I., Bokretsiou, R. G., van Staden, J. F., Aboul-Enein, H. Y., 2003. Simultaneous determination of creatine and creatinine using amperometric biosensors. *Talanta* 60, 1223-1228.
- [Str00] Strother, T., Cai, W., Zhao, X. S., Hamers, R. J., Smith, L. M., 2000. Synthesis and characterization of DNA modified silicon (111) surfaces. *J.Am.Chem.Soc.* 122, 1205-1209.
- [Str00] Strother, T., Knickerbocker, T., Russel, N. J. Jr., Butler, E. J., Smith, L. M., Hamers, R. J., 2001. Photochemical functionalization of diamond films. *J.Am.Chem.Soc.* 123, 968-971.
- [Su04] Su, X., Robelek, R., Wu, Y., Wang, G., Knoll, W., 2004. Detection of point mutation and insertion mutations in DNA using a quartz crystal microbalance and MutS, a mismatch binding protein. *Anal.Chem.* 76, 489-494.
- [Swa93] Swain, G. M., Ramesham, M., 1993. The electrochemical activity of boron-doped polycrystalline diamond thin-film electrodes. *Anal.Chem.* 65, 345-351.

- [Tak00] Takahashi, K., Tanga, M., Takai, O., Okamura, H., 2000. DNA bonding to diamond. *Bio.Ind.* 17, 44-51.
- [Tan95] Tang, L., Tsai, C., Gerberich, W. W., Kruckeberg, L., Kania, D. R., 1995. Biocompatibility of chemical-vapour-deposited diamond. *Biomaterials* 16, 483-488.
- [Ter05] Teraji, J., Hamada, M., Wada, H., Yamamoto, M., Arima, K., Ito, T., 2005. High rate growth and electrical-optical properties of high-quality homoepitaxial diamond (100) films. *Diamond Relat.Mater.* 14, 255-260.
- [Tro97] Troupe, C. E., Drummond, I. C., Graham, C., Grice, J., John, P., Wilson, J. I. B., Jubber, M. G., Morrison, N. A., 1997. Diamond-based glucose sensors. *Diamond Relat.Mater.* 7, 575-580.
- [Tur95] Turner, A. P., 1995. Electrochemical sensors for continuous monitoring during surgery and intensive care. *Acta Anaesthesiol.Scand.Suppl* 104, 15-19.
- [Uet07] Uetsuka, H., Shin, D., Tokuda, N., Saeki, K., Nebel, C. E., 2007. Electrochemical grafting of boron-doped single-crystalline chemical vapor deposition diamond with nitrophenyl molecules. *Langmuir* 23, 3466-3472.
- [Upd67] Updike, S. J., Hicks, G. P., 1967. The enzyme electrode. *Nature* 214, 986-988.
- [Ush02] Ushizawa, K., Sato, Y., Mitsumori, T., Machinami, T., Ueda, T., Ando, T., 2002. Covalent immobilization of DNA on diamond and its verification by diffuse reflectance infrared spectroscopy. *Chem.Phys.Lett.* 351, 105-108.
- [Usl04] Uslu, F., Ingebrandt, S., Mayer, D., Böcker-Meffert, S., Odenthal, M., Offenhäusser, A., 2004. Label-free fully electronic nucleic acid detection system based on a field-effect transistor device. *Biosens.Bioelectron.* 19, 1723-1731.
- [Ver07] Vermeeren, V., Bijmens, N., Wenmackers, S., Daenen, M., Haenen, K., Williams, O. A., Ameloot, M., vandeVen, M., Wagner, P., Michiels, L., 2007. Towards a Real-Time, Label-Free, Diamond-Based DNA Sensor. *Langmuir* 23, 13193-13202.
- What is a quartz crystal microbalance - QCM, <http://www.pharmaceutical-int.com/categories/qcm-technology/quartz-crystal-microbalance-qcm.asp>
- [Wa04] Wang, J., Firestone, M. A., Auciello, O., Carlisle, J. A., 2004. Functionalization of ultrananocrystalline diamond films by electrochemical reduction of aryldiazonium salts. *Langmuir* 20, 450-456.
- [Wan04] Wang, J., Kawde, A. N., Jan, M. R., 2004. Carbon-nanotube-modified electrodes for amplified enzyme-based electrical detection of DNA hybridization. *Biosens.Bioelectron.* 20, 995-1000.
- [Wang04] Wang, R., Tombelli, S., Minunni, M., Spiriti, M. M., Mascini, M., 2004. Immobilisation of DNA probes for the development of SPR-based sensing. *Biosens.Bioelectron.* 20, 967-974.

- [Wei03] Wei, J., Mu, Y., Song, D., Fang, X., Liu, X., Bu, L., Zhang, H., Zhang, G., Ding, J., Wang, W., Jin, Q., Luo, G., 2003. A novel sandwich immunosensing method for measuring cardiac troponin I in sera. *Anal.Biochem.* 321, 209-216.
- [Wen05] Wenmackers, S., Christiaens, P., Daenen, M., Haenen, K., Nesladek, M., vandeVen, M., Vermeeren, V., Michiels, L., Ameloot, M., Wagner, P., 2005. DNA attachment to nanocrystalline diamond films. *Phys.Stat.Sol.(a)* 202, 2212-2216.
- [Wen03] Wenmackers, S., Haenen, K., Nesladek, M., Wagner, P., Michiels, L., vandeVen, M., Ameloot, M., 2003. Covalent immobilization of DNA on CVD diamond films. *Phys.Stat.Sol.(a)* 199, 44-48.
- [Wen07] Wenmackers, S., Silaghi, S. D., Roodenko, K., Vermeeren, V., Williams, O. A., Daenen, M., Douhéret, O., D'Haen, J., Hardy, A., Van Bael, M. K., Hinrichs, K., Cobet, C., vandeVen, M., Ameloot, M., Haenen, K., Michiels, L., Esser, N., and Wagner, P. 2007. Structural and optical properties of DNA layers covalently attached to diamond surfaces.
- [Wil91] Wilks, J., Wilks, E., Properties and applications of diamond, Butterworth-Heinemann, Oxford, 1991
- [Will06] Williams, O. A., Nesládek, M., 2006. Growth and properties of nanocrystalline diamond films. *Phys.Stat.Sol.(a)* 203, 3375-3386.
- [Wu03] Wu, C. F., Valdes, J. J., Bentley, W. E., Sekowski, J. W., 2003. DNA microarray for discrimination between pathogenic 0157:H7 EDL933 and non-pathogenic Escherichia coli strains. *Biosens.Bioelectron.* 19, 1-8.
- [Yak02] Yakovleva, J., Davidsson, R., Lobanova, A., Bengtsson, M., Eremin, S., Laurell, T., Enneus, J., 2002. Microfluidic enzyme immunoassay using silicon microchip with immobilized antibodies and chemiluminescence detection. *Anal.Chem.* 74, 2994-3004.
- [Yam00] Yamanaka, S., Takeuchi, D., Watanabe, H., Okushi, H., Kajimura, K., 2000. Low-compensated boron-doped homoepitaxial diamond films. *Diamond Relat.Mater.* 9, 956-959.
- [Yan02] Yang, W., Auciello, O., Butler, J. E., Cai, W., Carlisle, J. A., Gerbi, J. E., Gruen, D. M., Knickerbocker, T., Lasseter, T. L., Russell, J. N., Jr., Smith, L. M., Hamers, R. J., 2002. DNA-modified nanocrystalline diamond thin-films as stable, biologically active substrates. *Nat.Mater.* 1, 253-257.
- [Yan04] Yang, W., Butler, J. E., Russell, J. N., Jr., Hamers, R. J., 2004. Interfacial electrical properties of DNA-modified diamond thin films: Intrinsic response and hybridization-induced field effects. *Langmuir* 20, 6778-6787.
- [Yan07] Yang, W., Butler, J. E., Russell, J. N., Jr., Hamers, R. J., 2007. Direct electrical detection of antigen-antibody binding on diamond and silicon substrates using electrical impedance spectroscopy. *Analyst* 132, 296-306.

- [Ye03] Ye, Y. K., Zhao, J. H., Yan, F., Zhu, Y. L., Ju, H. X., 2003. Electrochemical behavior and detection of hepatitis B virus DNA PCR production at gold electrode. *Biosens.Bioelectron.* 18, 1501-1508.
- [You00] Young, H. D., Freedman, R. A., University Physics, tenth edition, Addison Wesley, Boston, 2000
- [Zai01] Zaitsev, A. M., Optical properties of diamond: A data handbook, Springer-Verlag, Berlin, 2001

CURRICULUM VITAE

Education:

Veronique Vermeeren completed her high school education at the Humariora Virga Jesse, at the Guffenslaan 27 (first three years) and the Maastrichtersteenweg 62 (last three years) in Hasselt from 1993 to 1999. She obtained a diploma 'Algemeen Secundair Onderwijs (ASO)' in Latin-Modern Languages in 1999.

She attended Hasselt University from 1999 to 2003, at the campus in Diepenbeek and Maastricht, and obtained a degree in Biomedical Sciences in 2003. She completed a mandatory internship of seven months at the Vrije Universiteit Brussel (VUB), at the department of Experimental Pathology, in 2002-2003, under the supervision of Dr. Peter In 't Veld. This led to the completion of her graduating thesis entitled '*HER 2-amplificatie in borsttumoren: vergelijking van FISH en 'real-time' kwantitatieve PCR*'.

In 2003, she started her PhD studies, participating in a project entitled '*CVD Diamond: a novel multifunctional material for high temperature electronics, high power/high frequency electronics and bioelectronics*', funded by the Institute for the Promotion of Innovation by Science and Technology in Flanders (IWT). This was completed in 2008, with a PhD thesis entitled '*Towards label-free, real-time biosensors: A nanocrystalline diamond-based sensor platform for DNA- and immunosensors*'.

Bibliography:

Publications in peer reviewed proceedings

"Head-on immobilization of DNA fragments on synthetic CVD-Diamond layers"

S. Wenmackers, P. Christiaens, W. Deferme, M. Daenen, K. Haenen, M. Nesládek, P. Wagner, L. Michiels, M. vandeVen, **V. Vermeeren**, M. Ameloot, J. Wouters, L. Naelaerts, Z. Mekhalif

Materials Science Forum, 2005. 492-493, 267-272.

"DNA attachment to nanocrystalline diamond films for future biosensing applications"

S. Wenmackers, P. Christiaens, M. Daenen, K. Haenen, M. Nesládek, M. vandeVen, **V. Vermeeren**, L. Michiels, M. Ameloot, P. Wagner
Physica Status Solidi (a), 2005. 195, 1, 3-10.

"EDC-mediated DNA attachment to nanocrystalline diamond"

Vermeeren V., Christiaens P., Wenmackers S., Vandeven M., Ameloot M., Wagner P., Michiels L.
Communications in Agricultural and Applied Biological Sciences, 2005. 70, 285-288.

Publications in peer reviewed journals

"Impedimetric immunosensors based on the conjugated polymer PPV"

Cooreman P., Thoelen R., Manca J., vandeVen M., **Vermeeren V.**, Michiels L., Ameloot M., Wagner P.
Biosensors & Bioelectronics, 2005. 20, 2151-2156.

"EDC Mediated DNA attachment to CVD diamond films"

Christiaens P.*, **Vermeeren V.***, Wenmackers S., Daenen M., Haenen K., Nesládek M., vandeVen M., Ameloot M., Michiels L., Wagner P.
Biosensors & Bioelectronics, 2006. 22, 170-177.

"Towards a real-time, label-free diamond-based DNA sensor"

Vermeeren V.*, Bijmens N.*, Wenmackers S., Daenen M., Haenen K., Williams O.A., Ameloot M., vandeVen M., Wagner P., Michiels L.
Langmuir, 2007. 23, 13193-13202.

Articles submitted for publication:

"Topographical and functional characterisation of the ssDNA probe layer generated through EDC-mediated covalent attachment to nanocrystalline diamond using fluorescence microscopy"

Vermeeren V.*, Wenmackers S.*, Daenen M., Haenen K., Williams O.A., Ameloot M., vandeVen M., Wagner P., Michiels L.

Articles in preparation:

"Towards a real-time, label-free diamond-based immunosensor"

Bijnens N.*, **Vermeeren V.***, Wenmackers S., Daenen M., Haenen K., Williams O.A., Ameloot M., vandeVen M., Michiels L., Wagner P.

* contributed equally to the publication

DANKWOORD

Ik weet niet wat het precies is met dankwoorden, maar ik lees ze graag. Ik vind het altijd zo'n mooie getuigenis dat een groot werk alleen maar tot een goed einde kan komen dankzij de samenwerking en de hulp van welbepaalde personen. Hoe moeilijk het in feite is om zo'n dankwoord te schrijven, dat vertelt niemand er ooit bij. Hoe giet je in woorden hoe dankbaar je iemand bent dat hij of zij dag in dag uit met je bezig is geweest? Hoe maak je duidelijk hoe zeer je het apprecieerde wanneer je baas iets nog maar eens een keer uitlegde maar je brein het gewoon niet wilde horen? Hoe bedank je mensen voor het feit dat ze het fijn maakten om te komen werken? En hoe bedank je iemand die het heerlijk maakt om thuis te komen? Ik sta op dit moment voor die onmetelijke klus, die zovelen vóór mij toch schijnen geklaard te hebben. Here it goes.

Allereerst een woordje voor mijn promotor, Prof. Dr. Luc Michiels. Luc, waar moet ik beginnen? Als ik terugdenk aan mijn eerste weken, dan is het net of ik volledig nieuwe hersentakken heb gegroeid. Wat moet ik vroeger toch domme vragen hebben gesteld! Alhoewel, soms doe ik dat nog steeds. Oude gewoontes roesten niet ☺. Maar toch heb ik het gevoel dat ik ongelooflijk veel heb geleerd, en dat komt door jou. Ik ben zelfs een kei geworden in het ontcijferen van je handschrift ☺! Bedankt voor je tijd, je geduld, je humor, en je bemoedigende woorden als ik het maar weer eens niet zag zitten. En vooral, bedankt voor de kans om aan dit project te mogen beginnen.

Ik wil ook mijn copromotor, Prof. Dr. Marcel Ameloot, en de rest van het 'Biosensor'-team, Prof. Dr. Patrick Wagner en Dr. Martin vandeVen bedanken. Jullie stonden steeds paraat met hulp en ideeën, en dankzij jullie opmerkingen en opbouwende kritiek is dit eindwerk tot voltooiing gekomen. Martin, ik moest nog maar denken aan een vraag, en een uur later stak een lijst met literatuur in mijn mailbox die je voor me had uitgepluisd. Ik bewonder je grenzeloze kennis, en apprecieer enorm je interesse die boekdelen sprak elke keer je even kwam binnenwippen aan de confocale. Bedankt.

Verder richt ik ook een woord van dank tot de leden van de jury. Prof. Dr. Peter Dubruel, Prof. Dr. Frans Ramaekers, Prof. Dr. Jeroen Lammertyn, Prof. Dr.

Piet Stinissen en Prof. Dr. Andreas Offenhäusser. Bedankt voor de tijd en moeite die U stak in het nalezen en evalueren van dit eindwerk.

Dan uiteraard enkele mensen die dicht met me hebben samengewerkt. Zonder hen was dit eindwerk er nooit geweest. Sylvia, bedankt voor de leuke uurtjes aan de confocale, ik hoop dat er daar nog veel van mogen volgen. Ook geen enkele hulpverlening was je te veel gevraagd. Je weet enorm veel, en ik maakte daar, moet ik eerlijk toegeven, vaak en graag gebruik van. Niet in het minste als het maken van een stomme grafiek maar weer eens boven mijn mentale capaciteiten reikte ☺. Nathalie, zonder jou wist ik nu nog steeds niet wat een capaciteit is. Wat heb ik jou onnoemelijk vaak moeten lastigvallen met de meest banale fysicavragen die voor jou gewoon de logica zelf zijn, maar die mij rood voor de ogen deden zien. Je moet op den duur toch wel gedacht hebben: "Bioloog, blijf bij je leest!" Maar steeds nam je de tijd om het me uit te leggen, en steeds keerde de kleur voor mij weer terug. Bedankt voor de fijne uurtjes aan de impedantiemeter, zelfs als die stomme curve maar weer eens niets had gedaan, of een illustere persoon onze meting had afgezet ☺. Ik vraag me nog steeds af wie dat was... Ongetwijfeld zullen ook hier weer vele uren volgen. Ik kijk ernaar uit. Peter, Ronald en Evi, bedankt dat ik ook steeds aan jullie mijn vraagjes mocht stellen, en natuurlijk ook gewoon voor de leuke babbels op het IMO. Lars, Jan en Rob, succes met jullie doctoraat! Jullie zijn in goede handen!

En nu mijn lieve collega's. Marie-Paule, Iris, Danniëlle, Josianne en Johan, bedankt voor de heerlijke sfeer in het labo. Ik vind het geweldig om met jullie in hetzelfde lokaal te werken, en daaronder versta ik uiteraard ook de 'tettermomenten', vooral over mijn tuin! Want vruchtbaar werk begint met een gezellige babbel! Heb ik al gezegd dat de grasmatten er liggen ☺? En natuurlijk ook de rest van de bende: Niels, Veerle, Debbie, Ruth, Kurt, Koen, Leentje, Jerome, Kim, Sofie, Judith, Bieke, Leen, Jean-Paul, Christel, Igna, Brigitte, Erik en Jean, jullie zijn fantastisch. Agnes, dank je wel voor mijn reddende 'administratieve' engel te zijn, en steeds tijd te vinden voor een uitbundige babbel en een bemoedigende schouderklop, vooral tijdens mijn laatste periode.

Over de jaren heb ik ook met velen mijn bureau gedeeld. Cindy en Klaartje, jullie waren de laatsten. Ondanks het feit dat het niet superlang heeft mogen duren, heb ik mij wel rot geamuseerd. Er was altijd tijd voor een leuke babbel

en hilariteit. 'Twee emmertjes water halen' zal nooit meer hetzelfde klinken... ☺ Ilse, ook aan jou heb ik enorm veel gehad. Ik ben nog steeds niet vergeten hoe je in mijn eerste maanden mijn 'moederkloek' was, en me in het labo wegwijs maakte. Niet alleen dat uiteraard, maar je was een fantastische bureaugenoot. Ik ben heel blij dat we nog steeds contact hebben. Neja! Mijn eerste kamergezel! Mijn partner-in-crime! Wat hadden we eigenlijk een prachtige tijd. We hebben hilarische momenten gehad, ook toen het huilen ons nader stond als het lachen. Vooral de vrijdagnamiddagen zal ik nooit vergeten ☺! Je werd een echte vriendin, en ik prijs mezelf heel gelukkig dat we mekaar niet uit het oog zijn verloren, maar mekaar nog zo regelmatig zien. Onze avondjes uit zijn een welkome afwisseling van stressvolle werkperiodes. Heel erg bedankt voor al het plezier en de fijne babbels. En ik wil nog steeds je paranimf zijn ☺!

Ook mijn goede vrienden van iets verder weg mogen niet ontbreken: Caroline, Dieter, Lieve, Kurt, Saskia, Dirk, Brenda en Ivo, jullie zijn een geweldige bende. Ik bof dat ik jullie ken. Bedankt voor de fantastisch toffe momenten samen. Wanneer is de volgende gelegenheid? En Brenda, ik ben superbenieuwd naar jullie nieuwe huisje!

Mijn 'pleegfamilie' Vosch zal voor eeuwig een speciaal plaatsje in mijn hart hebben. Ik hoop dat jullie weten hoeveel jullie voor me betekenen. Caroline, ik denk niet dat ik kan omschrijven wat voor een soort vriendin je voor me bent. Ik denk dat wij twee dat wel weten. Ik ben de laatste maanden verschrikkelijk geweest, ik ben zelfs je verjaardag vergeten. Straal daar tegenover sta jij, die nog niet eens vergeet wanneer ik een spannende vergadering heb, en de dag erna al belt om te vragen hoe het geweest is. Ik vind je geweldig, en ik ben zo blij dat je met Rob zo'n fantastisch leven hebt gevonden. Ik ben zo trots dat ik je ken, en ik ga je vreselijk missen als je naar Brussel verhuist. Maar af en toe eens mogen deel uitmaken van je nieuwe appartement zal de pijn wel verzachten... ☺ Bedankt voor alles.

Ik ben aan mijn eigen familie aanbeland. Mijn ouders en grootouders, bedankt om me de kans te geven om te studeren wat ik wilde. Bon en bonne, jullie hebben mijn twintig jaar durende schooltijd op de eerste rij gevolgd. Jullie zijn onnoemelijke keren getuige geweest van één of andere hysterische aanval wanneer er een examen zat aan te komen. Maar toch zien jullie me nog steeds

graag komen. Ik weet niet hoe jullie het hebben gedaan, maar ik sta hier door en voor jullie.

Mijn lieve schoonfamilie, die ik zonder twijfel tot mijn familie reken. Wat heb ik het getroffen met jullie. Mama, papa, Inge, Stef en Aza, bedankt voor de fijne band die we hebben. En bedankt voor het geloof en het vertrouwen.

De laatste woorden zijn voor jou, Peter. Ballie, wat jij hebt gedaan is niet te beschrijven. Hoe kan ik me er dan met een simpele 'dank je wel' vanaf maken? Je bent mijn rots, mijn vuurtoren, mijn haven en mijn computerwizard. Zonder jou wist ik nog steeds niet hoe Reference Manager werkte, en was mijn laptop, met mij erbij, al vijfhonderd keer gecrasht. Bedankt voor alle lieve woorden, de knuffels, de afwas, je geduld, je vertrouwen, de liters koffie, de duizenden print-outs, de vijftien backups op evenveel computers, het upscalen van mijn figuurkwaliteit en het aanhoren van mijn gezaag. Wat zou ik toch zonder je moeten doen? Ik zal het je nooit kunnen terugbetalen, maar ik hou van je voor altijd. Ik hoop dat dat als wildcard mag dienen...